Canadian Journal of
pure&applied
sciences

an International Journal

The Canadian Journal of Pure and Applied Sciences (CJPAS-ISSN 1715-9997) is a peer reviewed multi-disciplinary specialist journal aimed at promoting research worldwide in Agricultural Sciences, Biological Sciences, Chemical Sciences, Computer and Mathematical Sciences, Engineering, Environmental Sciences, Medicine and Physics (all subjects).

Every effort is made by the editors, board of editorial advisors and publishers to see that no inaccurate or misleading data, opinions, or statements appear in this journal, they wish to make clear that data and opinions appearing in the articles are the sole responsibility of the contributor concerned. The CJPAS accept no responsibility for the misleading data, opinion or statements.

Volume 3, Number 1
February 2009

CANADIAN JOURNAL OF PURE AND APPLIED SCIENCES

Board of Editorial Advisors

CONTENTS

Canadian Journal of
pure&applied
sciences

A BASELINE STUDY TO EVALUATE THE ESTROGENIC ACTIVITIES USING *IN-VITRO* YEAST ESTROGENIC SCREEN IN THE SELECTED RAMSAR SITES AND CREEK AREAS

M Zaheer Khan, Francis CP Law, Jasen Nelson, Walter Leung and Hao-Feng (Howie) Lai
Department of Biological Sciences, Simon Fraser University, Burnaby, British Columbia, Canada

ABSTRACT

Pakistan has a great variety of natural and manmade wetlands, and 19 Ramsar Sites are designated as internationally important wetlands, with a unique variety of aquatic and bird biodiversity. In the present study, a baseline study was conducted for the evaluation of estrogenic activities in the waters of three Ramsar Sites and one Creek areas. Among the selected study points of Indus Dolphin Wetland (study point1), Indus Dolphin (study point 2), Kinjhar Wetland (study point1), Kinjhar Wetland (study point 2), Haleji Wetland (study point 1), Haleji Wetland (study point 2), Creek areas (study point1) and Creek area (study point 2). During the study, selected points were surveyed two times i.e. in summer and winter, and water samples were collected in the 2nd week of November 2006 and 3rd week of May 2007. *In-Vitro* Yeast Estrogenic Screen (YES) assays techniques were used to evaluate the estrogenic activities in the water samples. Estrogenic activity recorded in the November 2006 samples of the Indus Dolphin Wetland (study point 1) was 9.31 ng/L estradiol equivalents and of the Kinjhar (study Point1) was 2.77 ng/L estradiol equivalents. In the samples collected in May 2007, the estrogenic activity found in the Indus Dolphin Wetland (study point1) was 3.14 ng/L estradiol equivalents, in the Indus Dolphin (study point 2) was 4.54 ng/L estradiol equivalents, in the Haleji Wetland (study pont1) was 1.4 ng/L estradiol equivalents, while in the Creek areas (study point1) was 7.89 ng/L estradiol equivalents and in the Creek areas (study point 2) was 2.93 ng/L estradiol equivalents. Results of this baseline study have indicated that the wetlands under study are more polluted in summer than in winter.

Keywords: Estrogenic activities, 17 β -estradiol, wetlands, Indus dolphin, pollution.

INTRODUCTION

In recent years, evidence has shown that several chemicals like estradiol, nonylphenol, bisphenol A, PCBs and some pesticides at different concentrations can cause disruption to endocrine systems and can affect hormonal control of development in aquatic biodiversity (Damstra *et al*., 2002; Hayes *et al*., 2002; Lintelmann *et al*., 2003). These chemicals are described as endocrine disrupting chemicals (EDCs). Several chemicals released into the environment can disrupt normal endocrine function in a variety of aquatic biodiversity. Environmental exposure to low and often analytically undetectable (ng/L) concentrations of endocrine disrupting compounds (EDCs) has caused physiological malfunction, such as sex reversal in fishes (Jobling *et al*., 1998). The number of anthropogenic and natural EDCs, released into the environment, is unknown since few chemicals have been tested for hormonal activity (Colborn and Clement, 1992). Globally some of the identified EDCs of potential concern have been detected in surface waters (Colborn and Clement, 1992). Generally in the aquatic environment, exposure of organisms to EDCs has been linked to endocrine effects in male fish such as vitellogenin induction and feminine reproductive organs (Aherne and Briggs, 1989; Purdom *et al*., 1994; Routledge *et al*., 1998;

Tyler *et al*., 1998). It is suggested that industrial and municipal effluents as well as urban and agricultural runoff are the important sources of EDCs discharged into the aquatic environment (Desbrow *et al*., 1998; Snyder *et al*., 1999; Boyd *et al*., 2003). Pesticides and related chemicals destroy the delicate balance between species that characterizes a functioning ecosystem. Pesticides also produce many physiological and biochemical changes in fresh water organisms by influencing the activities of enzymes. Therefore, alterations in the chemical composition of the natural aquatic environment usually affect behavioral and physiological systems of the inhabitants, particularly those of the fish (Khan and Law, 2005).

The evaluation of estrogenic activities in the aquatic environment and other wildlife has not been systematically assessed in Pakistan. We have no published data about estrogenic activities in wetlands waters and their effect on aquatic biodiversity, especially economically important fish, mussels and prawn species. Pakistan has 19 Ramsar Sites designated as Internationally Important Wetlands, with a surface area of 1,343,627 hectares (Table 1). The globally endangered warbler *Prinia burnesii* and endangered Indus dolphin has been recorded in the Chashma Barrage. The Haleji Lake is a wintering site for the globally threatened pelican *Pelecanus crispus*, this wetland regularly hosts between

---

Table. 1. List of Internationally Important Wetlands in Pakistan, 2005. (Source: Khan, 2005).

S. No.	Name	Location	Area (ha)
01	Astola (Haft Talar) Island	Balochistan	5,000
02	Chashma Barrage	Punjab	34,099
03	Deh Akro-II Desert Wetland Complex	Sindh	20,500
04	Drigh Lake	Sindh	164
05	Haleji Lake	Sindh	1,704
06	Hub (Hab) Dam	Balochistan	27,000
07	Indus Delta	Sindh	472,800
08	Indus Dolphin Reserve	Sindh	125,000
09	Jiwani Coastal Wetland	Balochistan	4,600
10	Jubho Lagoon	Sindh	706
11	Kinjhar (Kalri) Lake	Sindh	13,468
12	Miani Hor	Balochistan	55,000
13	Nurri Lagoon	Sindh	2,540
14	Ormara Turtle Beaches	Balochistan	2,400
15	Runn of Kutch	Sindh	566,375
16	Tanda Dam	NWFP	405
17	Taunsa Barrage	Punjab	6,576
18	Thanedar Wala	NWFP	4,047
19	Uchhali Complex	Punjab	1,243

50,000 and 100,000 water birds. Indus Dolphin Reserve is important for the survival of more than 1500 remaining individuals of the Indus dolphin *Platanista minor* (Khan, 2006). This unique species is endemic to Pakistan and listed on Appendix I of CITES and the IUCN Red List. There is abundant, albeit fragmentary, evidence that agricultural pesticides and other anthropogenic contaminants are contaminating several wetlands extensively. Such inputs can affect fundamental ecosystem properties such as primary production, which, in turn, affects habitat and resource supply of wetland fauna. Presently Haleji Lake is being polluted by the runoff from water of agricultural fields.

The coast of Sindh is characterized by the presence of several creeks, backwaters and mangrove swamps. The topographic structure of Korangi and other adjacent creek possesses special features that support different aquatic biodiversity. These creeks along the Indus Delta constitute important nursery and feeding grounds for a variety of pelagic and demersal fish and commercial prawn species. On the eastern side of Karachi, between Karachi and Keti Bunder the area extending from Korangi/ Rehi Creek at the north-eastern side is commonly known as the Korangi Creek system which further extends to Phitti, Gizri, Khuddi, Khai, Pitiani, Dobbo, Sisa, Hajamro, Turshian and Khobar Creeks.

The most important ecosystems to be found in the coastal belt are the mangrove forest in the Indus delta, which are a rich source of nutrients for a variety of marine wild species. In Pakistan, sewage water is re-chanelled to irrigate crops, which contaminates them with pathogens. As a result 50% of the crops are contaminated. Groundwater may also be contaminated by untreated sewage. Water borne diseases are the killers in the city and health problems resulting from polluted water cost lot of money (Khan *et al*., 2007).

Although several natural and synthetic estrogens exist; the 17 β -estradiol (E2) has, however, been selected as the standard EDC for the development of the *in vitro* bioassays because it is the most potent natural estrogen in the endocrine system. As with many steroid hormones, 17 β -estradiol is derived from cholesterol, thus many similarities in structure exist (Fig. 1) [by sustitution of various functional groups and thus there are many similarities in structure]. E2 is primarily produced in the ovaries, and to a lesser extent in the testes; however, E2 is also produced in fat cells and brain cells (EPA, 1997; NIEHS, 2002). In testes, E2 is produced through steroidogenesis, which includes aromatization of testosterone into E2 (Fig. 2).
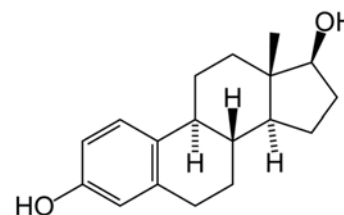
Fig. 1. Structure of 17 β -Estradiol.
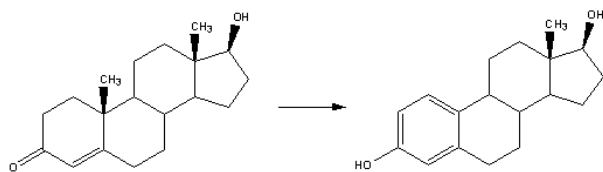
Fig. 2. Aromatization of Testosterone into 17 β -Estradiol.

17 β -estradiol is a water-soluble EDC with a log K_{ow} of 4.01; however, it may associate with organic material in water or exists in a freely dissolved form (Table 2). It is not a persistent molecule, thus exists only temporarily in aqueous media, soils, sediments and biota.

Table 2. Physical and chemical properties of 17- β - estradiol.

Property	Value
Molecular formula	$C_{18}H_{24}O_2$
Molecular weight	272.3864
Melting point	178.5°C
Vapour pressure	1.3×10^{-8} mm Hg
Log K_{ow}	4.01
Water solubility	3.6 mg/L
Sigma # (CAS)	E4285

MATERIALS AND METHODS

For this baseline study, we selected eight study points.

Lake water Haleji and Kinjhar Watlands area were chosen for sampling (both wetlands are Ramsar sites and important for aquatic biodiversity including resident and migratory birds).

River water The Indus Dolphin Reserve area, Indus dolphin (*Platanista minor)* is an endemic species of Pakistan from River water.

Creeks areas Korangi and adjacent Creeks areas were chosen for marine water [one from nesting area of Green turtle (*Chelonia mydas)*].

The water samples were collected about one to two feet away from the coast of river, lakes and beaches and about 10~15cm deep from the surface water. Samples were collected in pre-cleaned 4L glass bottles. The water samples were collected in the 2nd week of Nov 2006 and 3rd week of May 2007 in the mornings between 10:30 to 12:00 am.

Extraction Procedure
Water samples were extracted based on a modification of the method used by Soto *et al.* (2004). Samples were extracted on the next day of sample collection. Each 4 L sample was split into 4 aliquots (1 L), and transferred into its own 2L separatory funnel containing 60 mL of dichloromethane (DCM). The separatory funnel was shaken for 5 min and the layers were allowed to separate for 15 min. The bottom (DCM) layer was removed, and 60 mL of fresh DCM was added to the remaining aqueous solution, which was mixed for another 5 min and allowed to separate for 15 min. The second extraction step was repeated and the extracts from all three extractions were combined and concentrated down to approximately 4 mL using ROTAVAP and N-EVAP evaporators (Organomation Associates, Berlin, MA) at 40°C. A 2 mL aliquot was removed and extracted by ethanol (anhydrous). For selected samples, the remaining DCM (2 mL) was dried completely and stored at -40°C and then used for YES.

Preparation of growth medium for Gaido (Gaido *et al.*, 1997)
- 50mL 10X Yeast Nitrogen Base
- 50mL 20% Dextrose (20g/100mL)
- 5mL Lysine (1.8g L-lysine-Cl/500mL)
- 5mL Histidine (1.2g L-histidine-Cl/500mL)
- 1.73g Monobasic Sodium Phosphate (3.46g/L)
- 1.73g Dibasic Sodium Phosphate (3.54g/L)

Preparation of Standard Dilution Series
The 17β-estradiol (E2) standard dilution series ranged from 0.001 nM to 100 nM (i.e., 11 dilutions), plus a solvent (ethanol) blank. The dilutions of the aqueous samples were attained using ethanol. The concentrations used for bioassay exposures were 10, 1, 0.1, 0.01, 0.001times the initial concentration. Cytotoxicity was assessed by exposing sample dilutions to 1 nM E2; since this level of E2 produces maximal proliferation, decreased proliferation implies cytotoxicity. Cytotoxicity was confirmed visually using a microscope. Cytotoxicity affected the 10-fold aqueous samples, thus data analysis was limited to the 1-fold sample. An E2 equivalence quotient is obtained for the 1-fold sample based on the dose–response curve of E2. Trichloroacetic acid (TCA) fixation, sulforhodamine B (SRB) staining, and Tris buffer solubilization of dye, were performed according to Soto and Sonnenschein (1995). The 96-well microplates were scanned at 515 nm and 650 nm with a microplate reader.

The E2 standard dilution series was used for the YES assays. Standards and environmental extract dilutions were transferred (10 μL), in at least triplicate, into the microplate wells and allowed to dry (approximately 40 min). The YES bioassays were carried out with two different variations of recombinant yeast. These bioassays are similar in that they have been transformed to include the human estrogen receptor (hER) in their main genome, estrogen response elements (ERE) and lac-Z gene on a plasmid. Essentially, the estrogenic substance binds to an

hER which polymerizes and binds to the ERE, which controls the expression of the lac-Z gene, resulting in the transcription and subsequent release of β-galactosidase into the medium (Nelson *et al.*, 2007). The two YES bioassays employ different chromogenic substances, 2-nitrophenyl-β-D-galactopyranoside (ONPG) is used in the Gaido *et al.* (1997) method. The intensity of the color is then measured by absorbance; these values are then normalized for the background activity.

The yeast cell lines, *Saccharomyces cerevisiae* for the ERTA reporter gene assays, were obtained and used with permission from their respective authors (Gaido *et al.*, 1997). The Gaido strain was obtained directly from Dr. Gaido's laboratory in the Chemical Industry Institute of Toxicology (Research Triangle Park). The bioassay was performed, respective in accordance to the procedures of Gaido *et al.* (1997).

Cell cultures were verified by running the assay with standards for one month prior to the analysis of test substances. This was to ensure the passage number was similar and the cultures were consistent (Yeast Culturing Protocol). Every week new cultures were started from plates stored at 4 ^{o}C which were never older than one month. These plates were made each month from frozen stock (Yeast Freezing Protocol). Lorenzen *et al.* (2004) provided a modified version of the Gaido *et al.* (1997) procedure allowing for the use of a 96-well plate with spectrophotometric measurements of endpoints. Briefly, on day 0 at 10 a.m., a yeast culture is started by adding a single colony of yeast from a streaked plate into 5 mL selective media and incubated overnight at 30° C with shaking. On day 1 at 10 a.m., the culture is diluted 10 fold, by adding 45 mL of growth medium. On day 2 at 10 a.m., the culture was then diluted by 50% in growth media (Lorenzen *et al.*, 2004).

At 1 p.m., aliquots (10 μL) of standards or test solutions were transferred in triplicate to the microplate wells and allowed to dry (approximately 30 min). At 2 p.m., copper sulfate (0.1 M, final concentration in yeast culture) was added to the mid-log phase (OD$_{600nm}$ of 0.8-1.0) yeast culture to induce hER production prior to exposure. This yeast culture was added to the 96-well plate in aliquots of 200 μL/well. After mixing for 2 min, the microplates were sealed and incubated overnight at 30° C, without shaking. At the end of the 20 hours incubation, yeast cells were resuspended and 100 μL aliquots were transferred to a 96-well microplate containing 100 μL of assay buffer solution. After 2 min of shaking, the microplates were kept at room temperature for an additional 40 min, until the absorbance was read at 415 nm and 595 nm.

Results from the YES bioassays were plotted by Prism. The E2 dose–response curve was used to quantify the unknown samples. The E2 equivalence (EEQ) was generated based on the E2 dose–response curve (Fig. 3).
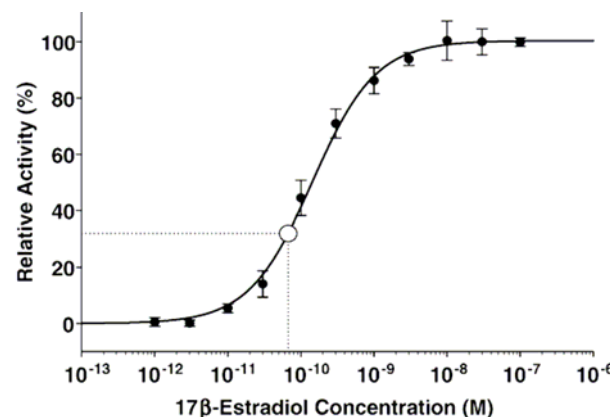
Fig. 3. A typical dose–response curve for 17β-estradiol.

RESULTS AND DISCUSSION

The environmental fates of estrogens in aquatic environment are very complex and there is no universally accepted bioassay or chemical technique to quantify EDCs in the aquatic environment. Chemical analysis of EDCs is sensitive and specific but limited in that only target substances are analyzed. In vitro bioassays which are based on the interaction between EDCs and estrogenic receptors can be very useful in determining the total estrogenic activity of EDCs in a mixture.

From literature, it was found that 17-β-estradiol (E2) has the highest relative estrogenic potential in the environmental water as shown in table 3 (Tanaka *et al.*, 2001). Therefore, for evaluating the level of the estrogenic activities in the water samples, the dose-response curve of 17-β-estradiol was used and the concentration of estradiol was measured in each water samples.

Table 3. The relative estrogenic potential in the environmental water.

Chemicals	Relative estrogenic potential
17-β-estradiol	1.00
Estron	0.3
4-nonylphenol	0.001
4-n-octylphenol	0.000005
Di-n-butyl phthalate	------
Di-2-ethylhexyl phthalate	------
Butyl benzyl phthalate	------
Di-2-ethylhexyl adipate	------
Bisphenol A	0.00006

Table 4. Estrogenic activities of eight different study points of Sindh areas, water samples collected in November 2006.

Study Point	Data (average)	Predicted estrodial equivalence concentration n (M)	Predicted estrodial equivalence concentration n (ng/L)
Indus Dophin (P-1)	3.575431	11.031	9.31
Indus Dolphin (P-2)	2.948023	00	00
Kinjhar (P-1)	4.252245	10.5578	2.77
Kinjhar (P-2)	3.077898	00	00
Haleji (P-1)	2.382564	00	00
Haleji (P-2)	10.62091	00	00
Creek area (P-1)	2.773354	00	00
Creek area (P-2)	2.945462	00	00

Table 5. Estrogenic activities of eight different study points of Sindh areas, water samples collected in May 2007.

Study Point	Data (average)	Predicted estrodial equivalence concentration n (M)	Predicted estrodial equivalence concentration n (ng/L)
Indus Dophin (P-1)	10.5163	7.50327	3.14
Indus Dolphin (P-2)	10.72072	7.3425	4.54
Kinjhar (P-1)	2.52951	00	00
Kinjhar (P-2)	2.432803	00	00
Haleji (P-1)	5.879606	8.85275	1.4
Haleji (P-2)	1.865288	00	00
Creek area (P-1)	9.012585	8.10309	7.89
Creek area (P-2)	3.584123	10.5337	2.93

In the present study, a baseline study was conducted for the evaluation of estrogenic activities in the waters of three Ramsar Sites and one Creek areas among the selected study points. *In-Vitro* Yeast Estrogenic Screen (YES) assays techniques were used to evaluate the estrogenic activities in the water samples. Summarized data obtained for the estrogenic activities of water samples of Indus Dolphin Wetland (study point1), Indus Dolphin (study point 2), Kinjhar Wetland (study point 1), Kinjhar (study point 2), Haleji Wetland (study point 1), Haleji (study point 2), Creek areas (study point 1) and Creek area (study point 2) for the two seasons are shown in table 4 and 5. Estrogenic activity was recorded in the November 2006 samples as Indus Dolphin Wetland (study point 1) 9.31 ng/L estradiol equivalents and Kinjhar (study Point 1) 2.77 ng/L estradiol equivalents (Table 4), while samples collected in May 2007, estrogenic activity was found in Indus Dolphin Wetland (study point 1) 3.14 ng/L estradiol equivalents, Indus Dolphin (study point 2) 4.54 ng/L estradiol equivalents, Haleji Wetland (study point 1) 1.4 ng/L estradiol equivalents, Creek area (study point 1) 7.89 ng/L estradiol equivalents and Creek areas (study point 2) 2.93 ng/L estradiol equivalents (Table 5).

Estrogenic activities observed in Indus Dolphin samples collected from point P1 and P2, Kinjhar P1, Haleji P1, and Creek areas P1 and P2 in November 2006 and May 2007, respectively. As evident from the table 4 estrogenic activities of Nov 2006 winter samples were found varied from the summer samples May 2007 (Table 5), in the case of summer samples, estrogenic activity was found 3.14 ng/L estradiol equivalents (Indus Dolphin P1) and 4.54 ng/L estradiol equivalents (Indus Dolphin P2) in Indus Dolphin (P1 and P2) that is lower than November 2006 samples. These results indicated that the summer May 2007 samples were more polluted then the winter samples.

CONCLUSION

Results of our study have indicated that the Indus Dolphin Wetland (P1) and Kinjhar Wetland (P1) are polluted areas due to anthropogenic activities and this study also indicates the presence of Estrogenic activities in both seasons. Of the eight study points, the highest estrogenic activity has been recorded at creek P1 area. This area is busy for local fisherman activities including the cleaning of fishing boots and other related work. Normally in the summer season creek areas are very active for fishing activities and as result, the summer samples are more polluted than the winter samples. Further studies are recommended for determination of possible effects of estrogenic activities on aquatic biodiversity.

REFERENCES

Aherne, GW. and Briggs, R. 1989. The relevance of the presence of certain synthetic steroids in the aquatic environment. J. Pharm. Pharmacol. 41:735-736.

Boyd, GR., Reemtsma, H., Grimm, DA. and Mitra, S. 2003. Pharmaceuticals and personal care products (PPCPs) in surface and treated waters of Louisiana, USA and Ontario, Canada. Sci. Total Environ. 311:135-149.

Colborn, T. and Clement, C (eds.). 1992. Chemically induced alterations in sexual and functional development: The wildlife/human connection. Ad Mod Environ Toxicol. Princeton. Princetion Sci. Publ. Co. 403-451.

Damstra, T., Barlow, S., Bergman, A., Kavlock, R. and Van Der Kraak, G. 2002. Global assessment of the state-of-the-science of endocrine disruptors. WHO/PCS/EDC/02/2.http://www.who.int/pcs/emerg_site/edc/global_edc_TOC.htm.

Desbrow, C., Routledge, EJ., Brighty, GC., Sumpter, JP. and waldock, M. 1998. Identification of estrogenic chemicals in STW effluent. Chemical fractionation and in vitro biological screen. Environ. Sci. Technol. 32:1549-1558.

EPA-Environmental Protection Agency. 1997. Special Report on environmental endocrine disruption: An effects assessment and analysis. EPA, USA.

Gaido, KW., Leonard, LS., Lovell, S., Gould, JC., Babai D., Portier, CJ. and Mcdonnell, DP. 1997. Evaluation of Chemicals with Endocrine Modulating Activity in a Yeast-Based Steroid Hormone Receptor Gene Transcription Assay. Toxicology and Applied Pharmacology. 143:205-212.

Hayes, TB., Collins, A., Lee, M., Mendoza, M., Noriega, N, Stuart, AA. and Vonk, A. 2002. Hermaphroditic, demasculinised frogs after exposure to the herbicide atrazine at low ecologically relevant doses. PANS. 99:5476-5480.

Jobling, S., Nolan, M., Tyler, CR., Brighty, G. and Sumpter, JP. 1998. Widespread sexual disruption in wild fish. Environ. Sci. Tecnol. 32:2498-2506.

Khan, MZ. and Law, FCP. 2005. Adverse Effects of Pesticides and related Chemicals on Enzyme and Hormone Systems of Fish, Amphibians and Reptiles. Proc. Pakistan Acad. Sci. 42(4):315-323.

Khan, MZ. 2006. Current Status and Biodiversity of Indus Dolphin Reserve and Indus Delta Wetlands (Ramsar Sites). Proc. 9th International River Symposium, Brisbane, Australia. 01-26.

Khan, MZ., Nelson, J., Law, FCP., Leung, W. and (Howie) HL. 2007. Assessment of Estrogenic Contamination using *In-Vitro* Yeast Estrogenic Screen in the Wastewater of Karachi. Canadian Journal of Pure and Applied Sciences. 1(1): 67-72.

Lintelmann, J., Katayama, A., Kurihara, N., Shore, L. and Wenzel, A. 2003. Endocrine disruptors in the environment (IUPAC technical report). Pure & Applied Chemistry. 75(5):631-681.

Lorenzen, A., Hendel, JG., Conn, KL., Bittman, S., Kwabiah, AB. and Lazarovitz, G. 2004. Survey of hormone activities in municipal biosolids and animal manures. Environ Toxicol. 19:216-25.

National Institute of Environmental Health Sciences (NIEHS). 2002. Current status of test methods for detecting endocrine disruptors: *In vitro* estrogen receptor transcriptional activation assays. NIH Publication No: 03-4505.

Nelson, J., Bishay, F., Albert van Roodselaar., Ikonomou, M. and Law, FCP. 2007. The use of in vitro bioassays to quantify endocrine disrupting chemicals in municipal wastewater treatment plant effluents. Science of the Total Environment. 374: 80-90.

Purdom, CE., Hardiman, PA., Bye, VJ., Eno, NC., Tyler, CR. and Sumpter, JP. 1994. Estrogenic effects of effluents from sewage treatment works. Chem Ecol. 8:275-85.

Routeledge, EJ., Sheahan, D., Desbrow, C., Brighty, GC., Waldock, M. and Sumpter, JP. 1998. Identification of estrogenic chemicals in STW effluents. 2. In vivo responses in trout and roach. Environ Sci Technol. 32:1559-65.

Soto, AM. and Sonnenschein, C. 1995. The E-Screen assay as a tool to identify estrogens: an update on estrogenic environmental pollutants. Environ Health Perspect. 103:113-22.

Soto, AM., Calabro, JM., Nancy, V., Prechtl, NV., Yau, AY., Orlando, EF., Daxenberger, A., Kolok, AS., Guillette, Jr., LJ., Bruno le Bizec., Iris G. Lange, IG. and Sonnenschein, C. 2004. Androgenic and Estrogenic Activity in Water Bodies Receiving Cattle Feedlot Effluent in Eastern Nebraska, USA. Environ Health Perspet. 112(3):346-352.

Snyder, SA., Keith, TL., Verbrugge, DA., Snyder, EM., Gross, TS., Kannan, K. and Giesy JP. 1999. Analytical methods for detection of selected estrogenic compounds in aqueous mixtures. Environ. Sci. Technol. 33:2814-2820.

Tanaka, H., Yakou, Y., Takahashi, A., Higashitani, T. and Komori, K. 2001. Comparison between estrogenicities estimated from DNA recombinant yeast assay and from chemical analyses of endocrine disruptors during sewage treatment. Water Science and Technology. 43:125-132.

Tyler, CR., Jobling, S. and Sumpter, JP. 1998. Endocrine disruption in wildlife: a critical review of the evidence. Crit Rev Toxicol. 28:319-61.

Canadian Journal of
pure&applied
sciences

RELATIONSHIP BETWEEN THE SOCIO-DEMOGRAPHIC FACTORS AND THE CLINICOPATHOLOGICAL CHARACTERISTICS WITH THE INTRINSIC BIOMARKERS OF BREAST CARCINOMA OF WOMEN IN PAHANG, MALAYSIA

*Khurshid Anwar[1] and Tanveer Ahmad Khan[2]
[1]College of Medicine, University of Sharjah, Sharjah 27272, United Arab Emirates (UAE)
[2]College of Clinical Pharmacy, King Faisal University, Al-Ahsa 31982, Kingdom of Saudi Arabia

ABSTRACT

Globally Breast cancer is the most common malignancy in women. The aim of this retrospective study was to determine the relationship between the socio-demographic factors and clinicopathological characteristics, with the known predictors of aggressive biological behaviour of breast cancer women in Pahang, Malaysia.The biomarkers included in this study were estrogen receptor (ER), cyclin E, p27 and nm23. Routine formalin-fixed, paraffin sections of tumor samples were used and immunohistochemically stained with antibodies against ER, cyclin E, p27 and nm23 in 93 cases of breast carcinoma in women attending at Breast clinic in Hospital Tengku Ampuan Afzan, Pahang, Malaysia during January, 1996-December, 2000. All markers studied were more common in the older age group >45 years and were roughly equally distributed among the Malays and Chinese with the exception of cyclin E which is more commonly expressed among the Malays (54.5% versus 43.9%). Breast carcinoma was found to be more common in patients over age 45 years. Most patients were diagnosed at a relatively early stage and were ER positive. ER positivity was more common in the older age, in tumors < 2cm in diameter, in early stages and in tumors with low histological grade. ER positivity was found more in patients who were alive for more than 25 months after their initial diagnosis. The cancer patients survival was significantly associated with ER (p=0.034) and nm23 (p=0.011), ER and tumor stage (p=0.031). Cyclin E expression appeared to influence the recurrence rate of primary tumor which may be a reflection of the secondary effect of treatment modality. Both markers p27 and nm23 were significantly associated with ER (p<0.001). The prognostic value of individual biological factors could be more effective in combination as opposed to single factors.

Keywords: Demographic, breast cancer, biomarkers, *ER, cyclin E, p27, nm23,* immunohistochemistry.

INTRODUCTION

Breast cancer is the most common malignancy among women, excluding non-melanoma skin cancers; and the second most leading cause of cancer deaths in women today lagging only behind lung cancer (Ries *et al*., 2004; Parkin *et al.,* 2002; Jokhio and Ansari, 2005). There is a strong inherited familial risk of breast cancer in some families and recent data reveals up to 27% of breast cancers may be attributed to inherited factors and mutated *BRCA1* and *BRCA2* genes are responsible for approximately 30-40% of inherited breast cancers (Lichtenstein *et al*., 2000). Some racial groups have a higher risk of developing breast cancer, notably; women of North American and European descent have been noted to have a higher rate of breast cancer than women of African and Asian origin (Parkin *et al*., 2001). Risk factors for breast cancer include, increasing age, genetics, personal and family history of breast cancer, past history of benign breast conditions, prolonged reproductive period, delayed childbirth and null parity, obesity, high fat diet, previous radiation therapy and hormonal replacement therapy beside smoking and daily consumption of alcohol (King and Schottenfeld, 1996). In

Malaysia, breast cancer has been the top leading cause of cancer death among women (Yip and Ng, 1996; Joseph, 1998). The incidence of breast cancer in Malaysia is estimated to be around 27 per 100,000 populations, with close to 3,000 new cases annually. Acording to the second report of the Malaysian National Cancer Registry in 2003, breasts cancer was the most common cancer in all ethnic groups and comprised 30.4% of all newly diagnosed cancer cases among Malaysian women. The majority of women initially diagnosed with breast cancer are aged between 40 and 49 years. Breast cancer also seems to be predominant among Chinese women with an incidence of 25 per 100,000 population and Malay women with an incidence of 16 per 100,000.

What kills women with breast cancer is not the original tumor but the tumor's spread to other sites. The initial tumor can be removed by surgery, disease that has spread to nearby lymph nodes may be effectively treated by radiation therapy (Joshi *et al*., 2008) and the risk of distant metastases can be decreased by chemotherapy. However, chemotherapy is not always be an effective means of treatment and has significant side effects. Only 20 to 30 percent of women with node-negative breast

cancer will develop metastatic disease (Schwartz *et al*., 1993). If physicians could predict who was at risk they could increase the intensity of chemotherapy for those women and reduce or even eliminate the therapy and its side effects for those not at risk.

Recently published data demonstrates that ovarian hormones, principally estrogens, play a major role in the etiology of breast cancer by affecting the rate of breast epithelial cell proliferation, perhaps via stimulation of the expression of genes encoding for growth factors (Key and Pike, 1988; Thomas *et al*., 1997; Lippman and Dickson, 1989). Intracellular ERs bind and transfer estrogen to the nucleus, where it interacts with estrogen response elements on DNA, thereby activating nearby target genes and resulting in the synthesis of proteins involved in cell division (Goodman, 1988; Brody *et al*., 1994). Although ERs exist in normal breast epithelial cells to regulate breast development during puberty and pregnancy, they are usually present in extremely low quantities (Pike *et al*., 1993; Ricketts *et al*., 1991). On the other hand, 30% of premenopausal and 60% of postmenopausal breast cancers have measurable ERs (McCarty *et al*., 1983; Huang *et al*., 2000). In general, tumors expressing these receptors tend to respond more favorably to hormonal therapies and have a better overall outcome than tumors not expressing ERs or PRs (Clark and McGuire, 1988).

The WHO estimates that at least one-third of all cancers including breast cancer are preventable (Albert, 1991) and if possible enlightened Public Health Policy should prioritize prevention and early diagnosis.

There have been an ever-expanding number of potential prognostic factors reported for patients with breast cancer. Prognostic factors correlate with survival independent of systemic therapy, and are used to select patients at risk (Wyld *et al*., 2003; Esteva and Hortobagyi, 2004; Jakic-Razumovic *et al*., 2005; Bare *et al*., 2006). The prognostic significance of histological grade has been reported by several investigators (Bay, 2006). Histological type and grade of cancer, tumor size, lymph node (Callagy *et al*., 2006), metastasis, stage and certain immunohistochemical markers like estrogen receptor (ER)/progesterone receptor (PR) status and C-erbB-2 have consistently been shown to be important prognostic factors for breast cancer survival. Poorer prognosis is associated with larger, higher grade tumors, with axillary lymph node involvement, distant metastasis, negative hormone status and positive C-erbB-2 staining *(*William, 1997). Unfortunately, the standard tools for assessing risk of metastasis such as the size of the tumor, its grade, the presence of estrogen receptors and the proportion of dividing cells are probably insufficient for clinical decision making (Osborn *et al*., 2004).

The expression of molecular markers in breast cancer has been examined extensively in order to provide early

diagnosis and prediction outcome (Naguib *et al*., 1999; Bay, 2006; Kröger *et al*., 2006). Thus, looking for "biomarkers", proteins expressed at varying levels in early breast cancer, to provide clues about the expected behaviour of cancer and whether it is likely to spread or has spread, is a target worth aiming at. Currently, many biomarkers, particularly the hormonal and epidermal growth factor receptors, are being utilized for breast cancer prognosis. Unfortunately, none of the biomarkers in use have sufficient diagnostic, prognostic and/or predictive power across all categories and stages of breast cancer. It is recognized that more useful information can be generated if tumors are assessed with multiple markers. But choosing the right combination of biomarkers is challenging, because 1) multiple pathways are involved, 2) up to 62 genes and their protein products are potentially involved in breast cancer-related mechanisms and 3) the more markers evaluated, the more the time and cost involved (Osborn *et al*., 2004; William, 1997). It has been reported that there was significance ethnic variations in the incidence of breast cancer among women (Ahmad, 2003).

For all of these reasons, our objective of this retrospective study was therefore to examine the correlations of the markers with the socio-demographic and histo-pathological data of the breast cancer among women attending Breast clinic in Hospital Tengku Ampuan Afzan (HTAA) Kuantan, Pahang, Malaysia. In this study, we evaluated the interrelationship of the expression of the cell cycle controller gene products p27, a negative regulator, and cyclin E (Keyomarsi *et al*., 1994; Sgambato *et al*., 1997; Tan *et al*., 1997; D1Arciero *et al*., 2003; Keyomarsi *et al*., 2003; Hlupić *et al*., 2004) a positive regulator, together with the expression of the tumor suppressor gene nm23 (Hlupić *et al*., 2004; Zhao *et al*., 2004) and one of the steroid receptors, the estrogen receptor (ER).

MATERIALS AND METHODS

Patients
The study included 100 randomly collected histologically confirmed breast carcinoma cases. The cases were all women who attended the breast clinic in Hospital Tengku Ampuan Afzan (HTAA), Kuantan, Pahang, Malaysia, during January, 1996- December, 2000. The criterion for inclusion was determined by the availability of sufficient tissue for H & E (Hematoxylin and eosin) staining and further immunohistochemical studies. Based on theses criteria 93 cases were included in the present study. The available demographic and clinicopathological data were collected from the biopsy request forms or patient's files wherever possible. However, for some patients we couldn't obtain sufficient relevant information due to patient default, incomplete entry of data in patient's files or their referral to another center for treatment. At least

two blocks of the tumor tissue from each patient were analyzed to reconfirm the original histological diagnosis and to determine the histological grade. Tumors were classified in accordance with NHSBSP guidelines and histological grading was established using modified Bloom's grading system described by Elston and Ellis (1991). The tumors were staged according to the American Joint Committee on Cancer staging system, grouping patients based on the tumor size (T), lymph node status (N), and distant metastases (M) into 4 stages, thus allowing clinicians to derive prognostic information necessary for therapeutic decisions (Fleming *et al*., 1997).

Immunohistochemistry
Formalin-fixed paraffin sections of breast cancer tissue were mounted on glass slides coated with 3-aminopropyl-triethoxysilane (APES; Sigma, Poole, Dorset, UK) and were baked for 30 min at 56–60°C, before being dewaxed in xylene. The tissue sections were rehydrated by sequential immersion in 100% and 50% ethanol to distilled water and then subjected to heat antigen retrieval for 40 min in citrate buffer (pH 6) in a jar containing preheated (95-99 ^{0}C) target retrieval solution. After cooling, tissue sections were incubated for 5 min in 0.3% (v/v) hydrogen peroxide. Subsequently, the sections were washed in tap water and Tris-Buffer (pH 7.45) and were exposed to normal rabbit serum (diluted with Tris) for 30 min at room temperature (20–24°C). Diluted primary antibody (anti-ER) was applied and incubated overnight at 4°C (18 hours). After washing with Tris, biotinylated rabbit anti-goat secondary antibody, together with the Strept-AB Complex/HRP (0377, DAKO, Glostrup, Denmark) was applied for 30 min at room temperature. Staining was revealed by development in the chromogen 3, 3-diaminobenzidine tetrahydrochloride (DAB) for 5–30 min. Sections were rinsed with distilled water and were mounted using cover slip with aqueous bases mounting medium.

Evaluation of immunohistochemistry
The intensity of immunostaining was labeled as +, less than 25% of cells stained intensely, ++, 25-50% of cells stained intensely, +++, 51-75% of cells stained intensely and ++++, more than 75% of cells stained intensely. The pattern of staining varied (nuclear, cytoplasmic, membranous) depending on the type of antibody used e.g. against ER receptor, cyclin E, p27 and nm23. A single pathologist scored all immunohistochemistry and the binary system (positive versus negative) was used for the out come of all of the markers.

STATISTICAL ANALYSIS

The data were analyzed for significant associations between the expression of immunohistochemical tumor markers and other tumor biological characteristics and behavior by the non-parametric Chi square method using SPSS 11.0 for windows. Differences were considered significant when $p < 0.05$.

RESULTS

In the period studied, from January, 1996 to December, 2000, 93 confirmed cases of breast carcinoma were included in this investigation. Table 1 shows age distribution in investigated breast carcinoma patients. The mean age of the patients included in the study was 51.3 ranging between 32 and 89 year old. The majority of patients (60%) were 41-60 years of age. Table 2 summarizes the distribution of all investigational parameters (clinicopathological characteristics) in 93 breast carcinoma cases included in this study. The results of the quantitative immunohistochemical assays were correlated with clinical and histological findings such as patient age, ethnic distribution, breast side, histological type, tumor size, lymph node metastatis, distant metastatis, stage and tumour grade. The ethnic distribution was comparable in Malays and Chinese constituting 50% and 44% of the total cases respectively. The Indian constituted only 6.5%. The most frequent histological type of breast cancer (93.6%:87/93 cases) in this study was infiltrating ductal carcinoma. The others were two non-invasive ductal carcinoma, two papillary carcinoma and one each medullary and mucinous carcinoma. Most of the patients (57%) had tumor size ranging between 2-5 cm in diameter (T2) and lymph node metastasis was observed in 50.5% of cases while distant metastases was observed in only 2 cases at the time of diagnosis. At the time of presentation 71% of the patients were in stage 2 and 60% had histological grade 2 tumors. Most of the patients (64.5%) presented with right sided tumors.

Table 1. Age distribution in investigated breast carcinoma cases (93).

Age group (years)	Number of cases (percentage)
31-40	15 (16.1%)
41-50	38 (40.9%)
51-60	18 (19.3%)
61-70	16 (17.2%)
71-80	05 (5.4%)
81-90	01 (1.1%)

Information about parity of the patents were available for only 44 cases, 19 of these were nulliparous, 14 had 1-3 children and rest of 11 had more than 3 children. Family history of cancer was available for 45 cases, 4 cases had family history of breast cancer, 3 cancers other than breasts and rest of 38 had no family history of any cancerous lesion. Out of 43 cases with information about prior hormonal treatment only seven had history of hormonal treatment in past few years. Eight cases were unmarried out of 44 for which marital status was known.

Table 2. Distribution of all investigational parameters (clinicopathological characteristics) in 93 breast carcinoma cases.

Factors	*Cases (%)
Age	
< 45	30 (32.3)
> 45	63 (67.7)
Ethnic distribution	
Malays	46 (49.5)
Chinese	41 (44.1)
Indians	06 (6.5)
Breast side affected	
Right	60 (64.5)
Left	33 (35.5)
Histological type of cancer	
Infiltrating ductal carcinoma	87 (93.5)
Non-infiltrating ductal carcinoma	02 (2.2)
Others	04 (4.3)
Tumor size	
T1	14 (15.1)
T2	53 (57)
T3	18 (19.4)
T4	08 (8.6)
Lymph node metastatis	
N0	46 (49.5)
N1	44 (47.3)
N2	03 (3.2)
Distant Metastasis	
M0	91 (97.8)
M1	02 (2.2)
Stage	
I	11 (11.8)
II	66 (71)
III	14 (15.1)
IV	02 (2.2)
Histological grade of tumor	
I	19 (20.4)
II	56 (60.2)
III	18 (19.4)

* Number of patients for which data were available.

The intrinsic biomarkers included in this study were the steroid receptor for estrogen (ER), the oncogene and tumour suppressor gene products such as cyclin E, p27 and nm23. The intensity and extent of staining in tumor tissue is graded as mentioned in material and methods. The overall presence of the cell cycle controller gene products cyclin E, p27, the anti-metastasis protein nm23 and estrogen receptor (ER) are shown in table 3. The nm23 shows the lowest expression 41.9% and ER the highest 54.8%. Cyclin E and p27 were expressed in 47.3% and 52.7% of breast cancers respectively. Most of the breasts cancer tissues (54.8%) were found positive for ER. Nuclear staining was positive in all cases, however 38 cases revealed variable degree of cytoplasmic staining

too. The tumors with positive marker expression showed mostly mild to moderate staining intensity with variable degree of nuclear and cytoplasmic staining (Figs. 1-4). The association of the tumor markers for ER, cyclin E, p27, and nm23 overexpression with other classical prognostic factors is shown in table 4. All markers were more commonly expressed in tumors of the older age group > 45 years than in those ≤ 45 (29.1%-38.7% vs. 11.8%-20.4%).
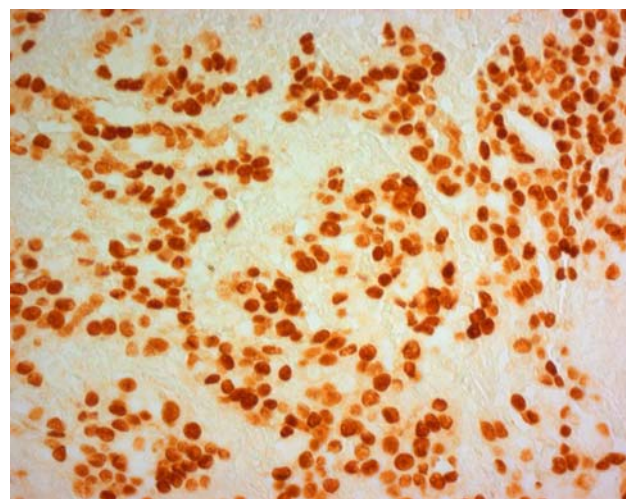
Fig. 1. Immunohistochemical staining of estrogen receptor (ER) in an infiltrating ductal carcinoma, which is entirely localized to the nuclei of the tumor cells (40 HPF).
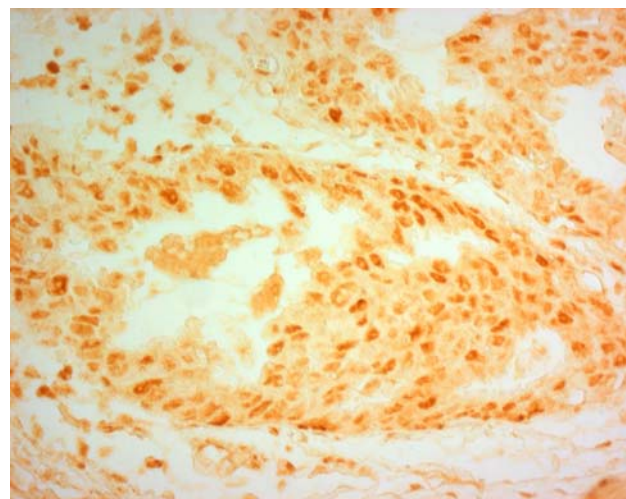
Fig. 2. Immunohistochemical staining of cyclin E in an infiltrating ductal carcinoma, which varies in intensity but still localized to the nuclei of tumor cells (40 HPF).

The ethnic distribution revealed approximately equal presence of all the markers among the Malays and the Chinese except for the cyclin E which showed substantially higher positivity rate among the Malays (54.5% vs. 43.9%), however, the difference is not quite

statistically significant. Since most tumors involved the right breast (64.5%), all markers were consequently more often expressed on that side but even when positivity was calculated within the breast side still marker expression for cyclin E *(*50.8% vs. 39.4) and ER (57.6 vs. 51.5) was higher in right-sided tumors. nm23 showed the least expression in infiltrating ductal carcinomas as compared to the other markers (39.8% vs. $\geq$ 45.2*)*, however, none of the markers showed significant association with a particular histological type probably because of the very small number of the non-infiltrating ductal carcinoma and the other types of cancer. However, nm23 showed the lowest positivity rate in non-metastasizing tumors when compared to other markers (39.8% vs. $\geq$ 46.2).
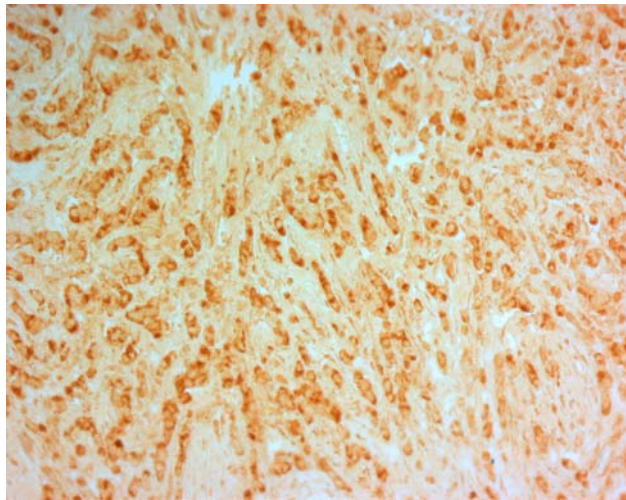
Fig. 3. Immunohistochemical staining of p27 in an infiltrating ductal carcinoma, which varies in intensity and is not only localized to the nuclei of the tumor cells (40 HPF).
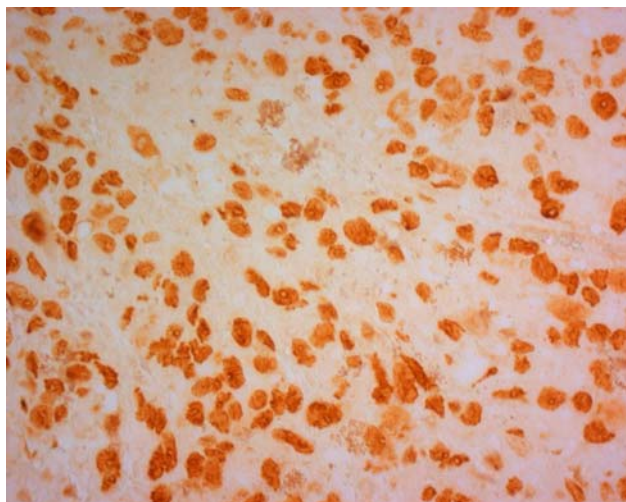
Fig. 4. Immunohistochemical staining of nm23 in an infiltrating ductal carcinoma, which is mostly confined to the nuclei of the tumor cells (40 HPF).

Table 3. Frequency and staining intensity of tumor biomarkers ER, cyclin E, p27 and nm23 in 93 breast carcinoma cases.

Tumor biomarkers	Staining Intensity	Cases* (%)
ER	Negative	42 (45.2)
	+	18 (19.4)
	++	17 (18.3)
	+++	11 (11.8)
	++++	5 (5.4)
Cyclin E	Negative	49 (52.7)
	+	17 (18.3)
	++	16 (17.2)
	+++	8 (8.6)
	++++	3 (3.2)
P27	Negative	44 (47.3)
	+	10 (10.8)
	++	20 (21.5)
	+++	11 (11.8)
	++++	8 (8.6)
nm23	Negative	55 (59.1)
	+	9 (9.7)
	++	18 (19.4)
	+++	6 (6.5)
	++++	5 (5.4)

* Number of patients for which data were available.

ER positivity was more common in patient over 45 year of age rather than in patients below 45(37/63 vs. 14/30). Both non-infiltrating ductal carcinoma and 3 of the 4 other types were positive for ER. Most of the tumors of less than 2 cm size (T1), (12/14) were positive for ER. Tumors with or without axillary lymph node metastasis had similar rate for ER positivity. 43 of 77 low stages (1 & 2) were positive for ER compared to 8 of 16 high stage tumors. More of low histological grade (G1) tumors (13/19: 68.4%) stained with ER antibody than the high histological grade (G2 & G3) (38/74: 51.4%). As for histological grade and stage only ER positivity showed significant association with earlier stages of cancer.

As shown in table 5, most of the patients alive without recurrence were variably positive for all different markers. Longer survival period was significantly associated with nm23 (p = 0.011) and ER (p = 0.034) positivity (Table 6). 25 of 39 cases with localized disease and 3 of 7 dead cases were ER positive. Most of the cases with 25-48 months survival period (19/25: 76%) and those with more than 48 months survival (12/21:57.1%) were positive for ER.

No significant association could be found between tumor size and markers expression. At the same time no substantial differences could be seen in between markers regarding their expression status in tumors of varying

Table 4. Crosstabulation of the association of the tumor markers for ER, cyclin E, p27, and nm23 over expression with other prognostic factors in 93 breast carcinoma cases.

Characteristics	Cyclin E		p27		nm23		ER	
	Positive~ cases (%)	Negative^ cases (%)	positive~ cases (%)	negative^ cases (%)	positive~ cases (%)	negative^ cases (%)	Positive~ cases (%)	negative^ cases (%)
Age								
≤ 45 Y	14 (15.1)	16 (17.2)	17 (18.2)	13 (14)	11 (11.8)	19 (20.4)	14(15.1)	16 (17.2)
> 45 Y	30 (32.2)	33 (35.5)	32 (34.4)	32 (34.4)	27 (29.1)	36 (38.7)	37 (39.8)	26 (27.9)
Ethnic distribution								
Malays	25 (54.5)	21(45.7)	24 (52.2)	22 (47.8)	21 (45.7)	25 (54.2)	26 (27.9)	20 (21.5)
Chinese	18 (43.9)	23 (56.1)	21 (51.2)	20 (48.8)	17 (41.5)	24 (58.5)	23 (24.7)	18 (19.4)
Indians	1 (16.7)	5 (83.3)	4 (66.7)	2 (33.3)	0	6 (100)	02 (2.2)	04 (4.3)
Breast side								
Right	30 (32.6)	29 (31.5)	32 (34.8)	27 (29.3)	25 (27.2)	34 (37)	34 (36.6)	26 (28)
Left	13 (14.1)	20 21.7)	49 (53.3)	16 (17.4)	13 (14.1)	20 (21.7)	17 (18.2)	16 (17.2)
Histological type IDC*	42 (45.2)	44 (47.3)	47 (50.5)	39 (41.9)	37 (39.8)	49 (52.7)	46 (49.5)	41(44.1)
NIDC#	1 (1.1)	1 (1.1)	0	2 (2.2)	1 (1.1)	1 (1.1)	02 (2.2)	0
Others	1 (1.1)	4 (4.3)	2 (2.2)	3 (3.2)	0	5 (5.4)	03 (3.2)	01 (1.1)
Tumor size					5 (5.4)	9 (9.6)	12 (12.9)	02 (2.2)
T1	4 (4.3)	10 (10.8)	9 (9.7)	5 (5.4)				
T2	26 (28.0)	27 (29.0)	28 (30.1)	25 (26.9)	20 (21.5)	33 (35.5)	26 (27.9)	27 (29)
T3 & T4	14 (15.0)	12 (12.9)	12 (12.9)	14 (15.1)	13 (14.0)	13 (14.0)	13 (14)	13 (14)
Lymph node metastatis								
N0	19 (20.4)	27 (29.0)	22 (23.7)	24 (25.8)	14 (15.1)	32 (34.4)	25 (26.9)	1 (22.6)
N1 & N2	25 (26.9)	22 (23.7)	27 (29.0)	20 (21.5)	24 (25.9)	23 (24.8)	26 (27.9)	21 (22.6)
Distant Metastasis								
M0	43 (46.2)	48 (51.6)	47 (50.5)	44 (47.3)	37 (39.8)	54 (58.1)	49 (52.7)	42 (45.1)
M1	1 (1.1)	1 (1.1)	2 (2.2)	0 (0.0)	1 (1.1)	1 (1.1)	02 (2.2)	0
Stage								
I & II	35 (37.6)	42 (45.2)	42 (45.2)	35 (37.7)	30 (32.3)	47 (51.6)	43 (46.2)	34 (36.4)
III & IV	9 (9.7)	7 (7.6)	7 (7.6)	9 (9.7)	8 (8.6)	8 (8.6)	08 (8.6)	08 (8.6)
Histological grade								
I	7 (7.5)	12 (12.9)	10 (10.8)	9 (9.7)	6 (6.5)	13 (14.0)	13 (14)	06 (6.5)
II & III	37 (39.8)	37 (39.8)	39 (41.9)	35 (37.7)	32 (34.4)	42 (45.1)	38 (40.9)	36 (38.7)

Number of positive (~) and negative (^) cases with data, *Infiltrating ductal carcinoma, Non-infiltrating ductal carcinoma.

Table 5. Association of intrinsic tumor markers status with clinical outcome of 93 breast carcinoma cases.

Clinical outcome	Cyclin E		P27		Nm23		ER	
	+ve cases (%)	-ve cases (%)	+ve cases (%)	-ve cases (%)	+ve cases (%)	-ve cases (%)	+ve cases (%)	-ve cases (%)
Alive without recurrence	16 (17.2)	11 (11.8)	15 (16.1)	12 (12.9)	10 (10.8)	17 (18.3)	15 (16.1)	12 (12.9)
Alive with recurrence	9 (9.7)	3 (3.2)	9 (9.7)	3 (3.2)	7 (7.5)	5 (5.4)	10 (10.8)	02 (2..2)
Dead	1 (1.1)	6 (6.5)	2 (2.2)	5 (5.4)	3 (3.2)	4 (4.3)	03 (3.2)	04 (4.3)
Lost to follow up	18 (19.4)	29 (31.2)	23 (24.7)	24 (25.8)	18 (19.4)	29 (31.2)	23 (24.7)	24 (25.8)
P value	0.02		0.223		0.611		0.171	

sizes. Lack of significant association was also noted between markers expression and lymph node involvement or distant metastasis. Only ER positivity showed significant association with earlier stages (I & II) of cancer than late stages (III & IV). Significant association between tumor clinicopathological features and intrinsic tumor markers was observed for tumor stage and patient survival with ER and for clinical outcome with cyclin E (Table 7). Tumor markers p27 and nm23 expressed significant association (p = <0.01) with ER but no significant association was found between the other markers (Table 8).

Table 6. Association of intrinsic tumor markers status with the survival of 93 breast carcinoma cases from HTAA Kuantan during 1996-2001.

Patients' survival in months	Cylin E		P27		Nm23		ER	
	+ve cases (%)	-ve cases (%)	+ve cases (%)	-ve cases (%)	+ve cases (%)	-ve cases (%)	+ve cases (%)	-ve cases (%)
<12	6 (6.5)	5 (5.4)	7 (7.5)	4 (4.3)	3 (3.2)	8 (8.6)	6 (6.5)	5 (5.4)
12-24	9 (9.7))	6 (6.5)	9 (9.7)	6 (6.5))	9 (9.7)	6 (6.5)	8 (8.6)	7 (7.5)
25-48	10 (10.8))	15 (16.1)	15 (16.1)	10 (10.8)	15 (16.1)	10 (10.8)	19 (20.4))	6 (6.5)
>48	12 (12.9)	9 (9.7)	11 (11.8)	10 (10.8)	8 (8.6))	13 (14)	12 (12.9)	9 (9.7)
Not determined	7 (7.5)	14 (15.1)	7 (7.5)	14 (15.1)	3 (3.2)	18 (19.4)	6 (6.5))	15 (16.1)
P value	0.380		0.337		0.011		0.034	

Table 7. Association between tumor clinicopathological features and intrinsic tumor markers (p values for chi^2 tests)

Characteristic	Tumor Markers			
	ER Negative Positive	Cyclin E Negative Positive	P27 Negative Positive	Nm23 Negative Positive
Patient alive <1Y, 1-2Y, 3-4Y, >4Y	0.034	0.380	0.337	0.011
Tumor size	0.069	0.419	0.736	0.737
Clinical outcome	0.171	0.020	0.223	0.611
Metastasis	0.194	0.939	0.175	0.790
Axillary lymph node metastasis	0.274	0.460	0.203	0.110
Histological grade	0.327	0.592	0.722	0.595
Tumor stage	0.031	0.502	0.318	0.827
Treatment	0.142	0.034	0.060	0.162

Table 8. Association in between tumor markers ER, cyclin E, P27 and nm23 (p values for chi^2 tests)

Prognostic Markers	Cyclin E	p27	nm23
ER	0.231	0.001	0.009
Cyclin E	-	0.045	0.993
P27	-	-	0.208

DISCUSSION

Breast cancer is a complex disease that still imposes a significant healthcare burden on women worldwide. The hunt for prognostic markers of human cancers in general and breast cancers in particular continues to haunt investigators who keep struggling to elucidate the right ones that serve as the best prognostic and therapeutic predictors to be used in routine clinical practice (Pedrini et al., 2004). Currently, many biomarkers, particularly the hormonal and epidermal growth factor receptors, are being utilized for breast cancer prognosis (Pedrini et al., 2004). Unfortunately, none of the biomarkers in use have sufficient diagnostic, prognostic and/or predictive power across all categories and stages of breast cancer. It is recognized that more useful information can be generated if tumors are evaluated with multiple markers (William, 1997). Breast cancer risk increases markedly after 40 year of age. A women's chance of breast cancer increases from one out of 235 at age 40 to one in 54 at age 50 and then it continues to increase further with increasing with age (Ferlay et al., 2001). The age standardized incidence rate for breast cancer is 54.9 per 100,000 women per year in Singapore (Bay et al., 2006). In the present study 78 of 93 cases were in age group above 40. The Second report of Malaysian National Cancer Registry shows that most of breast cancers occurred in age group 40-60 (Lim and Yahaya, 2003) which is comparable to our results as 57/93 cases (61.3%) were in the same age group in our study.

Ethnic distribution of breast cancer was almost same as that reported in Malaysian National Cancer Registry report (Lim and Yahaya, 2003) and both Malay and Chinese patients had comparable distribution with slight predominance of the former, however, Indians were underrepresented in our study and constituted only 6.5% of total cases.

The predominant histological type of breast carcinoma in this study was infiltrating ductal carcinoma as reported in most of other studies (Fleming et al., 1997). Most of the patients (72%) presented with tumor size < 5 cm in diameter (T1-T2), while 46 of 93 cases (49.5%) had no metastasis to lymph nodes and only two cases were confirmed to have distant metastatic spread. These

findings suggest that most of the patients with breast cancer in our series presented at an early stage of the disease where 77 of 93 cases (82.8%) were either in Stage 1 or Stage 2. This indicates the efficacy of the breast cancer awareness programs carried out by the NGOs and Malaysian government agencies (Mahathevan, 2002).

In our study we described the individual status four well known immunohistochemical markers cyclin E, p27, nm23 and ER in the breast cancer tissues, and attempted at measuring the association of each with the various demographic and clinicopathological criteria of the cancer patients and also with each of the other markers. Although the higher cyclin E positivity rate among Malays as compared to Chinese in Malaysia (Table 4) is not statistically significant, it might still reflect genuine genetic difference between the tumors in the two races but failed the statistical test due to the small number of cases recruited in this study.

Histologically, most of the breast cancers were either in Grade 1 (20.4%) or Grade 2 (60.2%), once again indicating relatively good prognosis. Previous studies have confirmed the histological grade association with prognosis and chemotherapeutic response (Elston and Ellis, 1991; Pinder *et al.*, 1998).

Interestingly most of cases (64.5%) had right sided breast cancer in contrary to various other reports where left sided cancer was the commonest (Senie *et al.*, 1980). It has been suggested that in about 55% of women, the left breast is slightly larger than the right and therefore contains a larger amount of tissue at risk for becoming cancerous (Senie *et al.*, 1980). It will be interesting to evaluate this hypothesis regarding the increased incidence of right sided breast cancer in our patients. However, this discrepancy may be due to the limited number of cases in the present study.

Most of the patients were treated with only surgery (49 of 93 cases), most probably due to their presentation in early stages. The rests of the cases were additionally treated with other adjuvant modalities such as chemotherapy and radiation. Survival data and follow up of patients was not maintained according to the standard practice, as 50% of cases were lost to follow up after a few visits to hospital. However, 46 patients had follow up data available for more than 25 months and 21 of them for more than 48 months after their first diagnosis. Only 7 cases were confirmed to be dead in this series by July 2004 (the last date of follow up). Although longer follow up periods are required (at least 5 years), our data collectively suggest a better prognosis in this series of patients which we believe is due to the earlier stage at the time of presentation and also probably due to the appropriate treatment these patients received.

Thirty three of 44 cases (75%) with breast cancer were either nulliparous or had 1-3 children which indicate that reduced fertility is one of the common associations with breast cancer as shown in previous studies (King and Schottenfeld, 1996). Only 4 out of 45 had family history of breast cancer which is in confirmation with the previous data of familial breast cancer representing 5-10% of total breast cancers (King and Schottenfeld, 1996; Douglas, 2002). However, only 7 of 43 cases had prior history of any hormonal treatment in our study.

Moreover, patients with ER positive tumors have prolonged disease free survival after primary treatment, superior overall survival and longer survival after recurrence compared with patients having ER-negative tumors, which is independent of axillary node status (McGuire *et al.*, 1990). 54.8% (51/93) of the tumors in this study were positive for ER especially those with tumor size less than 2 cm in diameter (T1). Moreover, ER positivity was significantly more in stage 1 and 2 compared to stage 3 and 4 (p<0.05). Most of the cases having follow up for 25-48 months or more than 48 months were also ER positive and only 3 of 7 patients who died during our study period had ER positive tumor. This clearly indicates the good prognosis of tumors with positive ER status.

The significant association of early stage breast cancer and prolonged survival with ER positivity in our patients indicating that breast carcinomas expressing estrogen receptors have better prognosis because they are more differentiated and favorably respond to hormonal treatment compared with ER negative tumors (Clark and McGuire, 1988; McGuire *et al.*, 1990). Moreover, patients with ER positive tumors have prolonged disease free survival after primary treatment, superior overall survival and longer survival after recurrence compared with patients having ER-negative tumors (McGuire *et al.*, 1990).

The better survival (p=0.011) of those with increased expression of nm23 is probably related to the anti-metastatic effect of this marker (Zhao *et al.*, 2004), however no significant association could be established between nm23 and lymph node and distant metastasis (Table 4). Marginal association though a non-significant one was noted between decreased nm23 expression and lymph node metastasis (p = 0.11).

The influence of cyclin E on clinical outcome (p=0.02) is probably attributed to its influence on treatment strategy and its association with other poor prognostic parameters like high grade, late stage and negative estrogen receptor status (Donnellan and Chetty, 1999). However, it could not be substantiated in our present study.

The two markers p27 and nm23 that are known to have anti-tumor effects (Osborn *et al*., 2004; William, 1997; Tan *et al*., 1997; Porter *et al*., 1997) and thus favorably influence prognosis were unsurprisingly found to be significantly associated with ER which also has a favorable prognostic influence (Hlupić *et al*., 2004).

CONCLUSION

The present study showed that most of the breast cancer patients attending the breast clinic in HTAA Kuantan, present at an early stage and are ER-positive, thus having good prospect for favorable prognosis if appropriately treated. *nm23* in this study appears to be the only marker besides ER that significantly influenced patients' survival while cyclin E had an influence on clinical outcome. The combination of markers examined in this study might have an influence on the prospective biological behavior of breast tumors and the ultimate survival and well being of these patients. The prognostic value of individual biological factors could, therefore, be more effective in combination as opposed to single factors (Schindlbeck *et al*., 2005). Since we are still a long way, short of accurately defining the right combination of prognostic markers. It is suggested, that a more comprehensive and statistically reliable data can be obtained, if a much larger number of breast cancer cases from all over Malaysia is to be included in this type of research work.

ACKNOWLEDGEMENTS

REFERENCES

Ahmad, M. 2003. Risk factors for breast cancer among women attending breast clinic in university Malaya medical centre Kuala Lumpur NCD Malaysia. 2 (4):23-31.

Albert, KHL. 1991. Cancer- A Major Health Problem in Malaysia. Medical Journal of Malaysia. 46(2):114-115.

Bare, M., Bonfill, X. and Andreu, X. 2006. Relationship between the method of detection and prognostic factors for breast cancer in a community with a screening programme. J Med Screen. 13:183-191.

Bay, BH., Jin, R, Huang, J. and Tan, PH. 2006. Metallothionein as a Prognostic Biomarker in Breast Cancer. Exp Biol Med. 231:1516-1521.

Brody T., Larner J., Minnerman K. and Neu, H. 1994. Human Pharmacology. Molecular to Clinical. MS Mosby-Year Book, Inc. St. Louis, USA.

Callagy, GM., Pharoah, PD., Pinder, SE., Hsu, FD., Nielsen, TO., Ragaz, J., Ellis, IO., Huntsman, D. and Caldas, C. 2006. Bcl-2 Is a Prognostic Marker in Breast Cancer Independently of the Nottingham Prognostic Index. Clin Cancer Res. 12(8):2468-2475.

Clark, GM. and McGuire, WL. 1988. Steroid receptors and other prognostic factors in primary breast cancer. Semin Oncol. 15:20–25.

D1 Arciero C, Somiari, SB., Shriver, CD., Brzeski, H., Jordan, R., Hu H., Ellsworth, DL. and Somiari, RI. 2003. Functional relationship and gene ontology classification of breast cancer biomarkers. Int J Biol Markers. 18(4):241-72.

Donnellan, R. and Chetty, R. 1999. Cyclin E in human cancers. The FASEB Journal. 13:773-780.

Douglas, FE. 2002. Familial risks of breast cancer. Breast Cancer Res. 4:179-181.

Elston, CW. and Ellis, IO. 1991. Pathological prognostic factors in breast cancer: the value of histological grade in breast cancer: experience from a large study with long-term follow-up. Histopathology. 19:403-410.

Esteva, SJ. and Hortobagyi, GN. 2004. Prognostic molecular markers in early breast cancer. Breast Cancer Res. 6:109-118.

Ferlay, J., Bray, F., Pisani, P. and Parkin, DM. 2001. GLOBOCAN 2000*:* Cancer Incidence, Mortality and Prevalence Worldwide IARC Cancer Base No. 5 [10]. Lyon, France. IARC. 23.

Fleming, ID., Cooper, JS. and Henson, DE (eds.). 1997. American Joint Committee on Cancer: AJCC Cancer Staging Manual (5th edition). Philadelphia. Pa. Lippincott-Raven. 171-80.

Goodman, HM. 1988. Basic Medical Endocrinology. Raven Press, New York, USA.

Hlupić, L., Jakić-Razumović, J., Božikov, J., Ćorić, M., Belev, B. and Vrbanec, D. 2004. Prognostic value of different factors in breast carcinoma. Tumori. 90:112-119.

Huang, WY., Newman, B., Millikan, RC., Schell, MJ., Hulka, BS. and Moorman, PG. 2000. Hormone-related factors and risk of breast cancer in relation to estrogen receptor and progesterone receptor status. Am. J. Epidemiol. 151:703-714.

Jakic-Razumovic, J., Bozikov, J., Sarcevic, B., Kosanovic, VSS., Jonjic, N., Mustac, E., Tomic, S., Bezic, J., Kruslin, B., Vucic, M., Tomas, D., Dmitrovic, B., Valerija, BV., Jakovina, T., Svagelj, D., Boric, I., Njirik, Z., Stitic, V., Mlinac-Lucijanic, M., Restek-Samarzija, N., Predrijevac, H. and Gosev, M. 2005. HER-2/neu over expression in Croatian breast cancer patients: Results of one-year multicentric prospective study. Cancer Therapy. 3:167-176.

Jokhio, R. and Ansari, AF. 2005. Cobra Snake Venom reduces significantly tissue nucleic acid levels in Human Breast Cancer. JPMA. 55:71-73.

Joseph, JK. 1998. Pilot study of Formerstane in post-menopausal women with breast cancer. Medical Journal of Malaysia. 53(1):37-41.

Joshi, SC., Pant, I., Shukla, AN. and Kumar, G. 2008. Radiation Therapy and Breast Conservative Surgery: A Concise Review. Journal of Clinical and Diagnostic Research. 2:668-673.

Key, TJA. and Pike, MC. 1988. The role of estrogen and progestagens in the epidemiology and prevention of breast cancer. Eur. J. Cancer Clin Oncol. 24:29-34.

Keyomarsi, K., O'Leary, N., Molner, G., Lees, E., Fingert, HJ. and Pardee, A.1994. Cyclin E, a potential prognostic marker for breast cancer. Cancer Res. 54:380-385.

Keyomarsi, K., Tucker, SL., Buchholz, TA. and Matthew, C. 2003. Cyclin E and Survival in Patients with Breast Cancer. N Engl J Med. 348(2):186.

King, SE. and Schottenfeld, D.1996. The "epidemic" of breast cancer in the U.S. determining the factors. Oncology. 10:453-462.

Kröger, N., Milde-Langosch, K., Riethdorf, S., Schmoor, C., Schumacher, M., Zander, AR. and Löning, T. 2006. Prognostic and Predictive Effects of Immunohistochemical Factors in High-Risk Primary Breast Cancer Patients. Clin. Cancer Res. 12(1):159-168.

Lichtenstein, P., Holm, NV., Verkasalo, PK., Iliadou, A., Kaprio, J., Koskenvuo, M., Pukkala, E., Skytthe, A. and Hemminki, K. 2000. Environmental and heritable factors in the causation of cancer: analyses of cohorts of twins from Sweden, Denmark, and Finland. N Engl J Med. 343(2):78–85.

Lim, GCC., Halimah, Yahaya (eds.). 2003. Second report of the National Cancer Registry. Cancer incidence in Malaysia 2003. National Cancer Registry. Kuala Lumpur.

Lippman, ME. and Dickson, RB. 1989. Mechanism of normal and malignant breast epithelial growth regulation. J. Steroid Biochem. 34:107-121.

Mahathevan. 2002. Cancer Education in Malaysia. Int. Med J. 1 (2):23-24.

Malaysian National Cancer Registry Report, 2003. The second report of the National Cancer Registry-Cancer Incidence in Malaysia 2003. (http://www.crc,gov.my/ncr).

McCarty, KSJ., Silva, JS., Cox, EB., Leight, GS., Wells, SA. and McCarty, KS. 1983. Relationship of age and menopausal status to estrogen receptor content in primary carcinoma of the breast. Ann. Surg. 197:123-127.

McGuire, WL., Tandon, AK., Allred, DC., Chamness, GC. and Clark, GM. 1990. How to use prognostic factors in axillary node-negative breast cancer patients. J. Natl. Cancer Inst. 82:1006-1015.

Naguib, RNG., Sakim, HAM., Lakshmi, MS., Wadehra, V., Lennard, TWJ., Bhatavdekar, J. and Sherbet, GV. 1999. DNA Ploidy and Cell Cycle Distribution of Breast Cancer Aspirate Cells Measured by Image Cytometry and Analyzed by Artificial Neural Networks for their Prognostic Significance. IEEE Transactions on Information Technology in Biomedicine. 3 (1):61-69.

Osborn, C., Wilson, P. and Tripathy, D. 2004. Oncogenes and tumor suppressor genes in breast cancer: Potential diagnostic and therapeutic applications. The Oncologist. 9:361-377.

Parkin, DM., Bray, FI. and Devesa, SS. 2001. Cancer burden in the year 2000. The global picture. Eur J Cancer. 37:54-566.

Parkin, DM., Whelan, SL., Ferlay, J., Teppo, L. and Thomas, DB. 2002. Cancer Incidence in Five Continents. Volume VIII. IARC Scientific Publication No. 155. Lyon.

Pedrini, P., Machado, S. and Grudzinski, Z. 2004. Reassessing tumor markers in local recurrences of breast cancer: a new insight. Med Sci Monit. 10 (12):462-467.

Pike, MC., Spicer, DV., Dahmoush, L. and Press, MF. 1993. Estrogens, progestogens, normal breast proliferation, and breast cancer risk. Epidemiol. Rev. 15:17-35.

Pinder, S.E., Murray, S., Ellis, IO., Trihia, H., Elston, CW., Gelber, RD., Goldhirsch, A., Lindtner, J., Cortes-Funes, H., Simoncini, E., Byrne, MJ., Golouh, R., Rudenstam, CM., Castiglione-Gertsch, M. and Gusterson, BA. 1998. The importance of the histologic grade of invasive breast carcinoma and response to chemotherapy. Cancer. 83:1529-39.

Ricketts, D., Turnbull, L., Ryall, G., Bakhshi, R., Rawson, NS., Gazet, JC., Nolan, C. and Coombes, RC. 1991. Estrogen and progesterone receptors in the normal female breast. Cancer Res. 51:1817-1822.

Ries, LAG., Eisner, MP., Kosary, CL., Hankey, BF., Miller, BA., Clegg, L., Mariotto, A., Feuer, EJ. and Edwards, BK (eds.). 2004. SEER Cancer Statistics Review, 1975-2001, National Cancer Institute. Bethesda, MD, USA.

Schindlbeck, C., Kampik, T., Janni, W., Rack, B., Jeschke, U., Krajewski, S., Sommer, H. and Friese, K. 2005. Prognostic relevance of disseminated tumour cells in the bone marrow and biological factors of 265 primary breast carcinomas. Breast Cancer Research. 7:R1174-R1185.

Schwartz, GF., Schwartlng, R., Rabindranauth, P. and Finkel, GC. 1993. Clinical Applications of Serum and Tissue Markers in Malignant Disease: Breast Cancer as the Paradigm. Clin Chem. 39/11(B):2404-2412.

Senie, RT., Rosen, PP., Lesser, ML., Snyder, RE., Schottenfeld, D. and Dutchie, K. 1980. Epidemiology of breast carcinoma II: factors related to the predominance of left-sided disease. Cancer. 46:1705-1713.

Sgambato, A., Doki, Y., Schieren, I. and Weinstein, IB. 1997. Effects of cyclin E overexpression on cell growth and response to transforming growth factor ß depend on cell context and p27Kip1 expression. Cell Growth Differ. 8:393-405.

Tan, P., Cady, B., Wanner, M., Worland, P., Cukor, B., Magi-Galluzzi, C., Lavin, P., Draetta, G., Pagano, M. and Loda, M. 1997. The cell cycle inhibitor p27 is an independent prognostic marker in small (T1a,b) invasive breast carcinoma. Cancer Res. 57:1259-1263.

Thomas, HV., Reeves, GK. and Key, TJA. 1997. Endogenous estrogen and post-menopausal breast cancer: a quantitative review. Cancer Cause Control. 8:922-928.

William, LD. 1997. Tumor-Related Prognostic Factors for Breast Cancer. CA Cancer J Clin. 47:28-51.

Wyld, L., Gutteridge, E., Pinder, SE., James, JJ., Chan., SY., Cheung., KL., Robertson, JFR. and Evans, AJ. 2003. Prognostic factors for patients with hepatic metastases from breast cancer. Brit J Cancer. 89:284-290.

Yip, CH. and Ng, EH. 1996. Breast Cancer- A comparative study between Malaysian and Singaporean Women. Singapore Medical Journal. 37:264-267.

Zhao, H., Jhanwar-Uniyal, M., Datta, PK., Yemul, S., Ho, L., Khitrov, G., Kupershmidt, I., Pasinetti, GM., Ray, T., Athwal, RS. and Achary, MP. 2004. Nm23 and breast cancer metastasis. Int J Cancer. 109(1):65-70.

IN VITRO ANTIOXIDANT POTENTIAL OF *ASTILBE RIVULARIS* RHIZOME

*Palash Mandal, Tarun Kumar Misra and Prabhat Kumar Basu
Department of Botany, North Bengal University, Darjeeling, West Bengal 734013 India

ABSTRACT

The dried rhizomes of *Astilbe rivularis* Buch-Ham ex D.Don have been traditionally used for the treatment of inflammatory diseases, headache and infertility from the ancient period in India. The physiological mechanisms of action, especially anti-inflammatory effect of this plant extract are not yet well understood. In this study, we examined the free radical scavenging effect and anti-lipid peroxidation in successively extracted, purified solvent fractions. The fractions execute significant free radical scavenging potentiality on DPPH (95.23%) at dose of 100 μg/ml, superoxide scavenging activity (80.40%) and anti-lipid peroxidation (45.83%) at the same doses, which are comparable with reference standard. We also investigated the anti-inflammatory effect of this plant extract on rat. The oral application at the dose of 100 mg and 200 mg/kg body weight of this plant extract promoted healing action (56.20 % inhibition at the dose of 200 mg/kg after 24 hrs) on carrageenan induced rat paw inflammation; which is also comparable with standard of non steroidal anti-inflammatory drug (Ibuprofen) 20 mg/kg body weight (48.18% inhibition after 24 hours). The observations from these studies suggest the ethno medicinal use of *Astilbe rivularis* which could be commercially exploited by the pharmaceutical industry.

Keywords: *Astilbe rivularis,* solvent fractions, free radicals scavenging, antilipid peroxidation, anti-inflammatory.

INTRODUCTION

The therapeutic properties of *Astilbe rivularis* Buch.Ham.ex D.Don (AR) [local name: Buro okhati or Bhadhangoo] family Saxifragaceae have known for decades in several traditional therapeutics. It is predominant in gardens and waysides of Darjeeling Hills. High amount of polyphenols, flavonoids, coumarin berginin, triterpenoids, acetyl-β peltoboykniolic acid, peltoboykniolic acid and astilbic acid are present in AR rhizomes. Major traditional uses of its dried rhizomes are mainly for the treatment of headache and infertility by the tribal community of the hills**.** For several decades, numerous medicinal preparations of AR rhizomes have been used as potential phyto-therapeutics among different ethnic races (Chettri *et al*., 2005)**.** In addition to medicinal uses, AR rhizomes are processed into various products like antecedent (Tandon *et al*., 1996).

The increasing interest in alimentary applications of herbal components rich in antioxidant is due to possible correlation between the oxidant action of the free radicals and the onset of some important pathology. The drugs which are in presently for the management of pain and inflammatory condition are either narcotic e.g. opoid or non-narcotics e.g. Salicylates and corticosteroids e.g. hydrocortisone. All these drugs have well known side and toxic effects. Moreover synthetic drugs are very expensive to develop for the successful introduction of new products. Therefore many medicines of plant origins has been used since long time without any side effects. In the very recent consumer preference has also shifted the

attention from costly synthetic to cheaply natural less toxic molecules (Dapkevicius *et al*., 1998). Several components present in plants have reported to be biologically active antioxidant and have bioregulatory properties. AR rhizomes are well known for their medicinal properties and thus have been used to treat many diseases like anti-herpes and anti-influenza (Rajbhandari *et al*., 2001). Proximate compositions and health benefit of these plants has been documented (Sastry *et al*., 1987). However no information is available on its anti-inflammatory properties, it is therefore essential that effort should be made to introduce new medicinal plants to develop cheaper phyto-products in this aspect. The lack of potent antioxidant and anti-inflammatory herbal drugs now actually in use prompted the present study, which *Astilbe rivularis* has been selected for their biological activities in successive extracts. The antioxidant potentiality and anti-inflammatory activity of AR rhizomes may guide the pharmaceutical industry to seek a large untapped source of structurally novel compounds that might serve as lead for the development of preventive phyto-pharmaceuticals.

MATERIALS AND METHODS

Materials
Description of plant
It is a perennial herb. Rhizome is erect with sparsely brown villous stem, narrowly racemose branch, alternate leaves are long and broad, leaflets ovate or elliptical, acuminate base rounded or cordate, double serrate margin, appressed brown hirsute on veins, long petiole

*Corresponding author email: nbubotanypalash@rediffmail.com

bearing brown hair specially at axils of leaflets. The small flowers are arranged in terminal panicles; peduncles pale brownish pubescent, calyx divided almost two bases into lanceolate teeth, petal absent, number of stamens five, opposite sepal ovary semi-inferior. All parts of the plant are slightly aromatic in odour.

Collection and treatment of rhizome
A. rivularis (Saxifragaceae) rhizomes are collected from the Kurseong local area, Darjeeling, West Bengal in December 2006. Taxonomic position was authenticated by the Taxonomy and Environmental Biology Laboratory, Department of Botany, University of North Bengal under accession number 9481 dated 05-02-2008. The collected rhizomes were then dried in shade at temperature between 21º to 30º C for 30 days after which 500 g of this part of plants were chopped and ground. Finally successive extractions were carried out in different solvents.

Preparation of rhizome extracts and purification
The ground plant materials approximately 100g were soaked in 100 ml of methanol and boiled for 8 hours on a hot plate with glass beads. The flask containing methanol extracts were kept overnight for cold percolations. The extracts were filtered through double layer of muslin cloth and volume was reduced by evaporation under reduced pressure in rotary evaporator. Percentage of methanol yield was obtained as 53.1. The residual part were treated with chloroform and filtered through the same. Residue was washed three times and extracts were concentrated. Finally condensed filtrate was used for purification of components from hydrophobic to hydrophilic in the silica gel column chromatography (Volume of the column 47.1 cc.). Different solvent were used for elution one after another in three different ratios 3:1, 1:1 and 1:3 respectively. All the solvent fractions were evaporated to dryness under reduced pressure. After removal of solvent, extracts were reconstituted in methanol, and then used for evaluation of DPPH free radical and superoxide scavenging and anti-lipid peroxidation assay at a dose of 100 µg/ml. The fractions showing considerable (>90% inhibition) total free radical scavenging activities were mixed and evaporated to dryness, then after reconstitution with normal saline (0.9% w/v) was only used for the evaluation of anti-inflammatory effects.

Study animals
Male albino rats for anti-inflammatory studies were used in the present study. Weights of the rats ranged from 150 to 200 g respectively. All animals were maintained in groups of three at 25º ±1ºC with light/dark cycle of 12:12 h. They were starved overnight but allowed fresh water before administration of the extracts.

Fresh goat liver used for anti-lipid peroxidation assay was purchased from slaughter house immediately after slay.

Chemicals
Solvent used for column chromatography were of analytical grades. Silica gel G-60; 2,2-diphenyl-1-picrylhydrazyl (DPPH); nitroblue tetrazolium (NBT); reduced nicotinamide adenine dinucleotide phosphate sodium salt monohydrate (NADPH); phenazine methosulphate (PMS); trichloro acetic acid (TCA); thiobarbituric acid (TBA); $FeSO_4$, 7 H_2O; KOH; KH_2PO_4; quercetine were either of Sigma or Hi Media analytical grades.

Drugs
All the drugs used in this study were of pharmaceutical grade. Carrageenan was purchased by Sigma Chemical Company and Ibuprofen; a propionic acid derivative was purchased from local retail medicine shop (Marketed by Albert- David, brand name Alfan).

Antioxidant assay
DPPH based free radical scavenging activity
The free radical scavenging activities of each reconstituted fraction were assayed using stable DPPH, according to the method of Blois (1958). Percentage of free radical scavenging activity was expressed as percent inhibition from the given formula.

$$\% \text{ inhibition} = \frac{\text{Abs. of cont. abs. of sample}}{\text{Abs. of cont.}} \times 100$$

Superoxide anion scavenging activity
The superoxide anion scavenging activity was performed using method of Nishikimi *et al.* (1972) followed by slight modification. Percentage inhibition was calculated using the formula given above.

Anti-lipid peroxidation (ALP) assay
The anti-lipid peroxidation assay in the goat liver homogenate was measured by the method of Ohkawa *et al.* (1979), followed by slight modification. ALP % was calculated using the following formula.

$$\text{ALP} \% = \frac{\text{Abs. of } Fe^{2+} \text{ induced peroxidation - abs. of sample}}{\text{Abs. of } Fe^{2+} \text{ induced peroxidation - abs. of control}} \times 100$$

Procedure for testing anti inflammatory activity
Hind paw edema method
In the present study anti inflammatory activity was determined in male Albino rats; following the method of Winter *et al.* (1962) using three animals in each group. Carrageenan (1% w/v suspension in normal saline) was injected to animals, in the right hind foot under the plantar aponeurosis (Goudgaon *et al.*, 2003). The test groups (1 and 2) of rats were given orally 100 and 200 mg/kg of normal saline reconstituted mixture of extract of AR one hour before the carrageenan injection. The controls were treated with the same volume of saline as in test group. Another group of rats were treated with 18 mg/kg (dose of

the drug were calculated as per body weight of the rat) of Ibuprofen (NSAID) orally one hour before carrageenan injection. The inflammation was quantitated by using vernier caliper immediately before carrageenan injection and then 1, 2 and 24 hours after carrageenan injection. The percentage inhibition of edema was calculated for each group with that of vehicle treated control group by using the following formula:

$$\frac{V_d V_p}{V_c V_p} \times 100$$

Where $V_d - V_p$ = Difference in paw volume after carrageenan injection and initial paw volume for drug treated animal, $V_c - V_p$ = Difference in paw volume after carrageenan injection and initial paw volume for control animals.

Statistical analysis
All the experiments were repeated three times and data were represented as mean ± S.D and were analyzed by SPSS (version 11.0 SPSS, Inc.). Analysis of variance (ANOVA) was used to determine the difference among the fractions. The Duncan's multiple range test (DMRT) was used for making comparison (Gomez and Gomez, 1984) $P < 0.01$ was regarded as significant.

RESULTS

DPPH Assay
Among the 33 extracts tested for antioxidant activity using DPPH method the successive diethyl ether in ethyl acetate and ethyl acetate in acetone extracts exhibited strong antioxidant activity as evidenced by their higher percentage of inhibition (Table 1). The values were comparable to that of standard quercetine. When considering the organic fractions of *A. rivularis*, the DPPH radical scavenging capacities increased with increasing the polarity of the solvent.

Inhibitory effect of different fractions on superoxide anion formation
Scavenging effect of different concentration of all extracts

Table 1. DPPH free radical scavenging activity in the different solvent fractions of AR rhizomes.

Solvent fractions v/v	100%	75%	50%	25%
Hexane in benzene	91.67 ± 0.58^D	27.17 ± 0.46^L	10.51 ± 0.50^O	8.06 ± 0.24^P
Benzene in chloroform	5.05 ± 0.05^{RS}	3.01 ± 0.04^T	12.98 ± 0.13^M	3.00 ± 0.05^T
Chloroform in diethyl ether	6.97 ± 0.15^Q	5.07 ± 0.21^{RS}	2.13 ± 0.15^U	44.10 ± 0.10^J
Diethyl ether in ethyl acetate	93.10 ± 0.36^C	95.23 ± 0.49^A	55.50 ± 0.44^I	60.60 ± 0.53^H
Ethyl acetate in acetone	35.03 ± 0.15^K	$93.78 \pm O.46^{BC}$	94.18 ± 0.18^B	93.20 ± 0.35^C
Acetone in ethanol	90.73 ± 0.31^E	84.37 ± 0.32^F	3.10 ± 0.10^T	70.70 ± 0.62^G
Ethanol in methanol	93.00 ± 0.10^C	93.01 ± 0.31^C	27.10 ± 0.36^L	4.30 ± 0.30^S
Methanol in water	1.17 ± 0.15^V	2.13 ± 0.15^U	15.22 ± 0.20^M	1.07 ± 0.21^V
Water	5.43 ± 0.15^R			
Quercetine(standard)	$44.67 \pm 0.1.53^J$			

$CD_{0.01} = O.8187$
Values indicate % inhibition of DPPH free radical over control ± S.D (n = 3), figures symbolized by the same alphabet/s (in superscript) are not significantly different at $P < 0.01$

Table 2. Superoxide radical scavenging activity in the different solvent fractions of AR rhizomes.

Solvent fractions v/v	100%	75%	50%	25%
Hexane in benzene	26.03 ± 0.55^E	12.03 ± 0.15^J	2.33 ± 0.15^N	1.63 ± 0.21^O
Benzene in chloroform	0.96 ± 0.02^{PQR}	0.77 ± 0.15^{QR}	1.47 ± 0.25^{OP}	1.37 ± 0.21^{OPQ}
Chloroform in diethyl ether	$1.07 \ 0.15^{OPQR}$	1.33 ± 0.15^{OPQR}	0.70 ± 0.10^R	18.80 ± 0.20^H
Diethyl ether in ethyl acetate	2.53 ± 0.15^N	2.47 ± 0.25^N	22.43 ± 0.25^G	11.47 ± 0.35^J
Ethyl acetate in acetone	24.83 ± 0.21^F	42.77 ± 0.25^D	48.77 ± 0.15^B	48.83 ± 0.15^D
Acetone in ethanol	46.33 ± 0.38^C	80.40 ± 0.36^A	2.50 ± 0.20^N	1.57 ± 0.15^{OP}
Ethanol in methanol	5.40 ± 0.20^K	16.87 ± 0.25^I	3.37 ± 0.25^M	2.47 ± 0.15^N
Methanol in water	2.67 ± 0.15^N	1.47 ± 0.35^{OP}	1.57 ± 0.15^{OP}	1.67 ± 0.25^O
Water	4.50 ± 0.20^L			
Quercetine(standard)	46.01 ± 0.79^C			

$CD_{0.01} = 0.5843$
Values indicate % inhibition of super oxide radical over control ± S.D (n = 3), figures symbolized by the same alphabet/s (in superscript) are not significantly different at $P < 0.01$

Table 3. Percentage of anti-lipid peroxidation in the different solvent fractions of AR rhizome.

Solvent fractions v/v	100%	75%	50%	25%
Hexane in benzene	15.87 ± 0.15^{L}	10.77 ± 0.15^{O}	5.63 ± 0.31^{Q}	4.67 ± 0.32^{R}
Benzene in chloroform	3.33 ± 0.31^{S}	2.67 ± 0.25^{T}	1.60 ± 0.10^{U}	1.63 ± 0.21^{U}
Chloroform in diethyl ether	2.43 ± 0.25^{T}	1.63 ± 0.21^{U}	1.73 ± 0.21^{U}	11.63 ± 0.06^{N}
Diethyl ether in ethyl acetate	30.30 ± 0.20^{H}	35.70 ± 0.20^{E}	18.63 ± 0.31^{K}	14.80 ± 0.26^{M}
Ethyl acetate in acetone	7.57 ± 0.35^{P}	34.57 ± 0.32^{F}	33.67 ± 0.21^{G}	28.60 ± 0.30^{I}
Acetone in ethanol	44.67 ± 0.17^{C}	42.50 ± 0.30^{D}	1.63 ± 0.23^{U}	19.47 ± 0.06^{J}
Ethanol in methanol	45.83 ± 0.15^{B}	35.67 ± 0.49^{E}	5.73 ± 0.15^{Q}	1.42 ± 0.27^{UV}
Methanol in water	0.73 ± 0.26^{W}	1.07 ± 0.02^{UVW}	2.60 ± 0.10^{T}	0.93 ± 0.05^{UW}
Water	1.29 ± 0.18^{UVW}			
Curcumin(standard)	$46.83\ \pm 0.76^{A}$			

$CD_{0.01}= 0.5854$
Values indicate ALP % over control $\pm$ S.D (n = 3), figures symbolized by the same alphabet/s (in superscript) are not significantly different at $P < 0.01$

on superoxide anions are shown in table 2. The superoxide radical scavenging activity of different organic extracts was measured by reduction of NBT. DMRT classification shows that the radical scavenging action was mostly concentrated in between ethyl acetate in acetone and acetone in ethanol solvent fractions. Polar solvent fractions like ethanol in methanol and methanol in water showed lesser superoxide anion scavenging property and the scavenging rates were in the range of 1.47 and 16.87 percent. Highly non-polar solvents like benzene in chloroform were inactive toward chemically generated superoxide radicals. The results showed that the acetone in ethanol fraction of *Astilbe rivularis* rhizome was found to be most potent antioxidant and was followed by ethyl acetate in acetone fraction. So these fractions are active against superoxide anion at only 5 fold higher concentration as that of the well known superoxide anion scavenger quercetine which was used as standard for positive control. The anti- lipid peroxidation effect of rhizome extract was observed in Fe^{2+} ion induced lipid peroxidation in goat liver homogenate against control. These effects in four fractions of AR rhizomes were significant as shown in table 3.

The mixture of four fractions possessed varying degree of anti-inflammatory activity which is comparable with the standard drug shown in table 4. The plant extract showed quicker anti-inflammatory response.

DISCUSSION

It has been observed that herbal antioxidants can prevent stress induced diseases in human beings. These activities of rhizome extract may be due to its polyphenolic contents. The free radicals scavenging activity is generally associated with the presence of reductions. Gordon (1990) reported that these activities of reducton's are believed to break radical chain by donation of a hydrogen atom, indicating the antioxidative properties concomitant with the development of reducing power. DPPH accept an electron or hydrogen radical to become a

diamagnetic molecule (Blois, 1958). It can react with specific antioxidant molecules which involves reduction of DPPH, therefore the marked free radical scavenging properties in different fractions may be related with its higher reducing power.

Other plants have proved their activities against superoxide radical scavenging viz. *Cissus quadrangularis* L. (Jainu *et al*., 2005), *Rosa damascene* Mill. (Achuthan *et al*., 2003). McCune *et al*. (2003) reported superoxide scavenging property of 35 different medicinal plant species. Superoxide anion scavenging activity has also been observed in the different fractions of AR rhizomes. Higher percentage of superoxide radical inhibition is the indication of the presence of bioactive compounds in the fractions of AR rhizomes. The superoxide can be formed enzymatically or non-enzymatically in the biological system. $O_2^{\cdot}$ may decrease the activity of other antioxidant defense, like catalase and catalase type enzymes (Halliwell *et al*., 1999). $O_2^{\cdot}$ radical requires a slight input of energy that is often provided by NADPH in biological system.

It is known that cleavage products of lipid peroxidation accumulate in the central nervous system and in cardiac muscle fibers (Nohl, 1993). AR extracts has been found reduce lipid peroxidation of microsomal tissues in goat liver. Generally Malonaldehyde formed during the lipid peroxidation, may serve as active antioxidant molecules in the AR extract inhibiting this type of reaction. This is why AR rhizome extract may be considered as a corroboration of Ayurveda claims for the plant.

NSAIDs are widely used for the treatment of inflammation and pain and they act via inhibition of synthesis of prostaglandins (Vane, 1971). The selective COX-2 inhibitors are as efficacious as NSAIDs in preventing inflammation and pain. This study showed that the mixture of nine best fractions with antioxidant activity inhibited carrageenan induced rat paw edema, which is a valuable test for predicting the anti-

Table 4. Anti-inflammatory effects of plant extract on carrageenan induced rat paw edema.

Treatment	Group	Dose/kg BW	Initial paw volume (cm)	After carrageenan treated paw volume (cm)		
				1 Hr.	3 Hr.	24 Hrs.
Normal saline (0.9% w/v, Nacl)	Control	0.00	2.19	3.74	3.88	2.68
			2.31	3.81	3.97	2.71
			2.11	3.85	3.99	2.59
AR extract (Experimental)	Test-1	100 mg	1.97	2.73	2.75	2.27
			1.85	2.67	2.77	2.18
			2.13	2.82	2.86	2.32
AR extract (Experimental)	Test-2	200 mg	1.83	2.47	2.58	2.08
			1.91	2.59	2.63	2.01
			1.89	2.45	2.53	2.14
Ibuprofen	Standard	18 mg	2.08	2.55	2.63	2.26
			2.01	2.61	2.72	2.31
			2.16	2.51	259	2.39
Mean values and standard deviation from difference calculated as compared to 0 hr reading						
Normal saline (0.9% w/v, Nacl	Control	0.00		1.60 ± 0.13	1.74 ± 0.12	0.46 ± 0.05
AR extract (Experimental	Test-1	100 mg		0.76 ± 0.07	0.81 ± 0.10	0.27 ± 0.07
AR extract (Experimental	Test-2	200 mg		0.63 ± 0.06	0.70 ± 0.06	0.20 ± 0.09
Ibuprofen	Standard	18 mg		0.47 ± 0.13	0.56 ± 0.14	0.24 ± 0.06
Percentage inhibition						
Normal saline (0.9% w/v, Nacl	Control	0.00		0.00	0.00	0.00
AR extract (Experimental	Test-1	100 mg		52.61	53.54	40.15
AR extract (Experimental	Test-2	200 mg		60.75	59.66	56.20
Ibuprofen	Standard	18 mg		70.35	67.69	48.18

inflammatory action of this plant extracts, acting by inhibiting the mediator induced inflammation and also comparable with standard NSAIDs. It appeared to inhibit induced prostaglandin in inflamed tissue possibly due to the presence of Berginin and astilbic acid present in the extracts mixture. Other plants of the same genera like *Astilbe thunbergii* Miq. (Kimura *et al.*, 2007), *Astilbe chinensis* Maxim. ex Knoll (Taechul *et al.*, 2005) and *Astilbe koreana* Nakai (Na *et al.*, 2004) has also been observed to show the anti-inflammatory activity due to the presence of the same kinds of active constituents. Quick anti-inflammatory action might be due to the rapid absorption of the bioactive component of this plant (Ahmad *et al.*, 1992).

Phytochemical investigation will also be needed in order to isolate the active fraction of pure compounds and in the same fraction pharmacodynamic studies should also be under taken to evaluate the mechanism of action.

ACKNOWLEDGEMENT

REFERENCES

Achuthan, CR., Babu, BH. and Padikkala, J. 2003. Antioxidant and hepatoprotective effects of *Rosa damascena*. Pharmaceutical Biology. 41(5):357-361.

Ahmad, F., Khan, RA. and Rasheed, S. 1992. Study of analgesic and anti-inflammatory activity from plant extracts of *Lactuca scariola* and *Artemisia absinthium*. Journal of Islamic Academy of Sciences. 5(2):111-114.

Blois, MS. 1958. Antioxidant determination by the use of stable free radicals. Nature. 181:1199-1200.

Chettri, N., Sharma, E. and Lama, SD. 2005. Non-timber forest produces utilization, distribution and status in a trekking corridor of Sikkim, India. Lyonia. 8(1):89-101.

Dapkevicius, A., Venskutonis, R., Beek, TAV. and Linssen, JPH. 1998. Antioxidant activity of extracts obtained by different isolation procedures from some aromatic herbs grown in Lithuania. Journal of Science and Food Agriculture. 77:140-146.

Gomez, KA. and Gomez, AA. 1984. Statistical procedures for Agricultural Research. (2nd edition). John Wiley and Sons Ltd., New York, USA.

Gordon, MH. 1990. The mechanism of antioxidant action in vitro. In: Food antioxidant. Eds. Hudson, BJF. Elsevier Applied Science, London.

Goudgaon, NM., Basavaraj, NR. and Vijayalaxmi, A. 2003. Antiinflammatory activity of different fractions of *Leucas aspera* spreng. Indian Journal of Pharmacology. 35:397-398.

Halliwell, B. and Gutteridge, JMC. 1999. Free radical, other reactive species and disease. In: Free Radical in biology and medicine. Oxford Science Publications. Clarendon Press. Oxford.

Jainu, M. and Shyamala Devi, CS. 2005. *In Vitro* and *In Vivo* evaluation of free-radical scavenging potential of *Cissus quadrangularis*. Pharmaceutical Biology. 43(9):773-779.

Kimura, Y., Sumiyoshi, M. and Sakanaka, M. 2007. Effects of *Astilbe thunbergii* rhizomes on wound healing part I. Isolation of promotional effectors from *Astilbe thunbergii* rhizomes on burn wound healing. Journal of Ethnopharmacology. 109(1):72-77.

McCune, LM. and Johns, T. 2003. Symptom-specific antioxidant activity of Boreal diabetes treatments. Pharmaceutical Biology. 41(5):362-370.

Nohl, H. 1993. Involvement of free radicals in ageing: a consequence or cause of senescence. British Medical Bulletin. 49:653-657.

Na, M., Min, BS., An, RB., Song, KS., Seong, YH. and Bae, K. 2004. Effect of *Astilbe koreana* on ultraviolet B (UVB) - Induced Inflammatory Response in Human Keratinocytes. Biological and Pharmaceutical Bulletin. 27(8):1301.

Nishikimi, M., Appaji, N. and Yagi, K. 1972. The occurrence of superoxide anion in the reaction of reduced phenazine methosulphate and molecular oxygen. Biochemical and Biophysical Research Communications. 46:849-854.

Ohkawa, H., Ohishi, N. and Yagi, K. 1979. Assay for lipid peroxides in animal tissues by thiobarbituric acid reaction. Analytical Biochemistry. 95:351-358.

Rajbhandari, M., Wegner, U., Jülich, M., Schöpke, T. and Mentel, R. 2001. Screening of Nepalese medicinal plants for antiviral activity. Journal of Ethnopharmacology. 74:251-55.

Sastry, BS., Vykuntam, U. and Rao, E. 1987. Chemical examination of the aerial parts of *Astilbe rivularis*. Indian Drugs. 24:354-59.

Taechul, M., Changxiu, L., JooSang, L., DongSeon, K., KihWan, B., KunHo. S., HyunPyo, K., SamSik, K., JongKeun, S. and HyeunWook, C. 2005. Antiinflammatory activity of astilbic acid from *Astilbe chinensis*. Pharmaceutical Bulletin. 28(1):24-26.

Tandon, M., Shukla, YN., Tripathi, AK. and Sharma, S. 1996. Antifeedant activity of bergenin isolated from *Astilbe rivularis*. Fitoterapia. 67:277-78.

Vane, JR. 1971. Inhibition of prostaglandin synthesis as a mechanism of action for aspirin –like drugs. Nature New Biology. 231:232-235.

Winter, CA., Risely, EA. and Nuss, GV. 1962. Carrageenin induced edema in hind paw of rat as an assay for anti-inflammatory drugs. Proceedings of the society for Experimental Biology and Medicine. 111:544-547.

Canadian Journal of
pure&applied
sciences

EFFECT OF PHLOEMIC STRESS ON CYTOKININ CONTENT
IN YOUNG PEACH TREES BY USING SOYBEAN CALLUS BIOASSY

*ABM Sharif Hossain[1] and Fusao Mizutani
The Experimental Farm, Department of Bioresource Production Science
The United Graduate School of Agricultural Science, Ehime University, Hattanji 498, Matsuyama shi 799-2424, Japan
*[1]Present address: Laboratory of Plant Physiology and Biotechnology, Institute of Biological Sciences
Faculty of Science, University of Malaya, 50603 Kuala Lumpur, Malaysia

ABSTRACT

Cytokinin content in roots of peach trees (*Prunus persica* Batsch cv. Hikawahakuho) as affected by phloemic stress (bark ring) was studied. The treatments were applied to the trunk as control (no ringing), partial ringing [(represented by phloemic stress) PR] and complete ringing (CR). Phloem ring was made by peeling out 2 cm length of bark (phloem) from the trunk leaving a connecting 2 mm thickness of phloem strip (a bridge) while complete ringing (CR) left no phloem strip. Trunk diameter was higher in PR and CR treated trees than in un-ringed trees. Trunk diameter was higher above the ring than in below the ring both in PR and CR treated trees. However, it was higher in above the ring in case of PR and CR treated trees than in lower the ring both in PR and CR treated trees. The cytokinin content represented by callus weight was higher in control trees than in PR and CR treated trees. The results showed that cytokinin content decreased in roots of PR and CR treated trees. The results also indicated that growth promoting hormone (cytokinin) in peach roots affected overall plant nutrition and growth inhibiting hormon that led small sized peach trees.

Keywords: Cytokinin, dwarfing, ringing.

[Abbreviations: CR, Complete ring; PR, Partial ring; PVP, Polyvinyl pyrollidone].

INTRODUCTION

Phloem ringing is a horticultural practice used to manipulate tree growth and development, and fruit growth, in a variety of fruit species. Small, compact, dwarfed or size controlled fruit trees provide easier pruning, thinning, spraying and harvesting, high production of high-grade fruit and lower cost of production (Tukey, 1964). The primary factor limiting the use of size controlling rootstocks in stone fruit production was the lack of suitable rootstocks with a wide range of compatibility among cultivars (De Jong *et al*., 2001). Jose (1997) found lower vegetative growth in girdling treatments in relation to control in mango trees.

Arakawa *et al*. (1997) reported that trunk growth of apple trees above girdling was significantly increased and below girdling trunk growth was reduced. Onguso *et al*. (2004) reported that the increase of trunk circumference above girdling might be caused by swelling of trunk with accumulation of carbohydrates. They also stated that girdling blocked the translocation of sucrose from leaves to roots through phloem bundles. The block decreased starch content in root system and accumulated of sucrose in the leaves. Rose and Smith (2001) found that complete girdling of stems killed the plants and partial girdling weakened the plants.

Mullins (1967) stated that cytokinin successfully stimulated for root growth of young grapes. Antognozzi *et al*. (1993) reported that cytokinin activating compound N_1-(2-chloro-4pyridyl)-N_3-phenylurea (CPPU) increased the transverse diameter, size and fresh weight of olives. Park *et al*. (1997) observed that stem growth of kinetin treated persimmon trees was higher than control trees.

There is not available literature on cytokinin as affected by bark ringing. That is why, this study was undertaken to determine the cytokinin content which occured during senescence as affected by phloemic stress on the trunk represented by girdling.

MATERIALS AND METHODS

Site

The experiment was carried out in an orchard at Ehime University Farm located in southern Japan.

Plant materials

Two-year-old peach (*Prunus persica* Batsch cv. 'Hikawakuho') trees grafted on peach seedling stocks (wild form) were used in this experiment in April 2004. The seedling rootstocks were collected from nursery and transplanted to the main field on April 13 2004. The transplantation was done by maintaining pit (hole) method in the main field. The pit (hole) was spaced at 0.60 m x 1.0 m. The tree height was 0.70 m initially.

---

*Corresponding author email: sharif@um.edu.my

Weeding was done by maintaining row as required. Granular fertilizers were applied after transplanting at the rate of N, P_2O_5 and K_2O 10g, 10g and 10g per tree respectively. Irrigation was applied once in a week by hose pipe. Insecticide was applied once in a month.

Treatment setting
Treatments were set on June 13, 2004. Phloem ringing [partial ringing (PR)] was done by using a small sharp knife removing a partial ringing 2 cm length to leave a connecting strip (band) 2 mm width (thickness) in the trunk, 20 cm above from the ground. In case of complete ringing (CR) there was no connecting strip (band). There were 3 treatments each with 4 replications used in different trees in the experiment. The treatments were control (no ringing) phloem ring and complete ring. Treatments were repeated in different trees. There were a total 12 (4 x 3) trees used for cytokinin (from roots) analysis.

Sample collection and preparation for cytokinin
Root samples (30 g) were collected on July 11 2004 after one month of treatment setting. Twelve (3 x 4) trees were uprooted and washed. Fresh roots were separated, washed and kept in the Freezer immediately after harvest and used for cytokinin analysis.

Cytokinin analysis
The samples were ground with mixture machine and added with 500 ml of 80% ethanol and kept for 12 h in the refrigerator. After 12 h, samples were filtrated and washed the residue with 500 ml of 80% ethanol and keep for 12 h. The same procedure was repeated 3 times. Total 1500 ml of 80% ethanol extractant was collected after 48 h. Extractant was concentrated in vacuo at 35^0C by using a rotary evaporator and made it to the volume of 100 ml. The P^H was adjusted to 2.5 with 1 N HCl. Polyvinyl pyrrolidone (PVP) 5 g was added with the sample and filtrated. The 30 ml ethyle.acetate was added with the sample. The samples were filtrated with Dowex 50 W X 4 (Mesh) and washed with 100 ml of 80% ethanol. The samples were diluted with 200 ml 5N NH_4OH and cytokinin was separated. Finally the samples were dried in vacuo by Rotary evaporato and 5 ml of 35% ethanol was added with samples and kept in the freezer.

Cytokinin samples were purified by using Column Chromatograpy SephadexLH_2O (2.5 cm x 90 cm) and impurities were separated. The 40 ml of cytokinin samples were taken and repeated 32 times. Samples were dried in vacuo by Rotary evaporato and mixed with 5 ml water and standards of kinetin were prepared at 0, 0.01, 0.05, 0.1 and 0.5 ml concentration.

Soybean callus bioassay preparation by micropropagation
Culture media were prepared by using Miller (1967) Media. First of all macro and micronutrients were measured and put into the cylinder. The α- NAA and

kinetin were put into the cylinder and poured macro and micronutrient solutions. Then vitamins were added. The media were adjusted with KOH to 5.8 prior to use. All solutions were heated for 30 min. with electric heater and stirred. They were autoclaved at 15 lb/in at 121^oC for 15 min.

Soybean seeds were obtained from National Institute of Agrobiological Sciences, Ibaraki, Japan. Soybean seeds were collected and washed with tap water followed by rinsing with distilled water in the clean bench. Soybean seeds were surface sterilized for one min. with 70% ethanol, soaked in 1% sodium hypochloride plus a drop of liquid detergent. Then seeds were shaken gently for 20 min. followed by 10 times rinse with distilled water. Seeds were put into culture tube containing 10 ml Miller medium. Culture tubes were placed in a growth chamber under the following conditions: 27^oC, in darkness, RH 70-80%. After 15 days calli were grown.

Culture media were prepared 2nd time as described above. In this step, extracted plant cytokinin from different treatments was used as growth regulator and kinetin was used as standard. Grown calli were cut into different pieces and cultured in different replication of treatments and standard of kinetin. The calli were weighed after 2 weeks of growth. This weight showed the grade of cytokinin conent in different treatments.

RESULTS AND DISCUSSION

The effect of partial and complete ringing on trunk diameter after treatments application was shown in figure 1. In control trees, there was no difference between above and below ringing of trunk diameter. Finally it was higher above ring and lower below the ring in PR and CR than control trees (Table 1). There was a difference in diameter between above and below ringing in case of PR and CR. Trunk diameter was higher in CR trees above ring than in PR trees above ring. However, it was lower in CR trees lower ring than in PR trees lower ring. Cytokinin content represented by callus weight was higher in control trees than partial and complete ringing (Fig. 2). There was a significantly difference of cytokinin represented by callus weight between complete ringing (PR) and partial ringing (PR) as well as control. The lowest callus weight was found in complete ringing trees.

The results showed that trunk growth (diameter) was higher above the ring than below the ring possibly due to bark ringing. It was effective as a dwarfing technique in young peach trees by stress phenomenon using bark (phloem) ringing as a result of producing more ABA content and less cytokinin content after blocking translocation of photosynthates from leaves to roots. Arakawa et al. (1997) also reported similar result. They mentioned that trunk growth above girdling was significantly increased and below girdling was reduced in apple trees. Hossain et al. (2006, 2007) reported similar

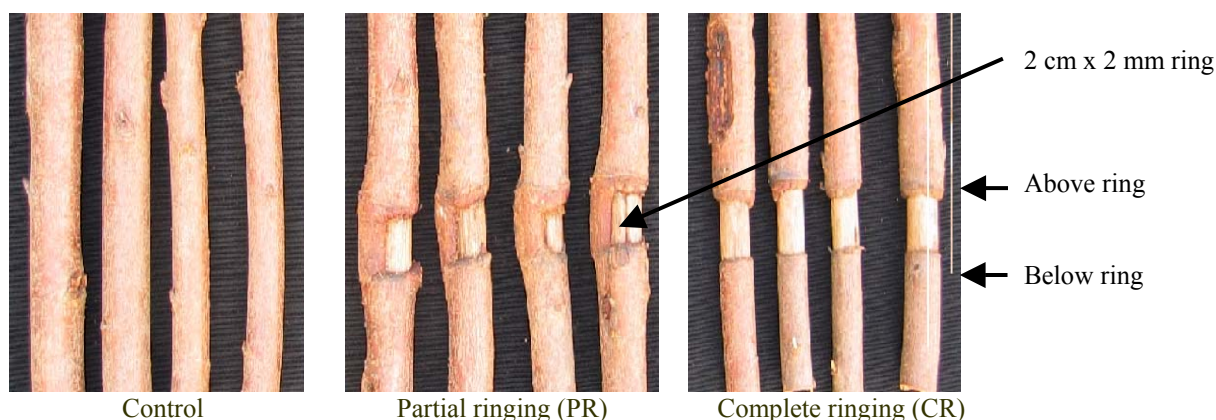| Control | Partial ringing (PR) | Complete ringing (CR) |

2 cm x 2 mm ring

Above ring

Below ring

Fig. 1. Photo shows ringing structure and trunkdiameter of peach trees as affected by partial and complete ringing (PR and CR).

result. They stated that trunk circumference was higher above the ring than below the ring in peach trees. Onguso *et al.* (2004) reported that sugar and starch contents were higher above the ringing than below the ringing. The block decreased starch content in root system and accumulated of sucrose in the leaves (Schneider, 1969; Plaut and Reinhold, 1967).

Table 1. The nutrient media (Miller, 1967) were used in soybean callus induction for cytokinin analysis.

Compound	Concentration	
Macronutrients:		
Ammonium nitrate (NH_4NO_3)	1000	(mg/l)
Potassium nitrate (KNO_3)	1000	100
Calcium nitrate {$Ca(NO_3)_2.4H_2O$}	500	-
Magnesium sulphate ($MgSO_4.7H_2O$)	71.5	-
Potassium phosphate (KH_2PO_4)	300	-
Potassium chloride (KCl)	65	-
Na2-EDTA	37.3	-
Iron sulphate ($FeSO_4.7H_2O$)	27.8	-
*From macronutrients 100ml/l was used		
Micronutrients:	-	-
Boric acid (HBO_3)	1.60	(mg/l)
Manganese sulphate ($MnSO_4.4H_2O$)	14.00	-
Zinc sulphate ($ZnSO_4.4H_2O$)	3.80	-
Potassium iodide (KI)	0.75	-
Ammonium molybdate {$(NH_4)_6Mo_7O_{24}.4H_2O$}	0.10	-
Copper nitrate {$Cu(NO_3)_2.3H_2O$}	0.35	-
*From micronutrients 1ml/l was used.		
Vitamins and plant growth regulators:		
Sucrose	30.0	(g/l)
Agar	10.0	-
α-NAA	2.0	(mg/l)
Kinetin	0.50	-
Myo-inositol	100	-
Nicotinic acid	0.5	-
Pyridoxin.HCl	0.2	-
Thiamine.HCl	0.2	-

Table 2. Trunk diameter of peach trees as affected by partial ringing (PR) and complete ringing.

Treatment	Trunk diameter (mm)			
	Initial	Above ring	Below ring	Ratio (A/B)
Control (no ring)	31.0a	32.0b	32.5a	1.01b
Partial ringing	30.5a	34.0a	33.0a	1.03b
Complete ringing	30.5a	34.5a	31.5b	1.09a

Mean in column followed by the same letter is not statistically significant at the 5 % level by DMRT.
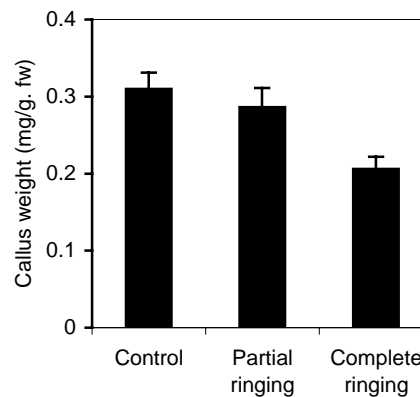
Fig. 2. Cytokinin content in peach root represented by callus weight in different treatments. Bars represented SE (n = 4). Mean in column followed by the same letter is not statistically significant at the 5 % level by DMRT.

Mullins (1967) stated that cytokinin successfully stimulated for root growth of young grapes. Antognozzi *et al.* (1993) reported that cytokinin activating compound N_1-(2-chloro-4pyridyl)-N_3-phenylurea (CPPU) increased the transverse diameter, size and fresh weight of olives. Park *et al.* (1997) observed that stem growth of kinetin treated persimmon trees was higher than control trees. Cytokinin and other plant growth hormones stimulated cell division (cytokinesis) and influenced the pathway of differentiation by stimulating RNA and protein synthesis
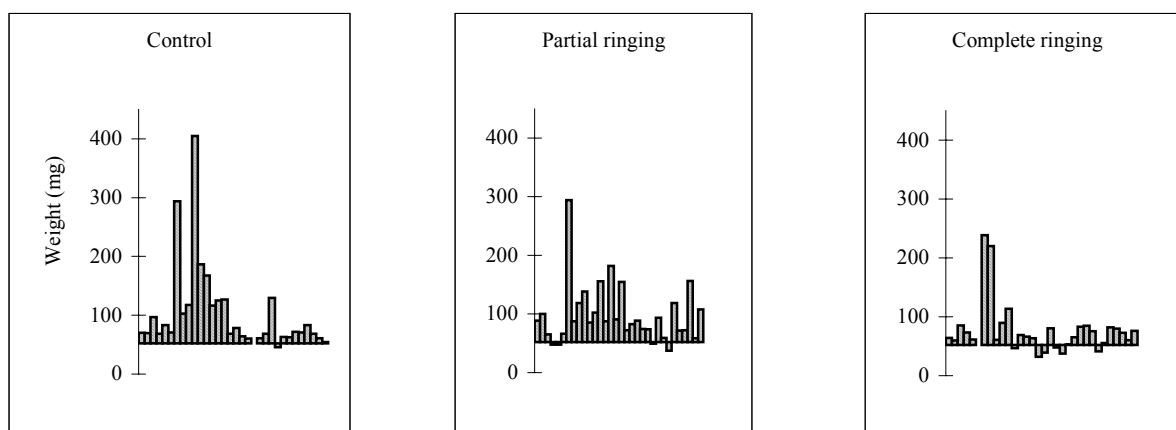
Fig. 3. Callus weight separately of different treatments at 32 times replicated by cytokinin samples.

(Khamis and Holubowicz, 1978). They might accumulate in leaves and cause the stomata to close, reducing transpiration and preventing further water loss. This way they may affect the tree physiological process.

In case of PR and CR trees, sucrose accumulated in the leaves and caused stomata closure resulting ABA increased and cytokinin decreased in leaves, shoots and twigs then it became growth inhibitory effect. A Sudden increase of endogenous ABA has been demonstrated also for several stress phenomena (Wright and Hiron, 1969).

Hossain (2006) found that ABA was higher in PR and CR trees than control. This might be due to more stress (partial ringing) or blocking (complete ringing) of translocation of photosynthates (sugar and starch) from leaves to roots by making restriction of bark ringing in the trunk. In this study, it was found that cytokinin content was lower in PR and CR than in control trees. This might be due to more stress induced by partial ringing (PR) or blocked by complete ringing (CR) of photosynthates translocated from leaves to roots.

CONCLUSION

Our results conclude that PR produced less cytokinin content than trees that have not been ringed (control) by causing nutrient and water stress which can inhibit the trunk growth. As a result, dwarfing is exhibited by whole peach tree. This result can also be effective for other fruit species.

ACKNOWLEDGEMENTS

REFERENCES

Antognozzi, E., Proietti, P. and Boco, M. 1993. Effect of CPPU (cytokinin) on table olive cultivars. Acta Hort. 329: 153-155.

Arakawa, O., Kanno, K., Kanetsuka. A. and Shiozaki, Y. 1997. Effect of girdling and bark inversion on tree growth and fruit quality of apple. Acta Hort. 45:579-586.

De Jong, DTM., Weibel, A., Tsuji, W., Doyle, JF., Johnson, RS. and Ramming, D. 2001. Evaluation of size controlling rootstocks for California peach production. Acta Hort. 557:103-110.

Goldschmidt, EE., Goren, R., Chen, ZE. and Bittner, S. 1973. Increase in Free and bound Abscsic acid during neutral and ethylene induced senescence of citrus fruit peel. Plant Physiol. 51:879-882.

Hossain, ABMS. 2006. Dwarfing peach trees grafted on vigorous rootstock by summer pruning and partial ringing. Ph.D. Thesis. Ehime University, Japan.

Jose, A. 1997. Effect of girdling treatments on flowering and production of mango. Acta Hort. 455:132-134.

Khamis, M. and Holubowicz, T. 1978. Effect of foliar application of alar, ethrel, ABA and CCC on the frost resistance of peach trees. Acta Hort. 81: 67-72.

Miller, C. 1967. Cytokinins in Zea mays. Ann NY Acad Sci. 14: 251-257.

Mullins, MG. 1967. Morphogenetic effects of roots and some synthetic cytokinins in Vitis vinifera L. J. Exptl. Bot. 18:206-214.

Onguso, JMF., Mizutani, F. and Hossain, ABMS. 2004. Effects of partial ringing and heating of trunk on shoot growth and fruit quality of peach trees. Bot. Bull. Acad. Sin. 45:301-306.

Park, M., Kim, B. and Kang, S. 1997. Effect of kinetin and B9 on the growth and carbohydrate partitioning in one-year-old trees of persimmon. Proc. 1st Int. Persimmon Symposium. Acta Hort. 436:365-373.

Plaut, Z. and Reinhold, L. 1967. The effect of water stress on the movement of ^{14}C-sucrose tritiated water within the supply of leaves of young bean plants. Aus. J. Biol. Sci. 20: 297-307.

Rose, MA. and Smith, E. 2001. Overwintering plants in the landscapes. Horticulture and Crop Science, Ohio State University Extension. Columbus. pp 4.

Schneider, H. 1969. Effect of trunk girdling on phloem of trunk of sweet orange trees on sour orange rootstocks. Hilgardia. 22:593-601.

Tukey, HB. 1964. Tree structure, physiology and dwarfing. Dwarf Fruit Trees, MacMillan Co., New York, USA. pp 562.

Wright, STC. and Hiron, RWP. 1969. Abscsic acid, the growth inhibitor induced in detached leaves and by a period of wilting. Nature. 224:719-720.

Canadian Journal of
pure&applied
sciences

CHEMICAL COMPOSITION, ANTIMICROBIAL AND CYTOTOXIC ACTIVITIES OF ESSENTIAL OIL AND LIPOIDAL MATTER OF THE FLOWERS AND PODS OF *TIPUANA TIPU* GROWING IN EGYPT

*Amany Lotfy Kansoh[1], Manal Shafik Afifi[2], Omayma Dawood Elgindi[3] and Reham Omar Bakr[2]
[1]Microbial Chemistry Department, National Research Centre, Dokki, Cairo
[2]Natural and Microbial product Department, National Research Centre, Dokki, Cairo
[3]Pharmacognosy Department, Faculty of Pharmacy, Al-Azhar University, Cairo, Egypt

ABSTRACT

Hydrodistillation of the flowers of *Tipuana tipu* yielded 0.5% v/w of oil. Eighteen components were identified by GC/MS analysis and Perhydro-farnesyl (32.17%) was the major constituent. Qualitative a and quantitative analysis of fatty acids and unsaponifiable matter using GC/MS revealed the presence of fifteen fatty acids in leaves and fourteen in pods. Decosane was the major identified hydrocarbon representing (17.6%) in leaves and (12.72%) in pods. .The leaf extract and volatile oil of flowers showed a broad spectrum antimicrobial effect, while pods extract showed obvious activity on *Escherichia coli* (gram –ve bacterium) and yeast. The minimum inhibitory concentrations of the methanolic and chloroformic extracts of leaves and pods were ranged from 0.2-0.6 mg/ml while volatile oil of flowers was 0.05. Leaf extract was found to be stable at 37ºC for 25 h and the remaining activity was 72% to 86%. The activity against all tested microorganisms was completely lost after incubation at 50ºC for 15 h. Storage at room temperature (25ºC) for three months in air tight glass bottle retains the activity. The exposure of the isolated fractions to different pH (2 to 12) for 15 min incubation period showed that fractions retain about 52% to 74% of the activity at pH 2 and 45% to 65% at pH 8 and a complete loss in activity was observed at pH 12. The methanolic extract showed an obvious cytotoxic activity against breast and colon carcinoma cell lines, while the chloroformic extract showed cytotoxic activity against breast and cervix carcinoma cell lines. The volatile oil showed significant cytotoxic activity against the three examined cell lines.

Keywords: *Tipuana tipu,* fabaceae, volatile oil, lipoidal constituents, antimicrobial activity, cytotoxic activity.

INTRODUCTION

Globally Family Fabaceae (Leguminosae) is the 3rd largest family of flowering plants, comprising the three subfamilies: Mimosoideae, Caesalpinioideae and Papilionoideae with nearly 20000 species (Hickey *et al.*, 1997; Lewis *et al.,* 2005). The genus *Tipuana* belongs to the subfamily Papilionoideae and comprises only one species *Tipuana tipu* (Hickey and King, 1997). The plant is beautiful flowering trees with yellow flowers, and it is called pride of Bolivia and yellow jacaranda. It is an indigenous to South America, Southern Bolivia and Northern Argentina, and has been planted allover the world as an ornamental street and garden tree. Genus *Machaerium* is used in South America by indigenous population to treat diarhea (Heinrich *et al.*, 1992) menstruation cramps (Ginzbarg, 1977), coughs (Joly *et al*., 1987) and aphtous ulcers of the mouth. Certain *Machaerium* species were reported to have antimicrobial (Waage *et al*., 1984), antigiardial (Elsohly *et al.*, 1999) and antitumor activities (Seo *et al.,* 2001) with the view of developing new antitumor and antimicrobial substances with low toxic potential, nature-derived compounds still play a major role as drugs and as lead structures for the development of synthetic molecules. Screening for new drugs in plants implies the screening of extracts for the

presence of novel compounds and evaluation of their bioactivities. Nothing was reported in the available literature concerning the volatile constituents of the flowers of *Tipuana tipu*, as well as lipoidal matter of the leaves and pods. This directed the present work to carry out a comparative study of the lipid content of the leaves and pods, as well as to identify the constituents of volatile oil of fresh flowers and evaluate their antimicrobial and cytotoxic activities.

MATERIALS AND METHODS

Plant material
Fresh leaves, flowers and pods of *Tipuana tipu* L (Family Fabaceae) were collected from trees growing in Cairo, Egypt. The flowers were collected in the month of May, while leaves and pods in July [The plant was identified by Mrs. Traes Labib, Plant Taxonomist at El-Orman Botanical Garden, Giza, Egypt. A voucher specimen was deposited in Pharmacognosy Department, Faculty of Pharmacy, Al-Azhar University].

Microorganisms for Antimicrobial activity
Gram+ve bacteria: *staphylococcus aureus, Bacillus subtilis*, *Bacillus cerrus,* Gram –ve bacteria: *Escherichia coli.* Fungi: *Aspergillus niger*, *A. flavus, A.terru,* and Yeast: *Saccharomyces carle*s, *Candida albicans, Candida*

*Corresponding author email: amany_kansoh@yahoo.com

pseudotropicales. Microorcanisms were obtained from MIRCEN, Cairo, Faculty of Agriculture, Ein-Shams University, Egypt.

Cell lines for cytotoxic activity (Skehan *et al.*, 1990)
HELA (cervix carcinoma cell line), MCF7 (breast carcinoma cell line), HCT116 (colon carcinoma cell line), 96 multiwell plate (10^4cells/well), Sulphorhodamine B stain, and Tris-EDTA buffer were used.

APPARATUS
 GLC: GLC/PYE UNICAM PRO-GC with SP-2300 column for saponifiable matter coupled to an injector temperature 250ºC 1.5 X 4mm**.** GLC/PYE UNICAM PRO-GC with column of methyl phenyl silicone OV-17 1.5x4mm (Faculty of Agriculture, University of Cairo)**.**

Preparation of plant extracts
The powder (200g) of each of the leaves and pods of *Tipuana tipu* was exhaustively extracted by repeated refluxing with light petroleum ether (60-80), chloroform and methanol, in succession. The solvent-free extracts were stored in the dark at -20ºC for further studies.

Preparation of essential oil
Volatile oil of flowers was obtained by steam distillation of fresh plant material in Clevenger type apparatus for 5hrs, affording a pale yellow oil which was dried over anhydrous sodium sulphate. Percentage yield and physical

constants were determined according to Egyptian Pharmacopoeia.

GC/MS analysis of essential oil
Volatile oil was dissolved in dichloromethane; GC/MS analysis of was performed with GC/MS (Shimadzu GC/MS-QP5050A), operated in the electron impact mode. Column, capillary DBI, 25m x 0.53 mm ID, 1.5 nm film. Temperature-programming: 40-160ºC at 7.5ºC/min., 160-230ºC at 2.5ºC/min. till 250 ºC. Injector temperature: 250ºC, Detector: FID, maintained at 280ºC; Carrier gas: He, flow-rate of 10 ml/min. Identification of volatile components was achieved by comparison of their retention times and mass fragmentation pattern with published data Adams (1989), Ardakani *et al.* (2003), Stenhagen *et al.* (1970), McLafferty *et al.* (1993), as well as Wikkey 229 LIB data base. Relative percentages were determined by integration of peak areas. Results are presented in table 1.

Preparation and saponification of lipoidal matter
Air-dried powdered leaves and pods (200g) were separately, extracted with light petroleum ether (60-80) till exhaustion. The extracts were evaporated under reduced pressure at temperature not exceeding 40ºC. One gram of each of the extracts was saponified by refluxing with alcoholic potash (10%) for 2 hours (Paech, 1955; Yamaguchi, 1970; Vogel, 1961). After evaporation of the solvent and dilution with cold water, the unsaponifiable

Table 1. GC/MS analysis of essential oils of *Tipuana tipu* flowers.

Peak No.	RRt*	%	M+	Base peak	(M/Z%)	Constituents
1	0.312	0.58	136	93.10	41,77,93	α-thujene
2	0.325	0.81	226	57.10	43, 57, 69, 108	Heptane
3	0.334	1.34	178	81.10	41,67, 81, 93, 138	Unidentified
4	0.347	0.52	136	93.10	41, 77, 93, 136	α-Phellandrene
5	0.355	0.67	90	119.15	41, 65, 77, 91, 119, 134	p-Cymene
6	0.361	12.47	136	68.10	41, 67, 93, 107, 121, 136	Limonene
7	0.39	5.82	154	41.10	41, 55, 71, 81, 93, 96, 121, 136	β- linalool
8	0.45	0.75	154	59.10	43, 59, 81, 93, 107, 121, 136	α-Terpineol
9	0.482	1.31	154	69.15	41, 68, 69, 93, 123	Trans geraniol
10	0.563	1.25	172	73.10	41, 60, 73, 129	Decanoic acid
11	0.635	3.95	194	43.05	43, 67, 69, 93, 107, 121, 136, 151	Geranyl acetone
12	0.642	1.39	204	41.10	41, 67, 93, 107, 121, 133	α-Farnescene
13	0.661	15.68	226	57.15	43, 57, 71, 85, 99, 113, 127, 141, 183	Hexadecane
14	0.84	1.04	154	43.10	43, 57, 71, 83	Camphene hydrate
15	0.917	1.67	148	105.10	41, 60, 77, 91, 91, 105, 129, 212	Cumin aldehyde
16	1	32.17	226	43.10	43, 58, 71, 85, 109, 124, 149, 165, 210	Perhydro-farnesyl acetone
17	1.067	3.33	270	74.10	43, 55, 74, 87, 143, 227	Methyl palmitate
18	1.104	13.62	256	41.10	41, 55, 73, 83, 97, 115, 129, 157, 213	Palmitic acid
19	1.198	1.61	220	67.15	41, 67, 79, 95, 108	Caryophyllene oxide

RRt: Relative retention time to perhydrofarnesyl acetone with Rt=43.218
M+: Molecular ion peak
M/z %: mass/charge arranged according to their relative intensities in a descending order.

fraction was extracted with successive portions of diethyl ether (3x15ml) and the combined ethereal extract was washed with distilled water, dried over anhydrous sodium sulphate and filtered was under reduced pressure. The residue left after evaporation of the solvent was weighed and kept for further investigation of USM. The aqueous alkaline solution left after separation of USM in each case was acidified with dilute hydrochloric acid; the liberated fatty acids (FA) being extracted with ether (3x15ml) till exhaustion. The combined ethereal extracts were washed with water till free from acidity and dehydrated over anhydrous sodium sulphate. An aliquot of the fatty acids fraction (0.5g) of each of the two organs was subjected to methylation, evaporated under reduced pressure till dryness and kept in a desiccator for GLC analysis. The percentages of USM and total FA are listed in table 2.

GLC of USM
GLC/PYE UNICAM Pro-GC; column: OV-17 (methyl phenyl silicone); 1.5mx4mm; detector: FID, temperature 300ºC; injector temperature, 250ºC; temperature-programming, 70-270ºC at 10º/min.; carrier gas, nitrogen, flow-rate 30 ml/min; chart speed, 0.4 cm/min. The results are presented in table 3.

GLC of Fatty acids Methyl Esters (FAME)
GLC/PYE UNICAM Pro-GC; column: SP-2300, 1.5mx4mm; detector, FID, temperature, 300ºC; injector temperature, 250ºC; temperature programming: 70-190ºC at 8º/min.; carrier gas, nitrogen, flow-rate: 30ml/min; chart speed, 0.4cm/min. The results are presented in table 4.

Table 2. Percentage yield of lipoidal matter in leaves and pods of *Tipuana tipu* and percentage composition of unsaponifiable matter and total fatty acids.

Plant part	% lipoidal matter	% composition	
		Unsaponifiable matter	Fatty acids
Leaves	0.1	93%	7%
pods	0.2	40%	60%

Table 3. GLC analysis of unsaponifiable matter of *Tipuana tipu* leaves and pods.

Authentic	Carbon No.	RRt*	Relative %	
			Leaves	Pods
n-Tridecane	C13	0.315	0.797	0.2
n-Tetradecane	C14	0.445	1.003	2.050
n-Pentadecane	C15	0.54	1.522	2.294
n-Hexadecane	C16	0.63	4.067	1.067
n-Heptadecane	C17	0.6959	5.861	0.047
n-Octadecane	C18	0.76	0.226	0.358
n-Nonadecane	C19	0.839	0.786	2.912
n-Eicosane	C20	0.89	5.113	3.893
n-Heneicosane	C21	0.93	0.413	1.545
n-Decosane	C22	1.00	17.665	12.721
n-Tricosane	C 23	1.04	0.894	1.901
n-Tetracosane	C24	1.09	0.957	1.124
n-Pentacosane	C25	1.146	1.964	3.121
n-Hexacosane	C26	1.194	2.791	5.807
n-Heptacosane	C27	1.24	4.217	5.899
n-Octacosane	C28	1.295	8.194	7.323
n-Nonacosane	C29	1.36	10.890	8.923
n-Triacontane	C30	1.4	2.619	7.114
Sterols				
Cholesterol		1.6	7.654	2.297
Stigmasterol		2.2	-	1.817
β-Sitosterol		2.3	0.861	12.023
β-amyrin		2.4	1.421	1.007
Percentage of identified hydrocarbons			69.979	68.299
Percentage of identified sterols			9.936	17.144

*RRt: Relative retention time to decosane with Rt=18.95 min.

Antimicrobial Assay

The antimicrobial activities of methanolic and chloroformic extracts of leaves and pods of *Tipuana tipu* and volatile oil from flowers were determined by the agar diffusion technique (Bauer *et al.*, 1966; Wilkins *et al*., 1972). Sterile nutrient, malt extract and Czapek's dox agar media were inoculated, separately, with 100μl cell suspension of the tested bacteria, yeast and fungi and poured into Petri-dishes (15cm diameter). 2mg of each of the extracts or fractions was dissolved in 1 ml methanol; a concentration of 0.2 mg was chosen and was placed on filter paper disc (1cm diameter). Solvent was allowed to evaporate and the discs were deposited on the surface of inoculated agar plates and kept at low temperature before incubation which favors diffusion over microbial growth to detect the inhibition zone clearly. The plates were incubated at 35ºC for bacteria and at 30ºC for yeast and fungi. Tetracyclin and metronidazol were used as positive controls for bacteria and fungi, respectively. The antimicrobial activity was expressed as the diameter of inhibition zone in mm. For essential oil, the agar overlay technique using holes or cylinders as reservoir that contact with the inoculated medium was used; oil being diluted with diethyl ether at a concentration of 0.3% (v/v). The results are presented in table 5.

The minimum inhibitory concentration (MIC)

MIC of extracts from leaves and pods, as well as the volatile oil were determined using serial dilutions technique. Different concentrations ranging from 0.2 to 0.6 mg/ml for leaves and pods extracts and a concentration of 0.05 to 0.3% (v/v) of volatile oil were prepared and tested against the chosen microorganisms. Experiments were performed in

duplicate and diameters of inhibition zones were measured. MIC was expressed as the lowest concentration of plant extract that produced complete growth inhibition and the results are presented in table 6.

Thermostability of *Tipuana tipu* leaf extract

This was determined at 37ºC and 50ºC. Samples were pre-incubated for 5, 10, 15, 20 and 25hours at the appropriate temperature, followed by rapid cooling. The autoclaved sample was also bioassayed. The most sensitive strain of each group (Gram positive and Gram negative bacteria, yeast and fungi) was chosen as a representative organism. The remaining antimicrobial activity was estimated by the agar diffusion method (Dixon *et al*., 1983). Evaluation of the stability of leaf extract of *Tipuana tipu* at different pH values was carried out. The samples were incubated at different pH values for 15 min. and 30 min. at 4ºC, prior to evaluation of the remaining activity by the agar diffusion method. The results are shown in figures 1-4.

Evaluation of cytotoxicity (Skehan *et al.*, 1990)

Cells were plated in 96-multiwell plate (10^4 cells/well) for 24 hrs before treatment with the compounds to allow attachment of cells to the wall of the plate. Different concentrations of the compound under test (25-100μl/ml) were added to the cell monolayer. Triplicate wells were prepared for each individual dose. Monolayer cells were incubated with the compound for 48hrs at 37ºC in an atmosphere of 5% CO_2. After 48hours, cells were fixed with trichloroacetic acid (TCA), washed and stained with Sulphorhodamine B (SRB). Excess stain was washed with acetic acid and attached stain was recovered with Tris-

Table 4. GLC analysis of FAME of leaves and pods of *Tipuana tipu*.

Authentic of FAME	Carbon No	RRt*		Relative %	
		Leaves	Pods	Leaves	Pods
Caprylic	C8:0	0.329	0.248	0.506	0.531
Pelargonic acid	C9:0	0.437	0.312	0.138	0.039
Capric acid	C10:0	0.602	-	0.382	-
Lauric acid	C12:0	0.684	0.502	0.607	0.148
Lauroleic	C12:1	0.733	0.521	0.121	0.174
Myristic acid	C14:0	0.843	0.619	6.448	0.938
Myristoleic acid	C14:1	0.869	0.658	25.053	1.625
Pentadecanoic acid	C15:0	0.93	0.682	1.903	1.004
Pentadecenoic acid	C15:1	0.955	0.704	0.666	0.725
Palmitic acid	C16:0	1.0	0.734	27.262	20.396
Heptadecanoic acid	C17:0	1.125	0.830	13.954	1.078
Stearic acid	C18:0	1.22	0.907	11.892	6.848
Oleic acid	C18:1	1.29	0.933	0.531	11.743
Linoleic acid	C18:2	-	1.0	-	52.046
Linolenic acid	C18:3	1.45	-	0.678	-
Arachidic acid	C20:0	1.63	1.22	4.771	0.286
Percentage of total identified saturated FAME				67.863	31.268
Percentage of total identified unsaturated FAME				27.949	66.313

RRt*: relative retention time of palmitic acid (for leaves) =1, with Rt=17.53. In pods   relative retention time of linoleic acid =1, with Rt=22.483.

Table 5. Antimicrobial activity of *Tipuana tipu* leaves, pods and volatile oil of flowers.

Microorganism	*Inhibition zone diameters (mm)						
	**Leaves		**Pods		***Flowers, volatile oil	Positive control	
	MeOH	CHCl$_3$	MeOH	CHCl$_3$		****Tetra-cycline	****Metro-nidazol
Gram positive bacteria							
Staphylococcus aureus	16	16	-	-	23	12	12
Bacillus cerrrus	-	-	-	20	28	30	-
Gram negative bacteria							
Escherichia coli	12	12	12	30	28	30	30
Yeast							
Candida albicans	12	-	12	15	26	30	30
C. pseudotropicales	-	-	12	12	24	35	14
Sacchoromyces carles	20	12	12	20	25	-	-
Fungi							
Aspergillus niger	12	12	12	-	26	12	12
A.. flavus	12	12	-	12	28	-	12
A. terrus	12	12	12	-	24	24	12

*Average of three determinations, **conc. of extract=0.6 mg/ml, ***volatile oil =0.3%, ****conc. of antibiotic=0.05 mg/ 0.1 ml in each disc.
(-): inactive, 12-14: partially active, 15-20: very active.

EDTA buffer. The absorbance of the stain was read in a VMax microplate reader (ELISA reader) at 564nm. The relation between surviving fraction and drug concentration was plotted to get the survival curve of each tumor cell line after the addition of the specified compound and the results are presented in table 7.

RESULTS AND DISCUSSION

Hydrodistillation of the flowers of *Tipuana tipu* cultivated in Egypt yielded 0.5% v/w of a pale yellow oil having a pale yellow colour and a faint characteristic odour. The oil has a specific gravity of 0.85 and a refractive index of 1.508. GC-MS analysis of the oil allowed the identification of 18 components presented in table 1. The oxygenated components were found to be the main constituents (69.16%) while the percentage of hydrocarbons amounted to (29.48%). Monoterpene hydrocarbons were found mainly limonene (12.4%) and α-phellandrene (0.52%); while α-farnescene (1.39%) being the main sesquiterpene hydrocarbon. Major oxygenated monoterpenes were β- linalool (5.82%) and geranyl acetone (3.95%); while caryophyllene oxide (1.61%) being the main oxygenated sesquiterpene. The major constituent of the oil (32.17%) was pentadecanone (perhydrofarnesyl acetone). Fatty acids and esters exhibited (17.84%) of the volatile constituents, of which palmitic acid represented (13.26%). The percentage of FA is higher in pods (60%) than in leaves (7%); while the percentage of USM is higher in leaves (93%) than in pods. GLC analysis of USM indicated that the percentage of identified hydrocarbons in leaves and pods was 69.975

% and 68.299%, respectively. The major hydrocarbon in leaves and pods was Decosane (17.6%) in leaves and (12.72%) in pods. The major hydrocarbons in leaves were n-nonacosane C_{29} (10.89%), n-octacosane (8.194%), n-eicosane C_{20} (5.43%), n-heptacosane C_{27} (4.217%), n-heptadecane C_{17} (5.861%), n-hexacosane C_{26} (2.8%) and n-pentacosane C_{25} (1.96%), while in pods the major hydrocarbons were n-nonacosane C_{29} (8.923%), n-octacosane C_{28} (7.323%), triacontane C_{30} (7.114%), n-hexacosane C_{26} (5.8%) n-heptacosane C_{27} (5.899%), n-eicosane C_{20} (3.89%) , n-pentacosane C_{25} (3.121%) and n-tetradecane C_{14} (2.05%). GLC revealed that β-sitosterol, Cholesterol and β-amyrin were the major sterol contents in leaves in addition to stigmasterol in pods.Campesterol and avensterol were previously reported from the seed of *Tipuana tipu* using GC-MS (Maestri *et al.*, 2002). GLC analysis of the fatty acid methyl ester of the leaves and pods of *Tipuana tipu* showed fifteen fatty acids in leaves and fourteen in pods. The percentage of unsaturated FAME is (27.949%) in leaves and (66.313%) in pods. The major unsaturated FAME in leaves was myristoleic acid (25.053%), while that of pods was linoleic acid (52.046%). The percentage of saturated FAME was (67.863%) in leaves and (31.268%) in pods. Palmitic acid represents the main saturated FAME in both organs with a relative percentage of (27.262%) in leaves and (20.393%) in pods.

Antimicrobial activity
The antimicrobial activities of the leaves, pods extracts and volatile oil of flowers of *Tipuana tipu* were screened using agar diffusion method (Table 5). It is noticed that the leaf
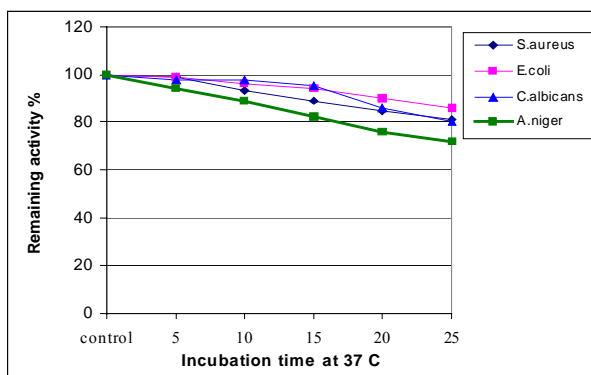
Fig. 1. Effect of different incubation time at 37ºC on antimicrobial activity of *Tipuana tipu* leaves.
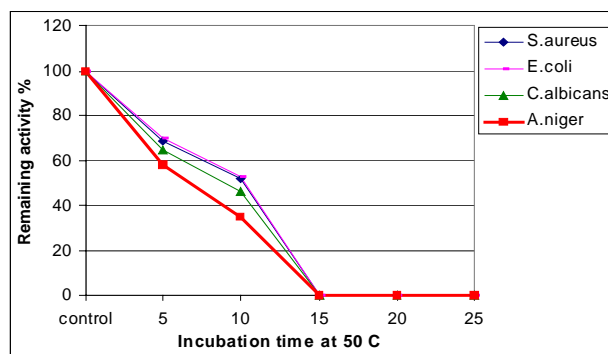

Fig. 2. Effect of different incubation time at 50ºC on antimicrobial activity of *Tipuana tipu* leaves.
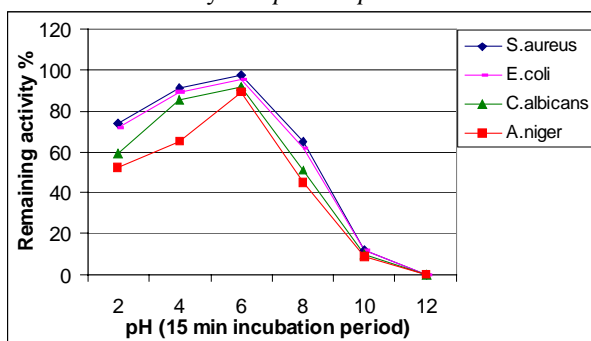

Fig. 3. Effect of different pH on antimicrobial activity of *Tipuana tipu* leaves after 15min incubation period.
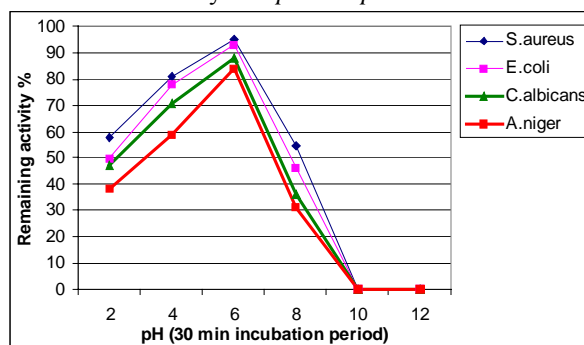

Fig. 4. Effect of different pH on antimicrobial activity of *Tipuana tipu* leaves after 30 min incubation period.

extract and volatile oil of flowers showed a broad spectrum antimicrobial effect while pods extract has more obvious activity on *E. coli* (gram –ve bacterium) and yeast. Regarding the chemical composition of essential oils with respect to the antimicrobial activity (Cimanga *et al.*, 2002), Linalool has previously been reported as having antibacterial and antifungal activity (Mazzanti *et al.*, 1998), as well as limonene having a higher concentration (12.47%) was active against gram positive and negative bacteria (Pepeljnjak *et al.,* 2005). A recent study reported Perhydrofarnesyl acetone to have moderate antibacterial activity (Yayli *et al.,* 2006; Sanches *et al.,* 2005). Palmitic acid is present at high concentration in the three fractions and is known for its high antibacterial activity (Yff *et al.,* 2002).

The minimum inhibitory concentration
The minimum inhibitory concentrations of the methanolic and chloroformic extract of leaves and pods presented in table 6, were ranged from 0.2-0.6 mg/ml while volatile oil of flowers was 0.05%. This indicates that the isolated fractions have a good activity against microorganisms.

The properties of *Tipuana tipu* leaf extract
The effect of different incubation time at 37ºC on the antimicrobial activity (Fig. 1) shows that leaf extract was stable at 37ºC for 25 h and 72% to 86% of the activity was remained. Incubation at 50ºC showed a noticeable decrease in activity with increasing the incubation time. About 35%

to 53% remaining activity was detected after 10h incubation. The activity against all tested microorganisms was completely lost after 15hours of incubation at 50ºC (Fig. 2). When the fraction was autoclaved at 121ºC for 10 min, no antimicrobial activity was retained. Storage at room temperature (25ºC) for three months in air tight glass bottle retains its activity.

The exposure of the isolated fraction to different concentrations of hydrogen ion (pH 2 to 12) for 15 min and 30 min incubation period showed that the incubation for 15 min (Fig. 3) retain about 52% to 74% of the activity at pH 2 and 45% to 65% at pH 8. The remaining activity was about 9% to 12% at pH 10 while a complete loss in activity was observed at pH 12.

Incubation for 30 min. at different pHs showed a noticeable decrease at highly acidic and basic solutions (Fig. 4). The remaining activity was about 38% to 58% at pH 2 and about 31% to 55% at pH 8, while no activity was noticed at   pH 10 and 12. Thus the best storage pH range was 4 to 6 at room temperature.

It is to be noticed that the activity of the uncharged form of the phenolic compounds is able to penetrate the microbial cell and exhibit activity (Burkill *et al.,* 1985). So changes in the pH highly affect the activity. These results can serve as a guide in therapeutic drug development having a source of

Table 6. The MIC of methanolic and chloroformic extracts of *Tipuana tipu* leaves, pods and volatile oil of flowers.

Microorganism	Classification	MIC of *Tipuana tipu* extracts mg/ml				
		Leaves		Pods		Volatile oils
		MeOH	CHCl$_3$	MeOH	CHCl$_3$	
Staphylococcus aureus	Gram positive bacterium	0.2	0.2	-	-	0.05%
Escherichia coli	Gram negative bacterium	0.4	0.4	0.6	0.4	0.05%
Candida albicans	Yeast	0.6	-	0.4	0.4	0.05%
Aspergillus niger	Fungi	0.4	0.4	0.6	-	0.05%

%: concentration of the volatile oil (v/v).

Table 7. *In vitro* testing for cytotoxic effect of the methanolic and the chloroformic extracts of *Tipuana tipu* on different cell lines.

Cell line	Sample	* % inhibition of cell viability				**IC$_{50}$
		10μg/ml	5μg/ml	2.5μg/ml	1μg/ml	
HELA	Methanolic extract	44.6	30.7	27.5	12.3	-ve
	Chloroformic extract	52.6	50.4	44.6	40.4	5.45 μg
	Volatile oil	50	45.8	42.3	40.5	5.3 μg
MCF7	Methanolic extract	57.3	53.6	43.1	12.4	4.30 μg
	Chloroformic extract	61.4	52.4	39.3	34.8	4.56 μg
	Volatile oil	60.2	53.5	44.5	30.6	4.6 μg
HCT116	Methanolic extract	51.3	39.7	30.9	29	9.97 μg
	Chloroformic extract	30.8	27	27.4	13.2	-ve
	Volatile oil	50.3	44.5	40.4	28.3	4.5 μg

*Each result is a mean of three tests
**IC$_{50}$: dose of the compound which reduces survival to 50%.

new compounds by the selection of some plants as *Tipuana tipu* having antimicrobial activities, and this will represent a non expensive as well as available source. It is probably useful in controlling some plant diseases (Suchiya *et al*., 1996).

Cytotoxic activity

The methanolic extract shows an obvious cytotoxic activity against breast and colon carcinoma cell lines, while the chloroformic extract shows cytotoxic activity against breast and cervix carcinoma cell lines. The volatile oil shows significant cytotoxic activity against the three examined cell lines.

REFERENCES

Adams, RP. 1989. Identification of Essential Oils by Ion Trap Mass Spectroscopy. Academic press Inc., Illinois, USA.

Ardakani, MS., Mosaddegh, M. and Shafaati, A. 2003. Volatile constituents from the aerial part of *Verbena officinalis L.* (Vernain). Iranian. J. pharmaceutical research. 39-43.

Bauer, AW., Kirby, WMM., Sheriss, JC. and Turck, M. 1966. Antibiotic susceptibility testing by a standardized single disk method. Am. J. Clinic, Path. 45:493-495.

Burkill, HM., Dalziel, JM. and Hutchinson, J. 1985. The useful plants of West Tropical Africa. Royal Botanic Gardens, (2nd edition).

Cimanga, K., Kambu, K., Tona , L., Apers, S., De Bruyne, T., Hermans, N., Totte, J., Pieters, L. and Vlietinck, AJ. 2002. Correlation between chemical composition and antibacterial activity of essential oils of some aromatic medicinal plants growing in the Democratic Republic of Congo. J. Ethnopharmacol. 79 (2):213-219.

Dixon, RA., Dey, PM. and Lamb, CJ. 1983. Phytoalexins: enzymology and molecular biology. Adv. Enzymol. 55:1-7.

Elsohly, HN., Joshi, AS. and Nimrod, AC. 1999. Antigiardial isoflavones from *Machaerium aristulatum*. Plant Med. 65(5):490-494.

Ginzbarg, S. 1977. Plantas medicinales de los indios bribris y cabécar. Am.Indigena. 37:367- 370.

Heinrich, M., Rimpler, H. and Barrera, HNA. 1992. Indigenous phytotherapy of gastrointestinal disorders in a low land mixe community Oaxaca, Mexico. J. Ethnopharm. 36:63-68.

Hickey, M. and King, C. 1997. Common Families of Flowering Plants. International Legume Database and Information Service. Cambridge University.

Joly, LG., Guerra, S., Septimo, R., Soli, SPN., Correa, M., Gupta, M., Levy, S. and Sandberg, F. 1987. Ethnobotanical inventory of medicinal plants used by the Guayami Indians in Western Panama. Part I. J. Ethnopharmacol. 20:145-149.

Lewis, G., Schrire, B., MacKinder, B. and Lock, M (eds.). 2005. Legumes of the world. Royal Botanical Gardens, Kew, UK.

Maestri, DM, Fortunato, RT., Guzman, CA., Torres, MM. and Lamarque, AL. 2002. Seed compositional studies of some species of Papilionoideae (leguminosae) native to Argentina. J. Sci. Food. Agriculture. 82(3):248- 244.

Mazzanti, G., Battinelli, L. and Salvatore, G. 1998. Antimicrobial properties of the linalool-rich essential oil of *Hyssopus officinalis* L. var. *decumbens* (Lamiaceae). Flav. Fragr. J. 13:289- 293.

McLafferty, FW. and Turecek, F. 1993. Interpretation of Mass Spectra, (4th edition). University Science Books, Mill Valley, California, USA.

Paech and Tracey 1955. Modern Methods of Plant Analysis IV. Berlin, Gottingen, Heidelberg.

Pepeljnjak, S., Kosalec, I., Kalodera, Z. and Blazevic, N. 2005. Antimicrobial activity of juniper berry essential oil (*Juniperus communis* L., *Cupressaceae*. Acta. Pharm. 55:417- 423.

Sanches, NR., Cortez, DAG., Schiavini, MS., Nakamura. CV. and Filho, BPD. 2005. An evaluation of antibacterial activities of *Psidium guajava*. Braz. arch. biol. technol. 48(3):429-423.

Seo, EK., Kim, NC., Mi, Q., Chai, H., Wall, ME., Wani, MC., Navarro, HA., Burgess, JP., Graham, JG., Cerbieses, F., Tan, GT., Farnsworth, NR., Pezzuto, JM. and Kinghorn, D. 2001. Two Cytotoxic Compounds from the Stem of *Machaerium aristulatum*. J. Nat. Prod. 64:1483-1488.

Skehan, P., Storeng, R., Scudiero, D., Monks, A., McMahon, J., Vistica, D., Warren, JT., Bokesch, H., Kenney, S. and Boyd. MR. 1990. New colorimetric cytotoxicity assay for anticancer-drug screening. J. Natl. Cancer Inst. 82:1107- 1110.

Stenhagen, E., Abrahamsson, S. and McLafferty, FW. 1970. Atlas of Mass Spectral Data. John Wiley and sons, New York, USA.

Suchiya, H., Sato, M., Miyazaki, T., Fujiwara, S., Tanigaki, S., Ohyama, M., Tanaka, T. and Iinuma, M. 1996. Comparative study on the antibacterial activity of phytochemical flavanones against methicillin-resistant *Staphylococcus aureus*. J. Ethnopharmacol. 50:27-31.

Vogel, AI. 1961. Practical Organic Chemistry, (3rd edition). Longmans Private LTD, Calcutta, Bombay, Madras, India.

Waage, SK., Hedin, PA. and Grimley, E. 1984. A biologically active procyanidin from *Machaerium floribundum*. Phytochemistry. 23(12):2785-2788.

Wilkins, TD., Holdeman, JJ., Abramson, IJ. and Moore, WEC. 1972. Standardized single-disc method for antibiotic susceptibility testing of anaerobic bacteria. Antimicrob Agents Chemother. I. 1(6):451-455.

Yamaguchi, K. 1970. Spectral Data of Natural Compounds. Elservier Publishing Co., New York, USA.

Yayli, N., Guleç, C., Úçűncű, OS., Yaşar, A., Ulker, S., Coşkunçelebi, K. and Terzioğlu, S. 2006. Composition and antimicrobial activities of volatile components of *Minuartia meyeri*. Turk. J. Chem. 30:71-74.

Yff, BTS., Lindsey, KL., Taylor, MB., Erasmus, DG. and Jager, AK. 2002. Pharmacological screening of *Pentanisia prunelloides* and isolation of the anti-bacterial compound palmitic acid. J. Ethnopharmacol. 79:101-109.

OSMOTIC STRESS IN THE CYANOBACTERIUM *NOSTOC MUSCORUM* OVERCOME BY THE ACCUMULATION OF PROLINE

Rajesh Kumar Kachouli[1], Rakesh Maithil[2], Sachin Dubey[1], Vipin Kaithwas[1],
Vinod Krishna Sethi[2] and *Santosh Bhargava[1]
[1]Division of Microbiology, Department of Botany, Government Motilal Science College, Bhopal 462003
[2]School of Biotechnology, Rajiv Gandhi Technological University, Gandhi Nagar, Bhopal 462038 (MP) India

ABSTRACT

Growth and percent survival in the cyanobacterium *Nostoc muscorum* severely inhibited, when challenged with salinity (NaCl) and osmotic (sucrose) stresses. The spontaneously occurring NaCl-R and sucrose-R (Su-R) mutant clones were examined with regards to their cross-resistant relationships. The NaCl-R mutant when challenged with salinity and osmotic stresses simultaneously showing cross-resistance with the sucrose stress. In contrast, the Su-R mutant showing resistant only to osmotic stress and was salinity sensitive. The physiological response towards osmotic stress in both the mutant clones was the over-production of proline. The ionic component of the salinity stress in the NaCl-R mutant was overcome by the Na^+-efflux. The Su-R mutant clones missing Na^+ efflux mechanism, consequently, they became salt sensitive. These findings highlight that the organic osmolyte strategy in *N. muscorum* assured osmotic resistance.

Keywords: Cyanobacterium, intracellular proline, *Nostoc muscorum*, osmotic stress, salinity stress.

INTRODUCTION

Cyanobacteria are prokaryotic, photoautotroph growing and multiplying luxuriantly in natural and agricultural ecosystems, despite facing substantial fluctuation in the range of environmental conditions including salinity and osmotic stresses. They exhibit photo-assimilation of nitrogen, CO_2 and contribute to O_2 production. Some of the cyanobacterial forms are the progenitor of chloroplast evolution in eukaryotes through the process of endosymbiosis. Therefore, they are considered as evolutionarily the most important group of organisms (Douglas, 1994). Saline soil creates ionic stress as well as osmotic stress and inhibiting microbial and crop productivity by creating water stress and Na^+ toxicity. Therefore, the microorganisms that thrive in such stressful habitat alter their physiology to cope up with the changing environment. The ionic component of the stress factor is readily overcome by the Na^+/H^+ antiporter activity (Inaba *et al*., 2001; Elanskaya *et al*., 2002; Waditee *et al*., 2002). The cytoplasmic osmotic potential is balanced either by accumulation or by synthesis of compatible solutes (Csonka, 1989; Alia and Gahiza, 2007). The synthesis of compatible solutes is usually regulated by the cyanobacterial habitat. The fresh water cyanobacterial strains were found to be least tolerant and are known to produce sucrose, trehalose and proline as compatible solutes (Hagemann *et al*., 1996; Singh *et al*., 1996). The moderately halotolerant cyanobacteria produces glucosyl-glycerol as organic osmolyte for such adaptation (Borges *et al*., 2002; Hincha and Hagemann, 2004; Marin *et al*., 2006).

In comparison, hyper saline cyanobacterial strains are known to produce glycine-betaine as compatible solutes (Warr *et al*., 1988).

The present study indicates that different biochemical mechanism operate to remove ionic (salinity) and non-ionic (osmotic) stresses in the *N. muscorum*. The ionic stress is overcome by Na^+ export and osmotic stress by the synthesis of low molecular weight organic compatible solute i.e. proline.

MATERIALS AND METHODS

The *Nostoc muscorum* used in the present study was a fresh water, filamentous, nitrogen fixing (diazotroph), heterocystous cyanobacterium. It was grown axenically in Chu No. 10 (Gerloff *et al*., 1950) at 28 ± 2^oC and illuminated with fluorescent tubes having a photon fluence rate of 50 μmol m^{-2} s^{-1} with 16/8 h light/dark cycle. The culture medium was buffered to pH 7.5 with 10 mol m^{-3} HEPES-NaOH.

Salt and osmotic concentrations were adjusted by adding 100 mol m^{-3} NaCl and 250 mol m^{-3} sucrose to the diazotrophic growth medium. Such diazotrophically grown cultures were periodically examined (3, 6, 9, 12 hours) for their respective characteristics.

NaCl at the concentration of 100 mol m^{-3} and sucrose at the concentration of 250 mol m^{-3} were found lethal to the diazotrophic growth of the cyanobacterium *N. muscorum*. NaCl-Resistant (NaCl-R) and Sucrose-Resistant (Su-R) mutants of the cyanobacterium were isolated by plating $2.5-3.0\times10^7$ colony forming units (CFUs) on diazotrophic growth medium containing 100 mol m^{-3} NaCl and 250

mol m^{-3} sucrose. The spontaneously occurring mutant clones were checked for their stability by the method described previously (Bhargava and Singh, 2006).

For the measurement of Na^+ efflux cyanobacterial strains were Na^+ starved by growing them in diazotrophic growth medium lacking Na^+ for 72 hours. The cyanobacterial strains were centrifuged, washed and resuspended in DH_2O buffered by 10 mol m^{-3} HEPES-NaOH at pH 7.5. Cultures were incubated for 30 min at 28 ± 2^oC under continuous light at a photon fluence rate of 50 $\mu mol\ m^{-2}\ s^{-1}$. NaCl at a concentration of 5 mol m^{-3} was added to the incubation mixture. The amount of Na^+ present in the buffer was measured with the help of Flame Photometer.

Estimation of growth, percent survival, chlorophyll *a* (Mackinney, 1941), protein (Lowry *et al.*, 1951) nitrogenase activity, intracellular proline contents and proline oxidase activity was done as described previously (Bhargava and Singh, 2006).

RESULTS

NaCl-R mutant and Su-R mutant clones reported here arose with a mutational frequency of $0.6 \sim 0.8 \times 10^{-7}$ suggesting that the resulting mutant phenotype is a product of point mutation in the chromosomal genes. The physiological response of *N. muscorum* and its spontaneously occurring NaCl-R and Su-R mutant clones were compared under NaCl stress and sucrose stress conditions. The percent survival decreases with the increasing time of stress exposure. A dose of 100 mol m^{-3} NaCl and 250 mol m^{-3} sucrose for 12 hours completely inhibit the growth of the wild type strain (Fig. 1).

A comparison of percent survival of the Su-R mutant under NaCl and sucrose stresses was done. The observation indicates that Su-R mutant clones were showing resistance only to sucrose stress. On further examination Su-R mutant clones were found to be sensitive to NaCl stress (Fig. 2). The NaCl-R mutant clones were compared for their percent survival in the diazotrophic growth medium containing 100 mol m^{-3} NaCl and 250 mol m^{-3} sucrose. The results (data not

shown) suggested that NaCl-R mutant clones exhibited almost complete resistance to growth inhibitory action of 100 mol m^{-3} NaCl and 250 mol m^{-3} sucrose.
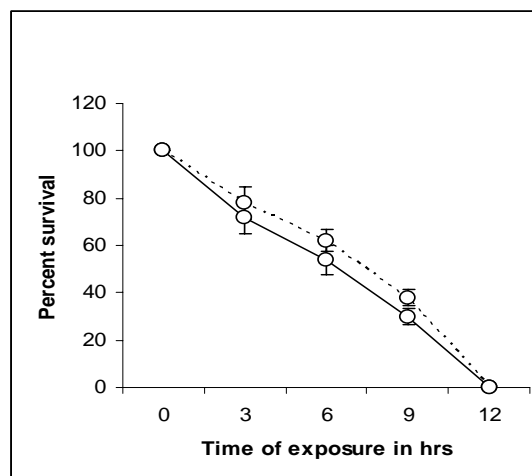

Fig. 1. Percent survival of the wild type *N. muscorum* challenged with NaCl stress (—) and under sucrose (---) stress conditions under diazotrophic growth condition. Each reading is an average (±SEM) of three independent experimental determinations.
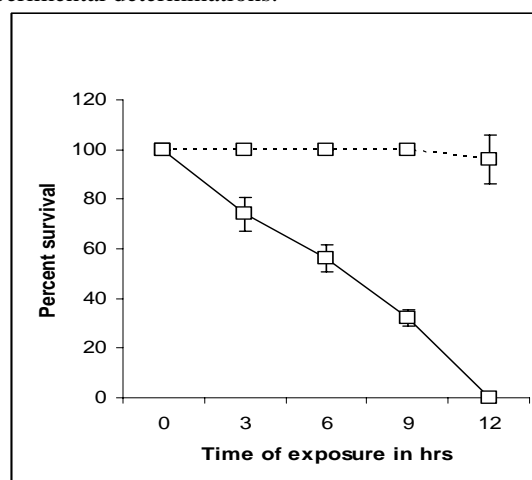

Fig. 2. Percent survival of the sucrose-R mutant clones challenged with NaCl stress (—) and sucrose stress (---) conditions under diazotrophic growth condition.

Table 1. Growth (OD change at 663nm), heterocyst frequency (HF %), nitrogenase activity (m mol C_2H_4 formed g^{-1} Chl *a* h^{-1}) and proline oxidase activity (m mol proline oxidized g^{-1} Chl *a* h^{-1}) of the *N. muscorum* and its various mutant clones.

Parameters	Wild type	NaCl-R	Sucrose-R
Growth	0.82 ± 0.08	0.78 ± 0.07	0.80 ± 0.08
HF%	7-8	7-8	7-8
Nitrogenase activity	12.28 ± 0.78	11.15 ± 0.81	11.54 ± 0.79
Proline oxidase activity	2.56 ± 0.14	0-0	0-0

Non-heterocystous NH_4^+ grown cultures were source of inoculum for the experiments. Such cultures were grown for six days in diazotrophic growth medium and then used for estimation of their characteristics.
Each reading is an average (±SEM) of three independent experimental determinations.

Each reading is an average (±SEM) of three independent experimental determinations.

Further experiments were done to compare various mutant clones with its wild type in respect to photoautotrophic growth, heterocyst frequency, nitrogenase activity, proline oxidase activity, intracellular proline contents and Na^+ uptake. The results as shown in the table 1 suggested that mutant strains showed almost similar level of photoautotrophic growth, heterocyst frequency and nitrogenase activity in the diazotrophic medium. The wild type strains did not produce heterocyst and nitrogenase activity in the growth medium containing 1 mol m^{-3} proline suggested that *N. muscorum* is capable of assimilating proline as a nitrogen source and its mutation to NaCl-R and Su-R phenotypes have resulted in loss of this ability. Thus it can be concluded that mutant clones have lost genetically proline repression control of heterocyst and nitrogenase activity. Further analysis in respect of proline catabolizing enzyme i.e., proline oxidase revealed the presence of this enzyme in the wild type and its absence in the mutant clones. Consequently, mutation to resistant phenotype resulted in over-production of proline and acquisition of osmotic resistance in the cyanobacterium.
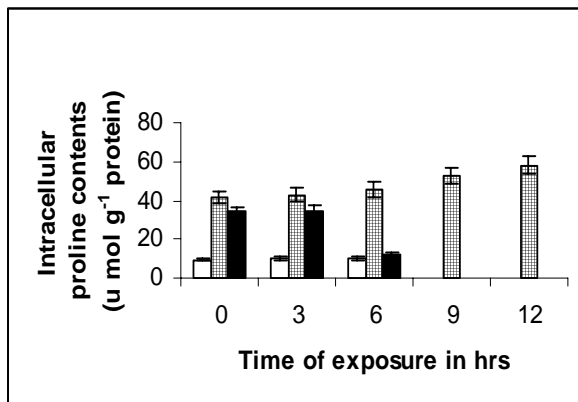

Fig. 3. Effects of salinity stress on intracellular contents of proline in the wild type *N. muscorum* (blank bars) and its NaCl-R (check bars) and sucrose-R (dark bars) mutant clones.
Each reading is an average (±SEM) of three independent experimental determinations.

The additional noteworthy characteristic of mutant clones (NaCl-R and Su-R) were its higher contents of the proline than that found in the wild type. In addition the proline contents of the NaCl-R mutant showed slight rise when stressed with NaCl (Fig. 3) or sucrose (Fig. 4). In comparison wild type with or without stress has not exhibit any variation in its proline contents. Similarly Su-R mutant was found similar to the wild type in intracellular proline contents under NaCl stress.

The pattern of Na^+-uptake was also examined in the wild type and in the NaCl-R and Su-R mutant strains. The

results as shown in the figure 3 indicates that Na^+ uptake pattern in the wild type and its Su-R mutant was more pronounced as compared to the NaCl-R mutant. This observation suggested that Na^+ uptake pattern in the Su-R mutant remained unaltered, while the acquision of NaCl-R phenotype mitigates the Na^+ entry.
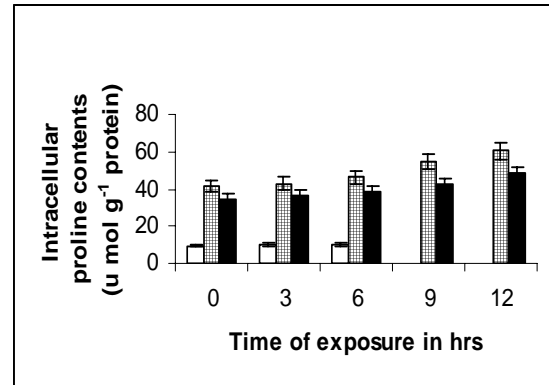

Fig. 4. Effects of osmotic stress on intracellular contents of proline in the wild type *N. muscorum* (blank bars) and its NaCl-R (check bars) and sucrose-R (dark bars) mutant clones.
Each reading is an average (±SEM) of three independent experimental determinations.

Fig. 5. Na^+ efflux pattern in the wild type *N. muscorum* (blank bars) and its NaCl-R (check bars) and sucrose-R mutant strains (dark bars).
Each reading is an average (±SEM) of three independent experimental determinations.

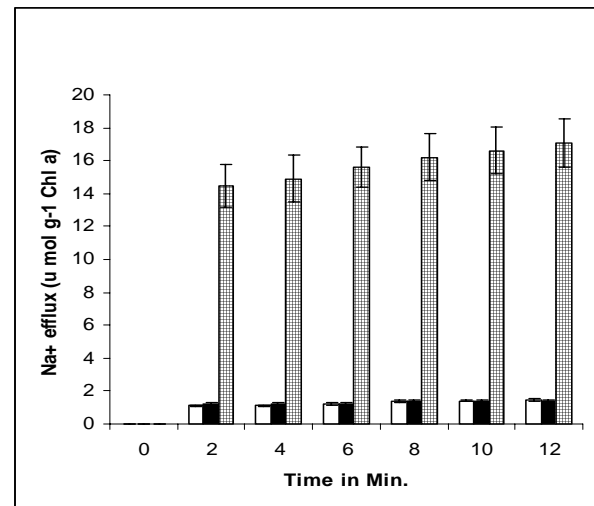## DISCUSSION

The physiological impact of salt and osmotic stresses has been analyzed in the *N. muscorum* and its spontaneously occurring mutant clones resistant to growth inhibitory action of salt and sucrose. NaCl-R mutant and Su-R

mutant were also analyzed for cross-resistant relationship with salt and osmotic stress. The NaCl-R mutant clones show cross relationship with osmotic stress, therefore, we suggest that mutation to NaCl-R phenotype may involve two different kinds of mutation one leading to ionic stress and another leading to osmotic stress components. On the contrary Su-R mutant clones showing resistant to sucrose stress only and are NaCl sensitive. Therefore, it can be concluded that Su-R phenotype involves mutation only in osmotic stress component.

Wild type *N. muscorum* and its mutant clones differ in a most noticeable way with regards to their intracellular proline contents. Wild type with or without stress has not exhibit any variation in its proline contents. In comparison NaCl-R and Su-R mutant exhibit manifold higher intracellular proline contents under normal growth condition. Since sucrose-R phenotype is not found cross-resistance to NaCl stress while having high intracellular proline contents the obvious cause for lack of cross-resistance of NaCl in Su-R mutant seem to be the efflux mechanisms which might have remain unaltered in the sucrose-R mutant clones.

The common molecular component in NaCl-R and Su-R mutants is high intracellular levels of proline. This common molecular phenotype correlates well with the physiological phenotype of osmo resistance (Mikkat *et al.*, 1996; Marin *et al.*, 1998; Marin *et al.*, 2006). We may conclude that intracellular accumulation of proline is the common cause of osmotic resistance in the mutant clones. Our observation regarding the compatible solute synthesis during osmotic stress is in agreement with results already published on *Synechocystis* (Marin *et al.*, 2006). The two genes *viz. put*P and *put*A are known to involve in accumulation or synthesis of proline in bacterial systems (Csonka, 1989). Mutational inactivation of the *put*A gene inhibits the catabolism of proline therefore such strains are proline-overproducer. Our findings supported by the above fact because the mutant clones reported here are also proline overproducer.

Singh *et al.* (1996) reported that enzyme proline oxidase is required to assimilate exogenous proline in the cyanobacterium *N. muscorum*. The mutants clones reported here missing proline oxidase activity, this could be the reason of proline over-production in the mutant clones. Similar findings were reported in bacterial systems by Dendinger and Brill (1970).

The NaCl-R mutant reported here involved two mutations leading to resistant phenotype. The osmotic stress component is overcome by the synthesis of compatible solute i.e. proline and the ionic component by the active efflux of Na^+. Our findings are quite in agreement with the previous reports regarding Na^+ efflux mechanism in bacterial and cyanobacterial systems (Padan and Schuldiner, 1994; Blumwald *et al.*, 1984; Apte *et al.*, 1987; Inaba *et al.*, 2001; Elanskaya *et al.*, 2002).

REFERENCES

Alia, EA. and Gahiza, IA. 2007. Accumulation of amino acids in *Anabaena oryzae* in response to sodium chloride salinity. Journal of Applied Sciences Research. 3(3):263-266.

Apte, SK., Reddy, BR. and Thomas, ST. 1987. Relationship between sodium influx and salt tolerance of nitrogen-fixing cyanobacteria. Applied and Environmental Microbiology. 53:1934-1939.

Bhargava, S. and Singh, K. 2006. Differential response of NaCl-Resistant mutants of the cyanobacterium *Nostoc muscorum* to salinity and osmotic stresses. World Journal of Microbiology and Biotechnology. 22:783-789.

Blumwald, E., Wolosin, JM. and Packer, L. 1984. Na^+/H^+ exchange in the cyanobacterium *Synechococcus* 6311. Biochemical and Biophysical Research Communications. 122:452-459.

Borges, N., Ramos, A., Raven, ND., Sharp, RJ. and Santos, H. 2002. Comparative study of the thermostabilizing properties of mannosylglycerate and other compatible solutes on model enzymes. Extremophiles. 6:209-216.

Csonka, LN. 1989. Physiological and genetic responses of bacteria to osmotic stress. Microbiological Reviews. 53: 121-147.

Dendinger, S. and Brill, WJ. 1970. Regulation of proline degradation in *Salmonella typhimurium*. Journal of Bacteriology. 103(1):144-152.

Douglas, SE. 1994 Chloroplast origin and evolution. In: The molecular biology of cynobacteria. Eds. Bryant, DA. Kluwer Academic Publishers, Dordrecht, The Netherlands. 91-118.

Elanskaya, IV., Karandashova, IV., Bogachev, AV. and Hagemann, M. 2002. Functional analysis of the Na^+/H^+ antiporter encoding genes of the cynobacterium *Synechocystis* PCC 6803. Biochemistry. 67:432-440.

Gerloff, GC., Fitzerald, GP. and Skoog, F. 1950. The isolation, purification and culture of blue-green algae. American Journal of Botany. 37:216-218.

Hagemann, M., Richter, S., Zuther, E. and Schoor, A. 1996. Characterization of a glucosyl-glycerol-phosphate-

accumulating, salt sensitive mutant of the cyanobacterium *Synechocystis* sp. strain PCC 6803. Archives of Microbiology. 166:83-91.

Hincha, DK. and Hagemann, M. 2004. Stabilization of model membranes during drying by campatible solutes involved in the stress tolerance of plants and microorganisms. Biochemistry Journal. 383:277-283.

Inaba, M., Sakamoto, A. and Murata, N. 2001. Functional expression in *Escherichia coli* of low-affinity and high-affinity Na^+ $(Li^+)/H^+$ antiporters of *Synechocystis*. Journal of Bacteriology. 183:1376-1384.

Lowry, OH., Rosebrough, NJ., Fall, AL. and Ransdall, RJ. 1951. Protein measurement with Folin-phenol reagent. Journal of Biological Chemistry. 193:265-275

Mackinney, M. 1941. Absorption of chlorophyll solution. Journal of Biological Chemistry. 140:315-322.

Marin, K., Stirnberg, M., Eisenhut, M., Kramer, R. and Hagemann M. 2006. Osmotic stress in *Synechocystis* sp. PCC 6803: low tolerance towards nonionic osmotic stress results from lacking activation of glucosylglycerol accumulation. Microbiology. 152:2023-2030.

Marin, K., Zuther, E., Kerstan, A. and Hagemann, M. 1998. The *ggpS* gene from *Synechocystis* sp. strain PCC 6803 encoding glucosyl-glycerol-phosphate synthase is involved in osmolyte synthesis. Journal of Bacteriology. 180:4843-4849.

Mikkat, S., Hagemann, M. and Schoor, A. 1996. Active transport of glucosylglycerol is involved in salt adaptation of the cyanobacterium *Synechocystis* sp. strain 6803. Microbiology. 142:1725-1732.

Padan, E. and Schuldiner, S. 1994. Molecular physiology of the Na^+/H^+ antiporter in *Escherichia coli*. Journal of Experimental Botany. 196:443-456.

Singh, AK., Chakravarthy, D., Singh, TPK. and Singh, HN. 1996. Evidence for a role of L-proline as a salinity protectant in the cyanobacterium *Nostoc muscorum*. Plant Cell & Environment. 19:490-494.

Waditee, R., Hibino, T., Nakamura, T., Incharoensakdi, A. and Takabe, T. 2002. Overexpression of a Na^+/H^+ antiporter confers salt tolerance on a freshwater cyanobacterium, making it capable of growth in sea water. Proceedings of National academy of Sciences USA. 99:4109-4114.

Warr, SRC., Reed, RH. and Stewart, WDP. 1988. The compatibility of osmotica in cyanobacteria. Plant, Cell & Environment. 11:137-142.

ACOUSTIC WAVES WITH THE IN-PLANE POLARIZATION IN PIEZOELECTRIC CUBIC STRUCTURES

AA Zakharenko
International Institute of Zakharenko Waves
660037, Krasnoyarsk-37, 17701, Krasnoyarsk, Russia

ABSTRACT

In this paper, calculations of the phase velocity V_{ph} of the dispersive nine-partial Rayleigh type waves (RTW9) were introduced in dependence on the kh (k is the wavenumber, and h is the layer thickness). The layered systems, consisting of a layer of $Bi_{12}SiO_{20}$ on a substrate of $Bi_{12}GeO_{20}$, and the reverse configurations were investigated. The calculated dispersion curves of the RTW9 lowest-order modes with both metallized and free surfaces have shown the existence of the non-dispersive nine-partial Zakharenko type waves (ZTW9) polarized like the Rayleigh waves. The non-dispersive ZTW9-waves split the RTW9 lowest-order modes into sub-modes with different dispersions, $V_{ph} > V_g$ and $V_{ph} < V_g$, where V_g is the group velocity. The RTW9 phase velocity V_{ph} is confined within a narrow V_{ph}-range that can be convenient for some technical devices. Also, cubic crystals with strong piezoelectric effect can be used for different cubic-structure magnetoelectric devices. It was found that the coefficient of electromechanical coupling (CEMC) K^2 for the RTW9 first type has its maximum value at $kh \sim 5$ for the structure $Bi_{12}SiO_{20}/Bi_{12}GeO_{20}$. The second type of RTW9-waves was also studied, which can propagate only in the structure $Bi_{12}SiO_{20}/Bi_{12}GeO_{20}$, because there is the condition $V_t(Bi_{12}GeO_{20}) > V_t(Bi_{12}SiO_{20})$ for the speed V_t of the bulk transverse wave, $V_t = [(C_{55}/\rho)(1 + K_0^2)]^{1/2}$ with $K_0^2 = e_{15}^2/C_{55}\varepsilon_{11}$. It was also discussed the existence possibility of new supersonic surface waves with the in-plane polarization and $V_{ph} \sim V_l$, where V_l represents the speed of the bulk longitudinal wave. Also, a calculation method with short computer program is described introducing the transverse and longitudinal dynamic CEMCs K_{Dt} and K_{Dl}. For comparison with [110] direction, the 20^0-x_2-rotated direction was also studied concerning propagation of the first and second types of pure RTW9-waves. Here, the existence of RTW9 second type depends on the velocity equivalents of the layer and substrate, but not on the corresponding velocities V_t, and solutions for the $V_{ph} > V_t$ were also found.

PACS: 51.40.+p, 62.65.+k, 68.35.Gy, 68.35.Iv, 68.60.Bs, 74.25.Ld

Keywords: layered systems, piezoelectric cubic crystals, dispersive Rayleigh waves, non-dispersive Zakharenko waves.

INTRODUCTION

Studying the propagation of elastic waves, especially the surface acoustic wave (SAW), in layered piezoelectric media have been of great interest since films deposited on supporting substrates are generally a requisite for acoustic devices (Nayfeh, 1991). Typically, a layered structure consists of two layers of different materials. Some technical devices, for instance, dispersive delay lines (Lardat *et al*., 1971) using layered structures to support propagation of dispersive waves require choosing materials for both the layer and substrate, in order to have a large range for the phase velocity V_{ph} in which dispersive waves can be confined. However, for some technical devices, a very narrow V_{ph}-range for dispersive waves can be preferable (Shiosaki *et al*., 1980) demonstrating a weak dependence of the dispersive wave V_{ph} on the non-dimensional value of kh, where k is the wavenumber in direction of wave propagation and h is the layer thickness. Also, (multi)-layered systems can be used for parameter optimization of technical devices, for example, see (Dvoesherstov *et al*., 2003). There is the

famous and classical book (Dieulesaint and Royer, 1980) on elastic waves in solids and their applications to signal processing. Also, an additional literature on crucial applications of SAWs can be found in (Henaff *et al*., 1982).

This paper relates to the studying the so-called "pure" dispersive nine-partial Rayleigh type waves (RTW9) in the layered systems, consisting of strongly piezoelectric cubic crystals $Bi_{12}SiO_{20}$ and $Bi_{12}GeO_{20}$, accounting the piezoelectric effect. Particularly, the attention of this work is paid to other possibilities to find dispersive SAWs with the Rayleigh-wave polarization in addition to the well-known surface Rayleigh waves (Rayleigh, 1885). It is thought that the two-layer systems using the crystals $Bi_{12}SiO_{20}$ and $Bi_{12}GeO_{20}$ can be readily manufactured. It is noted that over several hundred piezoelectric ceramics (composites) are known, for example, see (Pohanka and Smith, 1988). Today, they are widely used for different applications such as filters and sensors, as well as actuators and ultrasonic generators. Concerning fabrication of a structure consisting of two dissimilar crystals, a process called wafer bonding (Goesele and

_____

*Corresponding author email: aazaaz@inbox.ru

Tong, 1998; Alexe and Goesele, 2003) is commonly used in the semiconductor industry allowing two different materials to be rigidly and permanently bonded along a plane interface.

In this paper, the RTW9-waves propagate in [110] direction for both materials as shown in figure 1. The so-called work coordinate system $\{x_1, x_2, x_3\}$ in the Figure was obtained by 45^0-rotation around the Z-axis of the so-called crystallographic coordinate system with the $\{X, Y, Z\}$ axes corresponding to [100], [010], and [001] directions, respectively. It is noted that both the x_1 and x_3-axes lie in the sagittal plane in Figure 1, and the x_3-axis is perpendicular to the Figure plane, where the vector **N** is parallel to the surface normal, and the vector **M** is directed towards the propagation direction. The existence possibility of "pure" RTW6 and RTW9-waves was studied in the very famous works (Farnell and Adler, 1972; Lardat et al., 1971). In the studied layered systems, a weak dependence $V_{ph}(kh)$ can occur with peculiarities such as the phenomenon called the non-dispersive Zakharenko type wave (ZTW) recently discovered in (Zakharenko, 2005[a]). The non-dispersive ZTW-wave can exist in complex systems, which possess dependence of the V_{ph} on both the wavenumber k and the angular frequency ω. For example, the non-dispersive ZTW-waves can split some higher-order modes of Lamb type waves in anisotropic plates (Anisimkin, 2004; Solie and Auld, 1973; Parygin et al., 2000) into several sub-modes (modes). It is noted that Anisimkin in 2004 has thought that higher-order modes of Lamb type waves possessing the non-dispersive ZTW-waves represent modes of new dispersive waves, because Lamb (type) waves are defined as dispersive waves. It is well-known that there are many types of dispersive waves polarized in the sagittal plane such as dispersive Rayleigh and Lamb type waves, as well as dispersive leaky Sezawa waves. The non-dispersive Stoneley type waves propagating at the interface of two solids can also have the "in-plane" polarization. Love type waves (Love, 1911) and surface Bleustein-Gulyaev (BG) type waves (Bleustein, 1968; Gulyaev, 1969) possess unique polarization perpendicular to the sagittal plane. However, the non-dispersive ZTW-waves representing extreme points of $V_{ph}(kh)$ can also split a mode of dispersive BG-waves (Liu et al., 2003). It is noted that the non-dispersive ZTW-waves were understood as corresponding dispersive waves in all papers before the work (Zakharenko, 2005[a]).

Note that a dispersive mode can possess three non-dispersive ZTW-waves that were schematically shown by Ivanov and Kessenikh (1987) for non-piezoelectric materials. Probably, their result shows how many non-dispersive ZTW-waves can exist in the same mode of dispersive wave, omitting the fact that a lowest-order mode can split. Therefore, they introduced their results as being one dispersive mode, and their theory must be

verified in experiments. It is thought that only structures with a relatively weak dependence $V_{ph}(kh)$ can possess non-dispersive ZTW-waves. It is thought that a layered system with the non-dispersive ZTW-waves could be used in technical devices instead of a monocrystal (several monocrystals). In addition, Zhang and Lu (2003) have also found that the lowest-order mode can split into several sub-modes that could be called the Zhang-Lu law. However, their result does not give information about where this splitting occurs and how many sub-modes can exist.

Several layered systems are today well-known possessing a weak dependence $V_{ph}(kh)$ in the lowest-order mode of dispersive RTW-waves. Cubic crystals are crystals with zero temperature coefficients, and they can have strong piezoelectric coupling. However, transversely-isotropic crystals are widely studied in contrast to the cubic crystals studied in this paper. For example, there is a strong interest in the layered system, consisting of a weakly-piezoelectric AlN-layer on a fused-quartz–substrate, for SAW-devices with a weak dependence $V_{ph}(kh)$, see (Volyansky et al., 1987; Bondarenko et al., 1983; Shiosaki et al., 1980; Tsubouchi and Mikoshiba, 1985). In the work of Volyansky et al. (1987) a calculation method was simplified omitting the piezoelectric effect, and a close correlation between theoretical calculations and experimental measurements of the V_{ph} was obtained. A very interesting case was treated in the work of Solie (1971) for the layered system, consisting of a fused-quartz–layer on a (YZ)-LiNbO$_3$–substrate. In the case by Solie (1971), the first sub-mode is also confined in a narrow V_{ph}-range ~ 3 ms^{-1} at small values of kh, and the next sub-modes are confined in larger V_{ph}-ranges interrupting within the kh-range: $1.2 < kh < 3.35$. The layered system, consisting of a ZnO-layer on a weakly-piezoelectric GaAs-substrate, is also interesting because it is possible to monolithically integrate such SAW-devices with GaAs-electronics. The lowest-order mode with no shorting plane for that layered system was recently calculated in (Zhang et al., 2001). Here, the V_{ph}-range is more than 300 ms^{-1} for the second sub-mode and smaller than 2.5 ms^{-1} for the first sub-mode with $V_g > V_{ph}$ at small values of kh. Schmidt and Voltmer (1969) have shown the lowest-order mode for the two-layer structure, consisting of a piezoelectric CdS-layer on a fused-quartz–substrate, where there is a relatively large dependence $V_{ph}(kh)$. The same $V_{ph}(kh)$ was found in (Nakamura and Hanaoka, 1993) by studying the layered system, consisting of a ZnO-layer on a 128^0-rotated Y-cut LiNbO$_3$-substrate. In both latter cases, the peculiarities were not found in the RTW9 lowest-order mode. In the layered system, consisting of the isotropic silicon–layer on the ZnO-substrate treated in (Farnell, 1978) the V_{ph} of dispersive RTW-wave is confined between the RTW-wave for the ZnO-substrate and the corresponding bulk transverse waves for the substrate, because the latter is the V_{ph} upper

limit. The next section describes theory of propagation of dispersive waves with the in-plane polarization. The third section describes different boundary conditions. Results and discussions are written in the fourth section. The fifth section discusses the other possibilities of finding waves with the in-plane polarization in addition to the dispersive Rayleigh type waves. For comparison with [110] direction, the sixth section describes theoretical results of studying in-plane polarized waves in more complicated case of monoclinic symmetry material constants when the theory of section 2 cannot be used.

THEORY

In different layered structures, consisting of piezoelectric materials, propagation equations are written, according to (Farnell and Adler, 1972; Lardat *et al.*, 1971), with components of both the mechanic displacements U_i and the electric field E_J. The constitutive equations for a piezoelectric material can be expressed in terms of the strains and the electric field. Strains are related to mechanic displacements: $\tau_{ij} = (U_{i,j} + U_{j,i})/2$ (Lyamov, 1983). The governing mechanical equilibrium is $ST_{ij,j} = 0$, and the governing electrostatic equilibrium is $D_{i,i} = 0$, where ST_{ij} and D_i are the stress tensor and electric displacement components, respectively. The comma denotes coordinate differentiation with respect to x_i. Each medium possesses the elastic C_{pqrw} and piezoelectric e_{pqr} coefficients, the dielectric constants ε_{pq}, and the medium density ρ. Because dispersive Rayleigh-polarized waves are treated in this paper, only two components of the mechanical displacements, U_1 along the x_1-axis and U_3 along the x_3-axis in Figure 1, are used which lie in the sagittal plane. The components U_1 and U_3 as well as the components E_1 and E_3 can be written in view of plane waves:

$$U_{1,3} = U_{1,3}^0 \exp\left[j\left(k_1 x_1 + k_3 x_3 - \omega t\right)\right]$$
$$E_{1,3} = E_{1,3}^0 \exp\left[j\left(k_1 x_1 + k_3 x_3 - \omega t\right)\right] \tag{1}$$

where k_1 and k_3 are components of the wavevector $\mathbf{K}_s$ along the x_1-axis and the x_3-axis, respectively, and ω and t are the cycle frequency and time; $j = (-1)^{1/2}$. $U_{1,3}^0$ and $E_{1,3}^0$ are initial amplitudes. The electric field E_J is defined by the electric potential ϕ: $E_J = - \partial\phi/\partial x_J$, $J = 1, 2, 3$.
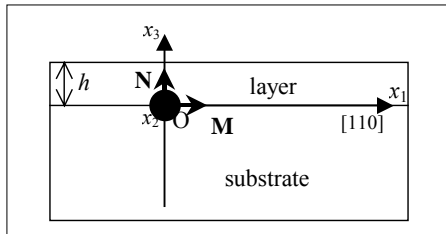

Fig. 1. The propagation direction in the layered system, where the vectors **N** and **M** are directed along the surface normal and propagation direction, respectively. Here the so-called work coordinate system $\{x_1, x_2, x_3\}$ is used, where the x_2-axis is perpendicular to the Figure plane and the sagittal plane (x_1Ox_3).

The piezoelectromechanical waves with polarization in the sagittal plane can propagate in a piezoelectric medium when the sagittal plane coincides with the symmetry plane of the medium, according to (Farnell and Adler, 1972; Lardat *et al.*, 1971). In such propagation directions, for example, [110] propagation direction for cubic crystals, there are the following zero GL_{rw}-components in the Green-Christoffel (GL) equation, $(GL_{rw} - \delta_{rw}\rho V_{ph}^2)U_r = 0$ (Farnell and Adler, 1972; Farnell, 1978; Lyamov, 1983): $GL_{21} = GL_{12} = GL_{32} = GL_{23} = GL_{24} = GL_{42} = 0$. In the GL-equation, r and w run from 1 to 4, δ_{rw} is the Kronecker delta for $r < 4$ and $w < 4$, $\delta_{rw} = 0$ for $r \neq w$ and $\delta_{44} = 0$, $U_r = \{U_1, U_2, U_3, \phi\}$. V_{ph} is the phase velocity, $V_{ph} = \omega/k$, where k is the wavenumber in direction of wave propagation. Therefore, the following equations can be written for the in-plane polarized waves:

$$\begin{pmatrix} C_{55}n_3^2 + C_{11}A_l^2 & \left(C_{13} + C_{55}\right)n_3 & \left(e_{15} + e_{31}\right)n_3 \\ \left(C_{13} + C_{55}\right)n_3 & C_{33}n_3^2 + C_{55}A_t^2 & e_{15} \\ \left(e_{15} + e_{31}\right)n_3 & e_{15} & -\varepsilon_{11} - \varepsilon_{33}n_3^2 \end{pmatrix}\begin{pmatrix} U_1 \\ U_3 \\ \phi \end{pmatrix} = 0 \tag{2}$$

In equation (2), $C_{11} \neq C_{33}$, C_{55}, and C_{13} are the corresponding non-zero components of the elasticity tensor (Voigt notation). $e_{15} = e_{31}$ and $\varepsilon_{11} = \varepsilon_{33}$ are the non-zero piezoelectric and dielectric constants, respectively. It is noted that for cubic crystals in [110] propagation direction there is the following relationship between the elastic constants C_{11} and C_{33}: $C_{11} = C_{55} + (C_{33} + C_{13})/2$ (Stoneley, 1955; Tursunov, 1967). Also, in Eq. (2) there are $A_l^2 = 1 - (V_{ph}/V_l)^2$ and $A_t^2 = 1 - (V_{ph}/V_{t5})^2$. $V_l = [C_{11}/\rho]^{1/2}$ and $V_{t5} = [C_{55}/\rho]^{1/2}$ are the so-called velocity equivalents for [110] direction. However, they are the speeds of the bulk longitudinal and transverse waves for [100] direction, respectively. For [110] direction, the speed V_t of the bulk transverse wave is equal to $V_t = [(C_{55}/\rho)(1 + K_0^2)]^{1/2}$, and the bulk longitudinal wave propagates with the speed $V_{l3} = [C_{33}/\rho]^{1/2}$. K_0^2 is called the static coefficient of electromechanical coupling (CEMC):

$$K_0^2 = e_{15}^2 / C_{55}\varepsilon_{11}.$$ However, in the case of $C_{11} = C_{33}$, for example, in [100] propagation direction of cubic crystals (Zakharenko, 2005[a]) there is $V_{l3} = V_l$. Also, many non-cubic acoustic crystals with $C_{11} \sim C_{33}$ can be readily found in (Landolt-Boernstein Int. Tables, 1985; Blistanov *et al.*, 1982).

For definition, the non-dimensional complex component n_3 is $n_3 = k_3/k$, and there are $n_1 = 1$ and $n_2 = 0$ in Eq. (2). For piezoelectric cubic crystals, the material constants in [100] direction $\{(C_{11} = C_{22} = C_{33}, C_{12} = C_{13} = C_{23}, C_{44} = C_{55} = C_{66}); (e_{14} = e_{25} = e_{36}); (\varepsilon_{11} = \varepsilon_{22} = \varepsilon_{33}); \rho; (V_L, V_{FT} = V_{ST}, V_{RTW6})\}$ transform into the following material constants in [110] direction $\{(C_{11} = C_{22}, C_{33}, C_{12}, C_{13} = C_{23}, C_{44} = C_{55}, C_{66}); (e_{15} = e_{31} = -e_{32} = -e_{24}); (\varepsilon_{11} = \varepsilon_{22} = \varepsilon_{33}); \rho; (V_L, V_{FT}, V_{ST}, V_{RTW9})\}$, where V_L, V_{FT}, and V_{ST} represent the speeds of the bulk longitudinal, fast, and slow transverse waves, respectively: $V_{FT} = (C_{66}/\rho)^{1/2}$ and $V_{ST} = [(C_{55}/\rho)(1 + K_0^2)]^{1/2}$. The material constants for the

cubic crystals $Bi_{12}SiO_{20}$ and $Bi_{12}GeO_{20}$ are given in table 1 for both propagation directions.

For convenience, the corresponding determinant for the determination of the complex component n_3 can be transformed from Eq. (2) into the following view, after some transformations:

$$\begin{vmatrix} C_{55}m + C_{11}A_l^2 & (C_{13}+C_{55})m & 2m \\ (C_{13}+C_{55}) & C_{33}m + C_{55}A_t^2 & 1 \\ 2 & 1 & -a(1+m) \end{vmatrix} = 0 \quad (3)$$

with $m = n_3^2$ and $a = 1/(K_0^2 C_{55})$.

Expanding the determinant (3), the secular equation is obtained representing a sixth order polynomial for determination of the eigenvalues $n_3^{(N)}$, where the index N runs from 1 to 6. After some transformations, the obtained polynomial from (3) can be shown as follows:

$$m^3 + Am^2 + Bm + C = 0 \quad (4)$$

where

$$A = \left[\frac{C_{11}}{C_{33}} A_l^2 + A_t^2 + C^2 \right] + 1 + 4K_0^2$$

$$B = \left[\frac{C_{11}}{C_{33}} A_l^2 + A_t^2 + C^2 \right] + \frac{C_{11}}{C_{33}} A_l^2 A_t^2 + K_{Dt} \quad (5)$$

$$C = \frac{C_{11}}{C_{33}} A_l^2 A_t^2 + K_{Dl}$$

The coefficients A, B, and C in (5) consist of both the corresponding elastic anisotropy terms and the corresponding terms K_0^2, K_{Dt}, and K_{Dl} coupled with the piezoelectricity influence. The elastic constants are combined in the anisotropy term C^2 (Zakharenko, 2005[a]; Zakharenko, 2006) which appears in the square brackets of the coefficients A and B in (5) and has the following view for the studied direction:

Table 1. The characteristics for $Bi_{12}SiO_{20}$ and $Bi_{12}GeO_{20}$. The piezoelectric e_{14} and dielectric ε_{11} material constants are the same in both propagation directions. The corresponding elastic constants C_{ij} are given in [N/m²] $\times 10^{10}$ and all the velocities are in [m/s].

[100] propagation direction								
Material	ρ, [kg/m³]	C_{11}	C_{12}	C_{44}	e_{14}, [C/m²]	ε_{11}, 10^{-10} [F/m]	V_t	V_l	V_{RTW2}
$Bi_{12}SiO_{20}$	9070	12.962	2.985	2.451	1.122	3.63735	1643.87	3780.35	1606.08
$Bi_{12}GeO_{20}$	9200	12.852	2.934	2.562	0.983	3.336	1668.77	3737.59	1626.11
[110] propagation direction								
Material	C_{11}	C_{33}	C_{13}	C_{55}	C_{66}	V_l	V_{ST}	V_{FT}	V_{RTW3}
$Bi_{12}SiO_{20}$	10.4245	12.962	2.985	2.451	4.9885	3390.19	1756.10	2345.21	1681.50
$Bi_{12}GeO_{20}$	10.455	12.852	2.934	2.562	4.959	3371.07	1760.58	2321.68	1683.78

Table 2. The non-dimensional anisotropy term C^2 and the velocities V_t, V_l, and V^{th} for the piezoelectric cubic crystals in [100] propagation direction of (001) cut, in which Rayleigh-polarized waves do not coupled with the electric potential.

Nº	Cubic crystal	Structure type	Density ρ [kg/m³]	Elastic constants C_{ij}, 10^{10} [N/m²]			Anisotropy factor η	Anisotropy term C^2	Velocity V_t [m/s]	Velocity V_l [m/s]	Velocity V^{th} [m/s]
				C_{11}	C_{44}	C_{12}					
Piezoelectric class 23											
1.	$NaClO_3$	$NaClO_3$	2490	4.887	1.173	1.675	0.73	0.99	2170	4430	3370
2.	$NaBrO_3$	$NaClO_3$	3330	5.708	1.525	1.695	0.76	0.82	2140	4140	3192
Piezoelectric class $\bar{4}3m$											
3.	GaP	ZnS	4301	14.110	6.260	7.030	1.77	-1.30	3815	5728	2657
4.	GaAs	ZnS	5316	11.810	5.940	5.320	1.83	-1.32	3343	4713	2249
5.	β-ZnS	ZnS	4091	10.460	4.610	4.640	1.58	-1.07	3310	4897	2645
6.	ZnSe	ZnS	5264	8.720	3.920	5.240	2.25	-1.78	2729	4070	1063
7.	InSb	ZnS	5790	6.720	3.040	3.670	1.99	-1.54	2291	3407	1289
8.	CuCl	ZnS	3530	4.500	1.342	3.711	3.40	-2.58	1950	3570	i1303
9.	CuBr	ZnS	4720	4.624	1.413	3.512	2.54	-2.13	1730	3130	i546
10.	ZnTe	ZnS	5636	7.130	3.120	4.070	2.04	-1.60	2353	3557	1241
11.	CdTe	ZnS	5849	5.351	1.994	3.681	2.39	-1.93	1846	3025	417
12.	Tl_3TaS_4	-	6790	4.910	0.320	1.130	0.17	12.07	687	2689	2497
13.	Tl_3TaSe_4	-	7280	4.190	0.410	1.400	0.29	6.41	751	2399	2078
14.	$Bi_4(GeO_4)_3$	eulytine	7120	11.580	4.360	2.700	0.98	0.03	2475	4033	3006
15.	$Bi_4(SiO_4)_3$	eulytine	6800	13.570	5.180	2.270	0.92	0.21	2760	4467	3491

$$C^2 = \left[(C_{11} - C_{55})(C_{33} - C_{55}) - (C_{13} + C_{55})^2 \right] / C_{33} C_{55} \quad (6)$$

It is noted that the C^2 in Eq. (6) is a universal non-dimensional crystal characteristics, which can be suitable for all crystal symmetries, except the triclinic and monoclinic symmetries. However, for a particular case of C_{15}, $C_{35} \ll C_{55}$, C_{13}, C_{11}, and C_{33}, the C^2 is also suitable for the symmetries.

The corresponding piezoelectric parts in (5) coupled with the static CEMC K_0^2 are as follows: $(4K_0^2)$ or $(1 + 4K_0^2)$ in the coefficient A, the so-called dynamic CEMCs K_{Dt} and K_{Dl} in the coefficients B and C, respectively. The introduced non-dimensional characteristics K_{Dt} and K_{Dl} depend on both the cubic crystal anisotropy and the V_{ph}:

$$K_{Dt} = \frac{K_0^2}{C_{33}} \left[4 C_{55} A_t^2 - 4 C_{13} - 3 C_{55} \right] \quad K_{Dl} = K_0^2 \frac{C_{11}}{C_{33}} A_l^2 \quad (7)$$

It is clearly seen that the dynamic CEMC K_{Dt} depends only on the speed V_{t5} of the corresponding bulk transverse wave. However, the dynamic CEMC K_{Dl} depends only on the speed V_l of the bulk longitudinal wave. Therefore, they can be called as transverse and longitudinal dynamic CEMCs, respectively. For dispersive waves, the V_{ph} depends on the layer thickness kh, and hence, the K_{Dt} and K_{Dl} will also depend on the kh. The K_{Dt} originates from its value of $K_0^2 (C_{55} - 4C_{13})/C_{33}$ at $V_{ph} = 0$ and goes to its value of $- K_0^2 (4C_{13} + 3C_{55})/C_{33}$ at $V_{ph} = V_{t5}$. On the other hand, the K_{Dl} has its maximum value of $K_0^2 C_{11}/C_{33}$ at $V_{ph} = 0$ and equals to zero at $V_{ph} = V_l$. Both the dynamic CEMCs go to $- \infty$ with $V_{ph} \rightarrow + \infty$. Also, it is natural to note in Eq. (5) the following terms coupled with the cubic crystal anisotropy:

$$A_0 = \frac{C_{11}}{C_{33}} A_l^2 + A_t^2 + C^2 \qquad B_0 = \frac{C_{11}}{C_{33}} A_l^2 A_t^2 \qquad (8)$$

Figure 2 shows both the coefficients A_0 and B_0 as well as the K_{Dt} and K_{Dl} for the crystals $Bi_{12}SiO_{20}$, $Bi_{12}GeO_{20}$, and $Bi_{12}TiO_{20}$ in [110] propagation direction. Figure 2 clearly shows that values of the A_0 and B_0 can be one order greater than values of the K_{Dt} and K_{Dl}. It is noted that the

anisotropy terms $C^2(Bi_{12}SiO_{20}) \sim 1.71$, $C^2(Bi_{12}GeO_{20}) \sim 1.55$, and $C^2(Bi_{12}TiO_{20}) \sim 1.75$ in [110] direction are significantly smaller than those in [100] direction, in which they represent the maximum possible C^2 of suitable propagation directions: $C^2(Bi_{12}SiO_{20}) \sim 2.55$, $C^2(Bi_{12}GeO_{20}) \sim 2.30$, and $C^2(Bi_{12}TiO_{20}) \sim 2.64$. Also, the threshold velocities V^{th} (Zakharenko, 2006) for the cubic crystals studied in Figure 2 are as follows: $V^{th}(Bi_{12}SiO_{20}) \sim 2826$ m/s, $V^{th}(Bi_{12}GeO_{20}) \sim 2795$ m/s, and $V^{th}(Bi_{12}TiO_{20}) \sim 2617$ m/s. For comparison, the threshold velocities V^{th} for (001) [100] direction are: $V^{th}(Bi_{12}SiO_{20}) \sim 3216$ m/s and $V^{th}(Bi_{12}GeO_{20}) \sim 3160$ m/s. Some piezoelectric acoustic crystals are listed in Table 2, in which the unique cubic crystals Tl_3TaS_4 and Tl_3TaSe_4 of the Chalcogenide family have very great values of C^2.

Using the crystal characteristics of Eqs. (7) and (8), Eq. (4) can be rewritten as follows:

$$m^3 + \left(A_0 + 1 - K_0^2 \right) m^2 + \left(A_0 + B_0 + K_{Dt} \right) m + \left(B_0 + K_{Dl} \right) = 0 \quad (9)$$

After some transformations of Eq. (9), one can get the following equation

$$(m+1)\left(m^2 + A_0 m - K_0^2 m + B_0 + K_0^2 - K_{Dt} \right) + \left(K_{Dl} - K_{Dt} - K_0^2 \right) = 0 \quad (10)$$

It is clearly seen in Eq. (10) that for a weak piezoelectrics $K_0^2 \rightarrow 0$ ($K_0^2 = 0$ and $K_{Dl} = K_{Dt} = 0$) there is

$$(m+1)\left(m^2 + A_0 m + B_0 \right) = 0 \qquad (11)$$

The first factor in (11) represents equation corresponding to the pure electric potential wave:

$$n_3^{1,2} = \pm j \qquad (12)$$

The second gives the following four roots:

$$n_3^{3,4,5,6} = \pm \left[-\frac{1}{2} A_0 \pm \frac{1}{2} \left(A_0^2 - 4 B_0 \right)^{1/2} \right]^{1/2} \qquad (13)$$

which correlate with the roots of (Zakharenko, 2006) for (001) [110] propagation direction in non-piezoelectrics (Z-cut-X-direction in the crystallographic coordinate system).

Introducing the new function $y = m + A/3$, polynomial (4) can be rewritten to the following view $y^3 + 3py + 2q = 0$,
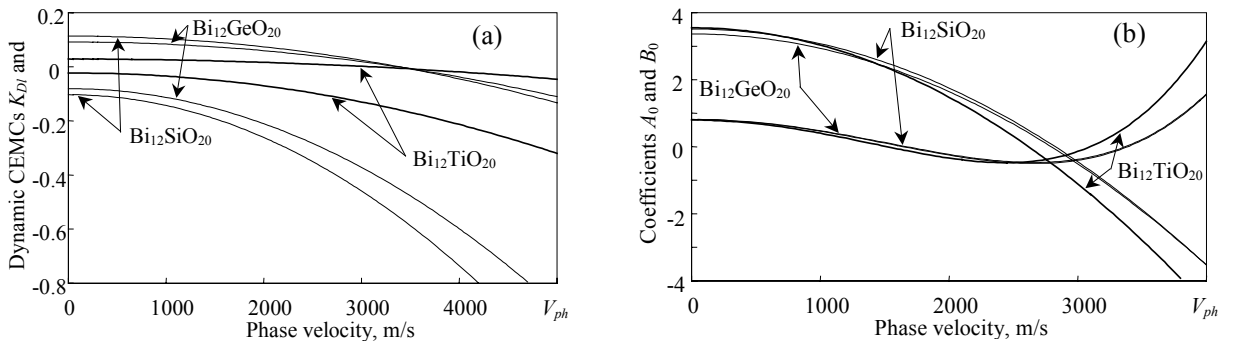

Fig. 2. The dynamic characteristics in [110] propagation direction for $Bi_{12}SiO_{20}$ (thin lines), $Bi_{12}GeO_{20}$ (normal), and $Bi_{12}TiO_{20}$ (thick): (a) K_{Dt} and K_{Dl} from Eq. (7), where there is $K_{Dl}(V_{ph} = V_l) = 0$ and $K_{Dt} < K_{Dl}$; (b) the coefficients A_0 and B_0 from Eq. (8), where there is $A_0(V_{ph} = V^{th}) = 0$ and $B_0(V_{ph} = V_t$ and $V_{ph} = V_l) = 0$.

for which the Cardano's formula can be applied, for instance, see the reference-book (Bronstein and Semendyaev, 2000). The coefficients q and p are defined as follows: $q = (A/3)^3 - (B/2)(A/3) + C/2$ and $p = B/3 - (A/3)^2$. Three roots $y_{1,2,3}$ depend on sign of the discriminant D, $D = q^2 + p^3$. If the D is negative due to $p < 0$, there are all three real roots. However, in the case of $D > 0$ there are one real and two imaginary roots. Also, if the coefficient C in (4) is positive, the real root is negative. It is clearly seen from (5) and (7) that the coefficient C can be positive both below the speed V_t and above the speed V_l. In addition, the coefficients A and B in (4) could be positive above the speed V_l for some cubic crystals with unique anisotropy properties, namely with a "gigantic" positive anisotropy term C^2 that was studied in (Zakharenko, 2006). It is noted that the anisotropy term C^2 can be both positive and negative, depending on the elastic constants. Therefore, there is a possibility to exist for the other type of surface waves polarized in the sagittal plane above the V_l, depending on both the crystal anisotropy and piezoelectric effect. For these waves, all complex/imaginary roots there are for polynomial (4). For the case of two real and four complex roots, there is also an existence possibility of in-plane polarized leaky waves with the $V_{ph} > V_t$.

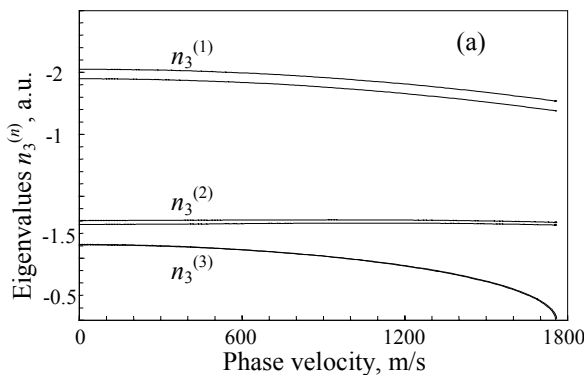Therefore, all six roots of polynomial (4) are as follows:

$$n_3^{1,2,3,4,5,6} = \pm\sqrt{-A/3 + y_{1,2,3}} \qquad (14)$$

According to (Bronstein and Semendyaev, 2000), three roots $y_{1,2,3}$ are functions of values of w_1 and w_2, as well as of the roots $\alpha_{1,2} = -1/2 \pm j\sqrt{3}/2$ of the square equation $x^2 + x + 1 = 0$:

$$y_1 = w_1 + w_2 \quad y_2 = \alpha_1 w_1 + \alpha_2 w_2 \quad y_3 = \alpha_2 w_1 + \alpha_1 w_2 \qquad (15)$$

where

$$w_1 = \sqrt[3]{-q + \sqrt{q^2 + p^3}} \qquad w_2 = \sqrt[3]{-q - \sqrt{q^2 + p^3}} \qquad (16)$$

It is noted that all three roots $y_{1,2,3}$ can be also found using the well-known Cardano's formula in the following view: $y_{1,2,3} = \xi - p/\xi$ with $\xi = [-q + \text{sqrt}(q^2 + p^3)]^{1/3}$.

For each eigenvalue $n_3^{(N)}$ there is the corresponding so-called eigenvector $(U_1^{(N)}, U_3^{(N)}, \phi^{(N)})$:

$$U_1^{(N)} = +\left[C_{33}(n_3^{(N)})^2 + C_{55}A_t^2 + \frac{e_{15}^2}{\varepsilon_{11}}\frac{1}{1+(n_3^{(N)})^2}\right]^{1/2}$$

$$U_3^{(N)} = -\left[C_{55}(n_3^{(N)})^2 + C_{11}A_l^2 + 4\frac{e_{15}^2}{\varepsilon_{11}}\frac{(n_3^{(N)})^2}{1+(n_3^{(N)})^2}\right]^{1/2}$$

$$\phi^{(N)} = 2\frac{e_{15}}{\varepsilon_{11}}\frac{n_3^{(N)2}}{1+(n_3^{(N)})^2}U_1^{(N)} + \frac{e_{15}}{\varepsilon_{11}}\frac{1}{1+(n_3^{(N)})^2}U_3^{(N)} \quad (17)$$

In addition, the components $U_1^{(N)}$ and $U_3^{(N)}$ can be also found from the first equation in (2) as follows:

$$U_1^{(N)} = -(C_{13} + C_{55})n_3^{(N)} - 2C_{55}K_0^2\frac{n_3^{(N)}}{1+(n_3^{(N)})^2}$$

$$U_3^{(N)} = C_{55}(n_3^{(N)})^2 + C_{11}A_l^2 + 4C_{55}K_0^2\frac{(n_3^{(N)})^2}{1+(n_3^{(N)})^2}$$

which are equivalent, using Eq. (2). It is clearly seen in the latter equations that $U_1^{(N)}$ is imaginary, and $U_3^{(N)}$ is real depending on an imaginary $n_3^{(N)}$ that results in real $\phi^{(N)}$. On the other hand, $U_1^{(N)}$ and $U_3^{(N)}$ can be real and imaginary, respectively, resulting in imaginary $\phi^{(N)}$, if the second equation in (2) is treated. It is also noted that $U_1^{(N)}$ or $U_3^{(N)}$ can be chosen to be equal to unity for simplicity. The eigenvalues $n_3^{(N)}$ with negative imaginary part and the corresponding eigenvector components $u_1^{(N)} = U_1^{(N)}$, $u_3^{(N)} = U_3^{(N)}$, and $u_4^{(N)} = \phi^{(N)}$ are shown in Figure 3 for $Bi_{12}SiO_{20}$ and $Bi_{12}GeO_{20}$. Note that the $n_3^{(3)}$ is zero at $V_{ph} = V_t$.

All six eigenvalues $n_3^{(N)}$ in (14) must be taken for a layer, while only eigenvalues $n_3^{(N)}$ with negative imaginary part are left for a substrate, in order to have wave damping towards the depth of the substrate for the coordinate
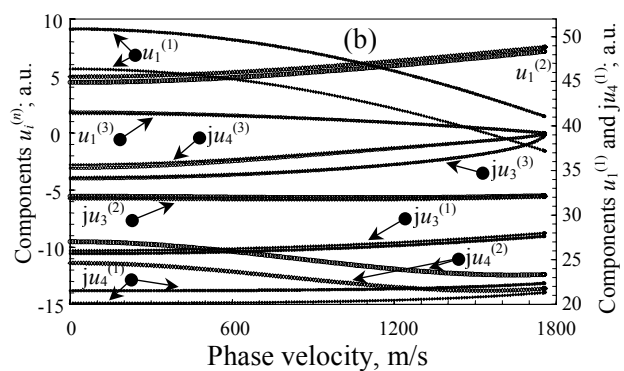

Fig. 3. (a) The eigenvalues $n_3^{(N)}$ for $Bi_{12}SiO_{20}$ (thin lines) and $Bi_{12}GeO_{20}$ (normal lines), where there is $n_3^{(1)} > n_3^{(2)} > n_3^{(3)}$; and (b) the eigenvector components $u_1^{(N)}$, $u_3^{(N)}$, and $u_4^{(N)} = \phi^{(N)}$ for $Bi_{12}SiO_{20}$ (cycles) and $Bi_{12}GeO_{20}$ (rhombs).

system shown in figure 1. Therefore, the complete mechanic displacements and the complete electric potential can be written as:

$$U_{1,3}^{\Sigma} = \sum_N F^{(N)} U_{1,3}^{(N)} \exp\left[j\left(k_1 x_1 + k_3^{(N)} x_3 - \omega t\right)\right]$$

$$\phi^{\Sigma} = \sum_N F^{(N)} \phi^{(N)} \exp\left[j\left(k_1 x_1 + k_3^{(N)} x_3 - \omega t\right)\right] \qquad (18)$$

where $F^{(N)}$ are the so-called weight coefficients, and the index N runs from 1 to 3 for a substrate and from 1 to 6 for a layer.

For the free space, the Laplace's equation of type $\Delta\phi = 0$ is written in the following view: $\varepsilon_0(k_1^2 + k_3^2)\phi_0 = 0$, where ε_0 is the dielectric constant for the free space, $\varepsilon_0 = 8.854\times 10^{-12}$ F/m. Because the wavevector component k_1 in the propagation direction is given the same in each medium (in a layer, a substrate and the free space), the electric potential for the free space is written as: $\phi_0 = F^{(0)}\exp(-k_1 x_3)\exp[j(k_1 x_1 - \omega t)]$. The ϕ_0 should decrease with increase in the coordinate x_3. The V_{ph} of such Rayleigh-polarized waves should satisfy boundary conditions described in the next Section. Suitable V_{ph} of dispersive waves are found when the boundary conditions determinant equals to zero.

BOUNDARY CONDITIONS

Now both the complete mechanic displacements and the complete electric potential of Eq. (18) are substituted in the equations of mechanical and electrical boundary conditions based on the following requirements at both the interface of two solids (at $x_3 = 0$ in Fig. 1) and the free surface, $x_3 = h$:

1) continuity of the mechanic displacement U_1 at $x_3 = 0$ ($U_1^S = U_1^L$) where

$$U_1^S = \sum_{S(N)} F^{S(N)} U_1^{S(N)} \text{ and } U_1^L = \sum_{L(N)} F^{L(N)} U_1^{L(N)} \qquad (19)$$

2) continuity of the mechanic displacement U_3 at $x_3 = 0$ ($U_3^S = U_3^L$) where

$$U_3^S = \sum_{S(N)} F^{S(N)} U_3^{S(N)} \text{ and } U_3^L = \sum_{L(N)} F^{L(N)} U_3^{L(N)} \qquad (20)$$

3) continuity of the normal component ST_{31} of the stress tensor at $x_3 = 0$ ($ST_{31}^S = ST_{31}^L$) where

$$ST_{31}^S = \sum_{S(N)} F^{S(N)}\left[C_{55}^S(k_3^{S(N)} U_1^{S(N)} + k_1 U_3^{S(N)}) + e_{15}^S k_1 \phi^{S(N)}\right]$$

$$ST_{31}^L = \sum_{L(N)} F^{L(N)}\left[C_{55}^L(k_3^{L(N)} U_1^{L(N)} + k_1 U_3^{L(N)}) + e_{15}^L k_1 \phi^{L(N)}\right] \quad (21)$$

4) continuity of the normal component ST_{33} of the stress tensor at $x_3 = 0$ ($ST_{33}^S = ST_{33}^L$) where

$$ST_{33}^S = \sum_{S(N)} F^{S(N)}\left[C_{13}^S k_1 U_1^{S(N)} + C_{33}^S k_3^{S(N)} U_3^{S(N)}\right]$$

$$ST_{33}^L = \sum_{L(N)} F^{L(N)}\left[C_{13}^L k_1 U_1^{L(N)} + C_{33}^L k_3^{L(N)} U_3^{L(N)}\right] \qquad (22)$$

5) continuity of the normal component D_3 of the electric displacements at $x_3 = 0$ ($D_3^S = D_3^L$) where

$$D_3^S = \sum_{S(N)} F^{S(N)}\left[e_{31}^S k_1 U_1^{S(N)} - \varepsilon_{33}^S k_3^{S(N)} \phi^{S(N)}\right]$$

$$D_3^L = \sum_{L(N)} F^{L(N)}\left[e_{31}^L k_1 U_1^{L(N)} - \varepsilon_{33}^L k_3^{L(N)} \phi^{L(N)}\right] \qquad (23)$$

6) continuity of the electric potential ϕ at $x_3 = 0$ ($\phi^S = \phi^L$) where

$$\phi^S = \sum_{S(N)} F^{S(N)} \phi^{S(N)} \text{ and } \phi^L = \sum_{L(N)} F^{L(N)} \phi^{L(N)} \qquad (24)$$

7) equality to zero of the stress tensor component: $ST_{31}^L = 0$ at $x_3 = h$, where

$$ST_{31}^L = \sum_{L(N)} F^{L(N)}\left[C_{55}^L(k_3^{L(N)} U_1^{L(N)} + k_1 U_3^{L(N)}) + e_{15}^L k_1 \phi^{L(N)}\right] \times \exp\left(j k_3^{L(N)} h\right)$$

$$(25)$$

8) equality to zero of the stress tensor component: $ST_{33}^L = 0$ at $x_3 = h$, where

$$ST_{33}^L = \sum_{L(N)} F^{L(N)}\left[C_{13}^L k_1 U_1^{L(N)} + C_{33}^L k_3^{L(N)} U_3^{L(N)}\right] \times \exp\left(j k_3^{L(N)} h\right) \quad (26)$$

9) continuity of the D_3 at $x_3 = h$ ($D_3^L = D_3^f$) where

$$D_3^L = \sum_{L(N)} F^{L(N)}\left[e_{31}^L k_1 U_1^{L(N)} - \varepsilon_{33}^L k_3^{L(N)} \phi^{L(N)}\right] \times \exp\left(j k_3^{L(N)} h\right)$$

$$D_3^f = -F^{(0)} \phi_0^f j k_1 \varepsilon_0 \exp(-k_1 h) \qquad (27)$$

10) continuity of the electric potential ϕ at $x_3 = h$ ($\phi^L = \phi^f$) where

$$\phi^L = \sum_{L(N)} F^{L(N)} \phi^{L(N)} \exp\left(j k_3^{L(N)} h\right) \text{ and}$$

$$\phi^f = F^{(0)} \phi_0^f \exp(-k_1 h) \qquad (28)$$

In the boundary conditions (19)–(28), the indices L and S refer to quantities relative to the layer and substrate, respectively, $k_1^{L(N)} = k_1^{S(N)} = k_1 = k$. These equations form the equation set of ten homogeneous equations with unknown factors $F^{L(N)}$, $F^{S(N)}$, and $F^{(0)}$. Solutions for the V_{ph} can be numerically obtained when the tenth-order boundary conditions determinant (BCD10), consisting of coefficients at the unknown factors, becomes zero. It is noted that BCD10 can be readily reduced to BCD9 for finding the RTW9 phase velocity because values of the ϕ and D_3 can be taken to be not independent, for example, see (Farnell and Adler, 1972; Lardat *et al.*, 1971; Ingebrigtsen, 1969). Once ϕ is given, a fixed value D_3 is also given. Therefore, two boundary conditions (27) and (28) at the free surface can be written as single boundary condition for simplicity:

$$D_3 = \sum_{L(N)} F^{L(N)}\left[e_{31}^L k_1 U_1^{L(N)} - (\varepsilon_{33}^L k_3^{L(N)} - j k_1 \varepsilon_0)\phi^{L(N)}\right] \times \exp\left(j k_3^{L(N)} h\right)$$

$$(29)$$

To study the dispersive RTW9-waves is a complicated problem that can probably be solved numerically. It is noted that the boundary conditions (19)–(29) are changed for the so-called case of "shorted" surface. It is also noted that for weakly-piezoelectric materials there is $e_{15} \to 0$ ($e_{15} = 0$) that can result in appearance of two BCDs instead of BCD9 substituting $e_{15} = 0$ in Eq. (2). The first BCD6 of sixth-order gives the suitable V_{ph} for the non-
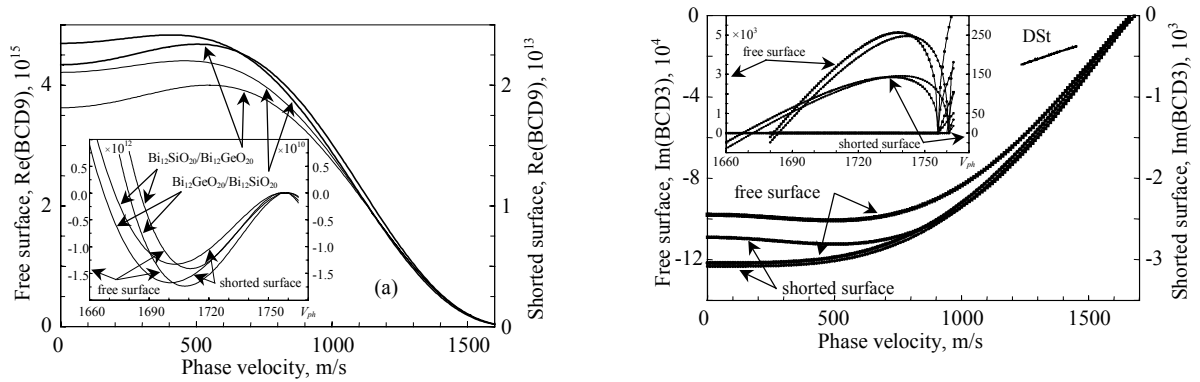
Fig. 4. The determinant behavior for (a) the RTW9-waves for the structures $Bi_{12}SiO_{20}/Bi_{12}GeO_{20}$ and $Bi_{12}GeO_{20}/Bi_{12}SiO_{20}$ with the free surface (thick lines, $kh \sim 1$) and the shorted surface (thin lines, $kh \sim 0.5$); and (b) the RTW3-waves for $Bi_{12}SiO_{20}$ (squares) and $Bi_{12}GeO_{20}$ (cycles), where "DSt" represents the determinant BCD6 for finding the Stoneley type waves.

piezoelectric RTW6-waves, and the second BCD corresponds to the electric potential wave. In this case, Eq. (4) goes into Eq. (11), which together with roots (12) and (13) give eigenvectors of the following view $(0, 0, \phi^{(N)})$ and $(U_1^{(N)}, U_3^{(N)}, 0)$. Also, a BCD6 of sixth-order can be formed from the boundary conditions (19)–(29) for finding the V_{ph} of Rayleigh-polarized Stoneley type waves (STW6). However, such a BCD6 is not described in this Section to minimize the paper size, because non-dispersive waves propagating at the interface of two infinite solids were not found in the studied case.

Figure 4 shows behavior of determinants investigating both dispersive RTW9-waves and non-dispersive RTW3-waves. Real parts of the BCD9 for Rayleigh-polarized surface waves are given in Figure 4a in the V_{ph}-range: $0 < V_{ph} < V_t$. Both boundary conditions of free and shorted surfaces were studied for the layered system $Bi_{12}SiO_{20}/Bi_{12}GeO_{20}$ and the reverse configuration. The insertion in figure 4a shows solutions for the dispersive RTW9-waves, which are close to the corresponding speeds V_t for the crystals $Bi_{12}SiO_{20}$ and $Bi_{12}GeO_{20}$. Figure 4b shows the BCD3 imaginary parts for finding surface wave solutions in single crystals $Bi_{12}SiO_{20}$ and $Bi_{12}GeO_{20}$ for the V_{ph}-range using free and shorted surfaces. The insertion in figure 4b gives the solutions of surface RTW3-waves. For comparison, the BCD6 behavior for finding the Stoneley type waves, which could be localized at the interface between the crystals $Bi_{12}SiO_{20}$ and $Bi_{12}GeO_{20}$, is also shown in Figure 4b. It is noted that the absolute values of BCD9 for surface wave investigations in the studied structures are ten orders greater than those of BCD3 for the investigations in monocrystals that makes an additional difficulty to study layered systems.

NUMERICAL RESULTS AND DISCUSSIONS

In this paper, the numerical results are introduced concerning calculations of the V_{ph} of the dispersive RTW9-waves, accounting the piezoelectric effect for both the $Bi_{12}SiO_{20}$-layer and the $Bi_{12}GeO_{20}$-substrate in [110] direction for both media, in which the sagittal plane coincides with the symmetry plane of the media. For the numerical calculations, the elastic C_{ijkl}, piezoelectric e_{ijk}, and dielectric ε_{ij} material constants, and densities ρ of the treated media were taken from (Aleksandrov et al., 1984; Blistanov et al., 1982). Figure 5 shows the lowest-order modes of RTW9-waves (the so-called first type of the waves (Lardat et al., 1971)), namely dependence of the RTW9 phase velocity on the non-dimensional value of kh, where k is the wavenumber in the direction of wave propagation and h is the layer thickness. In general, the RTW9 lowest-order modes must be confined between the piezoelectric non-dispersive three-partial Rayleigh type wave (RTW3) for the $Bi_{12}GeO_{20}$-substrate at $kh \to 0$ and the wave for the $Bi_{12}SiO_{20}$-layer at $kh \to \infty$. However, that is not so at small kh in both studied layered systems for both cases of the free and shorted surfaces due to some peculiarities, which will be further discussed.

The dispersion relations in figures 5a (free surface) and 5b (metallized surface) show the existence possibility of non-dispersive Zakharenko type waves (ZTWs) after the work of Zakharenko (2005[a]). For the free surface, the nine-partial non-dispersive ZTW9-waves exist at $kh \sim 1.0$ in the both studied structures. However, for the metallized surface, they exists at $kh \sim 0.5$ showing a significant shift to smaller value of the kh. These non-dispersive ZTW9-waves split the corresponding RTW9 lowest-order mode into several sub-modes with different dispersion ($V_{ph} > V_g$ or $V_{ph} < V_g$, where V_g is the group velocity, $V_g = d\omega/dk$). Therefore, it is possible to state that each dispersive sub-mode starts with a non-dispersive wave and comes to a non-dispersive wave. There are two sub-modes for each case in figure 5. The RTW9 group velocity must have one extreme point in each sub-mode, because the behavior of the V_g depends on the behavior of the V_{ph}, $V_g = V_{ph} + kh(dV_{ph}/dkh)$, that was analytically shown in (Zakharenko, 2005[a]). It is obvious that increasing function $V_{ph}(kh)$ leads to the inequality $V_g > V_{ph}$ due to $dV_{ph}/dkh > 0$. On the
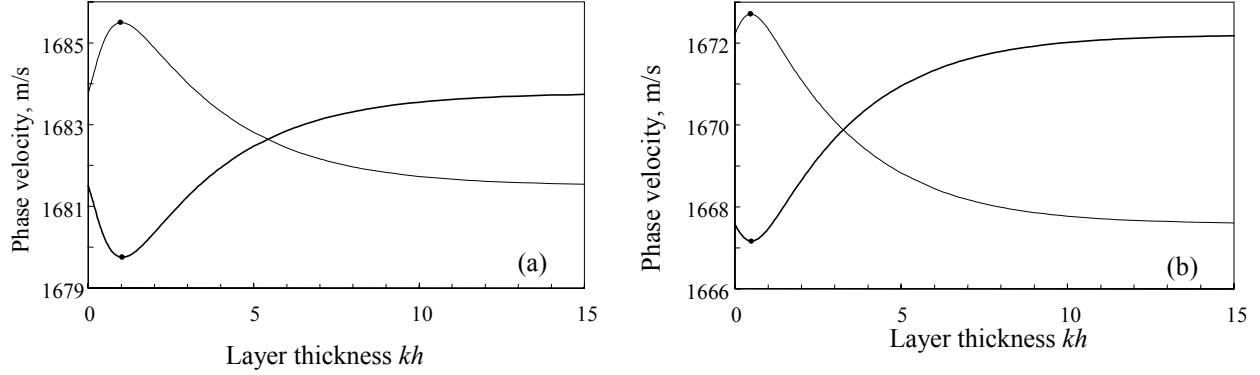
Fig. 5. The first type of dispersive RTW9-waves for the structures $Bi_{12}SiO_{20}/Bi_{12}GeO_{20}$ (thin lines) and $Bi_{12}GeO_{20}/Bi_{12}SiO_{20}$ (thick lines): a) for the free surface; b) for the metallized surface. The V_{ph} extreme points represent the non-dispersive ZTW9-waves.

other hand, decreasing $V_{ph}(kh)$ results in $V_g < V_{ph}$ because $dV_{ph}/dkh < 0$. The non-dispersive Zakharenko waves ($V_g = V_{ph} \neq 0$) existing in a mode of dispersive waves can be described by the following formulas, using the well-known Leibniz's formula for the complex derivative $d(u/v)/dx = (vdu/dx - udv/dx)/v^2$:

$$\frac{dV_{ph}}{dkh} = V_g \frac{dV_{ph}}{d\omega h} = 0 \qquad (30)$$

$$\frac{dV_{ph}}{dkh} = \frac{1}{kh}\left(V_g - V_{ph}\right) \qquad (31)$$

$$\frac{dV_{ph}}{d\omega h} = \frac{V_{ph}}{\omega h}\left(1 - \frac{V_{ph}}{V_g}\right) \qquad (32)$$

The relationship (30) between the derivatives of V_{ph} shows that there is independence of the V_{ph} on both the angular frequency ω and the wavenumber k in the same k-ω-domain with $V_g \neq 0$. The formulas (31) and (32) give clearance that formula (30) is satisfied as soon as $V_{ph} = V_g$ for the wavenumber $k \neq 0$ and $k < \infty$. Note that the mass sensitivity of a sensor is generally defined as the relative velocity change due to the application of a thin non-elastic mass of thickness h_M and density ρ_M on top of a sensor surface. The normalized mass sensitivity can be also determined from the appropriate velocity dispersion (Jungnickel *et al.*, 1997) because the sensitivity is proportional to the first derivative dV_{ph}/dkh_M. Note that the higher derivatives of the V_{ph} and V_g given in (Zakharenko, 2005[a]) can be also used to determine inflexion points (Zakharenko, 2005[b]).

The presence of the non-dispersive ZTW9-waves shown by points in figure 5 significantly broadens the V_{ph}-range of existence of the first type of dispersive RTW9-waves. The velocities V_{ph} of the RTW9 first type start with the corresponding non-dispersive RTW3-waves for the substrates at $kh = 0$ and approach the corresponding non-dispersive RTW3-waves at $kh \to +\infty$. It is noted that for the same layered systems, according to the numerical

results of (Zakharenko, 2005[a]) concerning [100] direction, the first sub-mode of the lowest-order mode of the non-piezoelectric RTW6-waves at small values of kh lies out of the V_{ph}-range between the corresponding two non-dispersive RTW2-waves. The existence of the non-dispersive ZTW9-waves at small values of kh also occurs in several layered systems (Solie, 1971; Zhang *et al.*, 2001). It is noted that the piezoelectric effect can significantly change the behavior of $V_{ph}(kh)$. Therefore, the electric potential ϕ must be considered together with dispositions of both the bulk longitudinal and corresponding transverse waves for materials in order to predict the existence possibility of non-dispersive ZTW-waves in different layered systems. For instance, for the studied layered systems (see Table 1) there are the following velocities: $V_L(Bi_{12}SiO_{20}) > V_L(Bi_{12}GeO_{20})$ and $V_{ST}(Bi_{12}SiO_{20}) < V_{ST}(Bi_{12}GeO_{20})$.

It is noted that the lowest-order modes for the studied layered systems are confined in a very narrow V_{ph}-range being smaller than ~ 6 ms^{-1} that can be convenient for some technical devices (Shiosaki *et al.*, 1980). This can be compared with lowest-order modes of other suitable layered systems (Volyansky *et al.*, 1987; Solie, 1971; Zhang *et al.*, 2001) which are of interest for the same purpose. It is noted that experimental techniques are currently unknown by which it would be possible to make measurements of the V_{ph} with a precision at least 0.1 ms^{-1}. As of yet, the improved optical method for measurements of both the V_{ph} and V_g described in (Kolosovskii *et al.*, 1998) allows one to measure the V_{ph} with an accuracy ~ 2 m/s. It may be possible to develop experimental technique for measurement of the derivative dV_{ph}/dkh (and/or $dV_{ph}/d\omega h$) together with the V_{ph}, in order to improve the measurement accuracy for weakly dispersive waves and to experimentally measure the non-dispersive ZTW-waves. It is noted that calculation accuracy of the V_{ph} in this work is about 10^{-3} m/s.
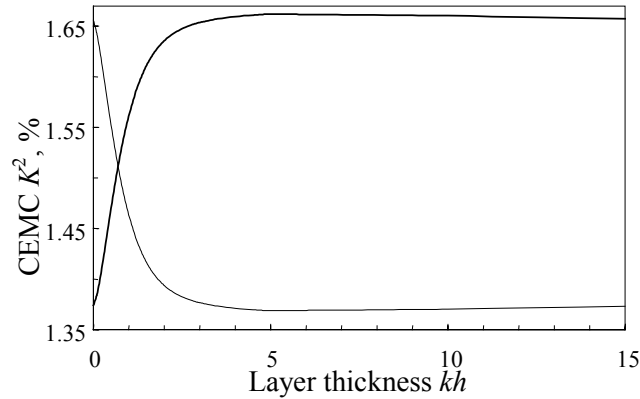
Fig. 6. The CEMCs K^2 (%) for the structures layer/substrate: $Bi_{12}SiO_{20}/Bi_{12}GeO_{20}$ (thick line) and $Bi_{12}GeO_{20}/Bi_{12}SiO_{20}$ (thin line).

The coefficient of the electromechanical coupling (CEMC) shown in figure 6 was calculated for the lowest-order modes of dispersive RTW9-waves with the following well-known formula:

$$K^2 = 2\frac{V_{Rf} - V_{Rm}}{V_{Rf}} \qquad (33)$$

where V_{Rf} and V_{Rm} are the RTW9 phase velocities for the free and metallized surfaces, respectively. The CEMC K^2 is shown in figure 6 for both studied layered systems. For the structure $Bi_{12}SiO_{20}/Bi_{12}GeO_{20}$, the CEMC K^2 starts with the K^2 for the $Bi_{12}GeO_{20}$ single crystal at $kh = 0$ and approaches the K^2 for the $Bi_{12}SiO_{20}$ single crystal at $kh \to \infty$. It is noted that in the kh-range between ~ 3.3 and ~ 50, the CEMC $K^2(Bi_{12}SiO_{20}/Bi_{12}GeO_{20})$ is slightly larger than the $K^2(Bi_{12}SiO_{20}) \sim 0.016558$ with a maximum value at $kh \sim 5$. On the other hand, for the structure $Bi_{12}GeO_{20}/Bi_{12}SiO_{20}$, the CEMC K^2 starts with the $K^2(Bi_{12}SiO_{20})$ at $kh = 0$ and approaches the $K^2(Bi_{12}GeO_{20})$ at $kh \to \infty$. It is also noted that in the same kh-range, the CEMC $K^2(Bi_{12}GeO_{20}/Bi_{12}SiO_{20})$ is slightly smaller than the $K^2(Bi_{12}GeO_{20}) \sim 0.013742$ with a minimum value at approximately the same $kh \sim 5$. Therefore, using a hard piezoelectric layer on a softer piezoelectric substrate can result in increasing the CEMC K^2. In addition to the first type of dispersive RTW9-waves representing a single lowest-order mode, modes of the second type of RTW9-waves can exist in layered systems. They can exist if the speed V_t for a substrate is higher than that for a layer. This existence condition is full-filled for the structure $Bi_{12}SiO_{20}/Bi_{12}GeO_{20}$, but not for the structure $Bi_{12}GeO_{20}/Bi_{12}SiO_{20}$. The velocities $V_{ph}(kh)$ for seven modes of the RTW9 second type are shown in figure 7a. It is clearly seen in the figure that the first mode starts at $kh_0 \sim 43.2$, but not at $kh_0 = 0$. It was found that each next mode starts at $kh_\mu \sim kh_0 + 73\mu$, where μ is an integer number, $\mu = 1, 2, 3, \ldots$. In addition, it was verified that the neighbour kh_μ are equidistant from each other on the kh-scale. Figure 7b shows the BCD9 behaviour in the V_{ph}-

range between the speeds V_t for the $Bi_{12}SiO_{20}$-layer and the $Bi_{12}GeO_{20}$-substrate for the RTW9 second type. It is clearly seen in figure 7b that the surface metallization does not change the V_{ph} that was verified at $kh = 500$ for the seven modes.

OTHER POSSIBILITIES FOR WAVE EXISTENCE

Ivanov and Kessenikh (1987) have assumed that in layered systems, consisting of a hard layer on a softer substrate both being the so-called transversely isotropic materials, Rayleigh-polarized dispersive waves such as slow surface waves can exist. These waves have a single mode starting with zero $V_{ph}(kh > 0)$ and approaching some non-dispersive velocity at $kh \to +\infty$ that they called Stoneley wave (SW). They have schematically shown that such slow surface mode could exist in the layered systems with $V_t^L > V_t^S > V_{R2}^S > V_{R2}^L > V_{St}$, where V_{St} represents the speed of the interfacial SW-wave, and V_t and V_{R2} are the speeds of the corresponding bulk transverse and surface RTW2 waves, respectively. However, it is thought that one of general features of a Stoneley wave is that it is faster than the slowest Rayleigh wave associated with the separated half-spaces (Destrade and Fu, 2006). Therefore, their representation of a dispersion branch originating from zero $V_{ph}(kh > 0)$ is a misconception. Hence, the problem on slow surface waves with the in-plane polarization is open concerning existence possibilities and specific conditions. The layered system $Bi_{12}GeO_{20}/Bi_{12}SiO_{20}$ studied in this paper possesses the following $V_t^L > V_t^S > V_{R3}^L > V_{R3}^S$, where V_{R3} is the surface RTW3-waves. Thus, STW-waves were not found in [110] direction. It is noted that such Rayleigh-polarized slow surface waves can be used for filter and sensor applications. For instance, there are Capacitive Micromachined Ultrasonic Transducers (CMUTs) of microelectromechanical system (MEMS) structures in integrated circuit (IC) technology (Yaralioglu *et al.*, 2001). Generally, the CMUTs are based on the Rayleigh-polarized Lamb waves (flexural plate mode) and could be also manufactured on the Love-wave polarized slow surface Zakharenko waves (SSZWs) recently introduced in (Zakharenko, 2005[b]).

Also, note that the other possibility of wave existence in addition to dispersive RTW-waves is the existence of non-dispersive Zakharenko type waves in different layered structures. However, the non-dispersive ZTW-waves were introduced as dispersive waves in all papers concerning investigations of dispersive waves. In addition, there are works in which there are attempts to represent results concerning dispersive waves with a very weak dependence $V_{ph}(kh)$ as non-dispersive waves, for example (Cherednik and Dvoesherstov, 2003; Dvoesherstov *et al.*, 2003). That is somewhat incorrect from the view point shown in this paper. It is noted that if one will draw phase velocities of dispersive electro-magnetic (EMW) and acoustic (AW) waves on the same

scale, one will find that the AWs become non-dispersive compared with the dispersive EM-waves, because the EM-waves are characterized by the V_{ph} being five orders higher than that of the AWs. It is also noted that the AW highest speed is ~ 20000 ms^{-1} for Diamond and some non-cubic crystals (Zakharenko, 2005[b]).

It was also assumed that there is an existence possibility to find Rayleigh-polarized supersonic surface waves in both monocrystals and layered systems. The V_{ph} of such supersonic surface waves will be higher than the speed V_t. The supersonic surface waves could exist in monocrystals with a great C^2 accounting possible effects: piezoelectric, piezomagnetic, etc. Some possible effects are shown in (Aboudi, 2000; Bednarcyk, 2002). The values of C^2 calculated in Section 3 for the studied monocrystals are not great. However, the coefficients A_0 and B_0 are relatively the same slightly above the corresponding speeds V_l up to 4000 m/s that is seen from figure 2b. The absolute values of the K_{Dl} and K_{Dt} are one order smaller than that of the A_0 and B_0 shown in figure 2a. It is noted that the coefficients A, B, and C in Eq. (5) should be all positive, in order to give two complex/imaginary roots plus one negative real root of the third order polynomial in (4) for surface waves. However, for surface waves, it is possible to have such the polynomial roots for Abs(A) ~ Abs(B) ~ Abs(C) with the coefficient A or B being negative. It is difficult to find such crystals because the K_{Dt} is negative for $V_{ph} > V_t$ giving negative B. Therefore, a computer program is given in the Appendix. Indeed, it is possible to treat crystals accounting other suitable effects in addition to piezoelectric/piezomagnetic effect. For instance, if the A, B, and C in Eq. (5) give the following polynomial $P_3 = x^3 + 0.5x^2 - 0.1x + 0.01$, the corresponding two complex and one negative real root solving the equation $P_3 = 0$ will be as follows: {$- 0.6712$; $0.0856 - I0.0870$; $0.0856 + I0.0870$}. That results in appearance of four complex and two imaginary roots for the sixth order polynomial in Eq. (4) with $m = n_3^2$, three of which with negative imaginary part are suitable for

surface wave existence: {$- I0.8193$; $0.3222 - I0.1350$; $- 0.3222 - I0.1350$} with $I = (- 1)^{1/2}$. Indeed, such situation is possible showing instability of some piezoelectric (piezomagnetic, etc.) crystals about the velocity V_l. That can happen in a very narrow V_{ph}-range with a very small C in Eq. (4). For example, the following polynomial $P_3 = x^3 + x^2 - 0.01x + 0.0001$ has its roots solving equation $P_3 = 0$: {$- 1.009999$; $0.0045 - I0.0086$; $0.0045 + I0.0086$}. That gives the following suitable roots of the sixth order polynomial {$- I1.0050$; $0.0865 - I0.0498$; $- 0.0865 - I0.0498$} for SAW existence.

Finally, it is noted that modes of dispersive leaky Sezawa type waves with the in-plane polarization can exist for $V_{ph} > V_t$ looking like corresponding continuations of the modes of dispersive RTW9 second type shown in figure 7a. Solutions for such ultrasonic leaky waves were not found with $V_{ph} > V_t$ by evaluating the BCD9 sign running up to the speed V_l, at which the complex BCD9 becomes zero. Probably, they are found above the speed V_t when minima of Abs (BCD9) are treated instead of monitoring changes in sign of the corresponding BCD9 part, because it is thought that the latter is preferable for finding SAWs.

PURE RTW9-WAVES IN 20^0-x_2-ROTATED DIRECTION

This Section studies pure RTW9-wave propagation in layered systems, consisting of cubic crystals $Bi_{12}SiO_{20}$ and $Bi_{12}GeO_{20}$ accounting the piezoelectric effect. The waves propagate in the so-called work coordinate system obtained from [110] direction by 20^0-rotation around the x_2-axis in figure 1 for both materials. In this propagation direction there are the following non-zero material constants: the elastic constants C_{11}, C_{33}, C_{13}, C_{55}, C_{15} with negative C_{35}, the piezoelectric constants e_{13}, e_{31}, e_{33}, e_{15}, e_{35} with negative e_{11}. They correspond to the complicated case of monoclinic crystals. The dielectric constants do not changed, $\varepsilon_{11} = \varepsilon_{33}$ with $\varepsilon_{13} = 0$. Therefore, the theory developed in the second and third Sections is not suitable
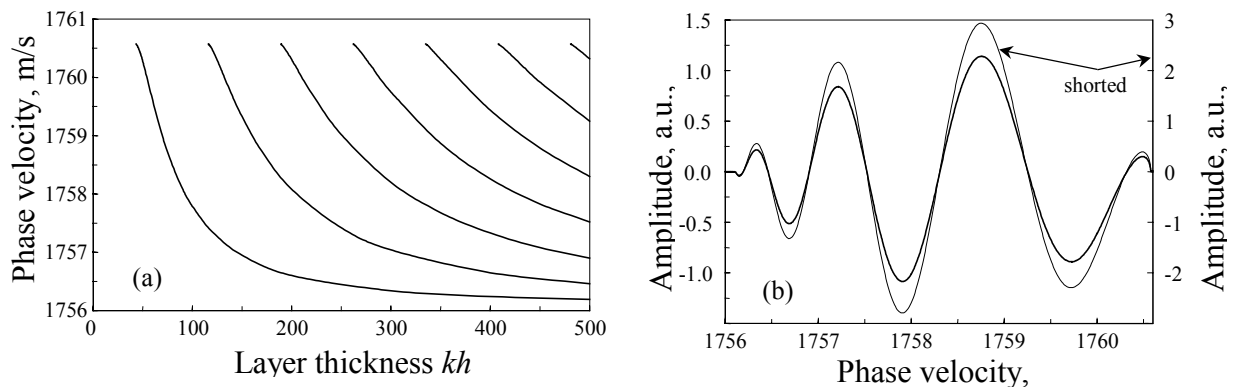

Fig. 7. For the structure $Bi_{12}SiO_{20}/Bi_{12}GeO_{20}$: (a) the seven modes of dispersive RTW9 second type; and (b) the corresponding BCD9 behavior at the layer thickness $kh = 500$ for the free (thick line) and metallized (thin line) surfaces.

here and there is only numerical analysis as a studying instrument. Figure 8a shows existence of the RTW9 first type for two different electrical boundary conditions: the free and metallized surface. The boundary conditions allow evaluation of the CEMC K^2 (%) shown in Figure 8b. It is clearly seen in the Figure that the CEMC is not larger than 1.5% for both studied structures: $Bi_{12}SiO_{20}/Bi_{12}GeO_{20}$ and the reverse configuration. Indeed, the CEMC starts at its value for the corresponding substrate at $kh \to 0$ and approaches its value for the corresponding layer at $kh \to \infty$ in the both cases. It is clearly seen in figure 8a that the first type of dispersive RTW9-waves possesses one non-dispersive Zakharenko type wave (ZTW9) at $kh \sim 1.39$ to 1.40 for the free surface and two for the metallized surface at $kh \sim 0.13$ to 0.15 and at $kh \sim 1.15$ to 1.18. The insertion in Figure 8b shows the first non-dispersive ZTW9-wave at small kh for the shorted case.

The dispersion relations for the structures $Bi_{12}SiO_{20}/Bi_{12}GeO_{20}$ and $Bi_{12}GeO_{20}/Bi_{12}SiO_{20}$ look like mirror reflections of each other. However, that is not completely true for both electrical boundary conditions. For instance, there is kh-position of the non-dispersive ZTW9-wave at $kh \sim 1.39$ for the structure $Bi_{12}SiO_{20}/Bi_{12}GeO_{20}$ and at $kh \sim 1.40$ for the structure $Bi_{12}GeO_{20}/Bi_{12}SiO_{20}$ that shows small asymmetry of the systems. A small asymmetry there is also for the shorted case. It is noted that calculation accuracy for finding the V_{ph} was possible to set at 1μm/sec. However, it is thought that it is necessary to take a trustable V_{ph}-accuracy about 1mm/sec. Therefore, it is possible to trust that the presence of the non-dispersive ZTW9-wave in both structures at small $kh \sim 0.13$ to 0.15 shown in the insertion is true. It is obvious that the existence of the non-dispersive ZTW9-waves at the small kh for the shorted case is caused by only piezoelectric properties, because they do not exist when the surface is free of metallization. On the other hand, the presence of the non-dispersive ZTW9-waves at larger $kh \sim 1.0$ to 1.5 for both the cases is caused by both the elastic and piezoelectric material

properties. It is thought that here the elastic properties play a major role. "Shortage" of the free surface results in significant change in the kh-position of the corresponding non-dispersive ZTW9-wave, namely there is a shift to smaller values of kh showing the piezoelectricity influence. Also, it is obvious that the presence of the non-dispersive ZTW9-waves broadens the V_{ph}-existence range of the dispersive RTW9-waves. Indeed, the V_{ph}-range for the RTW9-waves' localization is about three times greater than the initially given V_{ph}-difference of $V_{RTW3}(Bi_{12}GeO_{20})$ = 1734.674 m/s from $V_{RTW3}(Bi_{12}SiO_{20})$ = 1733.631 m/s (see the third column in Table 3). The RTW3 phase velocities with the metallized surface are as follows: $V_{RTW3m}(Bi_{12}GeO_{20})$ = 1723.997 m/s and $V_{RTW3m}(Bi_{12}SiO_{20})$ = 1720.775 m/s.

According to table 3, the RTW9 second type could exist in the layered system, consisting of the $Bi_{12}GeO_{20}$-layer on the $Bi_{12}SiO_{20}$-substrate, because for the slow transverse waves there is $V_{ST}(Bi_{12}SiO_{20}) > V_{ST}(Bi_{12}GeO_{20})$ representing the condition for the wave existence. The condition is true studying wave propagation in isotropic media as well as in many suitable propagation directions in anisotropic and piezoelectric materials. However, the existence of RTW9 second type does not obey the condition in the propagation direction studied in this Section. The waves exist in the reverse configuration, because it is necessary to treat the so-called velocity equivalent V_{ph0} listed in the last column of table 3. The velocity V_{ph0} corresponds to the case when imaginary part of one root with the smallest imaginary part disappears. That occurs for $V_{ph0}(Bi_{12}GeO_{20})$ = 1829.135307 m/s giving $m_3 = 0.217658 - I5.65406E{-}06$ and $V_{ph0}(Bi_{12}SiO_{20})$ = 1825.255744 m/s with $m_3 = 0.220269 - I1.81874E{-}05$, where $I = (-1)^{1/2}$. Therefore, the existence condition of the RTW9 second type is $V_{ph0}(Bi_{12}GeO_{20}) > V_{ph0}(Bi_{12}SiO_{20})$ instead of $V_{ST}(Bi_{12}SiO_{20}) > V_{ST}(Bi_{12}GeO_{20})$. That is an additional difficulty for finding the RTW9 second type. Several modes of the dispersive RTW9 second type are shown in figure 9 within relatively great kh-range: $0 < kh < 500$. The first mode begins at
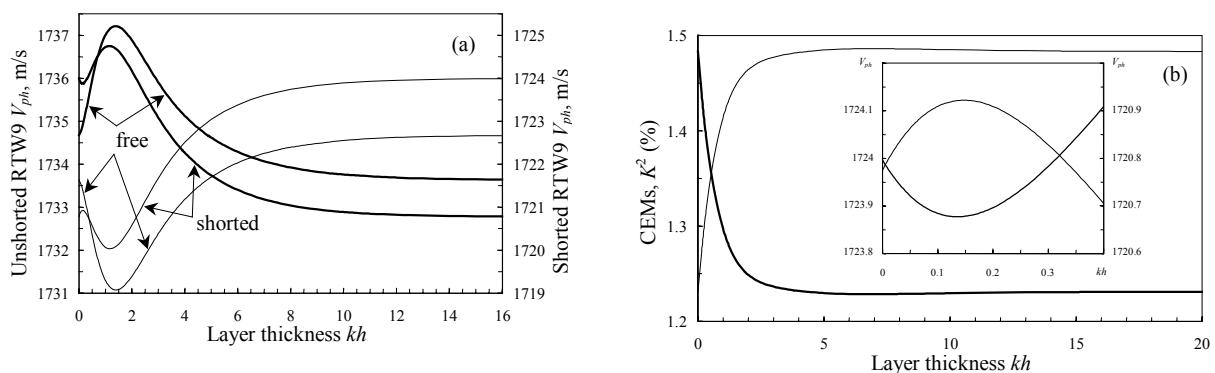

Fig. 8. (a) The dependence $V_{ph}(kh)$ for the RTW9 first type: the thick lines are for the structure $Bi_{12}SiO_{20}/Bi_{12}GeO_{20}$ and the thin lines are for the structure $Bi_{12}GeO_{20}/Bi_{12}SiO_{20}$; (b) the coefficient K^2 (%) with the insertion showing $V_{ph}(kh)$ at small kh.
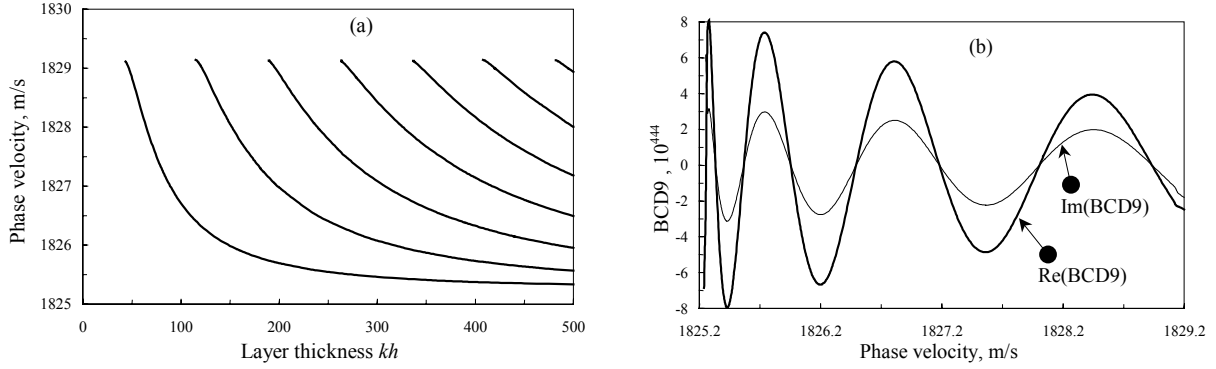
Fig. 9. (a) Several modes of the RTW9 second type for the structure $Bi_{12}SiO_{20}/Bi_{12}GeO_{20}$; (b) the corresponding complex BCD9 for the layer thickness $kh = 500$.

quite great values of $kh \sim 43.5$. Each next mode beginning looks like to be equidistant from the previous with the kh-step ~ 72 to 74. Figure 9b shows the sinusoidal behavior of both the real and imaginary parts of the complex BCD9.

It was found that both the boundary condition determinants BCD3 and BCD9 do not equal to zero at the corresponding bulk wave speeds V_{ST} listed in table 3. At the speed V_{ST} there is the following: one corresponding positive real root in addition to two complex roots with negative imaginary part changes its sign. It is noted that the velocity V_{ph0} is a common feature that appears not only studying pure RTW9-waves, but also studying pure Love type waves (LTWs) with the anisotropy factor $\alpha_f = (C_{44}C_{66} - C_{46}{}^2)^{1/2}/C_{44}$ (Lardat $et\ al.$, 1971; Zakharenko, 2005[b]). The LTW velocity equivalent β should be lower than the speed V_{FT} of the corresponding shear (fast transverse) bulk wave, $V_{FT} = \left(C_{66}/\rho\right)^{1/2}$, due to the condition $C_{66}C_{44} > C_{46}{}^2$ requiring for energy conservation (Lardat $et\ al.$, 1971). That may also be true for RTW9-waves giving $V_{ph0} < V_{ST}$. Here there is $C_{46} \neq 0$ for the 20^0-x_2-rotation from [110] direction. It is noted that there are the following waves: $V_{FT}(Bi_{12}SiO_{20}) = 2274.364$ m/s and $V_{FT}(Bi_{12}GeO_{20}) = 2255.092$ m/s giving higher V_{ph} of Love type waves compared with V_{ST} listed in Table 3 for RTW3-waves. The studied propagation direction is one of possible cuts using the x_2-rotation from $\sim 19^0$ up to $\sim 30^0$ with the condition $V^L_{ST} > V^S_{ST} > V^S_{RTW3} > V^L_{RTW3}$.

Solutions above the speed V_{ST} were also found. It was found that the complex BCD3 equals to zero at $V_{ph1} \sim 1963.492$ m/s studying wave existence in the monocrystal of $Bi_{12}GeO_{20}$. That happens when the negative real root of three roots $\{m_3{}^{(1)} = -0.644149 - I1.11408;\ m_3{}^{(2)} = 0.09105 - I0.818141;\ m_3{}^{(3)} = -0.0490123\}$ gives all zero components $(U_1{}^{(3)}, U_3{}^{(3)}, \phi^{(3)})$. It is noted that the zero components give the following weight factors $\{F^{(1)};\ F^{(2)};\ F^{(3)}\} = \{0;\ 0;\ F^{(3)}\}$ or $\{0;\ 0;\ 0\}$ in the complete characteristics

$$U_{1,3,4} = \sum_{N=1,2,3} F^{(N)} U_{1,3,4}^{(N)} \exp\left[jk\left(m_1 x_1 + m_3^{(N)} x_3 - \omega t\right)\right] \text{ with}$$

$U_4^{(N)} = \phi^{(N)}$ manifesting that such waves cannot exist. However, if suitable weight factors $\{F^{(1)};\ F^{(2)};\ 0\}$ will be found that is an additional investigation problem, it is possible to study two-partial waves instead of three-partial waves concerning wave propagation in monocrystals. As soon as the BCD3 equals to zero at V_{ph1}, the complex BCD9 for structures using any layer on the substrate, as well as all corresponding higher-order BCDs studying multi-layered structures, will be zero at the same V_{ph1} due to the zero components $(U_1{}^{(3)}, U_3{}^{(3)}, \phi^{(3)})$ for the substrate. The same there is for $Bi_{12}SiO_{20}$ and layered structures with the substrate of $Bi_{12}SiO_{20}$, where all zero components $(U_1{}^{(3)}, U_3{}^{(3)}, \phi^{(3)})$ are for the roots $\{m_3{}^{(1)} = -0.700865 - I1.13238;\ m_3{}^{(2)} = 0.105407 - I0.800113;\ m_3{}^{(3)} = -0.048674\}$ at $V_{ph1} \sim 1965.258$ m/s. It is noted that the speeds V_L of the longitudinal bulk wave for the 20^0-x_2-rotated direction are as follows: $V_L(Bi_{12}SiO_{20}) = 3359.358$ m/s and $V_L(Bi_{12}GeO_{20}) = 3337.419$ m/s. However, the second pair of complex roots disappears at a velocity equivalent V_{ph2}, which is lower than the speed V_L. For example, there is $V_{ph2}(Bi_{12}SiO_{20}) \sim 3355.468$ m/s. Probably, such the situation when the speeds V_{ST} and V_L do not coincide with the corresponding velocity equivalents V_{ph0} and V_{ph2} is common.

CONCLUSIONS

In this theoretical work, the possible existence of supersonic surface waves with the Rayleigh-wave polarization is shown. For these waves, the phase velocity V_{ph} could be found about the speed V_l depending on both the crystal anisotropy and the piezoelectric/piezomagnetic effect. The computer program is given in the Appendix, which can be used for finding the supersonic waves in addition to the RTW3 and RTW9-waves. Note that many crystals can possess both effects, according to Al'shits and Lyubimov (1990), as well as the other effects, see (Aboudi, 2000; Bednarcyk, 2002). That can significantly complicate calculations in numerical experiments. Also, both the longitudinal dynamic CEMC $K_{Dl}(V_l)$ and the

transverse dynamic CEMC $K_{Dt}(V_{t5})$ were introduced and discussed. Possible existence of slow surface waves with the Rayleigh-wave polarization was also discussed. The introduced calculations of the RTW9 lowest-order mode in the layered system, consisting of the materials $Bi_{12}SiO_{20}$ and $Bi_{12}GeO_{20}$, have shown the existence of the non-dispersive Zakharenko type waves (ZTW9) in the studied layered systems with both the free surface and surface metallization. It was found that the surface metallization can significantly shift the appearance of the non-dispersive ZTW9-waves to smaller values of kh. It was also found that at $kh \sim 5 - 6$ the CEMC K^2 for the structure $Bi_{12}GeO_{20}/Bi_{12}SiO_{20}$ is slightly larger than that for the $Bi_{12}GeO_{20}$ single crystal. The non-dispersive ZTW9-waves divide the RTW9 lowest-order mode into sub-modes with different dispersions, $V_{ph} > V_g$ or $V_{ph} < V_g$. This lowest-order mode of dispersive RTW9-waves is confined in the narrow V_{ph}-range between the non-dispersive RTW3-wave for the $Bi_{12}SiO_{20}$-layer and the wave for the $Bi_{12}GeO_{20}$-substrate. That can be convenient for some technical devices, for which a weak dependence of the V_{ph} on the layer thickness kh is required. For comparison, the 20^0-x_2-rotated propagation direction from [110] direction was also studied concerning the pure RTW9-waves. Here, it was found that existence of RTW9 second type does not depend on the speeds V_t of the corresponding bulk transverse waves in both materials.

ACKNOWLEDGEMENTS

Appendix. The Maple program for finding the phase velocity of the RTW3 and RTW9-waves:

```
restart: with(linalg): ms:=array(1..3,1..3):
ms1:=array(1..3,1..3): u1s:=array(1..6): u3s:=array(1..6):
u4s:=array(1..6): m3s:=array(1..6): c33s:=12.962:
c13s:=2.985: c55s:=2.451: c11s:=c55s+(c13s+c33s)/2:
c66s:=4.9885: ros:=9.07: es:=1.122: dps:=3.63735:
dp0:=0.08854: fdz:=fopen("RTW9_1.txt",WRITE):
c2s:=(c11s*c33s-c55s*(c11s+c33s)+c55s^2-
(c13s+c55s)^2)/(c33s*c55s); k0s:=es*es/(c55s*dps):
Vt5s:=1000*sqrt(10*c55s/ros);
Vt6s:=1000*sqrt(10*c66s/ros);
Vls:=1000*sqrt(10*c11s/ros);
Vts_new:=Vt5s*sqrt(1+k0s); mg:=array(1..3,1..3):
mg1:=array(1..3,1..3): u1g:=array(1..6): u3g:=array(1..6):
u4g:=array(1..6): m3g:=array(1..6): c33g:=12.852:
c13g:=2.934: c55g:=2.562: c11g:=c55g+(c13g+c33g)/2:
dp0:=0.08854: c2g:=(c11g*c33g-
c55g*(c11g+c33g)+c55g^2-
(c13g+c55g)^2)/(c33g*c55g); rog:=9.2: dpg:=3.336:
eg:=0.983: k0g:=eg*eg/(c55g*dpg):
Vt5g:=1000*sqrt(10*c55g/rog);
Vlg:=1000*sqrt(10*c11g/rog);
Vtg_new:=Vt5g*sqrt(1+k0g); st66:=array(1..6,1..6);
rw9:=array(1..9,1..9): for kh from 0 by 0.1 to 10 do
Drw9:=0: for i from 1675 by 0.1 to 1685 do  Vph:=i:
At2s:=1-(Vph/Vt5s)^2: Al2s:=1-(Vph/Vls)^2:
B0s:=(c11s/c33s)*At2s*Al2s:
A0s:=(c11s/c33s)*Al2s+At2s+c2s:
kdts:=k0s*(4*c55s*At2s-4*c13s-3*c55s)/c33s:
kdls:=k0s*c11s*Al2s/c33s: As:=A0s+1+4*k0s:
Bs:=A0s+B0s+kdts: Cs:=B0s+kdls:
Pls:=ns^3+As*ns^2+Bs*ns+Cs: sols:=[solve(Pls,ns)]:
At2g:=1-(Vph/Vt5g)^2: Al2g:=1-(Vph/Vlg)^2:
B0g:=(c11g/c33g)*At2g*Al2g;
A0g:=(c11g/c33g)*Al2g+At2g+c2g;
kdtg:=k0g*(4*c55g*At2g-4*c13g-3*c55g)/c33g;
kdlg:=k0g*c11g*Al2g/c33g; Ag:=A0g+1+4*k0g;
Bg:=A0g+B0g+kdtg: Cg:=B0g+kdlg:
Plg:=ng^3+Ag*ng^2+Bg*ng+Cg: solg:=[solve(Plg,ng)]:
for j from 1 by 1 to 3 do  m3s[j]:=-sqrt(sols[j]): m3g[j]:=-
sqrt(solg[j]): m3s[3+j]:=sqrt(sols[j]):
m3g[3+j]:=sqrt(solg[j]):  u1s[j]:=-
(es^2/dps)*(1/(1+m3s[j]^2))-(c33s*m3s[j]^2+c55s*At2s):
u3s[j]:=(c13s+c55s)*m3s[j]+(2*es^2/dps)*(m3s[j]/(1+m3
s[j]^2)):
u4s[j]:=(2*es/dps)*(m3s[j]/(1+m3s[j]^2))*u1s[j]+(es/dps)
*(1/(1+m3s[j]^2))*u3s[j]:
u1s[3+j]:=-(es^2/dps)*(1/(1+m3s[3+j]^2))-
(c33s*m3s[3+j]^2+c55s*At2s):
u3s[3+j]:=(c13s+c55s)*m3s[3+j]+(2*es^2/dps)*(m3s[3+j
]/(1+m3s[3+j]^2)):
u4s[3+j]:=(2*es/dps)*(m3s[3+j]/(1+m3s[3+j]^2))*u1s[3+
j]+(es/dps)*(1/(1+m3s[3+j]^2))*u3s[3+j]:
u1g[j]:=-(eg^2/dpg)*(1/(1+m3g[j]^2))-
(c33g*m3g[j]^2+c55g*At2g):
u3g[j]:=(c13g+c55g)*m3g[j]+(2*eg^2/dpg)*(m3g[j]/(1+
m3g[j]^2)):
u4g[j]:=(2*eg/dpg)*(m3g[j]/(1+m3g[j]^2))*u1g[j]+(eg/dp
g)*(1/(1+m3g[j]^2))*u3g[j]:
u1g[3+j]:=-(eg^2/dpg)*(1/(1+m3g[3+j]^2))-
(c33g*m3g[3+j]^2+c55g*At2g):
u3g[3+j]:=(c13g+c55g)*m3g[3+j]+(2*eg^2/dpg)*(m3g[3
+j]/(1+m3g[3+j]^2)):
u4g[3+j]:=(2*eg/dpg)*(m3g[3+j]/(1+m3g[3+j]^2))*u1g[3
+j]+(eg/dpg)*(1/(1+m3g[3+j]^2))*u3g[3+j]:
ms[1,j]:=c55s*(m3s[j]*u1s[j]+u3s[j])+es*u4s[j]:
ms[2,j]:=c13s*u1s[j]+m3s[j]*c33s*u3s[j]:
ms[3,j]:=es*u1s[j]-(dps*m3s[j]-dp0*I)*u4s[j]:
ms1[1,j]:=c55s*(m3s[3+j]*u1s[3+j]+u3s[3+j])+es*u4s[3
+j]:
ms1[2,j]:=c13s*u1s[3+j]+m3s[3+j]*c33s*u3s[3+j]:ms1[3
,j]:=es*u1s[3+j]-(dps*m3s[3+j]-dp0*I)*u4s[3+j]:
mg[1,j]:=c55g*(m3g[j]*u1g[j]+u3g[j])+eg*u4g[j]:
mg[2,j]:=c13g*u1g[j]+m3g[j]*c33g*u3g[j]:
mg[3,j]:=eg*u1g[j]-(dpg*m3g[j]-dp0*I)*u4g[j]:
mg1[1,j]:=c55g*(m3g[3+j]*u1g[3+j]+u3g[3+j])+eg*u4g[
3+j]:
mg1[2,j]:=c13g*u1g[3+j]+m3g[3+j]*c33g*u3g[3+j]:mg1
[3,j]:=eg*u1g[3+j]-(dpg*m3g[3+j]-dp0*I)*u4g[3+j]:
```

rw9[1,j]:=u1s[j]: rw9[1,3+j]:=-u1g[j]: rw9[1,6+j]:=-u1g[3+j]: rw9[2,j]:=u3s[j]: rw9[2,3+j]:=-u3g[j]: rw9[2,6+j]:=-u3g[3+j]: rw9[3,j]:=u4s[j]: rw9[3,3+j]:=-u4g[j]: rw9[3,6+j]:=-u4g[3+j]: rw9[4,j]:=ms[1,j]: rw9[4,3+j]:=-mg[1,j]: rw9[4,6+j]:=-mg1[1,j]: rw9[5,j]:=ms[2,j]: rw9[5,3+j]:=-mg[2,j]: rw9[5,6+j]:=-mg1[2,j]: rw9[6,j]:=ms[3,j]-dp0*I*u4s[j]: rw9[6,3+j]:=-(mg[3,j]-dp0*I*u4g[j]): rw9[6,6+j]:=-(mg1[3,j]-dp0*I*u4g[3+j]): rw9[7,j]:=0: rw9[8,j]:=0: rw9[9,j]:=0: rw9[7,3+j]:=mg[1,j]*exp(I*kh*m3g[j]): rw9[7,6+j]:=mg1[1,j]*exp(I*kh*m3g[3+j]): rw9[8,3+j]:=mg[2,j]*exp(I*kh*m3g[j]): rw9[8,6+j]:=mg1[2,j]*exp(I*kh*m3g[3+j]): rw9[9,3+j]:=mg[3,j]*exp(I*kh*m3g[j]): rw9[9,6+j]:=mg1[3,j]*exp(I*kh*m3g[3+j]): end do:
Ds:=det(ms): Dg:=det(mg):
ADs:=sqrt(Re(Ds)^2+Im(Ds)^2):
ADg:=sqrt(Re(Dg)^2+Im(Dg)^2): Drw91:=Drw9: Drw9:=det(rw9):
ADrw9:=sqrt(Re(Drw9)^2+Im(Drw9)^2):
if (Drw9*Drw91<0) then fprintf(fdz,"kh %g Vph %g Re(Ds) %g Im(Ds) %g ADs %g Re(Dg) %g Im(Dg) %g ADg %g Re(Drw9) %g Im(Drw9) %g ADrw9 %g",kh,Vph,Re(Ds),Im(Ds),ADs,Re(Dg),Im(Dg),ADg, Re(Drw9),Im(Drw9),ADrw9): end if: end do: end do: fclose(fdz):

REFERENCES

Aboudi, J. 2000. Micromechanical Prediction of the Effective Behavior of Fully Coupled Electro-Magneto-Thermo-Elastic Multiphase Composites. NASA/CR–2000-209787.

Aleksandrov, KS., Bondarenko, VS., Zaitzeva, MP., Sorokin, BP., Kokorin, YI., Zrazhevsky, VM. and Sobolev, BV. 1984. Nonlinear mechanical properties of sillenite type crystals. Soviet Journal of Solid State Physics (Physics of the Solid State, Moscow) 26:3603-3610, in Russian.

Alexe, M. and Goesele, U. 2003. Wafer Bonding, Springer, Berlin, Germany.

Al'shits, VI. and Lyubimov, VN. 1990. On existence of piezoelectric and piezomagnetic properties of anisotropic media. Soviet Krystallography (Moscow). 35(2):483-484, in Russian.

Anisimkin, IV. 2004. A type of acoustic modes of vibration of thin piezoelectric plates: quasi-longitudinal normal modes. Acoustical Physics Reports (Moscow). 50(4):442-447.

Bednarcyk, BA. 2002. A Fully Coupled Micro/Macro Theory for Thermo-Electro-Magneto-Elasto-Plastic Composite Laminates. NASA/CR–2002-211468, available electronically at http://gltrs.grc.nasa.gov/GLTRS.

Bleustein, JL. 1968. A new surface wave in piezoelectric materials. Applied Physics Letters. 13:412-413.

Blistanov, AA., Bondarenko, VS., Perelomova, NV., Strizhevskaya, FN., Chkalova, VV. and Shaskol'skaya, MP. 1982. Acoustical Crystals. Eds. Shaskol'skaya, MP. Nauka, Moscow, pp. 632, in Russian.

Bondarenko, VS., Zykov, AM., Polushkin, AN., Sergeev, AP., Sergeeva, GV. and Chkalova, VV. 1983. Application of layered system on fused-quartz for SAW delay lines. Materialy of Soviet Conference on Acoustoelectronics and Quantum Acoustics. Nauka, Saratov. 2:211-214, in Russian.

Bronstein, IN. and Semendyaev, KA. 2000. The reference-book on Mathematics for engineers and higher school students. Science, Moscow. pp.608, in Russian.

Cherednik, VI. and Dvoesherstov, MYU. 2003. Numerical calculation of surface and pseudo-surface acoustical wave features in multi-layered structures. Russian Journal of Technical Physics (Moscow). 73(10):106-112, in Russian.

Destrade, M. and Fu, YB. 2006. The speed of interfacial waves polarized in a symmetry plane. International Journal of Engineering Science 44:26-36.

Dieulesaint, E. and Royer, D. 1980. Elastic waves in solids: applications to signal processing, translated by Bastin, A. and M. Motz, Chichester [English]. J. Wiley, New York. pp511.

Dvoesherstov, MYU., Cherednik, VI., Chirimanov, AP. and Petrov, SG. 2003. Parameter optimization of surface acoustic waves by the way of multi-layered structures' usage. Russian Journal of Technical Physics (Moscow) 73(10):101-105, in Russian.

Farnell, GW. 1978. Types and properties of surface acoustical waves, in Acoustic Surface Waves. Topics in Applied Physics, Eds. Oliner, AA. Springer Verlag, Berlin-Heidelberg-New York. 24:26-96.

Farnell, GW. and Adler, EL. 1972. Elastic wave propagation in thin layers. in Physical Acoustics: Principles and Methods. Eds. Mason, WP. and Thurston, RN. Academic Press, New York. 9:35-127.

Goesele, U. and Tong, QY. 1998. Semiconductor wafer bonding. Annual Review of Material Science 28:215-241.

Gulyaev, YUV. 1969. Electroacoustical surface waves in solids. Soviet Physics Journal of Experimental and Theoretical Physics Letters (Moscow). 9:37-38.

Henaff, J., Feldmann, M. and Kirov, MA. 1982. Piezoelectric crystals for surface acoustic waves (Quartz, $LiNbO_3$, $LiTaO_3$, Tl_3VS_4, Tl_3TaSe_4, $AlPO_4$, GaAs). Ferroelectrics. 42:161-185.

Ingebrigtsen, KA. 1969. Surface waves in piezoelectrics. Journal of Applied Physics. 40(7):2681-2686.

Ivanov, LD. and Kessenikh, GG. 1987. Rayleigh surface wave in a transversally-isotropic substrate with rigid transversally-isotropic layer. Soviet Acoustical Journal (Moscow). 33(4):665-669, in Russian.

Jungnickel, F., Chillay, E., Makarov, S. and Froehlich, HJ. 1997. Coupling coefficient, temperature stability, and mass sensitivity of the Rayleigh-type mode on (001) [110] AlAs/GaAs. Smart Materials and Structures. 6:721-729.

Kolosovskii, EA., Tsarev, AV. and Yakovkin, IB. 1998. Improved procedure for measuring SAW velocity in anisotropic structures. Acoustical Physics Reports (Moscow). 44:793-800, in Russian.

Landolt-Boernstein International Tables. 1985. Elastic, piezoelectric, pyroelectric, piezooptic, electrooptic constants and non-linear dielectric susceptibilities of crystals, New Series, Group III, Vol. 18, Springer Verlag, Berlin–Heidelberg–New York–Tokyo. pp179.

Lardat, C., Maerfeld, C. and Tournois, P. 1971. Theory and performance of acoustical dispersive surface wave delay lines. Proceedings of the IEEE. 59(3):355-368.

Liu, H., Kuang, ZB. and Cai, ZM. 2003. Propagation of Bleustein-Gulyaev waves in a prestressed layered piezoelectric structure. Ultrasonics. 41:397-405.

Love, AEH. 1911. Some problems of Geodynamics, Cambridge University Press, London, England, UK.

Lyamov, VE. 1983. Polarization effects and interaction anisotropy of acoustic waves in crystals, MSU Publishing, Moscow. pp224, in Russian.

Nakamura, K. and Hanaoka, T. 1993. Propagation characteristics of surface acoustic waves in ZnO/LiNbO$_3$ structures. Japanese Journal of Applied Physics 32(5B-1): 2333-2336.

Nayfeh, AH. 1991. The general problem of elastic wave propagation in multilayered anisotropic media. Journal of Acoustical Society of America. 89:1521-1531.

Parygin, VN., Vershoubskiy, AV., Mozaev, VG. and Weinacht, M. 2000. Prolonged acousto-optic interaction with Lamb waves in crystalline plates. Ultrasonics 38: 594-597.

Pohanka, RC. and Smith, PL. 1988. Recent advances in piezoelectric ceramics. Electronic Ceramics. Eds. Levinson, LM. Marcel Dekker, New York, USA.

Rayleigh, Lord (J.W. Strutt), 1885. On waves propagated along the plane surfaces of an elastic solid. Proceedings of the London Mathematical Society. 17:4-11.

Schmidt, RV. and Voltmer, FW. 1969. Piezoelectric elastic surface waves in anisotropic layered media. IEEE Transactions on Microwave Theory and Techniques MTT. 17: 920-926.

Shiosaki, T., Yamamoto, T., Oda, T., Harada, K. and Kawabata, A. 1980. Low temperature growth of piezoelectric AlN film for surface and bulk wave transducers by RF reactive planar magnetron sputtering. in Proceedings of the IEEE Ultrasonics Symposium. 451-455.

Solie, LP. 1971. Piezoelectric acoustic surface waves for a film on a substrate. Applied Physics Letters. 18:111-112.

Solie, LP. and Auld, BA. 1973. Elastic waves in free anisotropic plates. Journal of Acoustical Society of America. 54(1):50-63.

Stoneley, R. 1955. The propagation of surface elastic waves in a cubic crystal. Proceedings of the Royal Society of London. A232:447-458.

Tsubouchi, K. and Mikoshiba, N. 1985. Zero-temperature-coefficient SAW devices on AlN epitaxial films. IEEE Transactions on Sonics and Ultrasonics SU. 32(5):634-644.

Tursunov, DA. 1967. Common surface waves in cubic crystals. Soviet Acoustical Journal (Moscow). 13:100-105, in Russian.

Volyansky, VF., Ivanov, LD., Kessenikh, GG. and Mogilevsky, ISH. 1987. Rayleigh surface wave in fused quartz substrate with AlN layer. Soviet Acoustical Journal (Moscow). 33(3):424-427, in Russian.

Yaralioglu, GG., Badi, MH., Ergun, AS., Cheng, CH., Khuri-Yakub, BT. and Degertekin, FL. 2001. Lamb wave devices using capacitive micromachined ultrasonic transducers. Applied Physics Letters. 78(1):111-113.

Zakharenko, AA. 2005[a]. Dispersive Rayleigh type waves in layered systems consisting of piezoelectric crystals bismuth silicate and bismuth germanate. Acta Acustica united with Acustica. 91(4):708-715.

Zakharenko, AA. 2005[b]. Analytical studying the group velocity of three-partial Love (type) waves in both isotropic and anisotropic media. Non-destructive Testing and Evaluation. 20(4):237-254.

Zakharenko, AA. 2006. On cubic crystal anisotropy for waves with Rayleigh-wave polarization. Non-destructive Testing and Evaluation. 21(2):1-17.

Zhang, B. and Lu, L. 2003. Rayleigh wave and detection of low-velocity layers in a stratified half-space. Russian Acoustical Journal (Moscow). 49(5):613-625, in Russian.

Zhang, VY., Lefebvre, JE. and Gryba, T. 2001. SAW characteristics in a layered ZnO/GaAs structure for design of integrated SAW filters. in Proceedings of the IEEE Ultrasonic Symposium, Atlanta, GA, USA, October. 1: 261-264.

A JAVA TCP SERVER LOAD BALANCER:
ANALYSIS AND COMPARISON OF ITS LOAD BALANCING ALGORITHMS

*Majdi Al-qdah[1] and Mohd Khir Bin Abu Yan[2]
[1]Faculty of Computer Science, University of New Brunswick, Canada
[2]Faculty of Information Technology, Multimedia University, Malaysia

ABSTRACT

In this study, a TCP server load balancer (SLB) programmed in Java is proposed as an affordable alternative to commercial or open source server load balancers for small companies by having all basic server load balancer features in order to maximize the usage of small companies financial, human and hardware resources. The features include load balancing algorithms namely Round Robin, Random, Least Connection and Hash IP Address. The Java TCP Server Load Balancer employs Rules which consist of the service, Virtual IP Address model, load balancing algorithm, and keep-alive. The Java TCP Server Load Balancer features are real server Health Checking and Graphical User Interface (GUI) for ease of configuration and administration. Subsequently the algorithms included in the balancer are studied and analyzed to compare their performance in the Linux Operating System environment with network traffic on different applications in order to find the most optimal use of the load balancing algorithms in the Java TCP Server Load Balancer. Analysis and comparison of the load balancing algorithms are conducted in experiments involving a number of test cases with clients, the Java Server Load Balancer, and real servers hosting HTTP and FTP applications. The most important conclusion from the experiments is that the performance of the two services tested namely HTTP and FTP is not actually directly influenced by the load balancing algorithm.

Keywords: Java, TCP, server, load balancer, balancing, algorithms.

INTRODUCTION

In the early years of websites, it was perfectly normal to have only one web server to serve million of requests from clients. This is due to the fact that most of the websites at that time have only static contents such as HTML and a few images (Ampornaramveth and Sanguanpong, 2002; Bourke, 2001). A server with average resource capacity was able to process these requests within acceptable response time to the clients (Casalicchio and Colajanni, 2001). As time went by, contents of websites have gradually shifted from static to dynamic types or in the case of FTP sites the downloaded file size is getting bigger. More websites are becoming interactive and more business driven websites, FTP sites and email service (Webmail) turn up as businesses see the opportunity of expanding their customer base through the Internet to gain more profit (DeRienzo, 2007). This has lead to websites having more dynamic contents due to data encryption, database applications, business logic, contents reformatting and others while FTP sites add more space for files and email service gets more subscribers (Chatterjee *et al*., 2005; Feng *et al*., 2000). Unfortunately, this causes these servers to process more data and receive more connections from clients. By using only one server, the service response time to clients starts to increase and in the Internet world even a few seconds increase can result in companies losing customers (Ho *et al*., 2004; Hong *et al*., 2006). The first reaction to this setback is to upgrade the server hardware such as CPU

and RAM. This approach has had its own problems since there is a limit to hardware capacity of any server and its network components (Extremenetworks, 2007). Network engineers worked hard to find a viable solution to this problem and eventually came up with a clever solution. This solution is server load balancing. A Server load balancer is able to make a group of servers behind a server load balancer appearing to clients as a single server and is capable of distributing clients' requests statically or dynamically to the actual servers (real servers) that provide the services to the clients (Viswanathan, 2001).

Load Balancing Algorithms
A server load balancer typically works by load balancing traffic to the real servers based on load balancing algorithms (Lu and Lee, 2005; Min *et al*., 1999). There are various load balancing algorithms used, with the most common ones to be Round Robin, Random, Least Connection, Source IP Address Hash (Hash IP), URL hash, and Cookie. There are also custom or proprietary load balancing algorithms which were developed by commercial server load balancer vendors or were developed for research. The algorithms are usually the variants of the common load balancing algorithms such as Weighted Round Robin or Weighted Least Connection. The purpose of these types of algorithms is usually to improve the performance of load distribution to the real servers by getting as much information as possible about the real servers or clients' states so that the server load balancer is able to determine the optimal traffic distribution.

---

*Corresponding author email: majdi.qdah@gmail.com

MATERIALS AND METHODS

The Java TCP SLB Software Operation

The Java TCP server load balancer is a software application written in Java that accepts TCP connections from clients and then distributes these connections to real servers which serve the clients' requests for specific TCP based services such as HTTP or FTP. The server load balancer is placed between the clients and the real servers in the network connections path. The client connections to the real servers are distributed using load balancing algorithms such as Round Robin or Least Connection. The load balancing configuration is done only on the Java TCP Server Load Balancer itself while the real servers provide the services to the clients. The Java TCP Server Load Balancer offers service availability discovery through Health Checking feature. The Java TCP Server Load Balancer application is administered and configured by using a Java GUI accessible from the host where the Java TCP Server Load Balancer is running.

Load Balancing Algorithms Comparison

The purpose of the comparison is to find the most optimal use of load balancing algorithm in the Java TCP Server Load Balancer. This is performed with simulated traffic from clients to real servers. In the Round Robin algorithm the traffic is sent to the real servers in ordered sequence and repeated in a loop. Each of the real servers receives equal number of connections from clients regardless of its capacity or load. The Random algorithm main use is to distribute connections randomly to any of the real servers. In the Least Connection algorithm, traffic is distributed to the server that has the least connections and the real server handles connections equally with other available servers. The Hash IP Address algorithm causes the subsequent connections from the same client IP address to connect to the real server where the first connection from that IP address is connected.

The Design
Network Architecture

As figure 1 show, the Java TCP Server Load Balancer runs on a host which has at least two network interface cards (NIC). One NIC is used for outside network connection such as Wide Area Network (WAN) and the Internet. The other NIC is used for the internal network where the real servers are located or inside a Local Area Network (LAN). Figure 2 shows the interface of the Load Balancing Algorithm.

In using the SLB, below is an example of a step-by-step how-to based on specific requirement below:

Service name:	http
Service port:	80
IP Address:	0.0.0.0
Terminate on Disable:	No
Half Close:	Yes
Connection TimeOut:	2 seconds
Connection Failure Limit:	5
Real servers:	realsever1.fit6z.com
	realsever2.fit6z.com
	realsever3.fit6z.com
	realsever4.fit6z.com
Algorithm:	Round Robin
KeepAlive:	HTTP
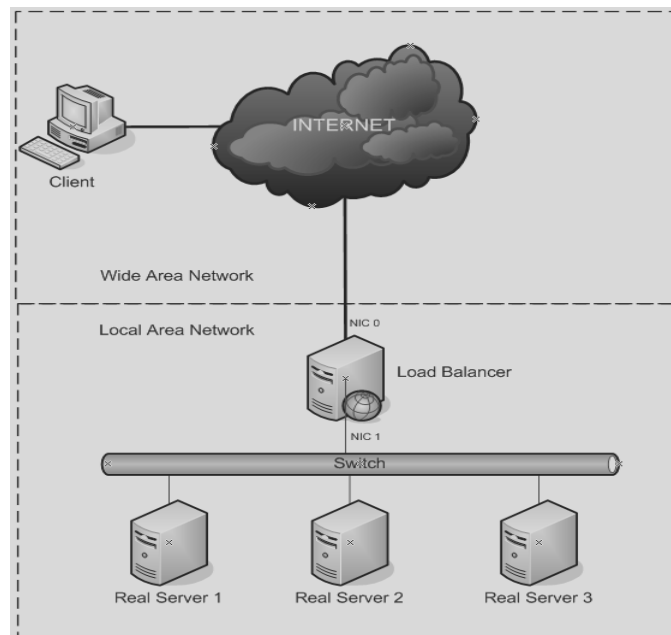
Fig. 1. Overall network architecture.

Frequency:	60 seconds
TimeOut:	5 seconds
Doc Path:	/index.html
Response Code:	200
Doc Text:	TARGET

In the experiments performed, the HTTP and FTP services were used for testing. Ten different clients with different private IP addresses were configured to simulate the traffic requesting for the services. Automated scripts on each client were configured to request the services above at thirty minutes interval. Each client had a script to measure the services' response time while the Java TCP Server Load Balancer and the real servers have a monitoring program to measure used resources: CPU and Memory load.
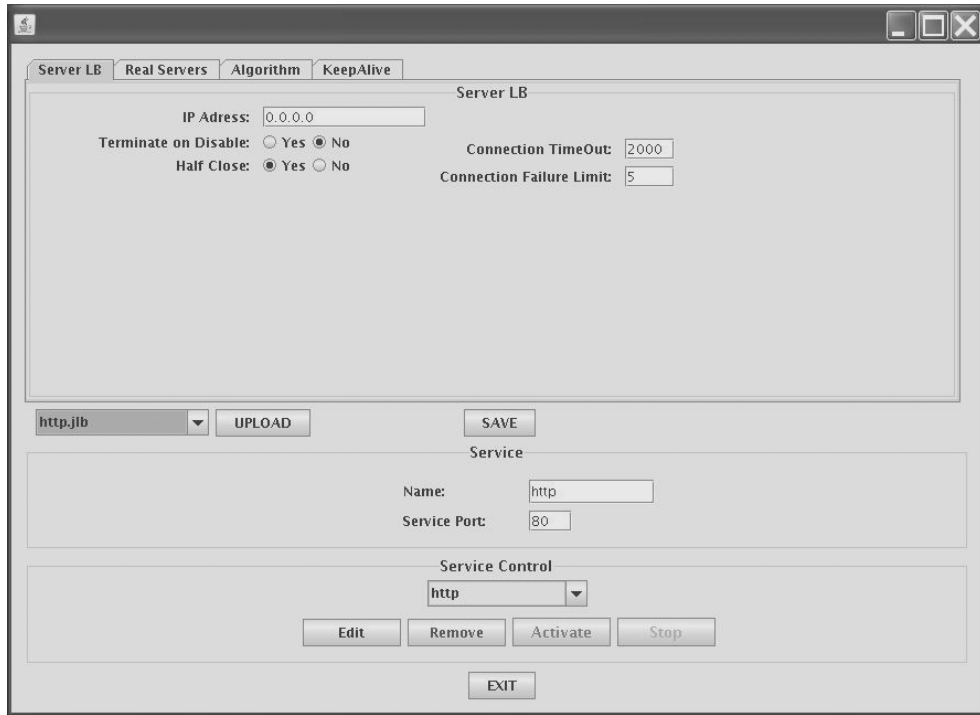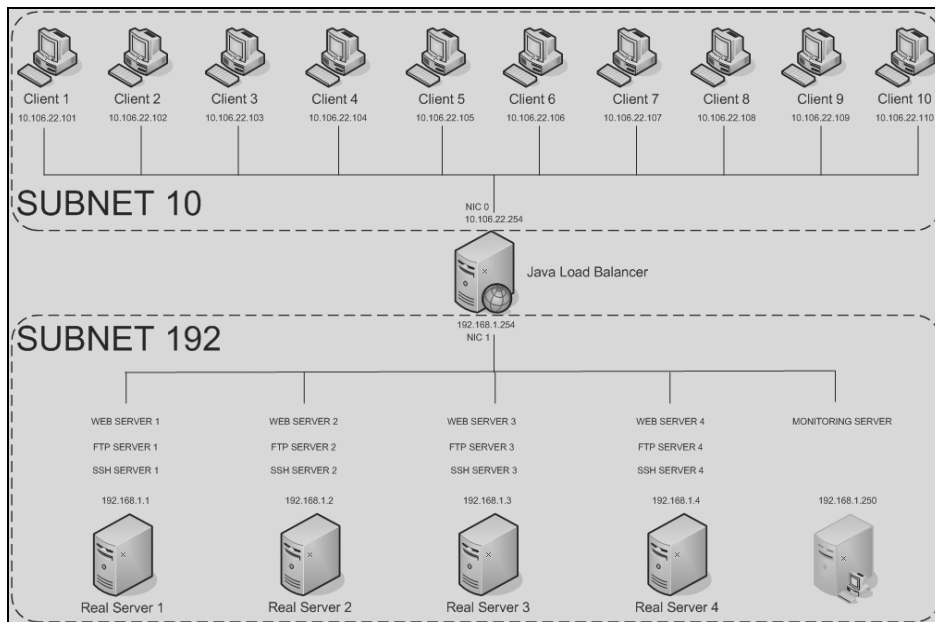

Fig. 2. Server LB tab.

Fig. 3. Experiment network diagram.

Comparison Metrics

Service Response Time
This is the most important metric as the performance of the service is very dependent on this metric. This metric show how long the client takes to complete access to the service. This metric has a definition that varies slightly from service to service. In HTTP, it is defined as the time it takes for a client to completely browse and download pages from a website with pre-configured path/links using Iceweasel add-on iMacros; while in FTP, it is defined as the time it takes for a client to complete a single FTP session to the FTP server by authenticating itself and then downloading 10 files with different sizes until the connection is closed.

Real Server and Java SLB CPU and Memory load
CPU and Memory load is defined as the total percentage of CPU and free Memory on the real server and the Java TCP SLB (RADirect, 2007). The CPU and Memory load on the Server Load Balancer is a good indication of how well is the performance of the individual algorithm running on SLB since the SLB software is the most active application running during the experiment in the SLB. However the CPU and Memory load on the real servers are not good indicators of the individual algorithm performance because the CPU and Memory load is the result of the process of accessing and running the application such as web server or FTP server. It is not the load from running the SLB software. However in order to see the performance of the algorithm, the distribution of the load among the servers was used. This can be achieved by calculating the standard deviation of the data gathered from the real servers CPU and Memory load. This is where CPU and Memory load on the real servers can be used, that is to measure the distribution of the CPU and memory load. The smaller the standard deviation the more even the distribution of the load among the real servers, which implies a better algorithm.

The experiment objective was to compare four load balancing algorithms which were employed by the Java TCP Server Load Balancer. In order to simulate real life environment, ten clients, four real servers and one monitoring station were required for the experiment apart from the most essential host running the server load balancer as illustrated in figure 3.

RESULTS AND DISCUSSION

Each client recorded the individual response time from each service test. One file was created for every service on each client using the script on the client. This file contained the response time from each algorithm test performed when the SLB was running Linux Debian 4.0.

HTTP
The average response time from each load balancing algorithm test was computed for each client for the HTTP service with SLB running on Linux Debian and was recorded in table 1.

The average of the values for each algorithm was then computed to get the average for specific algorithm response time using all the values from the clients. Based on the results from table 1, the algorithms' response times are close to each other, which imply that the performance of the HTTP service is generally the same among the real servers no matter which algorithm was used. Figure 4(a-d) shows the CPU load on the SLB against running each algorithm for thirty minutes.

These results show that the distribution process of the load on the SLB for HTTP service was very light. It was less than 10 percent of CPU usage on average for any algorithm. This indicates that the SLB does not require high CPU power to process clients' HTTP requests. Possible reasons for this event is the size of files i.e. data that was transferred from real servers to clients which was

Table 1. HTTP Service Response Time.

	Service Average Response Time (seconds)			
	Round Robin	Hash IP	Least Conn.	Random
Client 1	239.56	244.68	248.38	249.84
Client 2	291.12	125.94	299.85	303.45
Client 3	209.52	212.47	216.86	219.69
Client 4	224.54	227.84	233.24	236.28
Client 5	194.78	197.26	199.53	202.45
Client 6	219.41	225.44	225.11	231.00
Client 7	209.29	207.81	210.15	211.14
Client 8	115.05	115.47	116.82	118.54
Client 9	255.09	258.66	261.22	263.04
Client 10	165.18	165.93	167.24	174.11
Algorithm Average Response Time (seconds)	212.35	198.15	217.84	220.95

not very large. Thus the transfer of the static HTML files and images do not require high CPU usage. The total size of the website on the real server was 152 MB but the majority of individual websites files were small.

Figure 5(a-d) shows the Memory load on the SLB against running the algorithm for thirty minutes and a table 2 shows the maximum Memory usage in each thirty minute test.

The above results show that generally the SLB Memory usage gets higher as the test progresses. The difference is in the pattern of Memory usage. The pattern for Round Robin algorithm is especially a little bit different than those of the other three algorithms. With Round Robin, the usage fluctuation is significant; it is relatively high and occurs quite early compared to other algorithms. Looking at the Maximum Memory Usage table, Round Robin has the lowest usage of Memory. This means that the size of fluctuation of usage of the Round Robin algorithm actually is similar to the other algorithms because the graphs of the other three algorithms have a larger maximum value of y-axis so it appears that the fluctuation of usage is smaller. The difference with Round Robin is that the fluctuation of usage starts early. These results also show that for HTTP service, Round Robin is the best algorithm in terms of Memory usage on the SLB.
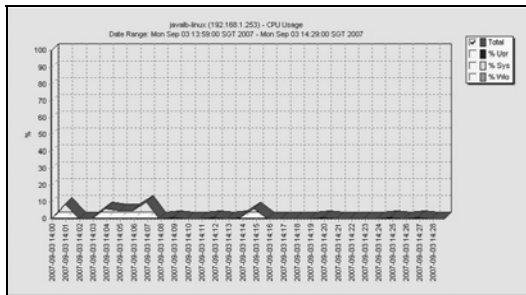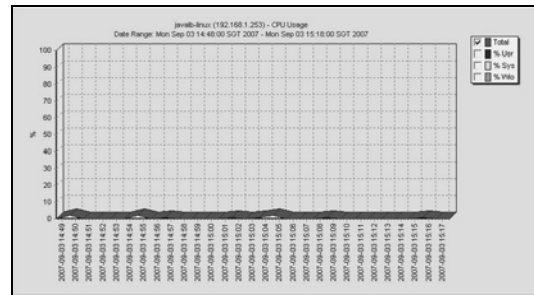
Fig. 4(a). Round Robin.
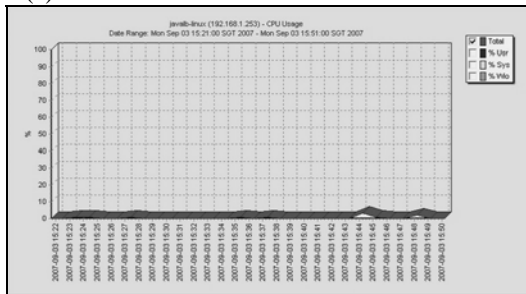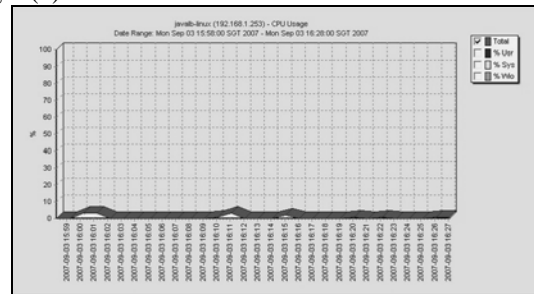
Fig. 4(b). Hash IP Address.

Fig. 4(c). Least Connection.

Fig. 4(d). Random.

Fig. 5(a). Round Robin.

Fig. 5(b). Hash IP Address.

Fig. 5(c). Least Connection.
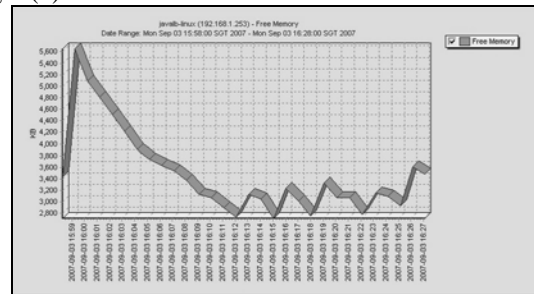
Fig. 5(d). Random.

Table 2. SLB maximum memory usage.

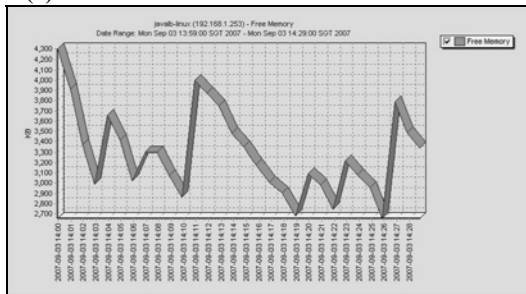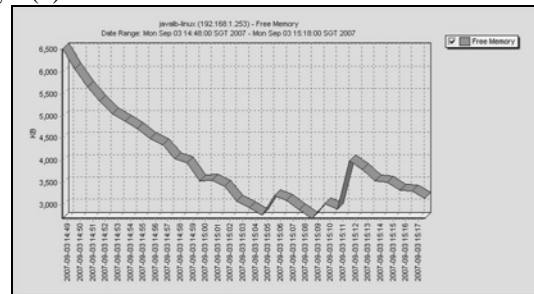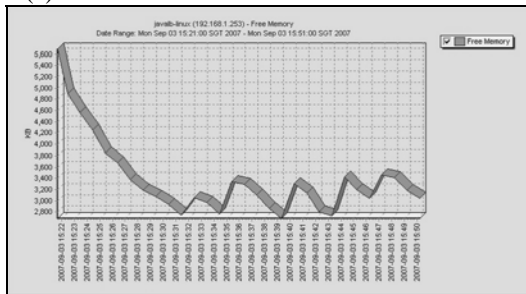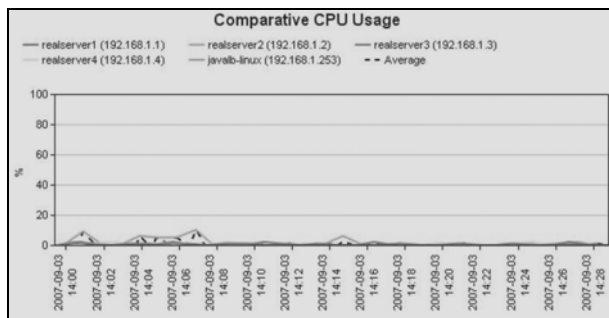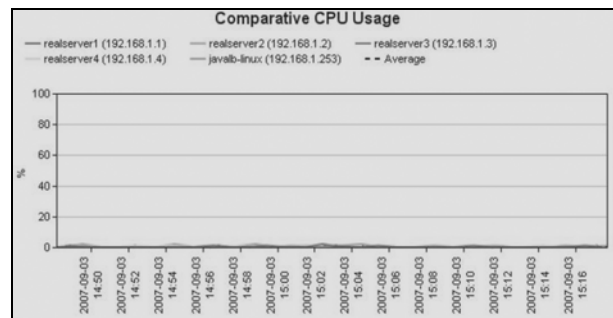| Java SLB	Round Robin	Hash IP	Least Conn.	Random
Maximum Memory Usage (kiloBytes)	1600	3800	2800	2800

Fig. 6(a). Round Robin.
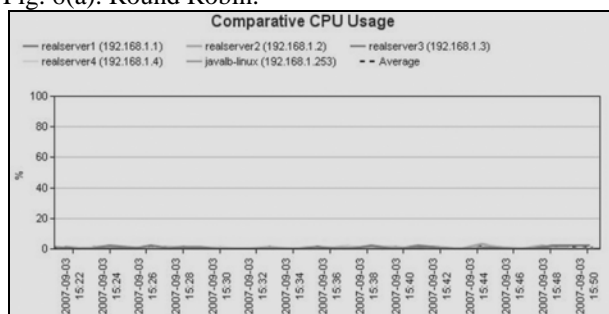

Fig. 6(b). Hash IP Address.
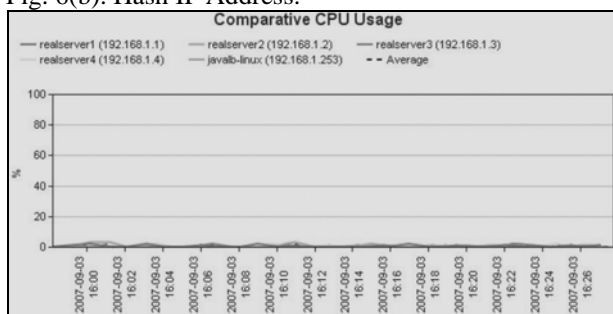

Fig. 6(c). Least Connection.

Fig. 6(d). Random.

Figure 6 (a-d) shows the CPU load on the real servers against running each of the algorithms for thirty minutes.

Based on the above results, the CPU usage on the real servers is very low for the same reasons mentioned previously i.e. the HTML files and images are small and also the HTTP server processes the client static files requests requiring only low CPU power. There is also no significant difference in performance among the algorithm. As mentioned under the "performance metric", it is not the CPU or Memory usage that indicates algorithm performance, it is the distribution of the load that is important. From these results since the load on each real servers are close to each other, it means that the load is distributed evenly among the real servers.

Figures 7(a-d) to 10(a-d) show the Memory load on the real servers against running each one of the algorithms for thirty minutes and tables that show the maximum Memory usage in each thirty minute test. Tables 3 to 6 show the maximum memory usage for each one of the algorithms.

The results show that in all test cases the free Memory was decreasing as the tests progressed. This was expected and the only difference was just the rate of usage towards the end of the test and the maximum usage. There was no significant event that needed attention based on these results.

FTP
The average of response times from each load balancing algorithm test was calculated for each client for FTP service with SLB running on Linux Debian and recorded in the table 7.

Based on the results from the table, the algorithm response times are quite close to each other which imply that the performance of the FTP service is generally the same among the real servers no matter which algorithm is used. This results show that the distribution process of the load on the SLB for FTP service requires more than 30 percent of CPU usage on average for any algorithm. This indicates that the SLB requires significant CPU power to process client request to transfer files. Possible reason for this event is the size of files i.e. data that is transferred from real servers to clients is bigger than that of in HTTP service. Thus the transfer of ten files with multiple sizes requires significant CPU usage. Also, the results show that generally the SLB Memory usage gets higher as the test progresses except for Hash IP Address and Least Connection algorithms. In Hash IP Address test, the rate of Memory usage decreases towards the end of the test (increase of the graph means increase of free Memory) while with Least Connection the Memory usage drops very rapidly after about 20 minutes. A possible explanation for this outcome is that the FTP session finishes early compared to other algorithms. The Least

Round Robin

Fig. 7(a). Real Server 1

Fig. 7(b). Real Server 2
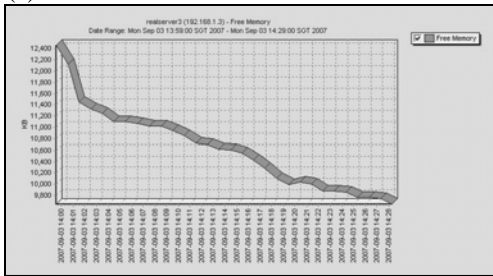
Fig. 7(c). Real Server 3.
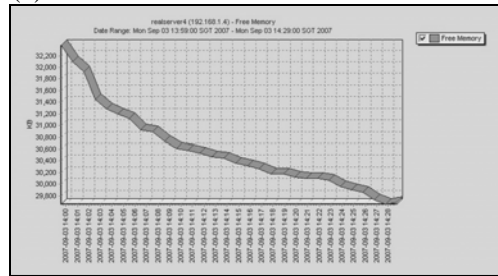
Fig. 7(d). Real Server 4.

Table 3. Maximum memory usage with Round Robin.

	real server 1	real server 2	real server 3	real server 4
Maximum Memory Usage (kiloBytes)	3200	3500	2800	2700

Hash IP Address
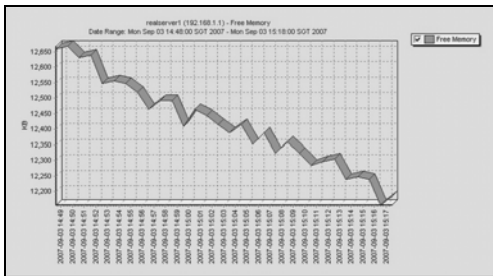
Fig. 8(a). Real Server 1.
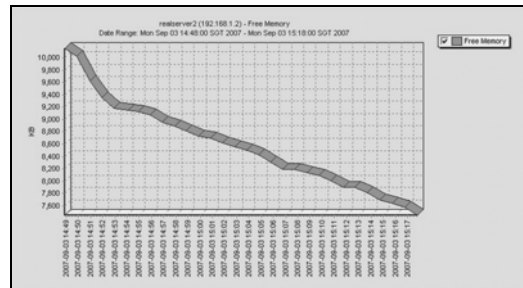
Fig. 8(b). Real Server 2.
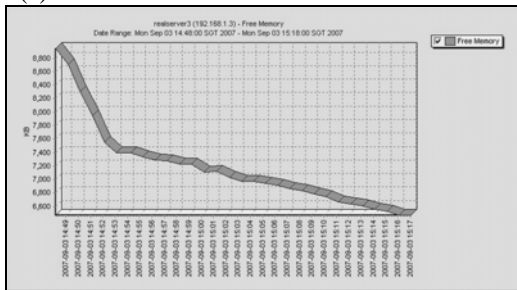
Fig. 8(c). Real Server 3.
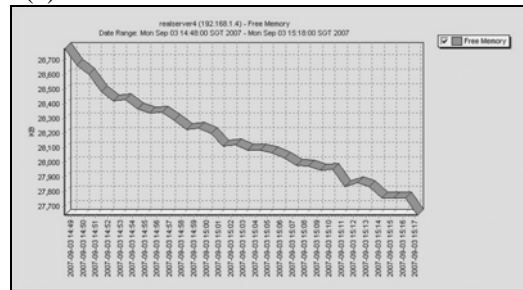
Fig. 8(d). Real Server 4.

Table 4. Maximum memory usage with Hash IP Address.

	real server 1	real server 2	real server 3	real server 4
Maximum Memory Usage (kiloBytes)	500	2600	2400	1100

Connection algorithm had the lowest usage of Memory. This value does not take into account the Memory usage drop because the values after the drop are not likely contributed by the FTP session. It is the maximum usage from the start of the test until the Memory usage starts to drop.

Least Connection
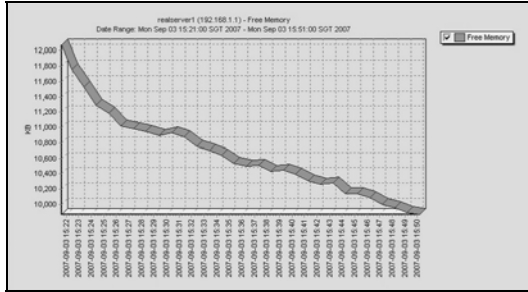
Fig. 9(a). Real Server 1.
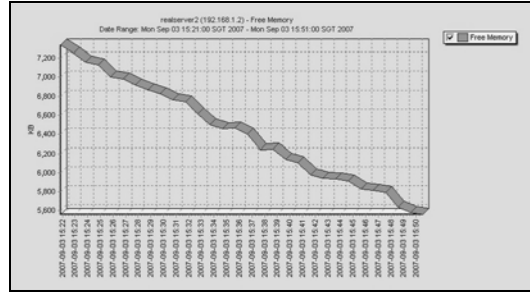
Fig. 9(b). Real Server 2.
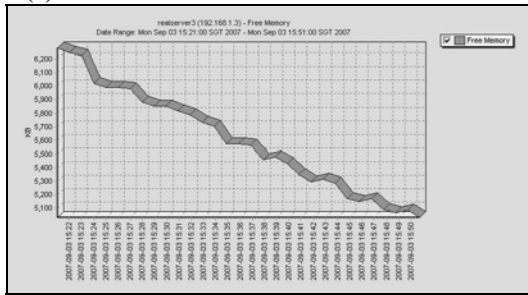
Fig. 9(c). Real Server 3.
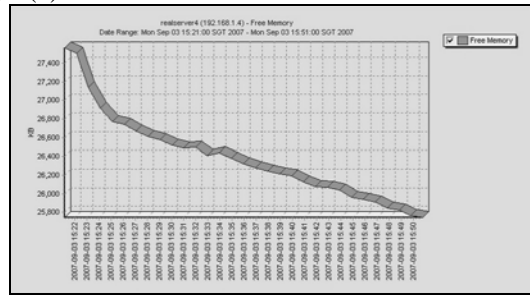
Fig. 9(d). Real Server 4.

Table 5. Maximum memory usage with Least Connection.

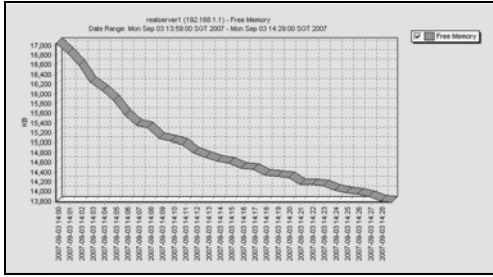|	real server 1	real server 2	real server 3	real server 4
Maximum Memory Usage (kiloBytes)	2200	1700	1200	2800

Random
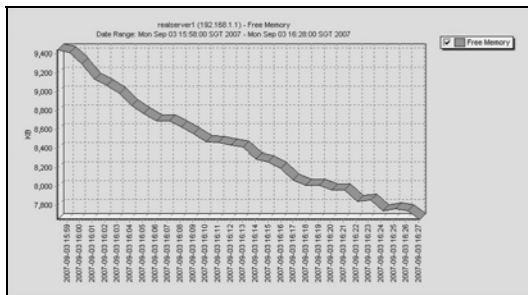
Fig. 10(a). Real Server 1.
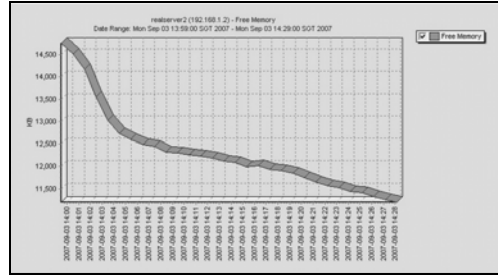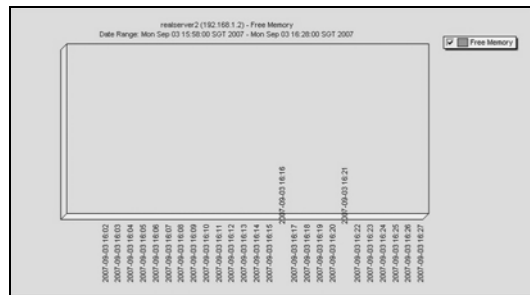

Fig. 10(b). Real Server 2.
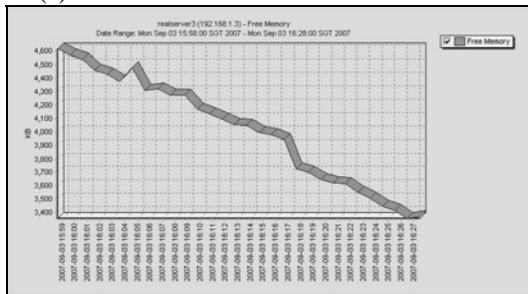
Fig. 10(c). Real Server 3.
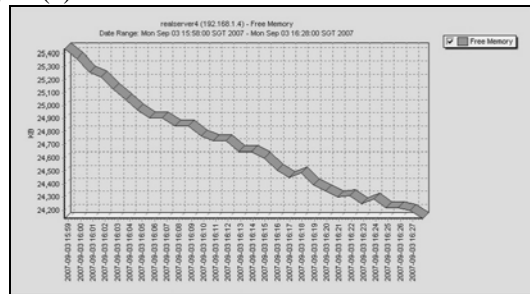
Fig. 10(d). Real Server 4.

Table 6. Maximum memory usage with Random.

	real server 1	real server 2	real server 3	real server 4
Maximum Memory Usage (kiloBytes)	1800	(N.A.)	1250	1300

In addition, the results show that for FTP session, the real servers have used a significant CPU power. There are two important characteristics that can be concluded: the first one is the closeness between the graph lines representing the CPU usage load and the second one is the fluctuation of individual line. The first characteristic represents the

Table 7. FTP Service Response Time.

	Service Average Response Time (seconds)			
	Round Robin	Hash IP	Least Conn.	Random
Client 1	300.11	338.26	319.27	336.49
Client 2	322.34	333.09	319.21	327.22
Client 3	321.91	302.50	340.92	344.02
Client 4	317.49	305.56	320.78	326.14
Client 5	332.97	356.43	326.97	328.49
Client 6	323.98	305.55	317.91	334.76
Client 7	388.45	371.68	346.08	345.18
Client 8	327.37	367.00	321.29	341.00
Client 9	326.45	330.74	337.63	339.72
Client 10	332.62	299.82	336.57	320.08
Algorithm Average Response Time (seconds)	329.37	331.06	328.66	334.31

Table 8. Algorithms Rank with Linux.

APPL	HOST	METRIC	ALGOIRTHMS' RANK				STD. DEV
			1st	2nd	3rd	4th	1st Algo
HTTP	Client	Response Time	HIP	RR	LC	RD	N.A.
	SLB	CPU	No significant difference				
		Memory	RR	LC	RD	HIP	N.A.
	Real Servers	CPU	LC	HIP	RD	RR	
		Memory	RD	RR	LC	HIP	304.13
FTP	Client	Response Time	LC	RR	HIP	RD	N.A.
	SLB	CPU	No significant difference				
		Memory	LC	HIP	RR	RD	N.A.
	Real Servers	CPU	LC	RR	RD	HIP	
		Memory	LC	HIP	RR	RD	221.27

load distribution among the real servers. Closer graph lines mean a more even distribution of load. The second characteristic represents the change of load on that particular real server. It can be observed that each graph shows both characteristics but differ in magnitude. The graph that has the closest lines with each other is the Least Connection algorithm graph and the least is the Random algorithm graph. This means Least Connection algorithm distributes load the most even among the algorithms and Random algorithm is the least efficient in distributing the load evenly based on the CPU usage. It is also observed that the Hash IP Address graph lines are the least fluctuating and the most fluctuating is Random algorithm. This is expected since Hash IP algorithm keeps the same source IP address into the same real server. This causes the CPU to process the same load from the same client which results in least fluctuating CPU usage. The real server results show that in all test cases the free Memory was decreasing as the tests progressed. This is expected and the only difference is just the rate of usage towards the end of the test and the maximum usage. The Memory usage is not directly contributed by the algorithm; instead it is a direct result from the processes running on the real servers themselves. There is no

significant event that needs attention based on these results.

Load Balancing Algorithms Rank
Based on the previous tables that summarized the results, it is possible to rank the algorithms in terms of the efficiency of the algorithms in distributing requests to specific application. The algorithm rank is shown in table below:
(N.A. means Not Applicable)

Legend: RR   =   Round Robin
          HIP =   Hash IP Address
          LC   =   Least Connection
          RD   =   Random

CONCLUSIONS

The Java TCP Server has been developed with big improvement to an existing load balancing algorithms. The most important of improvements is the addition of two more algorithms namely Least Connection and Random algorithms. In the experiment performed, three performance metrics have been used to determine the best

algorithm for each of the HTTP and FTP services. The performance metrics are service response time, CPU load and Memory load of the Java TCP Server Load Balancer and the real servers. The most important conclusion from the experiment is that the performance of the services tested namely HTTP and FTP is not actually directly influenced by the load balancing algorithm. Also, the experiments have concluded that each of the Java TCP Server Load Balancer algorithms distributes the load to real servers exactly the way it was suppose to do. This is proven by real servers CPU and Memory load usage data and graphs, specifically the standard deviation value. Smaller standard deviation means a more even load distribution.

REFERENCES

Ampornaramveth, N. and Sanguanpong, S. 2002. Optimization of Cluster Web Server Scheduling from Site Access Statistics. [Online]. Available: http://anres.cpe.ku.ac.th/pub/WebCluster-anscse2002.pdf [2007, 02 April].

Bourke, T. 2001. Server Load Balancing. O'Reilly and Associates, Inc., California, USA.

Casalicchio, E. and Colajanni, M. 2001. A Client-Aware Dispatching Algorithm for Web Clusters Providing Multiple Services. [Online]. Available: http://www10.org/cdrom/papers/434/colajanni_html.html #Sec:class [2007, 01 April].

Chatterjee, D., Tari, Z. and Zomaya, A. 2005. A Task-Based Adaptive TTL Approach forWeb Server Load Balancing. Proceedings of the 10th IEEE Symposium on Computers and Communications. 877-884.

DeRienzo, F. 2007. Choosing a Hardware Load-Balancing Device. Macromedia, Inc. [Online]. Available:

http://www.adobe.com/devnet/server_archive/articles/choosing_hardware_lbdevice.html [2007,05 April].

Extremenetworks. 2007. TechBrief Extreme Networks Server Load Balancing [Online]. Available: http://apps.extremenetworks.com/libraries/whitepapers/technology/Server_load_balancing.pdf [2007, 02 April].

Feng, Y., Li, D., Wu, H. and Zhang, Yi. 2000. A Dynamic Load Balancing Algorithm Based on Distributed Database System. The Fourth International Conference/Exhibition on High Performance Computing in the Asia-Pacific Region, 2000. Proceedings. 2:949-952.

Ho, LK., Sit, HY., Ho, KS., Leong, HV. and Luk, RWP. 2004. Improving Web Server Performance by a Clustering-Based Dynamic Load Balancing Algorithm. Proceedings of the 18th International Conference on Advanced Information Networking and Application. 2: 232-235.

Hong, YS., NO, JH. and Kim, SY. 2006. DNS-Based Load Balancing in Distributed Web-server Systems. Proceedings of the Fourth IEEE Workshop on Software Technologies for Future Embedded and Ubiquitous Systems and Second International Workshop on Collaborative Computing, Integration, and Assurance. pp4.

Lu, YC. and Lee, LT. 2005. On implementation of an efficient multi-purpose load balancing server. [Online]. Available:http://www.hpc.csie.thu.edu.tw/cthpc2005/pdf/II_4.pdf [2007, 01 April].

Min, D., Choi, E., Lee, D. and Park, B. 1999. A load balancing algorithm for a distributed multimedia game server architecture. 1999 IEEE International Conference on Multimedia Computing and Systems. 2:882.

RADirect. 2007. Server Load Balancing with Radware's WSD. [Online] Available: http://www.rad-direct.com/Application-server-load-balancing.htm [2007, 03 April].

Viswanathan, V. 2001. Load Balancing Web Applications. In O'reilly On Java.com [Online]. Available:http://www.onjava.com/pub/a/onjava/2001/09/26/load.html [2007, 02 April].

THE PARADOXES SHOW THE WAY: A CHANGE IN THE STRUCTURE OF LOGIC MEANS A CHANGE IN THE STRUCTURE OF RESEARCH

John Karakonstantis
Department of Mathematics, University of Patras, Filaretou 9, Galatsi, Athens, GR 11147, Greece

ABSTRACT

In this paper, the main paradoxes are interpreted in such a way that they lead to the equivalence of a sentence and its negative $s \Leftrightarrow s^c$.
In classical logic, paradoxes define sentences that contradict themselves. These sentences support strategies for proving theorems. In fuzzy logic, paradoxes lie at the center of hyper-cubes. It can then be established that changing the framework eliminates paradoxes. Paradoxes therefore show us how to change the "teaching process" framework so as to transcend the obstacles they bring about to teaching and learning.

- The meaning of "nearby"[1] is examined in two research frameworks.
- A criterion for evaluating the "teaching process" is developed through a classification of mental activity by means of the measurement of the "fuzzy entropy" determining the internalization of concepts in every context.

Finally, the contextual approach to mathematical certainties is accepted.

Keywords: characteristic function, fuzzy logic, membership function, classical logic, entitlement system, hyper-cubes, propositional type, fuzzy set, fuzzy entropy.

INTRODUCTION

The sentences defining paradoxes cannot be predicative, which means that paradoxes are usually introduced by interrogative sentences. These sentences are defined by fuzzy sets and reveal an inconsistency. The inconsistency of the interrogative sentences has an epistemological basis and expresses neutrality in order not to influence the answer. Semantically speaking, it is thus precisely in the middle of the two meanings, either of which can be expected as an answer. Their contradictory nature is determined by the initial defining experience. This experience relates to the use of a property describing a set of objects (Anapolitanos, 1985).

When this property is not monitored, it defines a "class". If a set is to be defined by this property, the property must relate to the elements of an extant set. This gives the mathematical activity a frame of reference. The frame of reference is defined by a function determining the degree to which a given element participates in a set, which is to say it is defined by its allowing us to construct a set by recognizing its elements. Of course, the elements may well belong only partially to the set. Thus, classical logic looks to the "characteristic" function $\mu_A x = \begin{cases} 1, & x \in A \\ 0, & x \notin A \end{cases}$

(King, 1998) as a membership function. In fuzzy logic, frameworks develop which are defined by the membership function pertaining in each case. Classical logic dominates thanks to its ability to construct logical categories which serve as a means of communication.

The Interpretation of Paradoxes

Paradoxes are sentences which reveal contradictions when they are subject to interpretation using classical logic. In a fuzzy logic context, these contradictions are eliminated, which brings into being a new mechanism for constructing mathematic concepts. It is common knowledge that, as well as using concepts, mathematics operates in the main by constructing them (Kant, 1781). The new perspective afforded by fuzzy logic introduced various new possibilities which served to maximize the possibility of constructing new concepts.

Applying modus ponens, axioms lead to sentences that do not contradict one another during the construction of mathematic concepts. The acceptance of the truth of a contradiction implies everything, allowing us to prove or reject anything in dual-value (classical) logic (1).

(1) In classical logic, the truth of a contradiction $s \cap s^c$ means that any sentence P is true.

Let $\quad s \cap s^c \to s \qquad (\alpha)$

$s \cap s^c \to s^c \qquad (\alpha)$

then $\quad [s \to s \cup P] \sim \quad s^c \to P$

$s^c \ (\alpha)$ Modus ponens

P : P $\quad$ anything $\qquad$ Kosko (1987)

If s $\to$ P if this s $\to$ P doesn't stand then $s^c \to$ P

$s \underline{\qquad} \qquad s^c \underline{\qquad}$

then P : P $\quad$ anything then P : P anything

---

*Corresponding author email: ikarako@sch.graazaaz@inbox.ru
[1] Fuzzy linguistic labels expressed by fuzzy variables.

There is near zero tolerance for views that accept contradictions. As far as classical logic is concerned, self-refuting sentences are complex intuition that cannot construct concepts (Kant, 1781).

Although paradoxes initially serving as a mechanism for constructing mathematic concepts of some form in a working framework, they subsequently came to obstruct the construction of mathematic concepts of a different texture. The explanation of paradoxes in a fuzzy logic context creates an obstacle-free space in order to optimize mathematical activity. Knowledge is improved and disseminated better in suitably-designed teaching environments.

In a classical logic context, the claim $A \cap A^c \neq \Phi$ is unfounded. Of course, if we insist on the force of truth in our argument, we have to change the structure of logic. An argument is wrong if it is found to contain a paradox. If, however, rather than rejecting the argument, we are rejecting the dual-value and ascribing a value of the truth of sentence s instead of t (s) = 0 or t (s) = 1, a value in the closed interval [0, 1], i.e. $0 \leq t(s) \leq 1$,[2],[3] (2) then the paradoxes generalize into fuzzy sets and logic into fuzzy logic.

In fuzzy logic, the value of the sentence s, t(s) and the value of the sentence s^c, $t(s^c)$ are linked by the relationship $t(s^c) = 1 - t(s)$. Sentence s is defined by a fuzzy set A and sentence s^c by a fuzzy set A^c in which the relationship $A \cap A^c \neq \Phi$ makes sense.

Paradoxes result in the equivalence of two sentences $s \Leftrightarrow s^c$, as a conjunction of two entailments.
The most ancient paradox is the following:
"Is the Cretan philosopher (Epimenides) telling the truth or is he lying when he claims: "Every Cretan is a liar?"[4]

Let s be the sentence: "The Cretan philosopher is telling the truth"

and s^c be the sentence: "The Cretan philosopher is lying"
Interpretation—Method

If "the Cretan philosopher is telling the truth", then, since every Cretan lies, it must be that "the Cretan philosopher is lying", i.e., $\boxed{s \Rightarrow s^c}$ (1)

If "The Cretan philosopher is lying", then, since every Cretan is lying, it must be that "The Cretan philosopher is telling the truth", i.e., $\boxed{s^c \Rightarrow s}$ (2)

From (1) and (2) we end up with, $s \Leftrightarrow s^c$.
Epimenides' paradox can be generalized for every self-referential sentence as follows:

"I tell the truth or lies when I claim that I lie".

Let s be the sentence: "I tell the truth" s^c the sentence: "I lie"
- If I am telling the truth, the claim that I lie is true. Therefore I lie: i.e. $s \Rightarrow s^c$.
- If I am lying, then my claim to be lying is false. Therefore I am telling the truth: i.e. is, $s^c \Rightarrow s$.

Finally, conjoining the two entailments I have, $s \Leftrightarrow s^c$.

We can see that every known paradox—and, indeed, every sentence that has still to be discovered to be internally contradictory—results in an equivalence between a sentence and its denial.

Let it be the table of truth of the logical propositional type of equivalence between two random sentences (Mytilineos, 1993).

P	Q	P <=> Q	
1	1	1	The logical operator of equivalence is true when both sentences have the same truth value, and then alone.
1	0	0	
0	1	0	
0	0	1	

- Classical logic defines an evaluation function U:Π → {0, 1}, where Π is the set of the sentences of language Γ.
- For fuzzy logic, the evaluation function is defined as: t: Π → [0, 1]

Classical logic: s<=>s^c or U(s) = U(s^c), since the values of U with S as an argument and U with s^c as an argument are, respectively, 0 or 1 and vice versa, we end up with a contradiction 0=1 or 1=0[5], (Anapolitanos, 1985).

Fuzzy logic: s <=> s^c or t(s) = t(s^c) or t(s) = 1 − t(s), [t(s^c) = 1-t(s)] hold under fuzzy logic, giving us t(s) = t(s^c) = ½. (Klir and Bo, 1995).

There is no contradiction, rather a half-empty / half-full glass perspective.

[2] This claim is an interpretation of the law of the union of opposites, a basic law of dialectics
[3] That the value of the sentence (s), t(s) lies within [0, 1] for empirical sentences is accepted by numerous theoreticians as corresponding incompletely with reality
[4] This sentence is not a real paradox in terms of the classical meaning of the term.

[5] Every contradiction results in a sentence of the form 0=1 or 1=0

The contradiction inherent to the self-negating sentences of the paradoxes is a statement to the effect that the mathematical object does not exist, which brings a strategy into play for constructing concepts: an indirect proof, proof by reduction ad absurdum. Applying this strategy, we make a hypothesis and then prove that the hypothesis leads to a self-contradiction (ad absurdum). We then go back to the hypothesis and disprove it[6] (Drossos and Papadopetrakis, 1985).

Only one step in this strategy is made by entailment: if (A => B) A presumes B and B is false or leads to the wrong way, then we deny A (we accuse the cause for the result].

A strategy with a similar form (which the creative subject uses to construct mathematical concepts) is where A or B presume Γ, and if Γ is false then either A is false or B is false or both are false.

But if we suppose that hypothesis Y (applying the laws of logic and mathematics) results in the sentence $s \cap s^c$, then by what authority can we conclude that the sentence is 100% wrong? Using similar powerful arguments, fuzzy logic tells us that $s \cap s^c$ are valid, except that both s and s^c are 50% true. We saw above that self-referential paradoxes correspond to the midpoint of the line connecting zero and one.

Paradoxes show that dual-value comes at a cost. We cannot always round off the description of a fact at no cost. Accuracy is exchanged for simplicity, and we pay for the exchange (Kosko, 1987).

"Paradoxes" as Hyper-Cube Centers
A single dimensional hyper-cube is the straight section of the line of real numbers from zero to one, that is [0,1].

In two dimensions, this is the unit square; in three dimensions, it is the unit solid cube and so on (Tzafestas, 1994).

Consider sentence s to be defined by a fuzzy set A. The fuzzy set A is defined as follows: Let X be a reference hyper-set X = {x_1, x_2}, $\mathcal{P}$(x) the power set of X.

$\mathcal{P}$(x) = {Φ, {x_1}, {x_2}, {x_1, x_2}}. A fuzzy sub-set of X, A = {(x_1, 1/3), (x_2, 3/4)}.

We define the Fit (fuzzy unit) vector of the fuzzy set fV: X → [0,1] x [0,1].

Φ = {(x_1,0), (x_2,0)}	has fit vector	(0,0)
{x_1} = {(x_1,1), (x_2,o)}	" " "	(1,0)

---
[6] Socrates would apply this strategy to prevail over his interlocutor

{x_2} = {(x_1,0), (x_2,1)}	" " "	(0,1)
{x_1,x_2} = {(x_1,1), (x_2,1)}	" " "	(1,1)
A = {(x_1,1/3), (x_2,3/4)}	" " "	(1/3, 3/4)

Geometrically illustrated as follows:

A^c = {(x_1, 2/3), (x_2, 1/4)}

$A \cap A^c$ = {(x_1, 1/3), (x_2, 1/4)}

$A \cup A^c$ = {(x_1, 2/3), (x_2, 3/4)}

The measure of entropy $E(A) = \frac{|A \cap A^c|}{|A \cup A^c|} = \frac{7}{17}$ used to gauge mental activity

$0 \leq E(A) \leq 1$
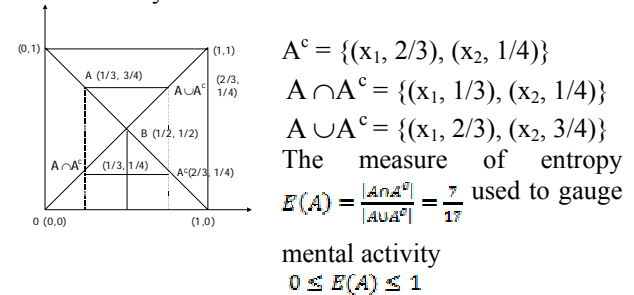
Fig. 1.   For the set B = {(x_1, 1/2), (x_2, ½)} we have E(B)=1

We observe that the maximum of entropy is consumed. We conclude that the perception of the paradoxes demands the consumption of the maximum mental entropy.

The angles of the hyper-cube remain dual-valued. All other points belong to fuzzy logic Kosko (1997). At the midpoint B, the fuzzy sets B^c, $B \cap B^c$, $B \cup B^c$ are identical to B. It is the point where paradoxes are illustrated. The centers of the hyper-cubes for all dimensions are the points where the "paradoxes" reside. The geometrical illustration in the two-dimensional hyper-cube provides an oversight of the square with apexes at A, A^c, $A \cap A^c$ and $A \cup A^c$ which imbue with meaning the fuzzy sets that define the amplitude of a concept with argument sentence s.

The interpretation of paradoxes lies at the center of the hyper-cubes. This new interpretation opens up new avenues in mathematical creation as new mathematical concepts are structured diachronically. The use of fuzzy sets and of fuzzy logic in the teaching process is an everyday practice. Awareness of this process has resulted in the successful mathematization of thought using language as a tool furthering the optimization of the teaching process.

Change of context
(First) A' Approach of the Concept of "Nearby"

We consider the sentence s: "Real numbers near five (5) included in the interval [0,10]".

Sentence s is defined by the fuzzy set A.

$$A = \left\{ (x, \mu_A(x)) : x \in [0,10], \mu_A(x) = \frac{1}{1+(x-5)^2} \right\}$$

Sentence s^c is defined by the fuzzy set A^c.

$$A^c = \left\{ (x, \mu A^c(x)) : x \in [0,10], \mu A^c(x) = \frac{(x-5)^2}{1+(x-5)^2} \right\}$$

The membership function $\mu_A(x)$ is defined intuitively. The two functions can be represented thus:
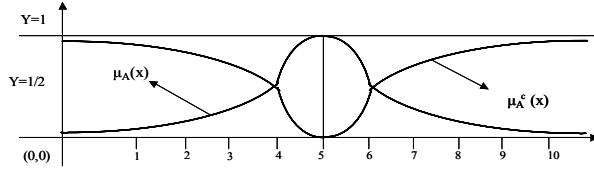
Fig. 2.

$$A \cup A^c = \left\{ \left(x, \mu_{A \cup A^c}(x)\right) : x \in [0,10], \mu_{A \cup A^c}(x) = \max\left\{ \mu_A(x), \mu_{A^c}(x) \right\} \right\}$$
and
$$A \cap A^c = \left\{ \left(x, \mu_{A \cap A^c}(x)\right) : x \in [0,10], \mu_{A \cap A^c}(x) = \min\left\{ \mu_A(x), \mu_{A^c}(x) \right\} \right\}.$$

The measure of fuzziness for fuzzy set A is defined by the price of fuzzy entropy $E(A) = \dfrac{|A \cap A^c|}{|A \cup A^c|}$ (Kosko, 1997).

It is calculated to

be $\dfrac{1}{2}|A \cap A^c| = \int_0^4 \dfrac{1}{1+(x-5)^2} dx + \int_4^5 \dfrac{(x-5)^2}{1+(x-5)^2} dx =$

$= \left[\tan^{-1}(x-5) \right]_0^4 + [x]_4^5 - \left[\tan^{-1}(x-5) \right]_4^5 \approx 0.6$

It is also calculated to be

$\dfrac{1}{2}|A \cup A^c| = \int_0^4 \dfrac{(x-5)^2}{1+(x-5)^2} dx + \int_4^5 \dfrac{1}{1+(x-5)^2} dx = 2,43$

So $E(A) = \dfrac{0.6}{2.43} = 0,2,$ $\boxed{E(A) = 0.2}$

In the particular framework, which is defined by $\mu_A(x)$, the mental system spends $E(A) = 0.2$ on interiorizing fuzzy set A.

Second Approach to the Concept of "Nearby" (vicinity) Sentence s is defined by a fuzzy set B,

$$B = \left\{ (x, \mu_B(x)) : x \in [0,10], \mu_B(x) = \begin{cases} \frac{1}{4}x - \frac{1}{4}, & 1 \le x < 5 \\ 0 & \forall x \\ -\frac{1}{4}x + \frac{9}{4}, & 5 \le x \le 9 \end{cases} \right\}$$

Sentence s^c is defined by the fuzzy set B^c,

$$B^c = \left\{ (x, \mu_{B^c}(x)) : x \in [0,10], \mu_{B^c}(x) = \begin{cases} \frac{1}{4}x + \frac{5}{4}, & 1 \le x < 5 \\ 0 & \forall x \\ \frac{1}{4}x - \frac{5}{4}, & 5 \le x \le 9 \end{cases} \right\}$$

The two functions are illustrated thus:
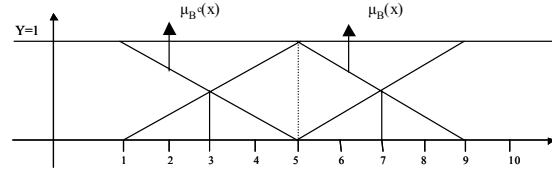
Fig. 3.

It is calculated that

$$\frac{1}{2}|B \cap B^c| = \int_1^3 \left(\frac{1}{4}x - \frac{1}{4} \right) dx + \int_3^5 \left(-\frac{1}{4}x + \frac{5}{4} \right) dx = 1$$

Also it is calculated that

$$\frac{1}{2}|B \cup B^c| = \int_1^3 \left(-\frac{1}{4}x + \frac{5}{4} \right) dx + \int_3^5 \left(\frac{1}{4}x - \frac{1}{4} \right) dx = 3$$

Thus $\boxed{E(B) = \dfrac{1}{3}}$

Partial Conclusions

During the mental function of interiorization (Cooper, 1739-1839) of the fuzzy sets A and B, different amounts of fuzzy entropy are expended. Fuzzy sets A and B comprise a definition for the same sentence s. The codification of the sentence is effected by means of different membership functions. The expense of mental entropy is different and scaled as follows: $E(A) < E(B)$.

The principle of maximum benefit tells us the quality of mental work is hierarchically superior when it expends less fuzzy entropy to accomplish the same mental activity.

Meaning that the teaching process must orientate itself towards developing the "membership function" in the student required for successful learning at minimum cost. This selection is often made "intuitively".

It is intuitively correct to say that the membership function's rate of transition should increase when the conviction that element x belongs to fuzzy set A is reinforced. Analytically this is expressed by the function:

$d\mu_A(x)/dx = k.\mu_A(x)(1-\mu_A(x))$

Winding this up, $\mu_A(x)=1/(1exp(a-bx))$, where the constants a, b derive from the conditions determined by the teaching process. Classical logic chooses the proper "membership function" to replace intuition, meaning the selection is made using scientific—and primarily mathematical—tools.

The development of the concept of "nearby" (vicinity) in Varied Teaching Contexts

The evaluation of whether the number (3) is near the number five (5) is clear in the first context $\mu_A(3) = \dfrac{1}{5} < \dfrac{4}{5} = \mu_{A^c}(3)$. Specifically, the number three (3)

is 20% near the number five (5). Approximating, we shift to a classical logic context and resolve that the number three (3) does not belong near the number five (5).

In the second interpretational context, $\mu_B(3)=\frac{1}{2}=\mu_{B^c}(3)$. The number three (3) is 50% near the number five and is 50% not near the number five (5). Which makes it impossible to approximate in classical logic; we therefore have a "paradox". Of course, changing the context eliminates the paradox in question. But there is a paradox inherent to the structure of the new context.

Specifically, in the initial context, the reply to the question whether the number four is in the vicinity of the number five (5) is not clear if we demand an interpretation in the context of classical logic. This is the case because $\mu_A(4)=\frac{1}{5}=\mu_{A^c}(4)$. Meaning there is even equivalence for the decision posed by the question, if the number four (4) belongs to fuzzy set A, which defines the numbers as being in the vicinity of five (5) and of its refusal, which determines the numbers that are not in the vicinity of the number (5).

The change of context and the approximation to knowledge in a variety of contexts is ultimately a condition with a sound basis.

The use of paradoxes for backing up arguments in a research framework is common practice in mathematical creativity. It is also a tool for constructing mathematical concepts, since paradoxes function as a primitive "taboo", meaning the prohibition of a "totem". [Murder or eating a sacred animal—a totem—is prohibited, except under particular conditions with a symbolic meaning] (Freud, 1913). The paradox is a contemporary "taboo" and comprises a prohibition on a symbolic level relating to a specific "totemic" element of knowledge. The breaking of taboos, brought about by a change in context, is necessary for those seeking to structure or teach knowledge. The context changes when the membership function changes. There are paradoxes in every context which, inherent to the structure of the context, constitute axes around which knowledge is structured. Mental procedures are codified in fuzzy sets which are handled by the mental system using fuzzy logic as its method. Paradoxes lead mental procedures towards the rational.

CONCLUSIONS

Paradoxes define prohibiting values upon which rational thinking is organized.

The sentences which define paradoxes end up with the equivalence of a sentence and its negative [$s \Leftrightarrow s^c$]. In a classic logic context, the logical type defines a contradiction. It is also a criterion for rejection and a useful tool for organizing thinking. Using this tool, man is better able to construct sets. In essence, this lays the foundations for the mathematization of thinking and develops the ability to construct mathematical concepts.

- A specific paradox does not exist in every mathematical universe; it exists in a context.
- The research context is defined by a function defining an element's membership percentage in a set: the so called "membership function".
- In a classical logic context, the membership function is the typical function $\mu_A(x)=\begin{cases}1, & x \in A \\ 0, & x \notin A\end{cases}$ (King, 1998).
- There are numerous research fields in fuzzy logic. In those fields, the research context is in each case defined by the membership function. It has been discerned that paradoxes are eliminated when the research context changes in a suitable way. In the new context, other paradoxes appear which are inherent to the context.
- The change in context and the mathematic activity linked to it are a fundamental research duty for all those researching the didactics of mathematics.
- Based on the above data, the teacher has a duty to plan suitable teaching environments with a view to optimizing the teaching process. The principle of maximum benefit tells us that optimization is achieved when a concept is "interiorized" to the maximum with the minimum expense of mental activity (i.e. at the cost of the minimum "fuzzy entropy").

REFERENCES

Anapolitanos, DA. 1985. Introduction to the philosophy of mathematics, Nefeli Press, Athens.

Drossos, C. and Papadopetrakis, E. 1985. Introduction to Mathematic Logic, University of Patras, Patras.

Freud, S. 1913. Totem and Taboos, W.W. Norton & Co. Ltd., USA.

Kant, I. 1781. Kritik der reinen Vernunft in 4 Bänden, ubersetzt, hrsg. und mit Anmerkungen von Michail F. Dimitrakopoulos (1983), Athens.

Kosko, BA. 1987. Foundations of Fuzzy estimation theory, University of California, Irvine, USA.

Kosko, B. 1997. Fuzzy Logic the New Science, A. Tsoukaladakis Press, Athens.

Klir, GJ. and Bo, Y. 1995. Fuzzy sets and Fuzzy Logic, printed in the USA.

King, P. 1998. Calculating Intelligence. Eds. P. Tavlos, P. and Kostaraki, E. Athens.

Mytilineos, M. 1993. Logic, A. Stamoulis Press, Athens.

Tzafestas, Spyros. 1994. Intelligent Automatic Control, NTUA Press, Athens.

Canadian Journal of
pure&applied
sciences

EFFECT OF UNCERTAINTIES IN THE ECONOMIC CONSTRAINED AVAILABLE TRANSFER CAPABILITY IN POWER SYSTEMS

*SU Prabha and C Venkataseshaiah
Faculty of Engineering and Technology, Multimedia University, Melaka Campus, 75450 Melaka, Malaysia

ABSTRACT

A key concept in the restructuring of the electric power industry is the ability to accurately and rapidly quantify the capabilities of the transmission system. Available transfer capability (ATC) calculation is a complicated task, which involves the determination of Total transfer capability (TTC) and its two margins -- Capacity Benefit Margin (CBM) and Transmission Reliability Margin (TRM). Transmission transfer capability is limited by a number of different mechanisms including thermal, voltage and stability constraints. ATC is a limit to the amount of power that can be exchanged between two buses or areas. The calculation of ATC has traditionally been a deterministic calculation. However, loads and line status are stochastic phenomena that possess uncertainties. Load flow is an essential tool in the assessment of ATC. Once the TTC is computed under one set of operating conditions or assumptions, it is useful to determine the effect of the uncertainties in the input parameters, namely load and line parameters. This paper presents the impact of these uncertainties on the transfer capability and its expected price. This would be particularly helpful in determining the appropriate reliability margin and the respective ATC. The proposed method has been tested on IEEE 14 bus test system and the results are presented. Further the results are compared with their respective deterministic values.

Keywords: Load flow, available transfer capability (ATC), total transfer capability (TTC), power system planning.

INTRODUCTION

The power system transfer capability indicates how much inter-area power transfers could be increased without compromising system security. Accurate identification of this capability provides vital information for both planning and operation of the power market. According to NERC's definition, *ATC is a measure of the transfer capability remaining in the physical transmission network for future commercial activity over and above already committed uses* (NERC, 1996). ATC can be mathematically defined as the total transfer capability (TTC) less the transmission reliability margin (TRM), less the sum of existing commitments and the capacity benefit margin (CBM), i.e., if there is no existing commitments, ATC can be expressed as, ATC = TTC-TRM-CBM.

TRM accounts for the inherent uncertainty in the system conditions and the need for operating flexibility to ensure reliable system operation as system conditions change. CBM is the transfer capability reserved by load serving entities to ensure access to generation from interconnected system to meet the generation reliability requirements. The currently used methods could be divided into three types, namely Continuation Power Flow (CPF) method, Repeated Power Flow (RPF) method and Security Constrained Optimal Power Flow (SCOPF) method. CPF is a general method for finding the maximum value of a scalar parameter in a linear function

of changes in injections at a set of buses in a power flow problem. In principle, CPF increases the loading factor in discrete steps and solves the resulting power flow problem at each step as formulated by Ajjarapu and Christy (1992). However, since CPF ignores the optimal distribution of the generation and the loading together with the system reactive power, it can give conservative transfer capability results. The CPF, in spite of its popularity has the disadvantage of its complexity. Hamoud (2000) proved that the Repeated Power Flow (RPF) method possesses several advantages which include the ease of implementation and less time to converge. SCOPF method derived by Yan and Chanan (2002) maximize the transfer capability between two control areas assuming all OPF-optimized parameters can be centrally dispatched. All of the above methods consider fixed input parameters (load demand and line parameters) to find the solution. These parameters are considered to be constant and deterministic. But in reality, the loads are uncertain and vary over a range. Currently many TTC techniques emphasizes on maximizing power transfers alone between interconnected areas, hence overlooking market operation considerations. It is of foremost importance that the dispatching of market should be incorporated into transfer capability assessments in the decentralized market. This paper addresses the issue of uncertainty in input parameters and a framework is proposed to quantify TTC with practical condition of market dispatch conditions.

---

*Corresponding author email: prabha.umapathy@mmu.edu.my

MATERIALS AND METHODS

Background of ATC
Quantifying the capabilities of a transmission system for interchange of power has been of interest over many years. A large percentage of ATC calculations performed today utilize linear load flow techniques. ATC indicates how much inter area power transfer could be carried out without compromising system security. Accurate identification of this capability provides vital information for both planning and operation of bulk power market. A system, which can accommodate large inter-area transfers, is generally more robust and flexible than a system with limited capability. ATC can also be expressed as

ATC = TTC – existing transmission commitments

The information of ATC is an important indicator of the system performance in the restructured energy market, as it provides the knowledge of power system capability about the present system condition.

The general procedure to evaluate ATC can be simplified as follows:

- Establish a base case without any violations
- Define a transfer, which includes a power source bus/area and sink bus/area
- Increase power input in the source bus/area and load in the sink bus/area until one of the limit is violated
- Calculate the maximum delivered power from source bus/area to sink bus/area through the transmission network

But due to uncertainty in bus loading, the power flows within a power network becomes uncertain. This in turn implies that the power flow is also probabilistic. Considering the probabilistic aspects of the system input parameters, the transfer capability is also of probabilistic nature. These uncertainties need to be accounted for system planning and operation.

Economic considerations

Market restructuring has posed a new challenge in the context of TTC computation as transfer capability is no longer bounded solely by system operating limits and security limits. In the present scenario, there are two main types of electricity markets: namely bilateral trade type market and Pool markets. The bilateral trade type market is dominated by independent contracts between generators and consumers; while the Pool Co market is a transparent structure that allows instantaneous matching of electricity supply and demand, whereby generators and consumers compete to bid for electricity supply and demand under a set of rules and regulations. It is the responsibility of the Independent System Operator (ISO)

to ensure economic generation, security of the system and reliability prior to dispatching in the decentralized market. Interconnected systems are aimed to improve economic operation and reliability. Therefore it is essential for ISOs to assess ATC and electricity pricing in order to meet the goals.

Proposed method

In electrical power system, the power flow problem is the calculation of line power flow for the given load / generator schedule and network data. It is quite impossible to estimate these precisely, but they could be predicted subject to certain variations. Conventionally the input parameters are considered deterministic by Ejebe *et al*. (1998) and Venkatesh *et al*. (2004). In this paper, the uncertainties due to the input load and line parameters are taken into account. The system is assumed to operate under normal conditions, but load and line parameters vary within certain range. A variation of 10% and 5% are considered for the load parameters and line parameters respectively. Various case studies have been simulated and results of the following are presented.

- System under normal operating conditions
- Uncertainties due to load parameters
- Uncertainties due to line parameters
- Uncertainties due to both load and line parameters

Optimal Power Flow (OPF) is an optimizing tool for power system planning, energy management, etc. This has been briefly discussed by Wood and Woolenberg (1996). Use of OPF is becoming more important in deregulated power industry to deploy the resources optimally. In this paper, the optimization of the ATC problem has been mathematically formulated as below from equations (1 – 5).

Objective Function
Maximize

$$f(x) = Max(\sum_{i \in SD} \Delta P_{Di}) \text{ and}$$

Minimize

$$C_g = \sum_{i=ng} a_i + b_i P_{gi} + C_i P_{gi}^2 \tag{1}$$

The objective function of the OPF reflects the maximum power transfer from one bus/area to another bus/area.

The objective function is subjected to the equality constraint:

- The power flow equation of the power network

$$g(|v|, \theta) = 0 \tag{2}$$

The inequality constraints are: generation limit, transmission line limit and voltage limit.

- Generator limit

$$|P_{Gi}|_{\min} \leq |P_{Gi}| \leq |P_{Gi}|_{\max} \qquad (3)$$

- Transmission line limit

$$|S_{ij}| \leq |S_{ij}|_{\max} \qquad (4)$$

- Voltage limit

$$|V_i|_{\min} \leq |V_i| \leq |V_i|_{\max} \qquad (5)$$

where,

ΔP_{Di} active power increment of load bus

P_{Gi} real power generation at   bus i

P_{Di} real load demand at bus i

n   bus number of the system

V_i voltage magnitude at bus i, j

S_{ij} transmission line MVA limit

C_g total generation cost of the system

a_i , b_i, c_i cost coefficients

Case Study

The IEEE 14 bus test system is used to demonstrate the calculations of ATC using the proposed scheme.   The uncertainties in the input load and line parameters are taken into account.   The simulation is carried out using the MATLAB.   Duane and Bruce (2001) provide an excellent reference for the same.

The diagram of the system is shown in figure1.
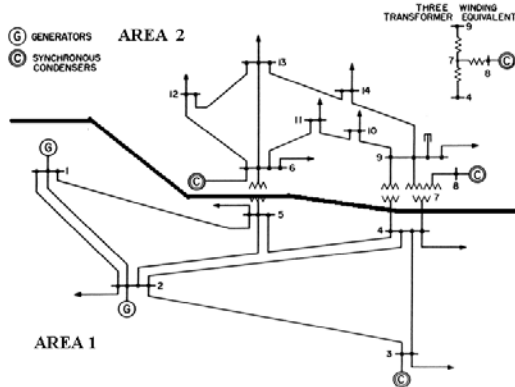
Fig.1. IEEE 14 bus test system.

Bus 1 is the swing bus. The study of ATC and the effect due to uncertainties in the input parameters are carried out by considering bus to bus transfer for the system. The bus data is given in table 1. The active power of all the

generators is kept constant except for the slack bus generator, so that the power increase in the load would be drawn from the slack bus. The maximum and minimum acceptable voltage magnitudes at all load buses are taken as 1.1 and 0.95 p.u. The flow limits in all transmission lines are given in table 2. When the system is operating under the normal operating conditions, the line flows are simulated and this gives the results for base case power flow. This is achieved by using the fast decoupled load flow introduced by Stott and Alsac (1974) which is further modified accordingly Prabha and Venkataseshaiah (2007). The Optimal Power Flow is used to make a step increase in transfer of power. It is taken care that the power flow solution does not have any limit violation. The TTC level is calculated. The ATC (Megawatt) is calculated by using the value of total transfer capability minus the base case transfer in the normal operating condition. In order to incorporate the uncertainties in the input load parameters P(k) and Q(k), a variation of 10% is considered and it is termed as P(k)$_{new}$ and Q(k)$_{new}$.

P(k)   = real power load of kth bus
P(k)$_{new}$ = real power load of kth bus
Q(k)   = reactive power load of kth bus
Q(k)$_{new}$ = reactive power load of kth bus

Similarly a variation of 5% is considered for the uncertainties in line resistance and reactance and R(jj)$_{new}$ and X(jj)$_{new}$ are calculated.

R(jj)   = resistance of the branch – jj
R(jj)$_{new}$ = resistance of the branch – jj
X(jj)   = reactance of the branch – jj
X(jj)$_{new}$ = reactance of the branch – jj

 The proposed simulation is demonstrated on this test case and the results are discussed.

Table 1. Bus Data.

Bus Number	Real Power (MW)	Reactive Power (MVar)	Generation (MW)
1	0	0	0
2	21.7	12.7	40
3	94.2	19	0
4	47.8	-3.9	0
5	7.6	1.6	0
6	11.2	7.5	0
7	0	0	0
8	0	0	0
9	29.5	16.6	0
10	9	5.8	0
11	3.5	1.8	0
12	6.1	1.6	0
13	13.5	5.8	0
14	14.9	5	0

Table 2. Line MVA Limits.

From Bus	To Bus	MVA Limit
1	2	130
1	5	130
2	3	130
2	4	130
2	5	130
3	4	130
4	5	130
4	7	130
4	9	130
5	6	130
6	11	130
6	12	130
6	13	130
7	8	130
7	9	130
9	10	130
9	14	130
10	11	130
12	13	130
13	14	130

RESULTS AND DISCUSSION

The IEEE 14 bus test system is used to perform the simulation. The simulation is performed considering two cases. Case 1 is simulated for the base case load flow without any contingency and case 2 is simulated for calculating ATC. For both cases, the different uncertainties are incorporated as individual sub problems and their results are discussed in this section.

Case 1: The voltage profile for the base case load flow is presented in table 3.

For all the uncertainties, it is observed that the actual real and reactive power generation has increased by around 10% from its original base case value. Also, real and reactive power losses in the lines are significantly increased. Particularly, when line uncertainty alone is taken into account, there is a considerable increase in the real and reactive power losses compared with uncertainty in load parameters.

Case 2: The ATC values calculated for different transactions between the buses are shown in table 4.

The ATC values are calculated for each of the transaction

Table 3. Voltage profile for different uncertainties.

Bus #	Base case	Load variation only	Line variation only	Load & Line variation
1	1	1	1	1
2	1	1	1	1
3	1	1	1	1
4	0.98	0.977	0.979	0.976
5	0.982	0.979	0.981	0.978
6	1	1	1	1
7	0.985	0.982	0.984	0.98
8	1	1	1	1
9	0.979	0.975	0.978	0.973
10	0.975	0.971	0.973	0.969
11	0.984	0.981	0.983	0.98
12	0.984	0.982	0.983	0.981
13	0.978	0.975	0.977	0.974
14	0.959	0.953	0.957	0.951

Table 4. Atc and expected price.

Sending Bus	Receiving Bus	ATC in MW	Expected Price in $	Limiting Element (Bus and Line limits)
3	6	2.41	241	Buses 5 and 6
2	9	8.15	815	Buses 4 and 7
3	13	14.57	1457	Buses 6 and 12
1	13	2.91	291	Line MVA limit 1-2
2	14	16.08	1608	Bus 14
1	3	4.71	471	Line MVA limit 1-2 and Bus14

between all the bus pairs. Also the ATC values are calculated for different uncertainties listed in this paper.

Effect of ATC considering load variation only
It is observed that the line MVA limits for the lines 1-2 got violated earlier than the base case ATC.

Effect of ATC considering line variation only
The voltages of bus 6 and bus 7 are violated and its value reached less than $V_{min.}$ Also, the line MVA limits violated for lines 1-2 earlier than the base case ATC.

Effect of ATC considering both load and line variation
When the uncertainties in both load and line parameters are considered, it is noted that the voltages of bus 4,5,6 and 7 violated and the line MVA limits for lines 1-2 violated much earlier than the base case ATC.

It is understood that whenever the uncertainties exist in load parameters, line parameters or both parameters together, the ATC value is considerably affected. In this paper, only a fixed percentage of variation is considered and the different scenarios are discussed.

CONCLUSION

The ATC calculation is performed by an Optimal Power Flow (OPF) routine, based on a Fast Decoupled power flow algorithm. The program is so designed that the voltage of all the buses, line MVA limits and Generator capacity limits are checked simultaneously in a parallel scheme. In general, the inputs to load flow solutions are considered to be deterministic values. But in reality, these values are subject to uncertainties due to load and line parameter variations. In the present work, these variations are incorporated in the evaluation of ATC. Various cases for uncertainties are simulated. It is observed that the uncertainties affect the allowable transactions between the buses and hence in turn it affects the ATC. The proposed approach is tested on IEEE 14 bus test system and the results are presented and discussed. It is suggested that the proposed method of evaluating ATC along with its electricity prices, considering the input line and load parameter uncertainties, could be useful for planners and operators in interconnected power systems.

REFERENCES

Ajjarapu, V. and Christy, C. 1992. The continuation power flow: A tool for steady state voltage stability analysis. IEEE Transactions on Power Systems. 7:416-423.

Duane, H. and Bruce, L. 2001. Mastering MATLAB 6-A comprehensive Tutorial and Reference, Pearson Education International.

Ejebe, GC., Tong, J., Waight, JG. , Frame, JG., Wang, X. and Tinney, WF. 1998. Available transfer capability calculations. IEEE Transactions on Power Systems. 13:1521-1527.

Hamoud, G. 2000.Assessment of available transfer capability of transmission systems. IEEE Transactions on Power Systems. 15, 1.

NERC. 1996. Available transfer capability definitions and determination.

Prabha, U. and Venkataseshaiah, C. 2007. A novel approach for the assessment of available transfer capability in power systems. College of Science in India. 1(3):1-4.

Stott, B. and Alsac, O. 1974. Fast de-coupled load flow. IEEE Trans. Power. App.Syst. PAS-93(3):859-869.

Venkatesh, P., Gnanadass, R. and Narayana, PP. 2004. Available transfer capability determination using power transfer distribution factors. International Journal of Emerging Electric Power System. 1,2.

Wood, AJ. and Woolenberg, BF. 1996. Power Generation, operation, and control, USA, Wiley and Sons.

Yan, OU. and Chanan, S. 2002. Assessment of available transfer capability and margins. IEEE Transactions on

Yan, OU. and Chanan, S. 2002. Assessment of available transfer capability and margins. IEEE Transactions on Power Systems. 17:463-468.

Canadian Journal of
pure&applied
sciences

INTEGRATED OPTIMAL SOLUTION FOR VARIABLE DETERIORATING INVENTORY SYSTEM OF VENDOR – BUYER WHEN DEMAND IS QUADRATIC

Ajay S Gor[1], *Nita H Shah[2] and Chetan Jhaveri[3]
[1]Pramukh Swami Science and H D Patel Arts College, Kadi
[2]Department of Mathematics, Gujarat University, Ahmedabad
[3]S L Institute of Business Administration, Ahmedabad, Gujarat, India

ABSTRACT

An integrated optimal policy for the vendor and the buyer is studied when units in inventory are subject to deterioration at different rates and demand is quadratic. It is shown numerically that the integrated approach reduces the total joint cost significantly when compared with the independent decision of both the players. To encourage the buyer to place order of larger size, a permissible trade credit is offered by the vendor to the buyer to settle the account. A negotiation factor is incorporated to share the benefits of cost savings.

Keywords: Integrated optimal strategy, deterioration, permissible delay period, quadratic demand.

INTRODUCTION

The inventory models under the assumption of linearly trended demand and exponentially time – varying demand are extensively analyzed by the researchers. When demand is taken as linear, it is assumed that the demand changes uniformly over the time which is not observed in the market, in general. On the other hand, an exponentially time – varying demand means exponential rate of change of demand which is unrealistic for the newly launched products in the market (Silver and Meal, 1969; Silver, 1979; Xu and Wang, 1991; Chung and Ting, 1993, 1994; Bose *et al.*, 1995; Hariga, 1995; Giri and Chaudhuri, 1997; Lin *et al.*, 2000; Mehta and Shah, 2003, 2004). In order to have alternative demand pattern quadratic demand is considered. This type of demand is partially constant, partially varies linearly with time and partially varies exponentially with time. This type of demand is observed for a substitutable products, seasonal goods, fashion apparels etc.

Most of the models so far derived where buyer is the sole decision maker for "when to order and how much to order?" The optimal solution of the buyer may not be agreeable for the vendor. So in competitive global market, an integrated policy should be thought when decision is to be made which is favorable to both the parties. The vendor – buyer integration was first studied by Clark and Scarf (1960). Banerjee (1986) developed a joint lot-size inventory model when production at vendor's end is finite. Goyal (1988) extended Banergee's model by relaxing the assumption of the lot – for –lot production.

Deterioration is defined as the decay, spoilage, evaporation and loss of utility of a product from the original one. Fruit and vegetables, cosmetics and

medicines, electronic items, blood components, radioactive chemicals, agriculture produce are some of the examples of deteriorating commodities. For articles on deteriorating inventory one can refer to Raafat (1991), Shah and Shah (2000) and Goyal and Giri (2001). Yang and Wee (2005) derived a win – win strategy for an integrated system of vendor-buyer when units in inventory are subject to constant rate of deterioration and deterministic constant demand. Shah *et al.* (2008) extended above model by incorporating salvage value to the deteriorated units.

In this article, an integrated vendor – buyer inventory system is studied when units in inventory deteriorate at different rate and demand is quadratic. A negotiation factor is incorporated to share the cost savings. A permissible delay in payment is offered to the buyer by the vendor to make a joint strategy beneficial. A numerical example is illustrated to support the proposed model. Sensitivity analysis is carried out to visualize the changes in cost savings.

Assumptions and Notations
The mathematical model is developed under following assumptions and notations:

Assumptions
1. An inventory system of single – vendor and single – buyer is considered.
2. The demand is quadratic in time t, i.e. $R(t) = a(1 + bt + ct^2)$, where $a > 0$ is constant demand, $0 < b, c < 1$ are rate of linear and exponential demand and t is the time.
3. Shortages are not allowed and lead – time is zero.
4. The deterioration rates of items in vendor's and buyer's inventory are different and proportional to on

---

hand stock in inventory. There is no repair or replacement of deteriorated units during a cycle time.
5. The permissible delay in payment is offered by the vendor to attract the buyer to cooperate in the integrated decision.

Notations

A_b Buyer's ordering cost per order
A_v Vendor's ordering cost per order
C_b Buyer's purchase cost per unit
C_v Vendor's purchase cost per unit
I_b Inventory carrying charge fraction per unit per time unit for buyer
I_v Inventory carrying charge fraction per unit per time unit for vendor
θ_b Deterioration of items in   buyer's inventory system
θ_v Deterioration of items in   vendor's inventory system; $0 < \theta_v < \theta_b < 1$
$I_b(t)$ Buyer's inventory level at instant of time t
$I_v(t)$ Vendor-buyer combined   inventory level at instant of time t
$R(t)$ $= a(1 + bt + ct^2)$ demand rate at the time t, where $a > 0$ is constant demand and $0 < b, c < 1$ are rate of change of demand and t is the time.
n Number of time of orders kept by buyer during cycle time.
K_b Buyer's total cost per time unit
K_v Vendor's total cost per time unit
K Integrated total cost for both vendor and buyer per time unit.
T Vendor's cycle time (a decision variable)
T_b $(= T/n)$, buyer's cycle time (a decision variable)
M Permissible delay period offered by the vendor to the buyer (a decision variable)
r Continuous interest rate

Mathematical Model
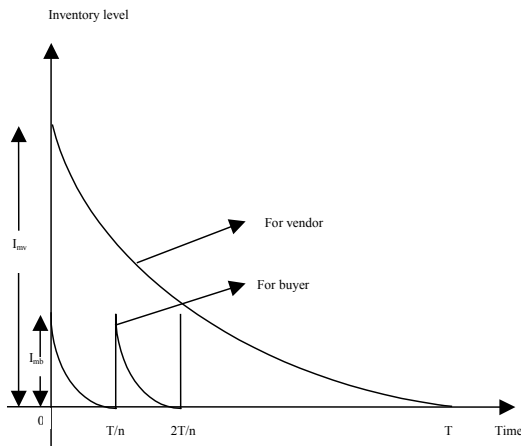Figure 1 represents time-varying inventory status for the vendor and the buyer.

Fig. 1. Time – Inventory status of Vendor and Buyer.

The inventory depletes due to quadratic demand and deterioration rate for both vendor and buyer. The rate of change of inventory for the vendor and the buyer is given by the differential equations:

$$\frac{dI_b(t)}{dt} + \theta_b\, I_b(t) = -a(1 + bt + ct^2)\ 0 \le\ t \le \frac{T}{n} \qquad (3.1)$$

and

$$\frac{dI_v(t)}{dt} + \theta_v\, I_v(t) = -a(1 + bt + ct^2)\ \ 0 \le\ t \le T \quad (3.2)$$

with the boundary conditions $I_b(\frac{T}{n})=0$ and $I_v(T) = 0$, $I_b(0) = I_{mb}$ and $I_v(0) = I_{mv}$.

The solutions of the differential equation are

$$I_b(t) = \frac{a}{\theta_b}[e^{\theta_b(\frac{T}{n}-t)} - 1] + \frac{ab}{\theta_b{}^2}[1 - e^{\theta_b(\frac{T}{n}-t)}] +$$

$$\frac{2ac}{\theta_b{}^3}[e^{\theta_b(\frac{T}{n}-t)} - 1] + \frac{aT}{n^2\theta_b{}^2}[n\theta_b b - 2cn + cT\theta_b]\, e^{\theta_b(\frac{T}{n}-t)}$$

$$+ \frac{a}{\theta_b{}^2}[2ct - \theta_b bt - \theta_b ct^2] \qquad (3.3)$$

and

$$I_v(t) = \frac{a}{\theta_v}[e^{\theta_v(T-t)} - 1] + \frac{ab}{\theta_v{}^2}[1 - e^{\theta_v(T-t)}] +$$

$$\frac{2ac}{\theta_v{}^3}[e^{\theta_v(T-t)} - 1] + \frac{aT}{\theta_v{}^2}[\theta_v b - 2c + cT\theta_v]\, e^{\theta_v(T-t)} +$$

$$\frac{a}{\theta_v{}^2}[2ct - \theta_v bt - \theta_v ct^2] \qquad (3.4)$$

Using $I_b(0) = I_{mb}$ and $I_v(0) = I_{mv}$, the purchase quantities for the buyer and the vendor are

$$I_{mb} = \frac{a}{\theta_b}[e^{\frac{\theta_b T}{n}} - 1] + \frac{ab}{\theta_b{}^2}[1 - e^{\frac{\theta_b T}{n}}] +$$

$$\frac{2ac}{\theta_b{}^3}[e^{\frac{\theta_b T}{n}} - 1] + \frac{aT}{n^2\theta_b{}^2}[n\theta_b b - 2cn + cT\theta_b]\, e^{\frac{\theta_b T}{n}}$$

and

$$I_{mv} = \frac{a}{\theta_v}[e^{\theta_v T} - 1] + \frac{ab}{\theta_v{}^2}[1 - e^{\theta_v T}] +$$

$$\frac{2ac}{\theta_v{}^3}[e^{\theta_v T} - 1] + \frac{aT}{\theta_v{}^2}[\theta_v b - 2c + cT\theta_v]\, e^{\theta_v T}$$

During the cycle time [0, T] , the buyer's holding cost is

$$IHC_b = n C_b I_b \int_0^{\frac{T}{n}} I_b(t)\, dt \ ,$$

Ordering cost is $OC_b = n A_b$ and number units deteriorated is ($I_{mb} - \frac{T}{n} R\left(\frac{T}{n}\right)$).

Hence cost due to deterioration of units is

$$CD_b = n C_b \left(I_{mb} - \frac{T}{n} R\left(\frac{T}{n}\right) \right).$$

Hence, the buyer's total cost, K_b per time unit is

$$K_b = \frac{1}{T}[IHC_b + CD_b + OC_b] \qquad (3.5)$$

The vendor's inventory in the joint two-echelon inventory model is the difference between the vendor-buyer combined inventory and the buyer's inventory. Therefore, vendor's holding cost is

$$IHC_v = C_v I_v \left[\int_0^T I_v(t)\, dt - n \int_0^{\frac{T}{n}} I_b(t)\, dt \right]$$

The units deteriorated at vendor's inventory system is ($I_{mv} - n^* I_{mb}$). Hence, cost due to deterioration of units is $CD_v = C_v(I_{mv} - n I_{mb})$.

and vendor's ordering cost is $OC_v = A_v$.

The vendor's total cost K_v per time unit is

$$K_v = \frac{1}{T} [IHC_v + CD_v + OC_v] \qquad (3.6)$$

The joint total cost; K is is the sum of K_b and K_v. Since $T_b = \frac{T}{n}$, K is the function of discrete variable n and continuous variable T.

Computation Procedure
There are two cases:

Case 1: when vendor and buyer make decision independently.

For given value of n, K_b can be minimized by solving $\frac{\partial K_b}{\partial T_b} = 0$ for T_b.

This solution (n, T_b) minimizes K_v provided

$$K_v (n-1) \geq K_v (n) \leq K_v (n+1) \qquad (4.1)$$

gets satisfied. Then the total cost without integration; K_{NJ} is given by

$$K_{NJ} = \min_n[\min_n K_b + K_v] \qquad (4.2)$$

Case 2 : when vendor and buyer make decision jointly.

The optimum values of T and n must satisfy the following condition simultaneously:

$$\frac{\partial K}{\partial T} = 0 \ \text{ and } \ K(n-1) \geq K(n) \leq K(n+1) \qquad (4.3)$$

The total integrated cost is $K_J = \min_{T,n}[K_b + K_v]$ (4.4)

Clearly, $K_J \leq K_{NJ}$. Hence, total cost savings, Sav_J is defined as $Sav_J = K_{NJ} - K_J$. Let the buyer's cost saving, Sav_b be defined as $Sav_b = \alpha Sav_J$, where α is the negotiation factor and $0 \leq \alpha \leq 1$. When negotiation factor equal to 1, all saving goes to buyer; when it is equal to zero, all saving goes to the vendor. When negotiation factor is 0.5, total savings is equally distributed between the vendor and the buyer. The present value of unit cost after a time interval M permissible credit period is $e^{-r m}$ where r is discounting rate. Solving the following equation

$$R(T) C_b (1 - e^{-r m}) = Sav_b \qquad (4.5)$$

The buyer's permissible delay in payment can be computed as

$$M = \frac{1}{r} \ln \left[\frac{C_b R(T)}{C_b R(T) - Sav_b} \right] \qquad (4.6)$$

Numerical Example and Sensitivity Analysis
To illustrate proposed model, consider following parameter values in proper units:
[a b c A_b A_v C_b C_v I_b I_v θ_b θ_v r] = [40000 0.03 0.04 600 3000 25 15 0.11 0.10 0.20 0.10 0.03]

In table 1, the solution is exhibited for independent and joint decision. The buyer's cost and cycle time increase when both players agree for joint decision. The vendor benefits \$12332 and buyer looses \$10601. This compels buyer not to agree for joint decision. To encourage and attract the buyer to cooperate, vendor offers the buyer a permissible delay in payment of 0.02867 yrs with equal sharing of the benefits. This reduces integrated total cost

defined as PJCR = $\frac{K_{NJ} - K_J}{K_J}$ by 4.2 %.

Table 1. The optimal solution with and without considering joint strategy

	Case 1	Case 2
n	3	1
T_b	0.065865	0.186356
T	0.197594	0.186356
K_b	18274.40	28875.20
K_v	22673.70	10341.40
K	40948.10	39216.60
PJCR	-	4.2285
M	-	0.02867

The sensitivity analysis for buyer's deterioration rate; θ_b, demand; a, exponential demand rate; c; and inventory carrying charge fraction of buyer; I_b is exhibited in table 2 to 5. From table 2, it is observed that increase in deterioration of units in buyer's inventory system decreases total cost savings and permissible delay in payments. The increase in fixed demand; a results in significant decrease cost savings and permissible trade credit is exhibited in table 3. In table 4;c; the exponential rate of change in demand is studied. It is observed that there is significant increase in total cost savings and allowable delay period. The total integrated cost is very sensitive to changes in c. The changes in I_b is studied in table 5. The smaller buyer's inventory carrying charge fraction is required for total cost savings and larger allowable delay period.

CONCLUSION

In this study, a mathematical model is developed for an optimal ordering policy in the joint strategy of vendor-buyer inventory system when demand is quadratic. The deterioration rate of units in vendor-buyer inventory system is considered to be different. It is established that integrated policy lowers the total cost of an inventory system, even though the buyer's cost increases significantly. To encourage the buyer for cooperation, a promotional incentive in terms of trade credit is offered by vendor to the buyer to settle the account.

Table 2.   Sensitivity Analysis of deterioration rate

θ_b	0.10	0.15	0.20	0.25	0.30
K_{NJ}	38697	39676.80	40948.10	42339	43773.70
K_J	35135.54	37232.30	39216.60	41105.17	42911.39
PJCR	9.2034	6.1610	4.2285	2.9141	1.9699
M	0.0589	0.0404	0.02867	.0204	0.014

Table 3. Sensitivity Analysis of demand rate

a	24000	32000	40000	48000	56000
K_{NJ}	31784.7	36656.20	40948.10	44829.10	48398.80
K_J	30246.25	35015.21	39216.60	43014.68	46508.20
PJCR	4.84043	4.4767	4.2285	4.0471	3.9062
M	0.04235	0.03391	0.02867	0.02505	.02238

Table 4. Sensitivity Analysis of demand rate

c	0.04	0.06	0.08	0.10
K_{NJ}	40948.10	40990.10	41034	41081.30
K_J	39216.60	38750.58	38258.80	37735.50
PJCR	4.2285	5.4635	6.7631	8.1443
M	0.02867	0.03705	0.04587	0.05524

Table 5. Sensitivity Analysis of inventory carrying charge fraction of buyer

I_b	0.066	0.088	0.11	0.132
K_{NJ}	38873	39917.10	40948.10	41964.50
K_J	34772.25	37068.43	39216.60	41245.22
PJCR	10.549	7.1364	4.2285	1.7140
M	0.06786	0.04715	0.02867	0.01191

REFERENCES

Banerjee, A. 1986. A joint economic lot size model for purchaser and vendor. Decision Science. 17:292-311.

Bose, S., Goswami, A. and Chaudhari, KS. 1995. An EOQ model for deteriorating items with linear time-dependent demand rate and shortage under inflation and time discounting. Journal of the Operational Research Society. 46(6):771-782.

Clark, A. J. and Scarf, H. 1960. Optimal policies for multi-echelon inventory problem. Management Science. 6:475-490.

Chung, K. J. and Ting, PS. 1993. A heuristic for replenishment of deteriorating items with a linear trend in demand. Journal of the Operational Research Society. 44(12):1235-1241.

Chung, KJ. and Ting, PS. 1994. On replenishment schedule for deteriorating items with time proportional demand. Production Planning and Control. 5:392-396.

Giri, BC. and Chaudhari, KS. 1997. Heuristic model for deteriorating items with shortages time-varying demand and costs. International Journal of System Sciences. 28(2):153-190.

Goyal, SK. 1988. A heuristic for replenishment of trended inventories considering shortages. Journal of the Operational Research Society. 39:885-887.

Goyal, SK. and Giri, BC. 2001. Recent trend in modeling of deteriorating inventory. European Journal of the Operational Research Society. 134:1-16.

Hariga, M. 1995. An EOQ model for deteriorating items with shortages and time-varying demand. Journal of the Operational Research Society. 46(4):398-404.

Lin, C., Tan, B. and Lee, WC. 2000. An EOQ model for deteriorating items with time-varying demand and shortages. International Journal of System Sciences. 31(3):394-400.

Mehta, NJ. and Shah, NH. 2003. An inventory model for deteriorating items with exponentially increasing demand shortages under inflation and time discounting. Invesigacao Operacional. 23:103-111.

Mehta, NJ. and Shah, NH. 2004. An inventory model for deteriorating items with exponentially decreasing demand shortages under inflation and time discounting. Industrial Engineering Journal. 33(4):19-23.

Raafat, F. 1991. Survey of literature on continuously deteriorating inventory models. Journal of the Operation Research Society. 40:27-37.

Shah, NH., Shah, YK. 2000. Literature survey on inventory models for deteriorating items. Economic Annals. 44:221-237.

Shah, NH., Gor, AS. and Wee, HM. 2008 Optimal joint vendor-buyer inventory strategy for deteriorating items with salvage value. Proceedings of 14th computing: The Australian theory of symposium (CATS). 77:63-68.

Silver, EA. and Meal, HC. 1969. A simple modification of the EOQ for the case of a varying demand rate. Production of Inventory Management. 10(4):52-65.

Silver, EA. 1979. A simple inventory replenishment decision rule for a linear trend in demand. Journal of the Operational Research society. 30:71-75.

Xu, H. and Wang, H. 1991. An economic ordering policy model for deteriorating items with time-proportional demand. European Journal of Operational Research. 24:21 -27.

Yang, PC. and Wee, HM. 2005. A win-win strategy for an integrated vendor-buyer deteriorating inventory system. Mathematical Modelling and Analysis. 541-546.

Canadian Journal of
pure&applied
sciences

ON SPECIAL GENERATED GOLDBACH TYPE SEQUENCES OF EVENS WITH A COMMON PRIME

Srilal Krishnan
Department of Mathematics, Iona College, New York, NY, USA

ABSTRACT

The aim of this paper is to study some special sequences of positive even integers that can be expressed as a sum of two primes; one of the primes being common. These special sequences of positive integers are generated by an algorithm. The algorithm, when supplied with a 'suitable' even integer n, and a prime p such that $p < n$, generates the aforementioned sequence of even integers. The study of these generated sequences lead to very interesting conjectures and also a possible alternate method of tackling the Goldbach conjecture. A very interesting feature of the algorithm is that in terms of computational complexity, it is very efficient in expressing a 'suitable' even integer n as a sum of two primes.

Keywords: Special goldbach, type sequences, common prime.

INTRODUCTION AND DISCUSSION

There have been various results in Number Theory that have been motivated by the 'Goldbach Conjecture'. The conjecture states that every even integer greater than 4 is expressible as the sum of two odd primes (Richard, 1994). One of the important results motivated by the Goldbach conjecture is 'Every prime greater than 7 can be expressed as a sum of 3 odd primes', also called Goldbach's weak conjecture. This conjecture has been verified by Vinogradov for sufficiently large odd numbers. Another interesting result that has been proved is that the Generalized Riemann hypothesis implies Goldbach's weak conjecture (Deshouillers *et al.*, 1997). It has also been proven that every large even integer is a sum of four squares of primes and 8330 powers of 2 (Jianya and Liu, 2000). Evidently, this area of Number Theory has become a very important area of research and is of interest to the Mathematical community in general. In this article, we conjecture that given a suitable positive integer n greater than 4 and a fixed prime p, such that $p < n$, a sequence of even integers generated by n can be found satisfying certain conditions and these conditions lead to various interesting results. We will first state the conjecture and follow it up with an algorithm and an example.

Conjecture

Conjecture: Let n be a given positive even integer greater than 4 and let p be a prime number less than n. Then one of the following conditions is satisfied:

a) n generates a sequence of even integers $m_1, m_{2,}...m_n$ and a sequence of primes $q, q_1, p_1, p_{2,}...p_n$ such that

---

*Corresponding author email: skrishnan@iona.edu

$n = q + q_1, m_1 = q + p_{1,} m_2 = q + p_{2,}...m_n = q + p_n$.
In other words, the even integer n and the sequence of even integers generated by n are expressible as the sum of two primes with one prime q in common

b) n generates a sequence of even integers $m_1, m_{2,}...m_n$ and n is expressible as a sum of two primes i.e. $n = q + q_1$ and also every even integer in a subset of the generated sequence is expressible as a sum of two primes with the prime q in common. In other words, the generated sequence of positive even integers $m_1, m_{2,}...m_n$ is either expressible as a sum of two primes with the prime q in common or expressible as the sum of the prime q and another composite positive integer.

c) n generates a sequence of even integers $m_1, m_{2,}...m_n$ and n is not expressible as a sum of two primes but every integer in a subset of the generated sequence is expressible as a sum of two primes with one prime in common. Consequently, if such an n is encountered again in a separate algorithmic process, then that n will not be expressible as a sum of two primes.

d) Given a range of positive even integers $[a, n]$, varying the prime p; $p < n$, enables us to write every even integer in $[a, n]$ as a sum of two primes.

Algorithm

An algorithm for the above conjecture is given below: Let n be an even integer greater than 4 and let the prime $p = 3$.

a) Start with the even number (greater than 4), n.
b) Check if $n = 3 + prime$

c) If not, find the numbers less than n and relatively prime to n i.e. find $\phi(n)$

d) Consider $m_1 = n - \varphi(n)$

e) Now check if $m_1 = 3 + prime$

f) If not repeat steps c) to step e) with m_1 replacing n.

g) Stop when $m_k = 3 + prime$, for some integer k.

h) Denote the prime in step g) by q.

i) Check if $m_{k-1} - q = prime, m_{k-2}$
$- q = prime, m_{k-3} - q = prime...m_1 - q = prime$

We will work out the steps in the algorithm for a given even integer greater than 4, say 156.

Example
The Algorithm for $n=156$ and prime $p=3$

a) $156 \neq 3 + prime$.

b) So find $\phi(156) = 48$.

c) $m_1 = 156 - \phi(156) = 156 - 48 = 108$.

d) Now check if $m_1 = 3 + prime$. But, $108 = 3 + 105$ (105 is not a prime)

e) If not repeat steps b) to step d) with m_1 replacing n.

f) Now $m_1 = 108$.

g) Find $\phi(108) = 36$.

h) $m_2 = 108 - \phi(108) = 108 - 36 = 72$.

i) Now check if $m_2 = 3 + prime$. But, $72 = 3 + 69$ (69 is not a prime)

j) So repeat steps b) to step d) with m_2 replacing m_1.

k) Now $m_2 = 72$.

l) So find $\phi(72) = 24$.

m) $m_3 = 72 - \phi(72) = 72 - 24 = 48$.

n) Now check if $m_3 = 3 + prime$. But, $48 = 3 + 45$ (45 is not a prime)

o) If not repeat steps b) to step d) with m_3 replacing m_2.

p) Now $m_3 = 48$.

q) So find $\phi(48) = 16$.

r) $m_4 = 48 - \phi(48) = 48 - 16 = 32$.

s) Now check if $m_4 = 3 + prime$. $32 = 3 + 29$ (29 is a prime)

t) So $q = 29$.

u) Check   if
$m_{k-1} - q = prime, m_{k-2} - q = prime,...,m_1 - q = prime$.

Note that $48 - q = 48 - 29 = 19 (prime)$. So $48 = 19 + 29$. $72 - q = 72 - 29 = 43 (prime)$. So $72 = 29 + 43$.

v) Next, $108 - q = 108 - 29 = 79 (prime)$. So $108 = 29 + 79$. Finally, $156 - q = 156 - 29 = 127$. So $156 = 29 + 127$.

Note that this has not only accomplished that $156 = 29 + 127$., but also that $72 = 29 + 43$., $48 = 29 + 19$. and $32 = 29 + 3$. The common prime is 29.

The number of steps required to get the common prime 29 is 4.

Tests for the range 4-100
At this stage, we will introduce some terminology. An even integer for which the algorithm works is termed *easy even*, otherwise it is termed *difficult even*. The algorithm generates a sequence of even integers and we call these even integers *intermediate evens*. An intermediate even for an *easy even* is called a *valid intermediate even* if is expressible as a sum of two primes, *one prime being common*. Else it is called an *invalid intermediate even*.

Next we run the algorithm for even integers between 6 and 100 (both inclusive)

The results of the algorithm are given in table 1.

As observed in the above table, in the range 6-100, the algorithm works for 38 even integers and does not work for the remaining 10 even integers. So there are 38 easy evens in the range 6-100 and 10 difficult evens. The difficult evens are 28, 38, 52, 58, 68, 78, 80, 94, 96, 98. Also we observe that for all the easy evens in the range 6-100, the intermediate evens are all valid. The first even integer that is an easy even and also has an invalid intermediate even is 114. The intermediate evens for 114 are 24,36,54,78 and the common prime is 13. Observe that $114 = 13 + 101, 54 = 13 + 41, 36 = 13 + 23, 24 = 13 + 11$ But $78 = 13 + 65$ and 65 is not a prime. So 54, 36, 24 are valid intermediate evens and 78 is invalid intermediate even. From table 1, observe that 78 is a difficult even. So in this situation, the invalid intermediate even is also a difficult even. This seems to be true in general and is a very interesting observation. In other words, if a difficult even is encountered in the algorithmic process, it turns out to be an invalid intermediate even for other even integers. This is noted in part c) of the conjecture.

It would be interesting to observe the changes if the prime p in the algorithm is changed from 3 to 5. Changing the prime 3 to the prime 5 in the algorithm results in the following observations.

Table 1.

Even Integer	Easy Even	Intermediate Evens	Valid Intermediate Even	Invalid Intermediate Even	Common Prime
6	Yes	None	N/A	N/A	3
8	Yes	None	N/A	N/A	5
10	Yes	None	N/A	N/A	7
12	Yes	8	8	N/A	5
14	Yes	None	N/A	N/A	11
16	Yes	None	N/A	N/A	13
18	Yes	8, 12	8, 12	N/A	5
20	Yes	None	N/A	N/A	17
22	Yes	None	N/A	N/A	19
24	Yes	16	16	N/A	13
26	Yes	None	N/A	N/A	23
28	No				
30	Yes	22	22	N/A	19
32	Yes	None	N/A	N/A	29
34	Yes	None	N/A	N/A	31
36	Yes	24,16	24,16	N/A	13
38	No				
40	Yes	None	N/A	N/A	37
42	Yes	22,30	22,30	N/A	19
44	Yes	None	N/A	N/A	41
46	Yes	None	N/A	N/A	43
48	Yes	32	32	N/A	29
50	Yes	None	N/A	N/A	47
52	No				
54	Yes	16,24,36	16,24,36	N/A	13
56	Yes	None	N/A	N/A	53
58	No				
60	Yes	44	44	N/A	19
62	Yes	None	N/A	N/A	59
64	Yes	None	N/A	N/A	61
66	Yes	46	46	N/A	43
68	No				
70	Yes	None	N/A	N/A	67
72	Yes	32,48	32,48	N/A	29
74	Yes	None	N/A	N/A	71
76	Yes	None	N/A	N/A	73
78	No				
80	No				
82	Yes	None	N/A	N/A	59
84	Yes	44,60	44,60	N/A	41
86	Yes	None	N/A	N/A	83
88	Yes	32,48	32,38	N/A	29
90	Yes	46,66	46,66	N/A	43
92	Yes	None	N/A	N/A	89
94	No				
96	No				
98	No				
100	Yes	None	N/A	N/A	97

The prime 3 is replaced by 5 in step b) and the algorithm is run for even integers between 6 and 100 (Table 2).

In the range 10-100, there are 36 easy evens and 10 difficult evens. The difficult evens are 32, 40, 44, 50, 56, 62, 82, 92, 98, and 100 and comparing with the results in table 1, we observe that all of these except 98 were easy evens when the algorithm was run with the prime 3. Thus running the algorithm with the primes p=3 and p=5, we were able to write every even integer in the range 6-100 except 98 as a sum of two odd primes. Replacing *p* by primes less than 100 but other than 3 and 5, enables us to write every even integer in the range 6 to 100 as a sum of two primes.

Table 2.

Even Integer	Easy Even	Intermediate Evens	Valid Intermediate Even	Invalid Intermediate Even	Common Prime
10	Yes	None	N/A	N/A	5
12	Yes	None	N/A	N/A	7
14	Yes	8	8	N/A	3
16	Yes	None	N/A	N/A	11
18	Yes	None	N/A	N/A	13
20	Yes	12	12	N/A	7
22	Yes	None	N/A	N/A	17
24	Yes	None	N/A	N/A	19
26	Yes	8, 14	8, 14	N/A	3
28	Yes	None	N/A	N/A	23
30	Yes	22	22	N/A	17
32	No				
34	Yes	None	N/A	N/A	29
36	Yes	None	N/A	N/A	31
38	Yes	12, 20	N/A	N/A	7
40	No				
42	Yes	None	N/A	N/A	37
44	No				
46	Yes	None	N/A	N/A	41
48	Yes	None	N/A	N/A	43
50	No				
52	Yes	None	N/A	N/A	47
54	Yes	36	36	N/A	23
56	No				
58	Yes	None	N/A	N/A	53
60	Yes	24, 44	24	44	19
62	No				
64	Yes	None	N/A	N/A	59
66	Yes	None	N/A	N/A	61
68	Yes	36	36	N/A	31
70	Yes	46	46	N/A	29
72	Yes	67	67	N/A	67
74	Yes	12, 20, 38	12, 20, 38	N/A	7
76	Yes	None	N/A	N/A	71
78	Yes	None	N/A	N/A	73
80	Yes	48	48	N/A	37
82	No				
84	Yes	79	79	N/A	79
86	Yes	24, 44	24	44	19
88	Yes	None	N/A	N/A	83
90	Yes	66	66	N/A	29
92	No				
94	Yes	None	N/A	N/A	89
96	Yes	64	64	N/A	59
98	No				
100	No				

Tests in an arbitrary range
After having verified the conjecture for the range 6-100, we will next test our algorithm for an arbitrary range of numbers 12000000-12000050 with prime $p=3$ and compile the results (Table 3).

In this range, the algorithm works for 3 numbers, 12000000, 12000020 and 12000032. The algorithm does not work for the remaining 23 numbers. We observe that the number of easy evens have declined and the number of difficult evens have increased.

With the prime '5', the algorithm works for 4 numbers, 12000000, 12000002, 12000022 and 12000034 as seen in table 4.

We conjecture that if we run the algorithm with all primes p less than 12000000, we should be able to express each of the even integer less than 12000000 as a sum of two

Table 3.

Even Integer	Easy Even	Intermediate Evens	Valid Intermediate Even	Invalid Intermediate Even	Common Prime
12000000	Yes	None	N/A	N/A	3
12000020	Yes	None	N/A	N/A	3
12000032	Yes	8800000	N/A	N/A	8799997

Table 4.

Even Integer	Easy Even	Intermediate Evens	Valid Intermediate Even	Invalid Intermediate Even	Common Prime
12000000	Yes	8800000; 5600000; 3680000; 2272000; 1376000; 838400; 505600; 305920; 184064; 92160; 67584	5600000; 1376000; 67584	8800000; 3680000; 2272000; 838400; 505600; 305920; 184064; 92160.	67579
12000002	Yes	6857186; 3918398; 242238; 1139558; 672542; 362150; 217310; 133310; 79990; 49750; 29950; 17990; 11846; 5924; 2964; 2100; 1620; 1188; 828	362150; 17990; 5924; 2964; 2100; 1620; 828	6857186; 3918398; 2242238; 1139558; 672542; 217310; 133310; 79990; 49750; 29950; 11846; 1188;	3
12000022	Yes	8800000	N/A	N/A	8799997
12000034	Yes	8800000	N/A	N/A	8799997

	0 -	1000	2000	3000	4000	5000	6000	7000	8000	9000
■ Working	2145	2000	1753	1699	1648	1648	1541	1534	1611	1566
■ Not Working	2853	3140	3248	3302	3353	3353	3460	3467	3390	3435
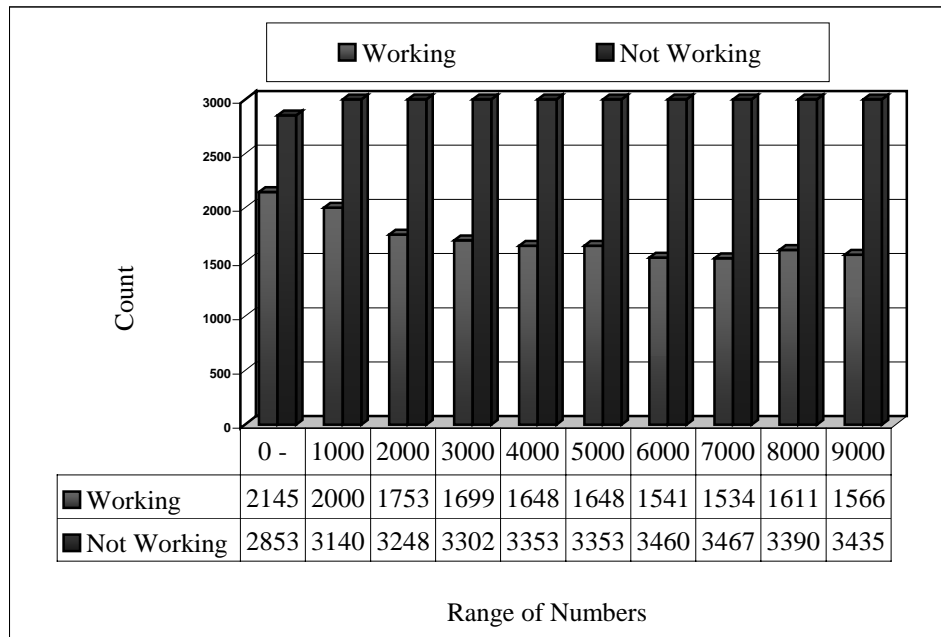
Fig. 1. Algorithmic Behaviour for even numbers from 4-100000.

primes. As seen above, for a fixed p in the algorithm, the number of easy evens appears to be decreasing as n gets larger. This phenomenon is observed for the range of even integers 4-100000 with the prime p=3 in the algorithm. Next, we explore this phenomenon.

Easy evens vs. Difficult evens in the long run
Even for this small range of numbers, the easy evens (blue bars-evens for which the algorithm works) decreases and the difficult evens (red bars-evens for which the algorithm fails) increases as n gets larger (Fig. 1). This along with the Prime Number Theorem might tempt one to speculate that the Goldbach conjecture might be false. But then if we were to vary the prime p in the algorithm and run the algorithm for all primes less than any given n, one might be tempted to speculate that the Goldbach conjecture is true. Further study could be done to determine the relationship between the even integers in the generated sequence to shed some light on these observations.
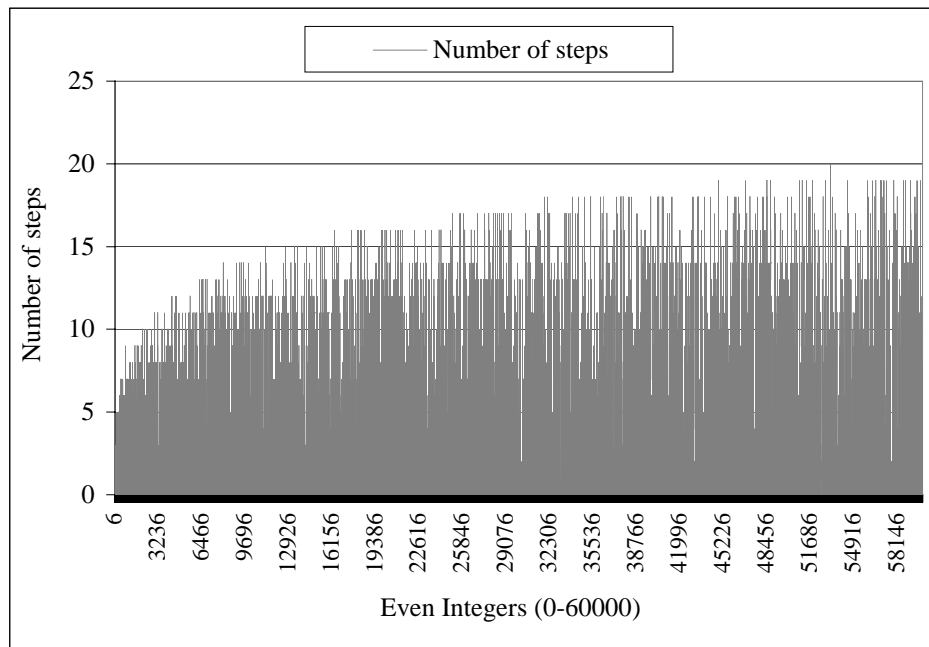
Canadian Journal of Pure and Applied Sciences

Fig. 2. Efficiency of Algorithm.

Efficiency of the Algorithm

The algorithm was tested for its efficiency for even integers in the range 0-60000 with the prime $p = 3$ in the algorithm. We will denote the number of steps required in the algorithm to express an easy even as a sum of two primes by $\chi(n)$. Fig. 2.

The algorithm is efficient in writing the given easy even as a sum of two primes and the maximum number of steps encountered for the range 6-60000 is 20. The graph of $\chi(n)$. seems to display the behavior of a logarithmic function. Also note that by the Prime number theorem, the number of primes less than or equal to a real number x is denoted by $\pi(x)$ and is approximated by $\dfrac{x}{\ln(x)}$. One might again be tempted to explore the relation between $\chi(n)$ and $\pi(n)$.

CONCLUSION

The program written for the algorithm was run on a personal computer with usual resources and an interested reader with access to better computing facilities can run the program by varying the prime p and make more interesting observations. The conjecture that any even that is a '*difficult even*' turns out to be an '*invalid intermediate even*' when it occurs again in a separate algorithmic process is interesting and this lends structure and validity to the algorithm. This has been verified to be true for all the *invalid intermediate evens* tried by the author. The algorithm also presents a different way of looking at the Goldbach conjecture. An interested reader can adopt the algorithm and the various observations and with more work, both numerically and mathematically, come up with interesting concrete results.

REFERENCES

Deshouillers, E., Te Riele. and Zinoviev. 1997. A Complete Vinogradov 3-primes theorem under the Riemann hypothesis. Electronic Research Announcements of the American Mathematical Society 3:99-104.

Jianya, L. and Ming-Chit Liu. 2000. Representation of Even Integers as Sums of Squares of Primes and powers of 2. Journal of Number Theory. 83(2):202-225.

Richard, KG. 1994. Unsolved Problems in Number Theory. (2nd edition). Springer-Verlag. 1:105-107.

Canadian Journal of
pure & applied
sciences

MATHEMATICAL MODEL AND NUMERICAL SIMULATION
OF THE DRUG ELUTING STENTS IN THE CAROTID ARTERY

*Ruchi Agarwal[1], VK Katiyar[2] and Prabhakar Pradhan[1]
Department of Mathematics
[1]Gurukul Kangari University, Haridwar, India, [2]Indian Institute of Technology, Roorkee, India

ABSTRACT

The release of substances in living tissues for therapeutic purposes is becoming quite important in medicine. Therefore the development of appropriate pharmacokinetic models for the numerical simulation of these release processes is important to increase the understanding. One of the main problems of the release processes from stents arises due to the different geometric changes caused by stenting in carotid arteries. To describe the drug release of stents to the wall of artery, a model is presented in this paper using appropriate transient flux boundary condition at the interface of arterial wall and fluid dynamical approach for the blood flow and arterial wall. This numerical simulation can provide a convenient way to study the effects of geometrical changes on the drug release of stents. The results are explained with appropriate plots presented at the end of the paper in order to illustrate the applicability of the present model under study.

Keywords: Drug delivery, stent, FEM, carotid artery, mass release.

INTRODUCTION

Every year, 800,000 angioplasty procedures are performed to treat plaque-clogged carotid arteries. This procedure consists of inserting a meshed metal-wire stent surrounding a balloon catheter into the carotid artery (Fig. 1). The balloon is inflated to expand and insert the stent into the arterial wall. The balloon-catheter is promptly removed while the expanded stent provides structural support in the artery wall to relieve constriction. However, in 15-30% of patients who undergo angioplasty, the artery becomes clogged again in a condition called restenosis in which endothelial cell growth proliferates around the device as part of the body's natural wound-healing response. To address this problem, many leading biomedical companies, such as Johnson & Johnson, Boston Scientific, and Medtronic, have developed drug-eluting stents, which have proven to significantly reduce the rate of restenosis.

The main mechanism of the drug-eluting stent is to allow diffusion of the drug from the polymer coating on the stent, into the arterial wall over a prolonged period of time. There are two layers of the arterial wall: the intima which is closest to the lumen or blood cavity and the adventitia which is the outer layer. Drugs currently on the market act solely in the intima layer by inhibiting microtubule formation and preventing smooth muscle growth in the artery. Any excess drug not taken up in the intima layer will continue to diffuse through the adventitia layer. The positioning of the stent can also be adjusted at the time of placement to allow for the maximal surface

area of contact between the stent surface and the arterial wall.

A number of recent studies has been devoted to the mass transfer process in the arterial wall, modeled as a multi-layered medium, coupled with the transport in the lumen (Kargol *et al.*, 1996; Lally *et al.*, 2005; Hwang *et al.*, 2001; Song *et al.*, 1997; Nicoud *et. al.*, 2005; Chen and Lu, 2006; Li and Kleinstreuer, 2006). Some work has been done to correlate the number and the location of the metallic net structure of a stent with the extension of the perfused area (Morris *et al.*, 2004; Zunino, 2004). Other mathematical models have been developed to predict the release of a substance in a tissue and the influence of the physical properties of the drug. However, computational difficulties in coupling different geometrical scales are reported Nicoud (2002), Chan *et al.* (2007), Alicea *et al.* (2004) and Natarajan and Dehghan (2000). The effect of drug release after stenting has also been studied previously using different vessels like carotid artery, aorta etc. These studied also explained the behavior of the wall shear stress due to stenting (Tortoriello and Pedrizzetti, 2004; Balakrishnan *et al.*, 2005; Pontrelli and de Monte, 2007; Safian *et al.*, 2006; Ackerstaff *et al.*, 2005; Wu *et al.*, 2007. In our study a mathematical model has been presented to include the stent coating by means of an appropriate transient flux boundary condition at the interface to the arterial wall. Though limited to an idealized configuration, the present model is shown to catch most of the relevant and combined aspects of the drug and fluid dynamics using a numerical approach (FEM). Results of numerical simulations are obtained for the drug mass, concentration of drug at the arterial wall and wall shear stress due to stenting is discussed and compared.

---

*Corresponding author email: ruchiiitr83@gmail.com

MATHEMATICAL MODEL

In this study we reduce our observations on the calculations of the drug distribution in the arterial wall of the internal carotid artery and, if needed, the stent coating. The arterial lumen is not considered. We will call the model that considers the transport in the wall and the drug coating the "two domain approach". The model that considers only the wall will be called "one domain approach". The fluid dynamical equations and the geometry of carotid artery is also been considered for the success of the presented strategy. They constitute a link between mass release and CFD and are possible indicators of an optimal delivery.

The two domain approach
In this model the solute transport of the drug is modeled in the stent coating and the arterial wall by using the macroscopic convection-diffusion equation Pontrelli and de Monte (2007). At the initial time, the drug is contained only in the coating Ω_c and it is uniformly distributed at a maximum concentration C_c and subsequently released into the wall.

Thus, the dynamics of the drug in the coating is described by the following 1D diffusion equation,

$$\frac{\partial c_c}{\partial t} - D_c \nabla^2 c_c = 0 \qquad \text{in } \Omega_c$$
$$\nabla c_c \cdot n_c = 0 \quad \text{(symmetry)} \qquad \text{on } \Gamma_w$$
$$\nabla c_c \cdot n_c = 0 \quad \text{(impermeability)} \quad \text{on } \Gamma_a$$
$$c_c = C_c \qquad \text{at } t = 0 \qquad (1)$$

In this work, D denotes the drug diffusivity and n the normal external to the considered medium, c_c denotes the concentration of the coated drug.

Let us now consider the drug dynamics in the wall. Here mass transfer is not governed by diffusion only, but convection due to the filtration velocity of the plasma results equally important and a transport term is added. Furthermore we account for a metabolic process (due to drug binding or chemical reaction) and a linear mass consumption is assumed. Similarly, $c_w = 0$ at Γ_b (the interface between wall and lumen) because of the wash out of the blood stream. Therefore, a fraction of drug is lost in the tissues adjacent to the adventitia and a fraction dispersed in the lumen. Thus, we have the following convection-diffusion-reaction problem

$$\frac{\partial c_w}{\partial t} + \nabla \cdot \left(\frac{\alpha_w}{\varepsilon_w} U_w \cdot c_w - D_w \nabla c_w \right) + \beta c_w = 0$$

in Ω_w

$$c_w = 0 \quad \text{(washout or large distance)} \qquad \text{on } \Gamma_b$$
$$\nabla c_w \cdot n_w = 0 \quad \text{(symmetry)}$$

on Γ_w

$$c_w = 0$$

at $t = 0$ $\qquad\qquad\qquad\qquad\qquad\qquad$ (2)

where U_w is a wall volume-averaged plasma filtration velocity, assumed assigned and constant, ε_w the wall porosity, $\beta > 0$ a consumption rate coefficient. The coefficient α_w is the so-called tortuosity in the axial direction (i.e., the hindrance to drug diffusion imposed by local boundaries).

To close the previous system of equations (1)-(2), the conditions at the coating-wall interface have to be assigned. The two transport domains are coupled by appropriate conditions at the interface Γ. One of them is obtained by imposing continuity of the mass flux

$$D_c \nabla c_c \cdot n_c = D_w \nabla c_w \cdot n_w \quad \text{on } \Gamma \qquad (3)$$

The one domain approach
In this model the transport of the solute is modeled by the macroscopic convection-diffusion equation only in the arterial wall with appropriate boundary conditions. Also, to slow down the drug release rate, a thin film (called *topcoat*) of permeability P (*cm/s*) is located at the interface. A continuous mass flux passes through it orthogonally to the coating film with a possible concentration jump. In the present case, the mass transfer through the topcoat can be described using the second Kedem-Katchalsky equation Kargol *et al.* (1996). Thus, the continuous flux of mass passing across the membrane orthogonally to the coating is expressed by

$$-D_c \nabla c_c \cdot n_c = P(c'_c - c'_w) \quad \text{on } \Gamma \qquad (4)$$
or, alternatively,
$$-D_w \nabla c_w \cdot n_w = P(c'_c - c'_w) \quad \text{on } \Gamma \qquad (5)$$

In equations (4)-(5) the fluid-phase concentration c' is used. This is related to the volume-averaged concentration c through the formula $c' = c/k\varepsilon$, where ε is the porosity and k is the partition coefficient. As one of the last three equations is redundant, we can choose any two of them, for example equations (4) and (5).
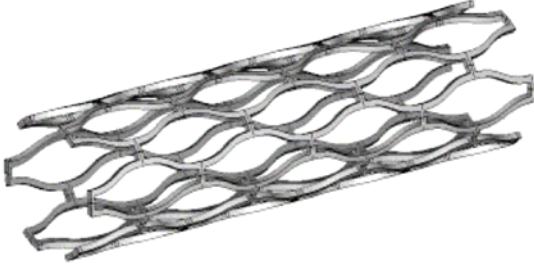
Fig.1. Typical structure of stent.

Fluid dynamical approach

Since the blood flow affects the lumen radius, the knowledge of the shear stress and the pressure drop are of paramount importance. In particular, once the shear stress τ is known, it is possible to experimentally individuate the correct formulation (polymer concentration, amount of crosslinker used, crosslinking time and so on yielding to a solute able to resist, at least sufficiently long time, to the erosive action played by the blood stream. Accordingly, a fluid dynamical analysis is needed. To this aim, we consider an artery of circular cross section R having a rigid wall (that is a reasonable assumption for a stented carotid artery). Let us assume the blood as a viscous fluid with rheological properties governed by a simple power-law viscosity Chen and Lu (2006)

$$\eta(\dot{\gamma}) = K \dot{\gamma}^{n-1} \qquad (6)$$

where $\dot{\gamma}$ is the shear rate,

$$\dot{\gamma} = \left(\frac{1}{2} tr\left(A_1^2 \right) \right)^{\frac{1}{2}} \quad \text{where } A_1 = \nabla v + (\nabla v)^T$$

with v the fluid velocity. In the case of steady and laminar flow, denoting by ρ and p the fluid density and the pressure, the mass and momentum conservation laws are

$$\nabla \cdot v = 0$$

$$\rho \left(\frac{\partial v}{\partial t} + v \cdot \nabla v \right) = \nabla \cdot T - \nabla p \qquad (7)$$

where T is the stress tensor and linearly dependent on the rate of deformation tensor A_1 with a relation of $T = \eta(\dot{\gamma}) A_1$, η represents the viscosity of the blood.

The equations (7) are solved in the present configuration in a tube of length L, letting as inlet condition a velocity profile obtained by integration of equations (7) in the case of an unstented artery

$$v(y,t) = \left(\frac{\Delta p}{2KL} \right)^{\frac{1}{n}} \frac{n}{n+1} R_A^{\frac{n+1}{n}} \left[1 - \left(\frac{y+R}{R_A} \right)^{\frac{n+1}{n}} \right]$$

$$-R \le y \le -d \qquad (8)$$

with $R_A(x,t) = R - d$, d is the thickness of the drug layer.

Numerical Simulation

We are interested in studying the variation of the concentration field in the wall with the geometrical parameters such as the penetration depth s that measures the stent embedding degree, or the mesh length directly related to the void fraction. Our aim is to compare the mass release in the configurations of conventional DES Pontrelli and de Monte (2007). Comparison is difficult because much of the parameters and the materials are intrinsically related to the specific methodology. Let us consider a stent coated by a thin layer of a drug and embedded into the arterial wall, as illustrated in figure 2. The following physical values are fixed for computational experiments:

$$L_y = 0.005 cm \text{ (Length of the stent), } D_w = 7 \times 10^{-8} cm^2 / s$$

All the concentrations (considered as averaged mass per area) are non-dimensionalized with respect to their initial values ($c \rightarrow c/C_c$). For the conventional stent, the following constants are considered:

$$P = 10^{-6} cm / s, \ D_c = 10^{-10} cm^2 / s, \ k_c = 1, \ k_w = 1,$$
$$\varepsilon_c = 0.1, \ \varepsilon_w = 0.61$$

They have been chosen according to a physical basis and in agreement with the typical scales in DES and data literature for the carotid arterial wall and heparin drug in the coating layer (Pontrelli and de Monte, 2007; Ackerstaff *et al.*, 2005; Wu *et al.*, 2007).

In case of preliminary fluid dynamics numerical simulations were independently carried out, based on the following set of parameters:

$$n = 0.6, \ K = 0.02423 Pa.s^{0.6}, \ \rho = 1.064 g / cm^3,$$
$$L = 6.5 cm, \ Q = 240 ml / \min$$

The radius of the carotid artery is taken based on the literature Safian et al., (2006), Ackerstaff *et al.* (2005) and Wu *et al.* (2007). These values imply a pressure gradient $\Delta p / L = 3296 Pa / m$ in equation (8) and a blood pressure p_b upstream the stented region equal to $21331.2 Pa (160 mmHg)$ (such flow rate and pressure values correspond to stressed physiological conditions). The fluid dynamics problem was solved in transient state with a finite element method using unstructured triangular mesh and an implicit second order Euler scheme as time integrator. The numerical problem has been solved by finite element method using MATLAB 7. The spatial domain has been discretized by a not uniform triangular mesh (having a number of elements ≈ 3200) with second order Lagrangian polynomial as shape functions and a Runge-Kutta integration scheme in time, using an
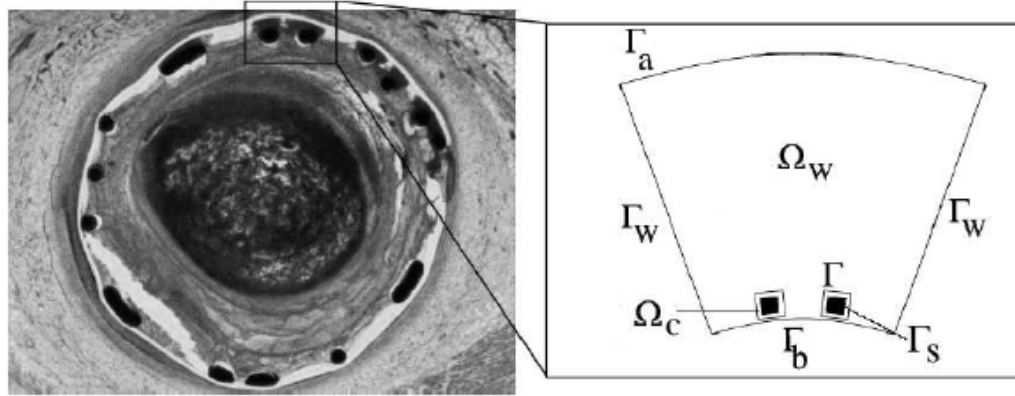
Fig. 2. Schematic representation of the considered transport domains consisting the arterial wall Ω_w and the stent coating Ω_c (Zunino, 2004).
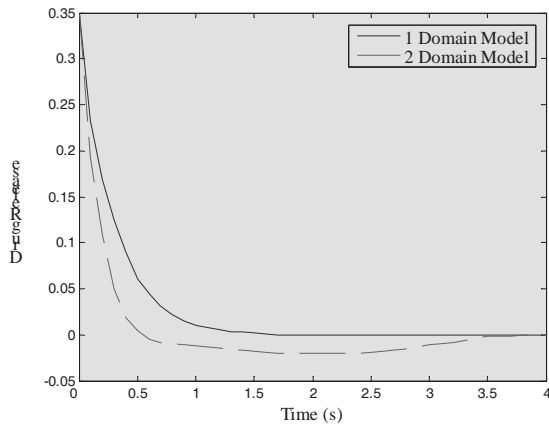

Fig. 3. Comparison of the amount of drug stored in the coating between the 2 domain (lower curve) and the 1 domain model (higher curve).
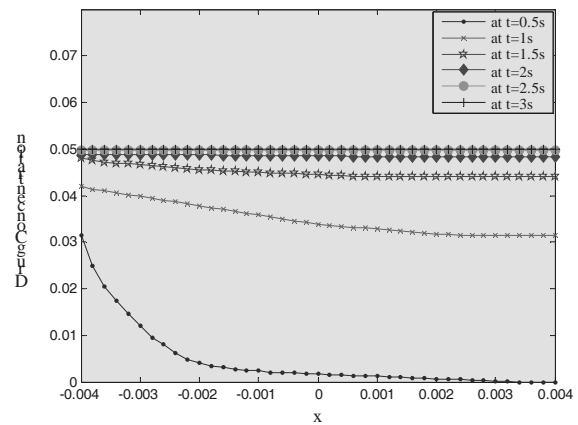

Fig. 4. Concentration profiles in the wall of the 2 domain problem at selected time points: t =0.5s (lowest curve), t=1s, t=1.5s, t=2s, t=2.5s, t=3s (higher curve).

adaptive time step with has been chosen (minimum $\Delta t \approx 10^{-2}$).

RESULTS AND DISCUSSION

Concentration of drug release
As figure 3 displays the comparison of the amount of mass in the coating between the 2 domain approach (lower curve) and the one domain approach (upper curve). It can be pointed out that the release in the simplified model is slower than in the two domain approach. This can be explained by the inner resistance that is taken into account in the computation of the flux (Pontrelli and de Monte, 2007). By taking an approximation of the release using an electrical analogy we linearize our problem. This model can't take into account the occurrence of a boundary layer resulting from the discontinuous initial condition ($c_0 = 1.0$ in the coating and $c_0 = 0.0$ in the wall). It can be seen that the largest error is made in the first time steps.

In figure 4 and 5 we show the concentration profile in the wall due to the drug coated stent. It can be noted that the error of the approximation of the flux at the beginning of the release significantly influences the concentration distribution in the arterial wall (Hwang *et al*., 2001; Pontrelli and de Monte, 2007; Wu *et al*., 2007). The concentration values of the first time step (*t = 0.5s*) is three times lower when using the one domain approach (Fig. 5). The figure 6 shows that drug mass in the coating layer is monotonically decreasing, while mass in the wall, first increasing to a maximum at time *t*, decreases to zero with the same rate as showed by the drug mass in the coating layer. Since drug is absorbed in the semi-permeable membrane, the total mass is not preserved and tends to zero at time large enough (Pontrelli and de Monte, 2007).

Wall shear stress due to stenting
After stenting there exist large hemodynamic changes due to the compliant and rigid surfaces of artery and stent. Figure 7 shows the wall shear stress in the non-stented
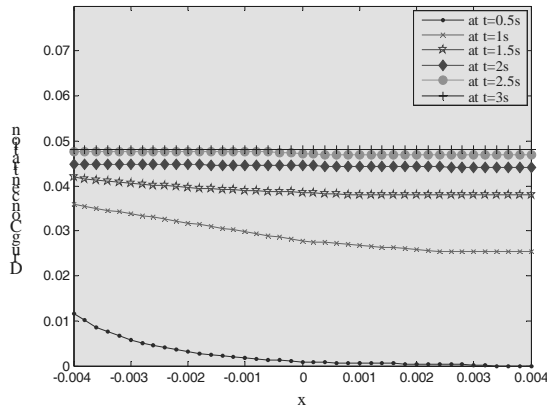
Fig. 5. Concentration profiles in the wall of the 1 domain problem at selected time points: t=0.5s (lowest curve), t=1s, t=1.5s, t=2s, t=2.5s, t=3s (highest curve).
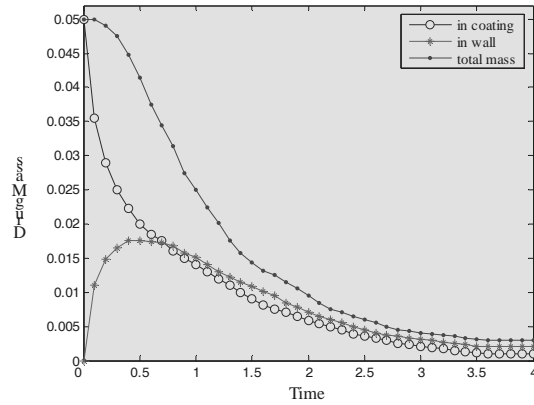

Fig. 6. Dimensionless drug mass in the coating, in the wall and total mass as function of time.
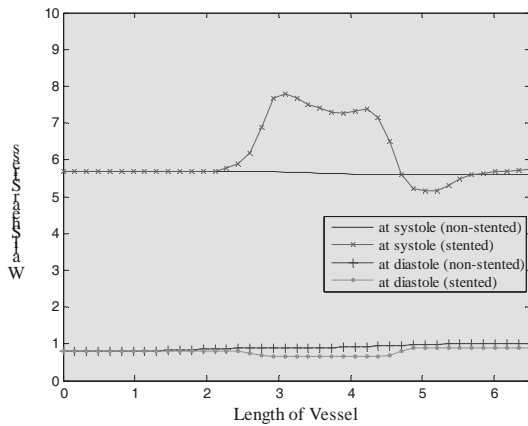

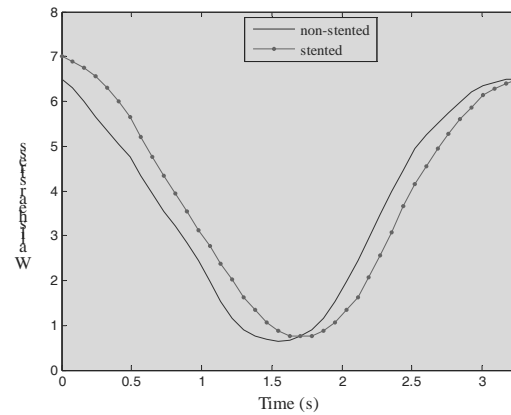Fig. 7. Wall shear stress for systole and diastole assuming both non-stented and stented internal carotid artery.

Fig. 8. Wall shear stress versus time for non-stented and stented internal carotid artery.

and stented internal carotid artery during systole and diastole. At systole, this quantity is larger in the medium part of the stented region than in the non-stented. This is consistent fact that the cross-sectional area at systole is smaller in that region. At diastole, the cross-sectional area within the stent is larger and the wall shear stress is smaller. In the transition zones between stent and artery, the stress experiences larger fluctuations, especially at systole (Tortoriello and Pedrizzetti, 2004; Nicoud, 2002). Extra stress is generated in the upstream transition zone, which acts as a convergence. Conversely, the downstream buffer region acts as a divergence at systole and tends to decrease the stress. Accordingly, the wall shear stress turns out to be locally smaller than its value in the non-stented artery. The transition zones have less effect at diastole, when the flow rate is smaller. Note that the numerical errors are much smaller than the physical effects related to the stent.

The figure 8 shows the time dependence of the stress in mid-region of the stent. The amplitude of this quantity over the cardiac cycle is larger for the stented vessel than for the non-stented (Nicoud *et al.*, 2005). It is worth noting that although the length of the stent is very small compared to the wavelength, the amplitude of the wall shear stress in case of stented behaves more like the non-stented one. If the increase in shear stress at systole is avoided the increase in stress amplitude limits drastically.

CONCLUSION

The release of a substance in a living tissue for therapeutic purposes is becoming quite common in medicine nowadays, through drug delivery devices. Drug-eluting stents are revealed a promising technique for healing the vascular wall and for the treatment of atherosclerosis and restenosis. However, the mechanism of release is quite complex and depends on many concurrent biochemical, physical and individual factors. The model presented here, although some simplifying assumptions, is able to simulate and predict the dynamics of a drug release from a stent. The model can be easily extended to a multi-layered structure, including both a more realistic wall configuration and a novel design for multi-coating DES. In addition, the mathematical formulation is able to incorporate the drug consumption

effect due to the tissue cell binding. The application of the dimensional analysis to the governing equations has indicated that the dynamics of a drug through an eluting stent is fully controlled by only four dimensionless operational parameters. Numerical experiments have been extensively carried out over several typical confi-gurations. Results have shown the influence of the solution on each single parameter, in particular drug mass, concentration in the arterial wall and the wall shear stress due to the stenting. Also, some biomechanical indicators, such as the emptying time of the coating, geometry of the carotid artery, are suggested to obtain an optimal drug elution and a desired tissue concentration.

REFERENCES

Ackerstaff, RGA., Suttorp, MJ., Van den Berg, JC., Overtoom, TTh. C., Vos, JA., Bal, ET. and Zanen, P. 2005. Prediction of early cerebral outcome by transcranial Doppler monitoring in carotid artery bifurcation angioplasty and stenting. Journal of Vascular Surgery. 41 (4):618-624.

Alicea, LA., Alvarado, JJT. and Martinez, AV. 2004. Biofluid Dynamics of the Angioplasty: Ballooning and stenting. Congress on Biofluid Dynamics of Human Body Systems. 1-25.

Balakrishnan, B., Tzafriri, AR., Seifert, P., Groothius, A., Rogers, C. and Edelman, ER. 2005. Strut Position, Blood Flow and Drug Deposition Implications for Single and Overlapping Drug-Eluting Stents. Circulation. 111:2958-2965.

Chan, K. H., Armstrong, J., Withers, S., Malik, N., Cumberland, D. C., Gunn, J. and Holt, CM. 2007. Vascular delivery of c-myc antisense from cationically modified phosphorylcholine coated stents. Biomaterials. 28:1218-1224.

Chen, J. and Lu, XY. 2006. Numerical investigation of the non-Newtonian pulsatile blood flow in a bifurcation model with a non-planar branch. Journal of Biomechanics. 39:818-832.

Hwang, CW., Wu, D. and Edelman, ER. 2001. Physiological Transport Forces Govern Drug Distribution for Stent-Based Delivery. Circulation. 104:600-605.

Kargol, A., Kargol, M. and Przestalski, S. 1996. The Kedem-Katchalsky equations as applied for describing substance transport across biological membranes. Cellular and Molecular Biology Letters. 2:117-124.

Lally, C., Dolan, F. and Prendergast, PJ. 2005. Cardiovascular stent design and vessel stresses: a finite element analysis. Journal of Biomechanics. 38:1574-1581.

Li, Z. and Kleinstreuer, C. 2006. Computational analysis of type II endoleaks in a stented abdominal aortic aneurysm model. Journal of Biomechanics. 39:2573-2582.

Morris, L., Delassus, P., Walsh, M. and McGloughlin, T. 2004. A mathematical model to predict the in vivo pulsatile drag forces acting on bifurcated stent grafts used in endovascular treatment of abdominal aortic aneurysms (AAA). Journal of Biomechanics. 37:1087-1095.

Natarajan, S. and Dehghan, MRM. 2000. A numerical and experimental study of periodic flow in a model of a corrugated vessel with application to stented arteries. Medical Engineering and Physics. 22:555-566.

Nicoud, F. 2002. Hemodynamic changes induced by stenting in elastic arteries. Center for Turbulence Research, CTR Annual Research Briefs. 335-347.

Nicoud, F., Vernhet, H. and Dauzat, M. 2005. A numerical assessment of wall shear stress changes after endovascular stenting. Journal of Biomechanics. 38: 2019-2027.

Pontrelli, G. and de Monte, F. 2007. Mass diffusion through two-layer porous media: an application to the drug-eluting stent. International Journal of Heat and Mass Transfer. 50:3658-3669.

Safian, RD., Bresnahan, JF., Jaff, MR., Foster, M., Bacharach, JM., Maini, B., Turco, M., Myla, S., Eles, G. and Ansel, GM. 2006. Protected Carotid Stenting in High-Risk Patients with Severe Carotid Artery Stenosis. Journal of the American College of Cardiology. 47 (12):2384-2389.

Song, CX., Labhasetwar, V., Murphy, H., Qu, X., Humphrey, WR., Shebuski, RJ. and Levy, RJ. 1997. Formulation and characterization of biodegradable nanoparticles for intravascular local drug delivery. Journal of Controlled Release. 43:197-212.

Tortoriello, A. and Pedrizzetti, G. 2004. Flow-tissue interaction with compliance mismatch in a model stented artery. Journal of Biomechanics. 37:1-11.

Wu, W., Qi, M., Liu, XP., Yang, DZ. and Wang, WQ. 2007. Delivery and release of nitinol stent in carotid artery and their interactions: A finite element analysis. Journal of Biomechanics. 40:3034-3040.

Zunino, P. 2004. Multidimensional Pharmacokinetic Models Applied to the Design of Drug-eluting Stents. Cardiovascular Engineering: An International Journal. 4: 181-191.

EFFECTS OF ENGINE SPEED ON INJECTION TIMING AND ENGINE PERFORMANCE FOR 4-CYLINDER DIRECT INJECTION HYDROGEN FUELED ENGINE

M M Rahman, Mohammed K Mohammed and Rosli Abu Bakar
Faculty of Mechanical Engineering, Universiti Malaysia Pahang
Tun Abdul Razak Highway, 26300 Gambang, Kuantan, Pahang, Malaysia

ABSTRACT

In this study, the effects of engine speed on the injection timing and engine performance of 4-cylinder direct injection (DI) hydrogen fueled engine were investigated. The 4-cylinder direct injection hydrogen engine model was developed utilizing the GT-Power commercial software. This model was employed one dimensional gas dynamics to represent the flow and heat transfer in the components of engine model. Sequential pulse injectors was adopted to the inject hydrogen gas fuel within the compression stroke. Injection timing was varied from 110^0 before top dead center (BTDC) until 0^0 top dead center (TDC) timing. Engine speed was varied from 2000 rpm to 6000 rpm. The validation was performed with the existing previous experimental results. The negative effects of the interaction between ignition timing and injection duration was highlighted and clarified. The acquired results show that the engine speeds are strongly influence on the injection timing and engine performance. It can be seen that the indicated efficiency increases with decreases of engine speed; power increases with the decreases of engine speed; indicated specific fuel consumption (ISFC) increases with increases of engine speed. The injection timing of 60^0 BTDC was the overall optimum injection timing with a compromise.

Keywords: Direct injection engine, injection timing, engine performance, engine speed, hydrogen fueled.

INTRODUCTION

With increasing concern about the energy shortage and environmental protection, research on improving engine fuel economy, hydrogen fueled engine is being developed into a hydrogen fueled engine with manifold injection, direct injection or duel injection according to the fuel supply method (Lee *et al*., 2002; William *et al*., 2002; Eichlseder *et al*., 2003; Kim *et al*., 2005). Of course, the hydrogen fueled engine with direct injection can fundamentally keep backfires from occurring so it can be utilized as a high powered hydrogen power system if the reliability of high pressure direct injection valve is secured (MacCarley and Van Vorst, 1980; Lee *et al*., 2001). Hydrogen gas is characterized by a rapid combustion speed, wide combustible limit and low minimum ignition energy. Such characteristics play a role to decrease engine cycle variation for the safety of combustion. However, it is frequently observed that the values of cycle variation for hydrogen fueled engines with direct injection are higher than those of hydrogen fueled engines with manifold injection or those of gasoline engines, due to a decrease in the mixing period by direct injection in the process of compressing hydrogen gas (Nakagawa *et al*., 1982; Kim *et al*., 1995; Varde and Frame, 1985). In today's modern world, where new technologies are introduced every day, transportation's

energy use is increasing rapidly. Fossil fuel particularly petroleum fuel is the major contributor to energy production and the primary fuel for transportation. Rapidly depleting reserves of petroleum and decreasing air quality raise questions about the future. As world awareness about environment protection increases so does the search for alternative to petroleum fuels. Hydrogen can be used as a clean alternative to petroleum fuels and its use as a vehicle fuel is promising in the effects to establish environmentally friendly mobility systems. So far, the extensive studies were investigated hydrogen fueled internal combustion engines (H$_2$ICE) with external mixture formation fuel delivery system (Stockhausen *et al*., 2002; Kahraman *et al*., 2007). However, the operation of these engines subjected to abnormal combustion, such as pre-ignition, backfire and knocking. Moreover, the power outputs of these hydrogen engines are about 30% less than those of gasoline engines (Tang *et al*., 2002). Therefore the premixed-charge spark ignition engines fueled with hydrogen can be used for significantly limited operation range (Tsujimura *et al*., 2003). It is a common conclusion achieved by many researchers that abnormal combustion can be controlled by direct injection (DI) of hydrogen inside the cylinder (Tsujimura *et al*., 2003; Rottengruber *et al*., 2004; Mohammadi *et al*., 2007).

Direct injection H$_2$ICE requires optimized operation strategies that enable the availability of high power output as well as the abolition of critical exhaust gas emission in

---

*Corresponding author email: mustafizur@ump.edu.my

combination with high efficiencies. Several parameters need to be optimized. Optimization of spark timing, valve timing, combustion chamber geometry, injection parameters such as injection timing, injection duration, injection pressure and nozzle hole numbers/arrangement, swirls intensity, etc. are indeed important to achieve an engine performance level competitive to that in the modern direct-injection diesel engines (Mohammadi *et al.*, 2007).

Injection timing plays a critical role in the phasing of the combustion, and hence the emissions and torque production. Therefore, extensive number of studies indicated the significance of optimization for ignition timing (Sierens *et al.*, 2005; Kim *et al.*, 2006; White *et al.*, 2006; Mohammadi *et al.*, 2007; White *et al.*, 2006) suggested that late injection can minimize the residence time that a combustible mixture is exposed to in-cylinder hot spots and allow for improved mixing of the intake air with the residual gases. This selection can control pre-ignition problem. The main challenge for selecting proper ignition timing that is in-cylinder injection requires hydrogen–air mixing in a very short time. For early injection (i.e., coincident with inlet valve closure (IVC)), maximum available mixing times range from approximately 20 ms to 4 ms across the speed range 1000 rpm to 5000 rpm. In practice, to avoid pre-ignition, start of injection (SOI) is retarded with respect to IVC and mixing times are further reduced. Regarding the behavior of the performance characteristic with ignition timing, there are several contradictories in the literature. Eichlseder *et al.* (2003) found that at low loads (or low equivalence ratio (ϕ)), indicated efficiency (IE) increases with retard of SOI. The increase was shown to be due to the decrease in the compression work caused by differences in mixture gas properties and charge mass with retarded SOI. Eichlseder *et al.* (2003) also found their study at high loads, IE first increases and then decreases with retard of SOI. The reversing trend is assumed to be a consequence of an unfavorable mixture formation. However, Kim *et al.* (2006) reported the results contradictory to Eichlseder *et al.* (2003) results, where they find that, for both low and high loads, indicated efficiency decreases monotonically with retard of SOI. These contradictory findings may be a result of differences in mixture formation (White *et al.*, 2006). Much effort has been devoted to optimize the injection timing which is ranging from IVC until the top dead center (i.e. within the compression stroke). However, Mohammadi *et al.* (2007) optimized the injection timing for three ranges:

- during the intake stroke, where they prevented backfire. However, thermal efficiency and output power are limited by knock due to reduction in volumetric efficiency;

- at compression stroke, where they prevented knock and gives an increase in thermal efficiency and maximum output power; and

at later stage of compression stroke, where they achieved thermal efficiency higher than 38.9% and brake mean effective pressure 0.95MPa.

This study attempts to optimize injection timing that gives the best performance of a 4-cylinders direct injection. The 4-cylinder direct injection hydrogen fueled engine model is developed for this purpose. The effects of engine speed on the injection timing and engine performance such as indicated efficiency indicated specific fuel consumption, power and torque for direct injection hydrogen fueled engine.

MODEL DESCRIPTION

The engine model for an in-line 4-cylinder direct injection engine was developed for this study. Engine specifications for the base engine are tabulated in Table 1. The specific values of input parameters including the AFR, engine speed, and injection timing were defined in the model. The boundary condition of the intake air was defined first in the entrance of the engine. The air enters through a bell-mouth orifice to the pipe. The discharge coefficients of the bell-mouth orifice were set to 1 to ensure the smooth transition as in the real engine. The pipe of bell-mouth orifice with 0.07 m of diameter and 0.1 m of length are used in this model. The pipe connects in the intake to the air cleaner with 0.16 m of diameter and 0.25 m of length was modeled. The air cleaner pipe identical to the bell-mouth orifice connects to the manifold. A log style manifold was developed from a series of pipes and flow-splits. The intake system of the present study model is shown in Fig. 1. The total volume for each flow-split was 256 cm^3. The flow-splits compose from an intake and two discharges. The intake draws air from the preceding flow-split. One discharge supplies air to adjacent intake runner and the other supplies air to the next flow-split. The last discharge pipe was closed with a cup to prevent any flow through it because there is no more flow-split. The flow-splits are connected with each other via pipes with 0.09 m diameter and 0.92 m length. The junctions between the flow-splits and the intake runners were modeled with bell-mouth orifices. The discharge coefficients were also set to 1 to assure smooth transition, because in most manifolds the transition from the manifold to the runners is very smooth. The intake runners for the four cylinders were modeled as four identical pipes with .04 m diameter and 0.1 m length. Finally the intake runners were linked to the intake ports which were modeled as pipes with 0.04 m diameter and 0.08 lengths. The air mass flow rate in the intake port was used for hydrogen flow rate based on the imposed AFR.

Table 1. Engine specification.

Engine Parameter	Value	Unit
Bore	100	mm
Stroke	100	mm
Connecting rod length	220	mm
Piston pin offset	1.00	mm
Total displacement	3142	(cm^3)
Compression ratio	9.5	
Inlet valve close, IVC	-96	^0CA
Exhaust valve open, EVO	125	^0CA
Inlet valve open, IVO	351	^0CA
Exhaust valve close, EVC	398	^0CA

The second major part of the engine model is the powertrain model which is shown in figure 2. In the powertrain, the induced air passes through the intake cam-driven type valves with 45.5 mm of diameter to the cylinders. The valve lash (mechanical clearance between the cam lobe and the valve stem) was set to 0.1 mm. The overall temperature of the head, piston and cylinder for the engine parts are listed in table 2. The temperature of the piston is higher than the cylinder head and cylinder block wall temperature because this part is not directly cooled by the cooling liquid or oil. The burning rate (X_b) of combustion process was modeled using Wiebe function, which can be expressed as Eq. (1):

Table 2. Temperature of the mail engine parts.

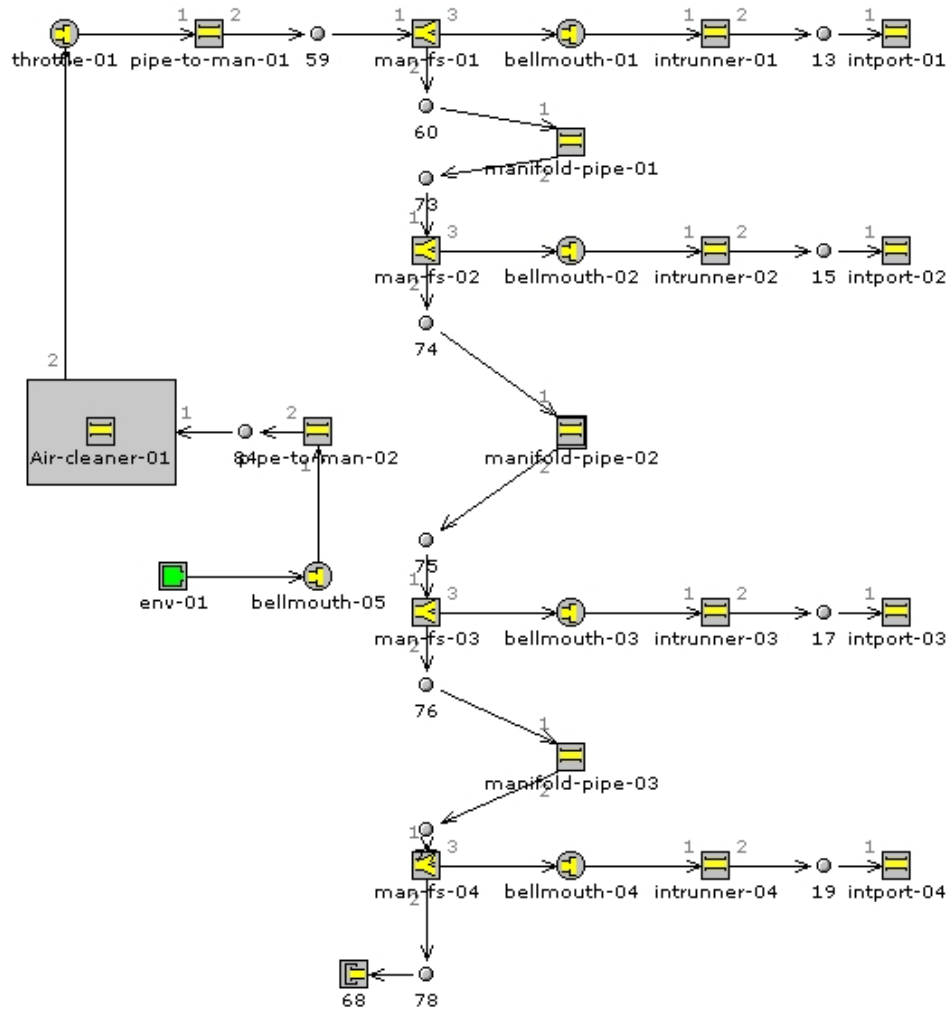| Components	Temperature (K)
Cylinder head	550
Cylinder block wall	450
Piston	590

Fig. 1. Intake system model.

$$X_b = 1 - \exp\left[-a\left(\frac{\theta - \theta_i}{\Delta\theta}\right)^{n+1}\right] \tag{1}$$

where θ is the crank angle, θ_i is the start of combustion, $\Delta\theta$ is the combustion period and a and n are adjustable constants.

Furthermore, the heat transfer in-side the cylinder was modeled using a formula which is closely emulates the classical Woschni correlation. Based on this correlation, the heat transfer coefficient h_c can be expressed as Eq. (2):

$$h_c = 3.26 B^{-0.2} p^{0.8} T^{-0.55} w^{0.8} \tag{2}$$

where B is the bore in meters, p is the pressure in kPa, T is temperature in K and w is the average cylinder gas velocity in m/s.

The hydrogen gas fuel was injected directly in-side the cylinders using the four sequential pulse fuel injectors. The AFR was imposed for the injectors. Then, the injected fuel rate was estimated using the Eq. (3):

$$\dot{m}_{\text{delivery}} = \eta_v \rho_{\text{ref}} N V_d (FAR) \frac{3}{2(PW)} \tag{3}$$

where $\dot{m}_{\text{delivery}}$ is the injector delivery rate (g/s), ρ_{ref} the reference density (kg/m³), N is the engine speed (rpm), V_d is the volume displacement (cm³), FAR is the fuel air ratio and PW is the injection duration (⁰CA).

The four cylinders were then connected together through the engine part which translates the force acting on each piston into the crankshaft (brake) power. Furthermore, engine friction model was imposed to model friction in the engine. The friction mean effective pressure *(FMEP)* was modeled based on Eq. (4):

$$FMEP = 0.4 + \left(0.005 \times P_{\max}\right)$$
$$+ \left(0.09 \times Speed_{mp}\right) + \left(0.0009 \times Speed_{mp}^2\right) \tag{4}$$

where $Speed_{mp}$ represents the mean piston speed and P_{max} is the peak cylinder pressure.

The last major part in the present model is the exhaust system which is shown in figure 3. The exhaust runners were modeled as rounded pipes with 0.03 m inlet diameter, and 80^0 bending angle for runners 1 and 4; and 40^0 bending angle of runners 2 and 3. Runners 1 and 4, and runners 2 and 3 are connected before enter in a flow-split with 169.646 cm³ volume. Conservation of

momentum is solved in 3-dimentional flow-splits even though the flow in GT-Power is otherwise based on a one-dimensional version of the Navier-Stokes equation. Finally a pipe with 0.06 m diameter and 0.15 m length connects the last flow-split to the environment. Exhaust system walls temperature was calculated using a model embodied in each pipe and flow-split. Table 3 are listed the parameters used in the exhaust environment of the model. Figure 4 shows the entire model of 4-cylinder direct injection engine.
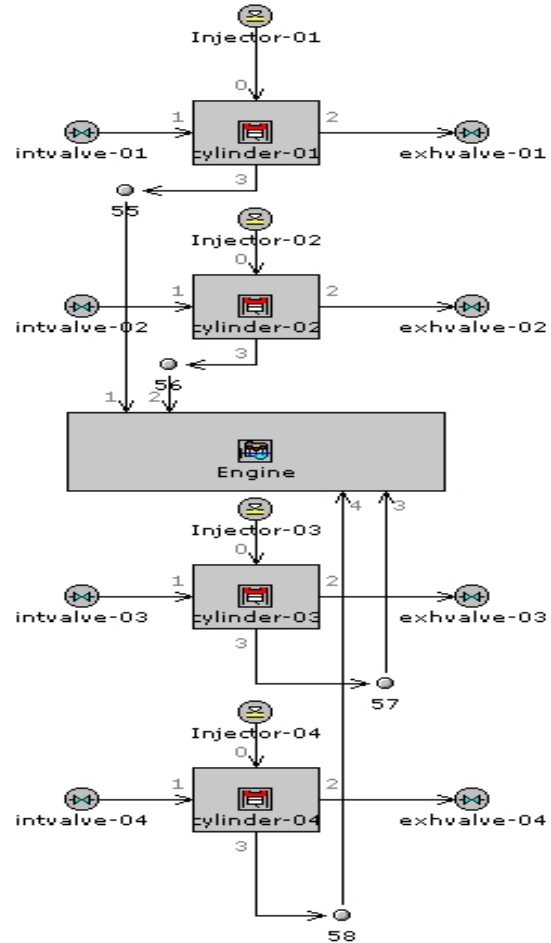

Fig. 2. Powertrain model.

Table 3. Parameters used in the exhaust environment.

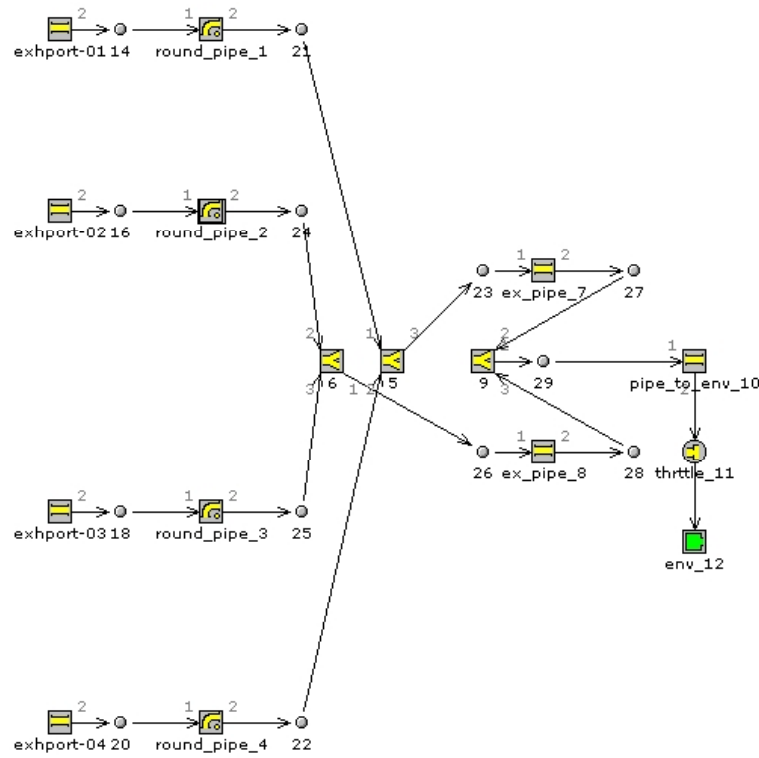| Parameters	Value	Unit
External environment temperature	320	K
Heat transfer coefficient	15	W/m²K
Radiative temperature	320	K
Wall layer material	Steel	
Layer thickness	3	Mm
Emissivity	0.8	

Fig. 3. Exhaust system model.

RESULTS AND DISCUSSION

The results in the following section show the engine performance behavior with injection timing for each condition under investigation. In order to check the validity and accuracy of the present model, comparison with published experimental results in the literature. The effect of AFR with injection timing on the engine performance parameters including efficiency, brake specific fuel consumption, power, and torque were discussed. The effects of engine speed with injection timing on the engine performances are also investigated.

Model Validation

The experimental results obtained from Mohammadi *et al.* (2007) were used for the purpose of validation in this study. Engine specifications of Mohammadi *et al.* (2007) and present single cylinder direct injection engine model are listed in Table 4. For the purpose of validation, single cylinder direct injection engine model converted to 4-cylinder direct injection model. Figure 5 shows the single cylinder direct injection engine model. Engine speed and AFR were fixed at 1200 rpm and 57.216 ($\theta = 0.6$) respectively in this comparison. Injection timing was varied from 130 ^{0}CA BTDC until 70 ^{0}CA BTDC to be coincident with Mohammadi *et al.* (2007).   The correlation of brake thermal efficiency of the baseline model and experimental results obtained from Mohammadi *et al.* (2007) is shown in Fig. 6. It can be

seen that the brake thermal efficiency are good match with the experimental results. Only small deviation was obtained due to the difference between the engine operation conditions that are not mentioned in Mohammadi *et al.* (2007). However, considerable coincident between the single cylinder model and experimental results can be recognized in spite of the mentioned model differences.

Table 4. Specifications of the engines models.

| Engine Parameter	Mohammadi *et al.* (2007)	Present Model	Unit
Bore	102	102	mm
Stroke	105	105	mm
Connecting rod length	NA*	220	mm
Piston pin offset	NA	1.00	mm
Total displacement	857	858	(cm^3)
Compression ratio	11.5	11.5	
Inlet valve close, IVC	580	624^0	ATDC
Exhaust valve open, EVO	130	125^0	ATDC
Inlet valve open, IVO	360	351^0	ATDC
Exhaust valve close, EVC	380	398^0	ATDC

* NA = not available
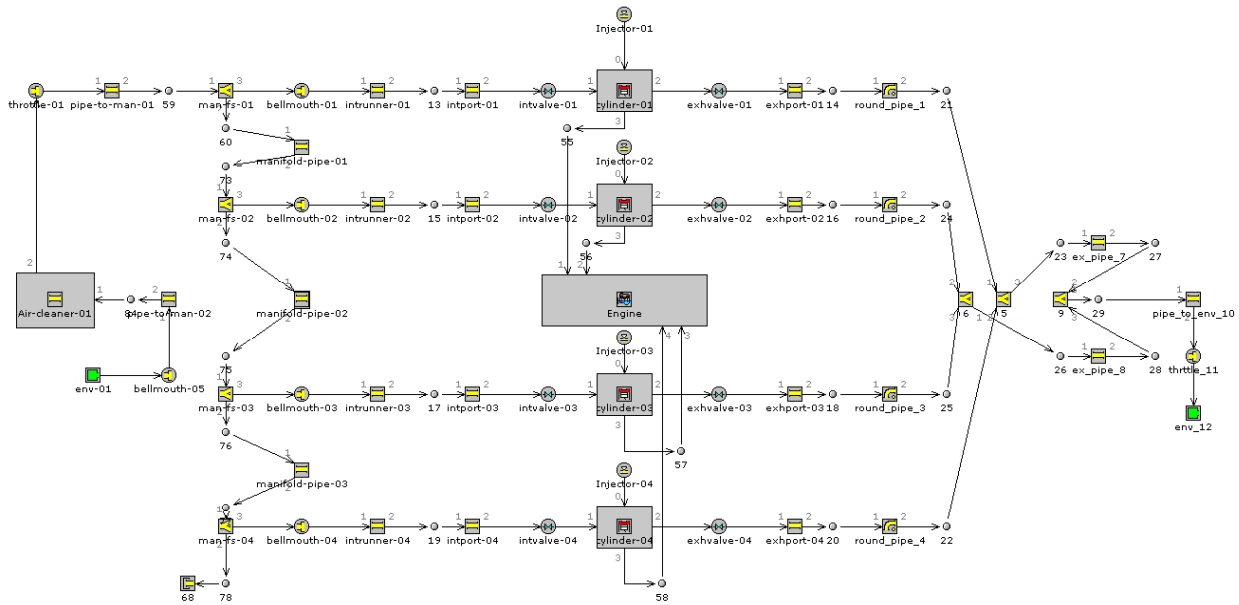
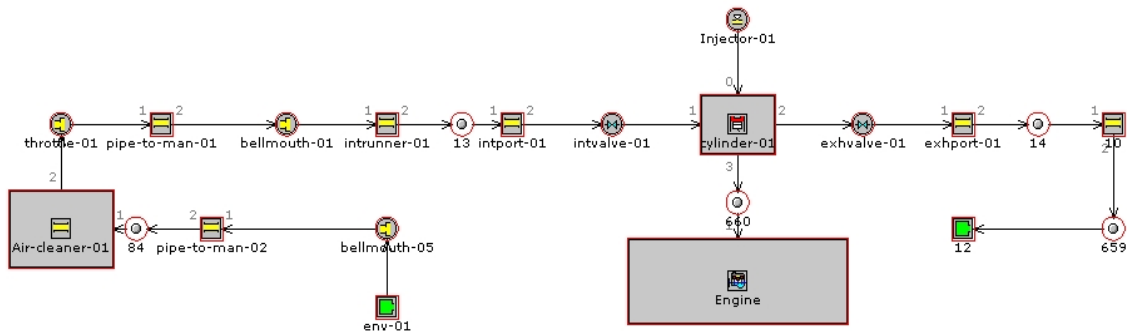Fig. 4. In-line 4-cylinder direct injection hydrogen fueled engine model.

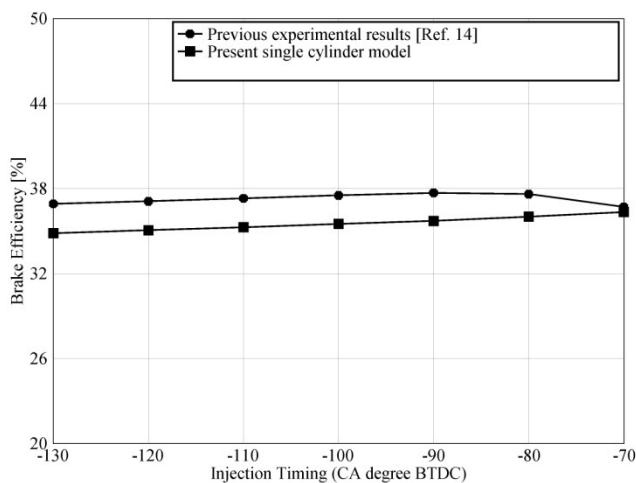Fig. 5. Single cylinder direct injection model.

Fig. 6. Comparison between published experimental results.

Mohammadi *et al*. (2007) and present single cylinder direct injection engine model based on brake efficiency.

Engine Speed Influence on Injection Timing

In the present model, hydrogen was injected into the cylinder within a timing range started just before IVC (-96^0 BTDC) until TDC (0^0). AFR was varied. Amount of hydrogen injected in one cycle is approximately 22 mg/cycle with injection pulse duration of 4.4 ms. Engine speed was varied from 2000 rpm to 6000 rpm. Stoichiometric condition was fixed throughout the investigation.

Figure 7 shows the variation of indicated thermal efficiency with the injection timing for the changes of engine speed. It can be seen that the indicated efficiency increases with decreases of engine speed. From the acquired results, indicated efficiency increases slightly with advances of injection timing towards TDC for all
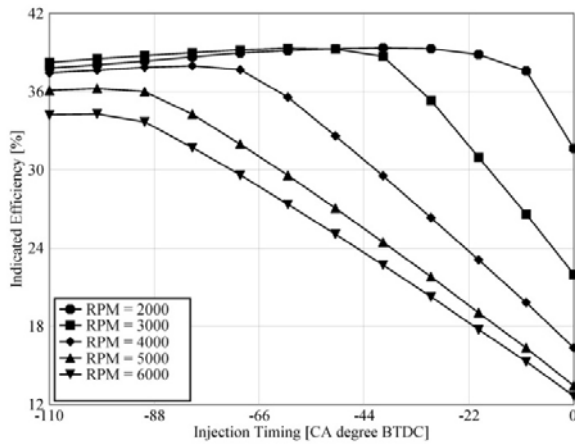
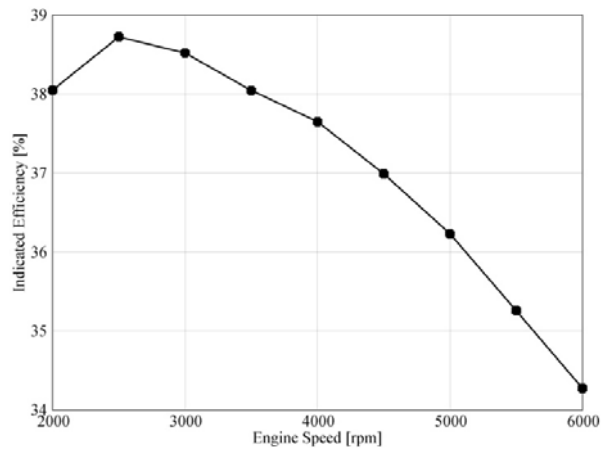Fig. 7. Variation of indicated efficiency with injection timing for various engine speeds.

Fig. 8. Effect of engine speed on indicated efficiency.

engine speed range. It is also seen that the slightly increase of indicated efficiency until about 30^0 BTDC for 2000 rpm then it drops down. The rate of change in indicated efficiency is higher for higher speed and drop occurs early in higher speeds. For very high speeds, the drop happens earlier due to the early interaction between the injection duration and ignition timing. Optimum injection timing under speeds from 2000 rpm to 5000 rpm was in the range (40^0-80^0) BTDC while the optimum injection timing for 6000 rpm was 100^0 BTDC. Obviously, engine speed has a strong contribution in specifying the optimum injection timing. The very limited acceptable injection timing range occurs for high speeds. The selection of the proper injection timing is crucial not only for performance aspects, but also for stable operation. However, one should keep in mind that this situation, described currently, is for stoichiometric condition. It was extensively emphasized by related studies that stable stoichiometric operation is not simple in hydrogen engines and it is accompanied by lot of difficulties. So, with higher AFR best situation is expected. The variation of engine speed on the indicated efficiency is shown in figure 8 for stoichiometric operation and injection timing of 100^0 BTDC. It can be seen that the maximum indicated efficiency is 38.55% corresponding to engine speed 2500 rpm. This variation of indicated efficiency is primarily due to the variation of the volumetric efficiency.

Figure 9 shows the influence of injection timing on ISFC for different engine speeds. Lower engine speeds operation consumes smaller amounts of hydrogen as well as permits wider range for injection timing. The inverse is true for higher speeds where very limited range is available for injection timing. For 2000 rpm, the fuel consumption rates are acceptable throughout the studied range with injection timing of 60^0 BTDC being the optimum. At injection timing of 100^0 BTDC, minimum hydrogen consumed at 6000 rpm.
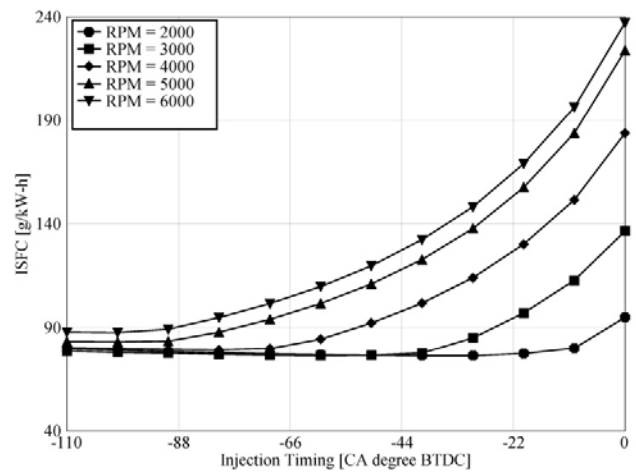

Fig. 9. Variation of ISFC with injection timing for various engine speeds.

Figure 10 illustrates the variation of power with injection timing with respect to changes the engine speed. It can be seen that the power gained increases with increases of engine speed except 6000 rpm case. However, this happens due to the interaction between injection duration and ignition timing. So, it does not represent the normal situation. This occurs at injection timing in the vicinity of TDC. The maximum power of 123 kW was gained at injection timing of 100^0 BTDC for 5000 rpm, while the optimum injection timing that gives at 2000 rpm was 40^0 BTDC and maximum power of 59 kW. The power shows a maximum at engine speed 5000 rpm. It is also observed that the power gained decreases at 6000 rpm due to the increase in the friction losses. The variation of engine speed on the power gained is shown in Fig. 11 for stoichiometric operation and injection timing of 100^0 BTDC. From the acquired results, the power increases slightly with advances of injection timing towards TDC for all engine speed range. It is also seen
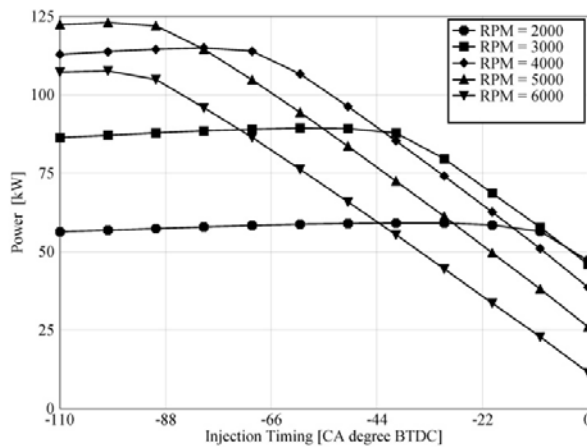
Fig. 10. Variation of power output with injection timing for various engine speeds.

Fig. 11. Effect of engine speed on power.

that the slightly increase of power until about 30^0 BTDC for 2000 rpm then it drops down. The rate of change in power is higher for higher speed and drop occurs early in higher speeds. For very high speeds, the drop happens earlier due to the early interaction between the injection duration and ignition timing and friction losses.

Figure 12 shows the trends of torque with injection timing with the interaction of engine speed effect. Higher torques is produced at lower speed with extra advantages of more acceptable operation range of injection timing. The severe drop with high speed introduces a challenge for injection timing optimization. Based on torque measure, the optimum injection timing throughout the studied speeds, ranged from 40^0 BTDC at 2000 rpm until 100^0 BTDC at 6000 rpm. This extended range imposes more control difficulties. However, compromise solutions can be applied.
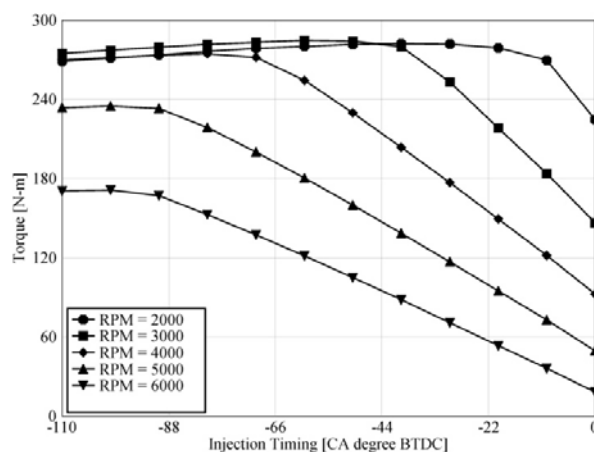

Fig. 12. Variation of torque output with injection timing for various engine speeds.

As a whole, there is optimum injection timing that gives the maximum efficiency, maximum power and torque and minimum desired indicated specific fuel consumption.
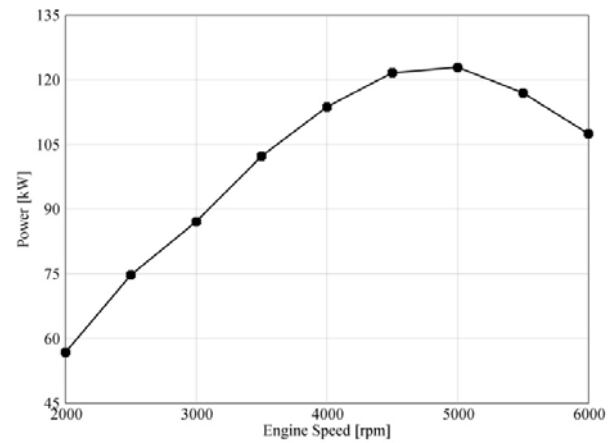
This optimum injection timing strongly depends on the engine speed. Shorter injection duration is required at lean conditions compared to rich conditions. Long injection duration can interact with spark timing which is highly undesirable because of it causes the unstable operation. Therefore, short injection duration is reflected in more extended acceptable injection range. Although, spark timing is restricted with injection timing, the stable operation can be obtained in wide range of engine speed as long as spark timing is adequately selected.

CONCLUSIONS

A computational model was developed for four cylinders direct injection hydrogen fueled internal combustion engine. The main task was to find the optimum injection timing and investigate the influence of AFR and engine speed on this optimum value. The main results are summarized as follows:

1. The engine performance is strongly depends on the engine speed. The engine speed 2500 rpm gives the maximum indicated efficiency.
2. Optimum injection timing depends also strongly on engine speed. Lower speeds advances optimum injection timing toward TDC timing.
3. As a compromise, injection timing of 60^0 BTDC can be considered as optimum for the present engine. However, this is for constant injection timing. The recommended operation is with different injection timing bases on engine speed.
4. Interaction between injection duration and spark timing is strongly undesired and can result in unstable operation. This is was apparent by the unaccepted performance parameters during interaction period. Avoidance of this interaction should take priority in specifying injection timing.
5. Spark timing is another parameter that should be optimized for hydrogen engines, especially direct injection hydrogen engines. The optimum values of

spark timing and injection timing are related strongly. The best way of optimizing injection timing is to fix spark timing on maximum brake torque timing.

ACKNOWLEDGMENTS

REFERENCES

Eichlseder, H., Wallner, T., Freymann, R. and Ringler, J. 2003. The potential of hydrogen internal combustion engines in a future mobility scenario. SAE 2003- 01-2267.

Kahraman, E., Ozcanlı, C. and Ozerdem, B. 2007. An experimental study on performance and emission characteristics of a hydrogen fuelled spark ignition engine. Int J Hydrogen Energy 2007. 32:2066-2072.

Kim, JM., Kim, YT., Lee, SY. and Lee, JT. 1995. Performance characteristics of hydrogen fueled engine with the direct injection and spark ignition system. SAE paper no. 952498.

Kim, YY., Lee, JT. and Caton, JA. 2006. The development of a dual-Injection hydrogen-fueled engine with high power and high efficiency. Journal of Engineering for Gas Turbines and Power, ASME. 128:203-212.

Kim, YY., Lee, JT. and Choi, GH. 2005. An investigation on the cause of cycle variation in direct injection hydrogen fueled engines. Int. J. Hydrogen Energy. 30:69-76.

Lee, JT., Kim, YY. and Caton, JA. 2002. The development of a dual injection hydrogen fueled engine with high power and high efficiency. Proceedings of the 2002 fall technical conference of the ASEM internal combustion engine division. 323-33.

Lee, JT., Kim, YY., Lee, CW. and Caton, JA. 2001. An investigation of a cause of backfire and its control due to crevice volumes in a hydrogen fueled engine. Trans ASME. 123:204-10.

MacCarley, CA. and Van Vorst, WD. 1980. Electronic fuel injection techniques for hydrogen energy. Int J Hydrogen Energy. 5:179-203.

Mohammadi, A., Shioji, M., Nakai, Y, Ishikura, W. and Tabo, E. 2007. Performance and combustion characteristics of a direct injection SI hydrogen engine. Int J Hydrogen Energy. 32:296-304.

Nakagawa, Y., Nakai, M. and Hamai, K. 1982. A study of the relationship between cycle-to-cycle variations of combustion and heat release delay in a spark-ignited engine. JSME. 25:54-60.

Rottengruber, H., Berckmüller, M., Elsässer, G., Brehm, N. and Schwarz, C. 2004. Direct-injection hydrogen SI-engine operation strategy and power density potentials. SAE paper No. 2004-01-2927.

Sierens, R., Verhelst, S. and Verstraeten, S. 2005. An overview of hydrogen fuelled internal combustion engines. Proceedings International Hydrogen Energy Congress and Exhibition IHEC 2005 Istanbul, Turkey. pp. 1-12.

Stockhausen, WF., Natkin, RJ., Kabat, DM., Reams, L., Tang, X., Hashemi, S, Szwabowski., SJ. and Zanardelli, VP. 2002. Ford P2000 Hydrogen Engine Design and Vehicle Development Program. SAE Paper No.2002-01-0240.

Tang, X., Kabat, DM., Natkin, RJ., Stockhausen, WF. and Heffel, J. 2002. Ford P2000 Hydrogen Engine Dynamometer Development. SAE Paper No.2002- 01-0242.

Tsujimura, T., Mikami, A. and Achiha, N. 2003. A Study of Direct Injection Diesel Engine Fueled with Hydrogen. SAE paper No. 2003-01-0761.

Varde, KS. and Frame, GA. 1985. Development of a high-pressure hydrogen injection for SI engine and results of engine behavior. Int. J. Hydrogen Energy. 10(11):743-48.

White, CM, Steeper, RR. and Lutz, AE. 2006. The hydrogen-fueled internal combustion engine: a technical review. Int. J. Hydrogen Energy. 31:1292–1305.

Stockhausen, WF., Natkin, RJ., Kabat, DM., Reams, L., Tang, X., Hashemi, S., Szwabowski, SJ. and Zanardelli, V. 2002. Ford P2000 hydrogen engine design and vehicle development program. SAE 2002- 01-0240.

Canadian Journal of
pure&applied
sciences

INFLUENCE OF VOLUMETRIC FLOW RATE AND TEMPERATURE ON MASS TRANSFER IN COMPOSITE CERAMIC MEMBRANES FOR MEMBRANE REACTORS

*A Hussain[1], A Seidel-Morgenstern[2,3] and E Tsotsas[3]
[1]Centre for Chemical Engineering and Material Sciences, (CCE&MS)
National University of Science and Technology (NUST), Islamabad, Pakistan
[2]Institute of Process Engineering, Otto-von-Guericke-University Magdeburg, Germany
[3]Max-Planck-Institut für Dynamik komplexer technischer Systeme Magdeburg, Germany

ABSTRACT

A dimensionless analysis of isobaric diffusion process has been conducted on both membrane sides to see the influence of volumetric flow rate and temperature on mass transfer. This analysis is based on the reduced form of dusty gas model appropriate for the evaluation of isobaric diffusion process in membrane reactors. The component mass balances in the two gas compartments are calculated by ignoring axial dispersion in terms of Bodenstein's number. Influence of volumetric flow rate and temperature on mass transfer in membrane reactors is evaluated in this work. Results are presented in form of dimensionless quantities solved by subsequent transformations.

Keywords: Dusty gas model, Isobaric diffusion, axial dispersion, mass transfer, membrane reactor.

INTRODUCTION

Multilayer asymmetric membranes usually consist of permselective material as a thin film on one or a series of porous supports, which provide the required mechanical stability without dramatically reducing the total transmembrane flux (Biesheuvel *et al.*, 1999). Such membranes are the primary component of membrane reactors and every reactor model must describe transport kinetics through the membrane accounting for its complicated structure. Many researchers have contributed to the characterization of porous inorganic membranes for their use in membrane reactors by identifying and validating the mass transfer parameters of the membrane during the recent years (Meixner and Dyer, 1998; Beuscher and Gooding, 1999; Tuchlenski *et al.*, 1997; Tuchlenski *et al.*, 1998; Capek and Seidel-Morgenstern, 2001; Uchytil *et al.*, 2000; Thomas *et al.*, 2001; Thomas, 2003). The axial spread along the membrane is characterized by a dispersion coefficient depending on the diffusivity and the fluid velocity. The influence of axial dispersion on mass transfer is normally neglected while modelling the membrane reactors. Though chemical reaction is not considered yet, the catalytic partial oxidation of hydrocarbons like butane to maleic acid anhydride is the background of the investigation. Thus present work focuses on the independent and separate analysis of isobaric binary diffusion through multilayer tubular ceramic membranes (porous aluminium oxide) to understand the effects volumetric flow rate and temeperature on the diffusion process, which is necessary

*Corresponding author email: arshad-ccems@nust.edu.pk

for modeling and optimization of membrane reactors. The paper is organized by first giving an overview of the mathematical modeling of isobaric diffusion in tubular membrane reactors. Then the model used for mass transfer is transformed into dimensionless form. Subsequently, the results of simulation analysis conducted for the isobaric diffusion process are discussed.

Mass transfer model

The Dusty Gas Model (DGM) has been used to describe mass transfer through the porous membrane. The model is based on the idea of considering the solid phase as large molecules ("dust") in a multicomponent gas mixture in order to capture the complex combination of viscous flow, Knudsen diffusion and molecular diffusion in porous media (Mason and Malinauskas, 1983). Viscous flow is bulk, non-separating flow caused by total pressure gradients, while in the Knudsen regime the transport is controlled by molecule-wall interactions, so that the molecules travel independently from each other. In contrary, molecule-molecule interactions define the molecular (ordinary, continuum) diffusion.

In its general form, the dusty gas model for species j in a mixture of N components is expressed by the relationship

$$\sum_{k=1,k\neq j}^{N} \frac{\tilde{x}_k \dot{n}_j - \tilde{x}_j \dot{n}_k}{D_{jk}^e} + \frac{\dot{n}_j}{D_{K,j}} = -\frac{P}{\tilde{R}T}\nabla\tilde{x}_j - \frac{\tilde{x}_j}{\tilde{R}T}\left(1 + \frac{B_0}{\eta_j D_{K,j}}\bar{P}\right)\nabla P$$

where   j = 1 to N.

(1)

The driving forces are included in the right-hand part of eq. (1) in terms of total pressure and molar fraction

(partial pressure) gradients, while the resulting fluxes, $\dot{n}_j$, appear at the left-hand side of the equation.

The mass balance for gas flowing in the annulus has been formulated in one-dimensional way to

$$D_{ax,o}\frac{d^2\widetilde{x}_{j,o}}{dz^2} - \frac{d}{dz}\left(u_{g,o}\frac{n_{g,o}}{n_{g,o,in}}\widetilde{x}_{j,o}\right) + \frac{2\pi r_{m,o}}{F_o n_{g,o,in}}\dot{n}_{j,m,o} = 0. \tag{2}$$

In the tube it holds

$$D_{ax,i}\frac{d^2\widetilde{x}_{j,i}}{dz^2} - \frac{d}{dz}\left(u_{g,i}\frac{n_{g,i}}{n_{g,i,in}}\widetilde{x}_{j,i}\right) - \frac{2\pi r_{m,i}}{F_i n_{g,i,in}}\dot{n}_{j,m,i} = 0. \tag{3}$$

The boundary conditions at the inlet and outlet of annulus and tube are taken after Danckwerts,
z = 0:

$$u_{g,o}\left(\widetilde{x}_{j,o,in} - \widetilde{x}_{j,o}\right) + D_{ax,o}\frac{d\widetilde{x}_{j,o}}{dz} = 0, \tag{4}$$

$$u_{g,i}\left(\widetilde{x}_{j,i,in} - \widetilde{x}_{j,i}\right) + D_{ax,i}\frac{d\widetilde{x}_{j,i}}{dz} = 0, \tag{5}$$

z = L:

$$\frac{d\widetilde{x}_{j,o}}{dz} = 0, \qquad \frac{d\widetilde{x}_{j,i}}{dz} = 0. \tag{6a,b}$$

At the membrane-gas interphaces it is:

$$\dot{n}_{j,m,o} = \beta_{g,o} n_{g,m,o}\left(\widetilde{x}_{j,m,o} - \widetilde{x}_{j,o}\right), \tag{7a}$$

$$\dot{n}_{j,m,i} = \beta_{g,i} n_{g,m,i}\left(\widetilde{x}_{j,i} - \widetilde{x}_{j,m,i}\right). \tag{7b}$$

The relationship between flow rates and fluxes can be written as

$$\dot{n}_{j,m,o} = \dot{N}_j/\left(2\pi r_{m,o}L\right), \tag{8a}$$

$$\dot{n}_{j,m,i} = \dot{N}_j/\left(2\pi r_{m,i}L\right). \tag{8b}$$

The coefficients for Knudsen and for molecular diffusion can be expressed in the form

$$D_{K,j} = \frac{4}{3}K_0\sqrt{\frac{8\widetilde{R}T}{\pi\widetilde{M}_j}} \tag{9}$$

and

$$D_{jk}^e = F_0 D_{jk}, \tag{10}$$

respectively. Consequently the model has three parameters B_0, K_0 and F_0, for capturing the influence of the structure of any specific porous body on viscous flow, bulk diffusion and molecular diffusion.

With the additional assumption of tortuous, mono-dispersed capillaries, which are neither interconnected, nor change their cross-sectional area with their length, the mentioned three parameters of the dusty gas model can be expressed as

$$B_0 = F_0\frac{d_P^2}{32}, \tag{11}$$

$$K_0 = F_0\frac{d_P}{4}, \tag{12}$$

$$F_0 = \frac{\varepsilon}{\tau}, \tag{13}$$

and are, thus, reduced to a set of only two morphological parameters, namely

$$d_p = \frac{8B_0}{K_0}, \tag{14}$$

the diameter of the assumed cappilaries, and

$$\frac{\varepsilon}{\tau} = \frac{(K_0)^2}{2B_0}, \tag{15}$$

Binary diffusion coefficients, D_{jk}, have been calculated in the present work by means of the Chapman-Enskog equation Reid *et al*. (1987).

Non-dimensional form of the model equations
Axial dispersion represents the transport in axial direction superimposed on that due to convection (Gunn, 2004; Tsotsas and Schlünder, 1988). The inclusion of axial dispersion coefficient in the mass transfer model might cause concentration gradients at the entrance of measuring cell but it is generally assumed that it has no considerable influence on the overall diffusion process in composite membranes. Hence, the component mass balances in the two gas compartments are calculated by ignoring axial dispersion. At low gas velocities, i.e. in the laminar flow regime, the dispersion is mainly caused by diffusion. The component mass balance equations (eqs (2) and (3)) considering simultaneous convection and diffusion in the flow system have been transformed to dimensionless form for annulus and tube respectively, yielding

$$\frac{1}{Bo_{o,in}}\frac{d^2\widetilde{x}_{j,o}^*}{d\zeta^2} - \frac{d\left(u_{g,o}^* n_{g,o}^* \widetilde{x}_{j,o}^*\right)}{d\zeta} + \frac{\dot{N}_{j,o}^*}{\widetilde{x}_{j,in}^{av}} = 0, \tag{16}$$

$$\frac{1}{\text{Bo}_{i,in}} \frac{d^2 \widetilde{x}_{j,i}^*}{d\zeta^2} - \frac{d\left(u_{g,i}^* n_{g,i}^* \widetilde{x}_{j,i}^*\right)}{d\zeta} + \frac{\dot{N}_{j,i}^*}{\widetilde{x}_{j,in}^{av}} = 0,$$
(17)

where

$$\zeta = \frac{z}{L},$$
(18)

$$\text{Bo}_{o,in} = \frac{u_{g,o,in}L}{D_{ax,o}}, \qquad \text{Bo}_{i,in} = \frac{u_{g,i,in}L}{D_{ax,i}},$$
(19a,b)

$$\dot{N}_{j,o}^* = \frac{\dot{N}_j}{F_o n_{g,o,in} u_{g,o,in}},$$

$$\dot{N}_{j,i}^* = \frac{\dot{N}_j}{F_i n_{g,i,in} u_{g,i,in}},$$
(20a,b)

$$u_{g,o}^* = \frac{u_{g,o}}{u_{g,o,in}}, \qquad u_{g,i}^* = \frac{u_{g,i}}{u_{g,i,in}},$$
(21a,b)

$$n_{g,o}^* = \frac{n_{g,o}}{n_{g,o,in}}, \qquad n_{g,i}^* = \frac{n_{g,i}}{n_{g,i,in}},$$
(22a,b)

$$\widetilde{x}_{j,o}^* = \frac{\widetilde{x}_{j,o}}{x_{j,in}^{av}}, \qquad \widetilde{x}_{j,i}^* = \frac{\widetilde{x}_{j,i}}{x_{,j,in}^{av}}.$$
(23a,b)

The average inlet molar fraction of regarded component

$$\widetilde{x}_{j,in}^{av} = \frac{u_{g,in}^* n_{g,in}^* F^* \widetilde{x}_{j,o,in} + \widetilde{x}_{j,i,in}}{u_{g,in}^* n_{g,in}^* F^* + 1},$$
(24)

is calculated by considering

$$u_{g,in}^* = \frac{u_{g,o,in}}{u_{g,i,in}}, \quad n_{g,in}^* = \frac{n_{g,o,in}}{n_{g,i,in}}, \quad F^* = \frac{F_o}{F_i}.$$
(25a,b,c)

The required boundary conditions for mass transfer are also transformed to

$$\zeta = 0: \quad u_{g,o}^* = 1, \quad u_{g,i}^* = 1,$$
(26a,b)

$$\zeta = 1: \quad d\widetilde{x}_{j,o}^* / d\zeta = 0, \quad d\widetilde{x}_{j,i}^* / d\zeta = 0,$$
(27a,b)

$$\zeta = 0: \quad \widetilde{x}_{j,o,in}^* - \widetilde{x}_{j,o}^* + \frac{1}{\text{Bo}_{o,in}} \frac{d\widetilde{x}_{j,o}^*}{d\zeta} = 0,$$
(28)

$$\widetilde{x}_{j,i,in}^* - \widetilde{x}_{j,i}^* + \frac{1}{\text{Bo}_{i,in}} \frac{d\widetilde{x}_{j,i}^*}{d\zeta} = 0,$$
(29)

$$\widetilde{x}_{j,o,in}^* = \frac{\widetilde{x}_{j,o,in}}{\widetilde{x}_{j,in}^{av}}, \qquad \widetilde{x}_{j,i,in}^* = \frac{\widetilde{x}_{j,i,in}}{\widetilde{x}_{j,in}^{av}}.$$
(30a,b)

The convective boundary conditions at the membrane have been transformed as

$$\frac{\dot{N}_{j,o}^*}{\widetilde{x}_{j,in}^{av}} = \frac{n_{g,m,o}}{n_{g,o,in}} \text{NTU}_{o,in} \left(\widetilde{x}_{j,m,o}^* - x_{j,o}^*\right),$$
(31)

$$\frac{\dot{N}_{j,i}^*}{\widetilde{x}_{j,in}^{av}} = \frac{n_{g,m,i}}{n_{g,i,in}} \text{NTU}_{i,in} \left(x_{j,i}^* - \widetilde{x}_{j,m,i}^*\right),$$
(32)

by considering

$$\widetilde{x}_{j,m,o}^* = \frac{\widetilde{x}_{j,m,o}}{\widetilde{x}_{j,in}^{av}}, \qquad \widetilde{x}_{j,m,i}^* = \frac{\widetilde{x}_{j,m,i}}{\widetilde{x}_{j,in}^{av}},$$
(33a,b)

$$\text{NTU}_{o,in} = \frac{\beta_{g,o} A_{m,o}}{\dot{V}_{g,o,in}},$$
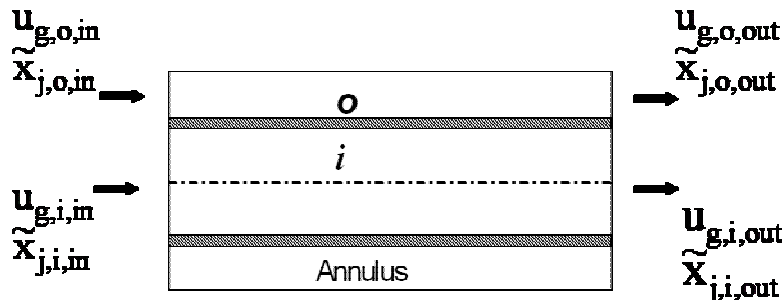

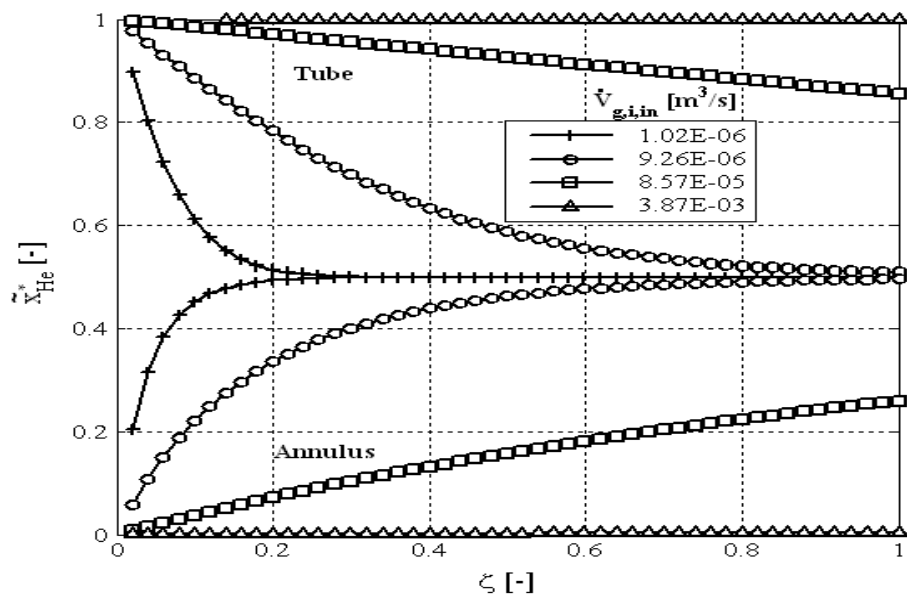Fig.1 . Experimental set-up for the isobaric diffusion experiment.

Fig. 2a. Mole fraction of helium (in annulus and tube) vs. dimensionless length; influence of volumetric flow rate on composition profiles of helium.
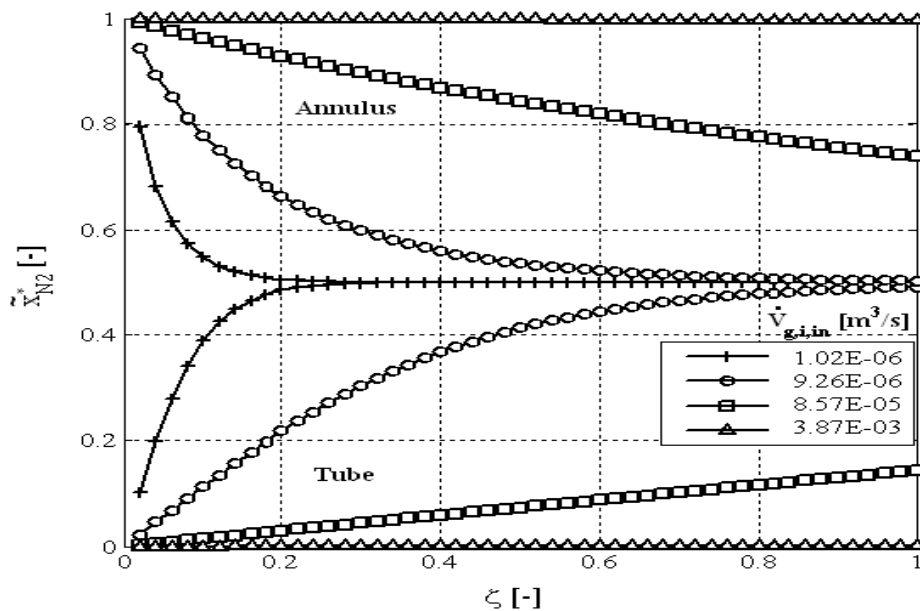

Fig. 2b. Mole fraction of nitrogen (in annulus and tube) vs. dimensionless length; influence of volumetric flow rate on composition profiles of nitrogen.

$$NTU_{i,in} = \frac{\beta_{g,i} A_{m,i}}{\dot{V}_{g,i,in}}.$$

(34a,b)

Dimensionless gas volumetric flow rates are defined as

$$\dot{V}_{g,o}^* = \frac{\dot{V}_{g,o}}{\dot{V}_{g,o,in}}, \qquad \dot{V}_{g,i}^* = \frac{\dot{V}_{g,i}}{\dot{V}_{g,i,in}}.$$

(35a,b)

and are equal to $u_{g,o}^*$ and $u_{g,i}^*$ (eqs (21a,b)) for the isothermic case. All simulations have been conducted with ProMoT/Diva. The dusty gas model is applied for quantifying mass transfer in every membrane layer (M1). The structural parameters of investigated inorganic membrane (M1) have been successfully identified and validated "Hussain et al. (2006)". The values of structural parameters of the each membrane layer are given in Table
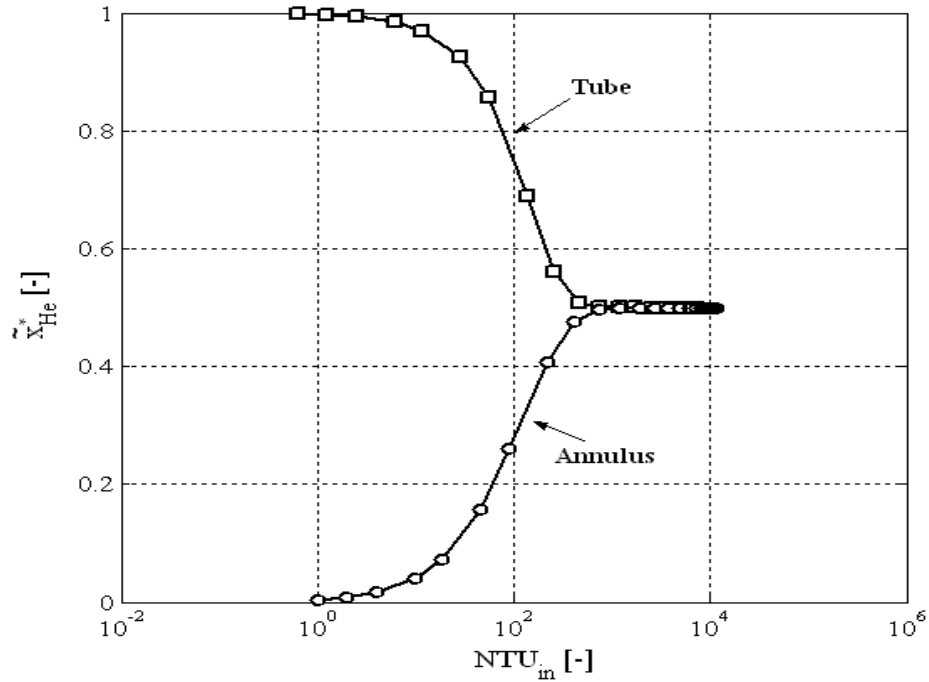
Fig. 3a. Mole fraction of helium (in annulus and tube) vs. the respective number of transfer units.
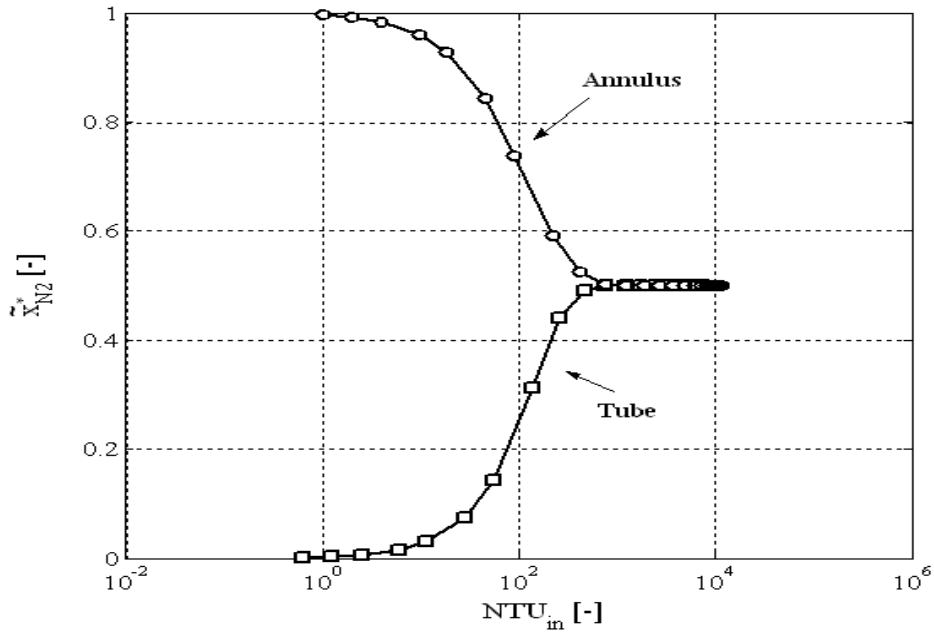

Fig. 3b. Mole fraction of nitrogen (in annulus and tube) vs. the respective number of transfer units.

1. A binary system of nitrogen (annulus) and helium (tube) has been considered for the simulations.

MATERIALS AND METHODS

Experimental method

Though focus is not on the experimental technique to investigate the diffusion process, however, figure 1 recapitulates the principle of isobaric diffusion experiment used in order to validate the mass transport parameters of the membrane and study the influence of different parameters on isothermal, isobaric diffusion process in a tubular membrane reactor. Notice that the sketch realistically shows the reactor geometry, consisting of a shell-side (annulus, index ''o'') and a tube-side (index ''i'') space.
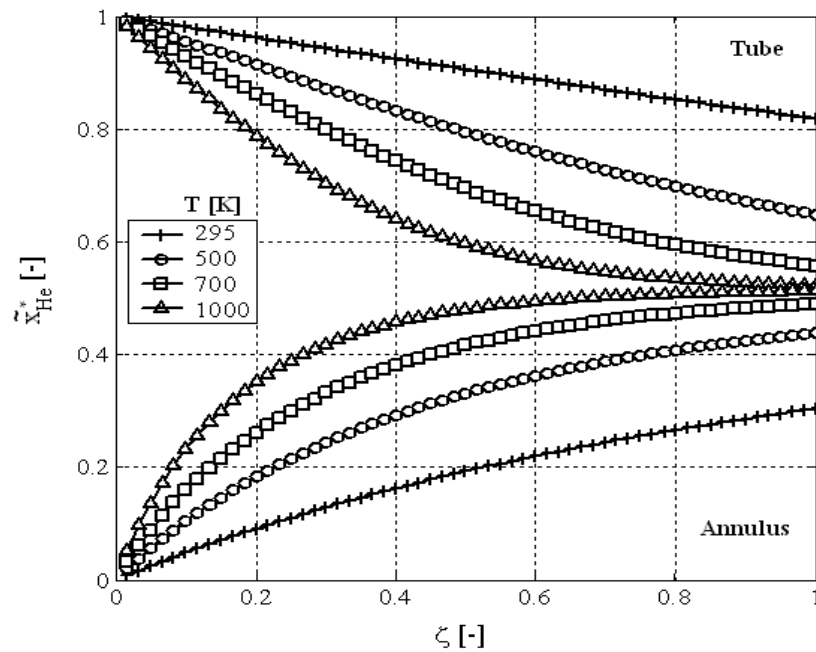
Fig. 4a. Mole fraction of helium (in annulus and tube) vs. dimensionless length; influence of temperature on composition profiles of helium.
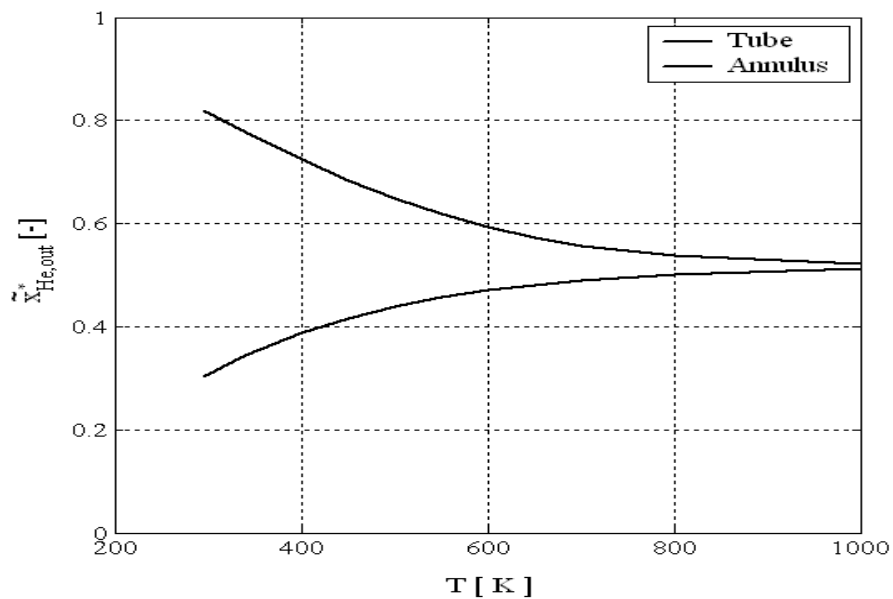

Fig. 4b. Mole fraction of helium at the outlet of annulus and tube vs. temperature.

RESULTS AND DISCUSSION

Influence of volumetric flow rate

In this case plug flow is assumed outside the boundary layer ($D_{ax} = 0$) and the influence of volumetric flow rate $(\dot{V}_{g,i,in} = \dot{V}_{g,o,in})$ on composition in terms of dimensionless quantities and numbers is investigated. By keeping all other parameters constant at $D_{ax} = 0$, the inlet volumetric flow rate of tube (i) and annulus (o) is varied at the same rate from 1.02×10^{-6} to 3.87×10^{-3} m³/s. The boundary or operating conditions used for the simulations of Figs 2 and 3 are:
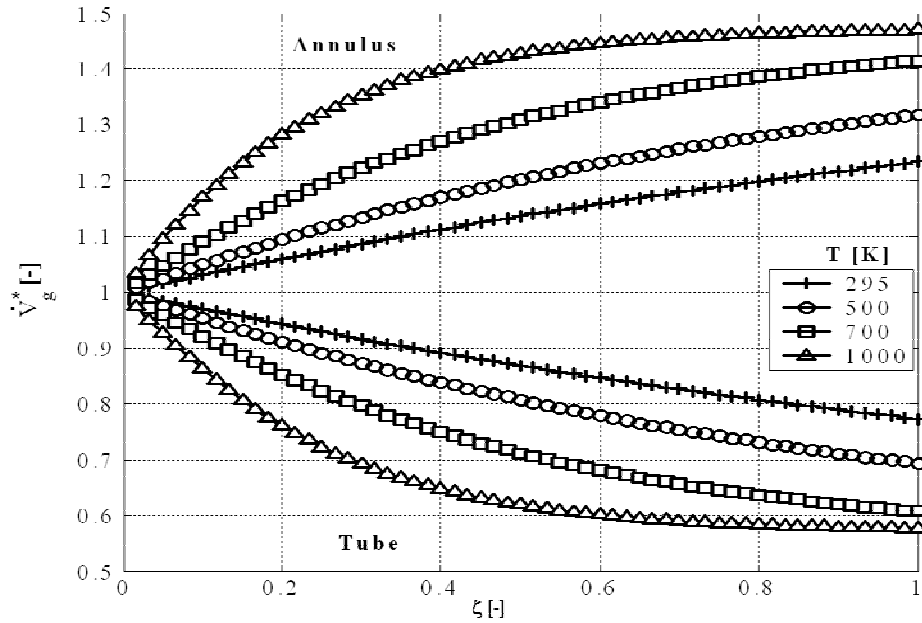
Fig. 5a. Dimensionless volumetric flow rate (in annulus and tube) vs. dimensionless length; influence of temperature on volumetric flow rates.
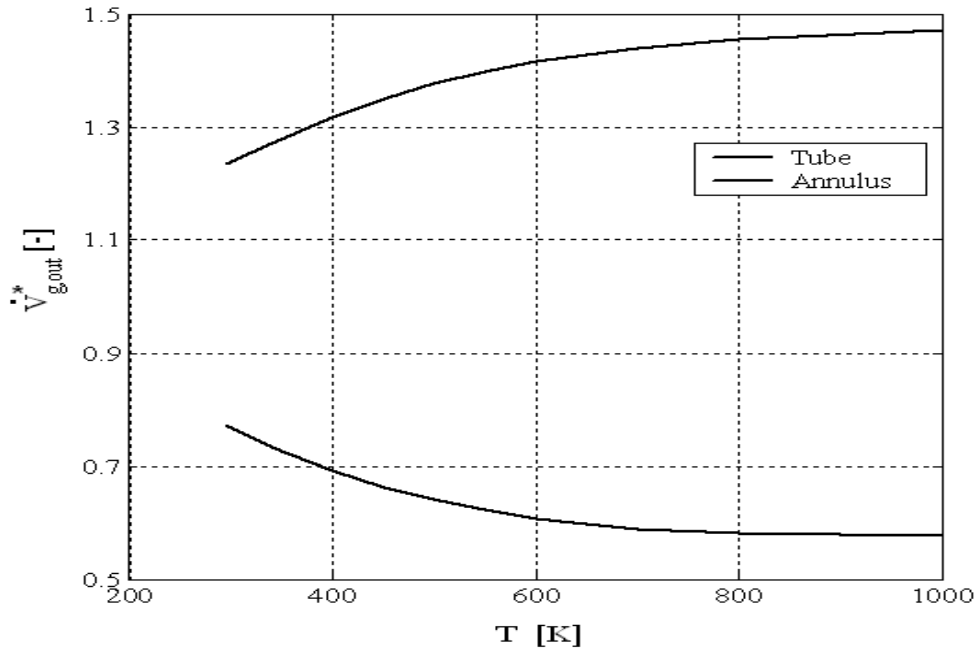
Fig. 5b. Dimensionless volumetric flow rate at the outlet of annulus and tube vs. temperature.

$$\widetilde{x}_{He,i,in} = \widetilde{x}_{N_2,o,in} = 1, \quad P_i = P_o = 1 bar,$$

$$T_m = T_{g,i,in} = T_{g,o,in} = 295.15\,K .$$

Figure 2 shows the dimensionless molar composition of helium and nitrogen plotted against the dimensionless length for varying gas volumetric flow rate in annulus and tube. It can be seen in figure 2a that by increasing the inlet flow rates helium composition tends to unity $(\widetilde{x}^*_{He,i} \to 1)$ in tube and tends to zero $(\widetilde{x}^*_{He,o} \to 0)$ in

Table 1. Producer information and identified mass transfer parameters of membranes (M1).

Layer	Composition	Nominal pore diameter (m)	Thickness (m)	K_o (m)	B_o (m^2)	d_p (m)	$\frac{\varepsilon}{\tau}$
Support	α-Al$_2$O$_3$	3.0×10^{-6}	5.5×10^{-3}	8.16×10^{-8}	2.96×10^{-14}	2.90×10^{-6}	0.112
1st layer	α-Al$_2$O$_3$	1.0×10^{-6}	25×10^{-6}	7.99×10^{-8}	2.73×10^{-14}	2.73×10^{-6}	0.124
2nd layer	α-Al$_2$O$_3$	60×10^{-9}	25×10^{-6}	2.98×10^{-9}	2.85×10^{-17}	76.5×10^{-9}	0.156
3rd layer	γ-Al$_2$O$_3$	10×10^{-9}	2×10^{-6}	2.03×10^{-9}	7.47×10^{-18}	29.4×10^{-9}	0.277

annulus and vice versa in Fig. 2b for the case of nitrogen. Similar effects are shown in Figs 3a and b, however in these figures, mole fraction of nitrogen and helium at the outlet is plotted against NTU. For instance Fig. 3a reveals that by increasing NTU (lower gas flow rate) gas composition reaches the equilibrium values. At low NTU (higher gas flow rate) helium composition tends to unity $(\widetilde{x}^*_{He,i} \to 1)$ in tube and tends to zero $(\widetilde{x}^*_{He,o} \to 0)$ in annulus and vice versa in figure 3b for the case of nitrogen. This can be attributed to the lower residence time of gases in the tube and annulus retarding the mass transfer of gases.

Influence of temperature
The influence of temperature on mass transfer at isothermal conditions is presented in this section. Simulations are conducted by varying temperature from 295.15 to 1000 K and the results for the steady state isothermal case are depicted in figures 4 and 5 for the following operating conditions:

$$\widetilde{x}_{He,i,in} = \widetilde{x}_{N_2,o,in} = 1, \qquad u_{g,i,in} = 0.096 \ m/s,$$

$$u_{g,o,in} = 0.058 \ m/s, \qquad P_i = P_o = 1 \, bar.$$

The temperature has a positive effect on membrane's transport parameters and a negative effect on density, which in the combination lead to increasing fluxes for higher temperatures and the here considered membrane. Consequently, an increase of temperature will enhance the diffusion process resulting in steeper composition profiles (Fig. 4) and higher differences in volumetric flow rate in tube and annulus (Fig. 5).

CONCLUSION

A non-dimensional analysis of isobaric diffusion, based on simulations, has been done to see the influences of volumetric flow rate and temperature on the isobaric diffusion process in terms of mole fraction and gas flow rates. The analysis reveals that system attains equilibrium at lower gas flow rates and rise in temperature enhances

the diffusion process in composite membrane which will lead to reach the equilibrium faster.

Nomenclature

B_0	m^2	Permeability constant in dusty gas model
Bo	-	Bodenstein number
d	m	Diameter
D_{ax}	m^{2}s^{-1}	Axial dispersion coefficient
D	m^{2}s^{-1}	Diffusion coefficient
F_0	-	Ratio of effective to molecular diffusion coefficient
F	m^2	Cross-sectional area
K_0	m	Knudsen coefficient in dusty gas model
L	m	Length
$\widetilde{M}$	kg mol^{-1}	Molar mass
n	mol m^{-3}	Molar density
$\dot{n}$	mol m^{-2}s^{-1}	Molar flux
$\dot{N}$	mol s^{-1}	Molar flow rate
NTU	-	Number of transfer units
P	Pa	Pressure
r	-	Radial coordinate
$\widetilde{R}$	J mol^{-1}K^{-1}	Universal gas constant
T	°C, K	Temperature
u	m s^{-1}	Flow velocity
$\dot{V}$	m^{3}s^{-1}	Volumetric flow rate
$\widetilde{x}$	-	Mole fraction
z	-	Axial coordinate

Greek symbols

β	m s^{-1}	Mass transfer coefficient
ε	-	Porosity
ζ	-	Dimensionless length
η	Pa s^{-1}	Viscosity
τ	-	Tortuosity

Indices

av	Average
D	Diffusivity
e	Effective
g	Gas
in	Inlet
i	Inner, tube side
j, k	Species in the mixture
K	Knudsen
m	Membrane
o	Outer, annulus side
out	Outlet
p	Pore
*	Dimensionless quantity

REFERENCES

Beuscher, U. and Gooding, CH. 1999. The influence of the porous support layer of composite membranes on the separation of binary gas mixtures. Journal of Membrane Science. 152(1):99-116.

Biesheuvel, PM. and Verweij, H. 1999. Design of ceramic membrane supports: permeability, tensile strength and stress. Journal of Membrane Science. 156(1):141-152.

Capek, P. and Seidel-Morgenstern, A. 2001. Multicomponent mass transport in porous solids and estimation of transport parameters. Applied Catalysis A Gen. 211(2):227-237.

Gunn, DJ. 2004. An analysis of convective dispersion and reaction in the fixed-bed reactor. International Journal of Heat and Mass Transfer. 47:2861-2875.

Hussain, A., Seidel-Morgenstern, A. and Tsotsas E. 2006. Heat and mass transfer in tubular ceramic membranes for membrane reactors, International Journal of Heat and Mass Transfer. 49:2239-2253.

Mason, EA. and Malinauskas, AP. 1983. Gas Transport in Porous Media: The Dusty Gas Model, Elsevier, Amsterdam.

Meixner, DL. and Dyer, PN. 1998. Characterization of the transport properties of microporous inorganic membranes. Journal of Membrane Science. 140(1):81-95.

Reid, RC., Prausnitz, JM. and Powling, BE. 1987. The Properties of Gases and Liquids, McGraw Hill, New York, USA.

Thomas, S., Schafer, R., Caro, J. and Seidel-Morgenstern, A. 2001. Investigation of mass transfer through inorganic membranes with several layers. Catalysis Today 67(1–3):205-216.

Thomas, S. 2003. Kontrollierte eduktzufuhr in membranreaktoren zur optimierung der ausbeute gewuenschter produkte in parallel- und folgereaktionen. Ph.D. Thesis. Otto-von-Guericke-Universitat Magdeburg, Germany.

Tsotsas, E. and Schlünder, EU. 1988. On axial dispersion in fixed beds with fluid flow. Chemical Engineering Process. 24:15-31.

Tuchlenski, A., Schramm, O. and Seidel-Morgenstern, A. 1997. Steady state and dynamic mass transfer of gases in porous materials. Coll. Czech. Chem. Commun. 62(7):1043-1056.

Tuchlenski, A., Uchytil, P. and Seidel-Morgenstern, A. 1998. An experimental study of combined gas phase and surface diffusion in porous glass. Journal of Membrane Science. 140(2):165-184.

Uchytil, P., Schramm, O. and Seidel-Morgenstern, A. 2000. Influence of the transport direction on gas permeation in two-layer ceramic membranes. Journal of Membrane Science. 170 (2):215-224.

DETECTION OF SOLAR AND TERRESTRIAL PHENOMENA BY 40 KHZ SUBIONOSPHERIC VLF SIGNAL: REPORT

*S S De[1], B Bandyopadhyay[1], B K De[2], D K Haldar[1] and Suman Paul[1]
[1]Centre of advanced Study in Radio Physics and Electronics
1, Girish Vidyaratna Lane, Kolkata 700 009
[2]Department of Physics, Tripura University, Tripura 799 130, India

ABSTRACT

At Agartala (Lat 23° N, Long 91° 24′ E), North-Eastern part of India, continuous monitoring of VLF/LF sferics and subionospheric transmitted signals are being continued since 1975. From the recording of one such subionospheric signal at 40 kHz from Japan (Lat 36° 11′ N, Long 139° 51′ E), some observed typical variations in the transmitted signal amplitude during solar flares and meteor showers will be presented in this paper.

Keywords: VLF signal modulation, solar flare effects, meteor shower detection.

INTRODUCTION

Solar X-ray flares, meteor showers, geomagnetic storms and other terrestrial phenomena while entering the earth's atmosphere produce electromagnetic waves in the VLF range due to interaction with the medium, which propagate and reach the ground at the same instance as the optical signals (Price and Blum, 2000; De *et al*., 2006; Chakrabarti *et al*., 2002; Keay, 1995; Beech *et al.,* 1995).

The effects of large electric field from any such origin introduce perturbation in ion composition, temperature and other physical parameters within the ionosphere at different levels of altitude extending from the lowest D-region to the magnetosphere height. Anomalous changes of amplitude and phase of VLF subionospheric signals would occur during their propagation through such perturbed regions (Volland, 1982; Rodger, 2003; Dowden and Adams, 1990; Garaj *et al*., 2000; Nickolaenko *et al.,* 1999). From VLF amplitude and phase observations, solar flare induced ionospheric D-region changes have been investigated (Nickolaenko and Hayakawa, 1998; Thomson and Clilverd, 2000).

Wave propagation below 300 kHz within the earth-ionosphere wave-guide is characterized by complex phenomena involving nonhomogeneous and anisotropic media. In recent period, based on FDTD computational solutions of Maxwell's equations, the effects of anomalous electric field during solar and different geophysical events upon subionospheric wave propagation are being successfully analysed (Thomson and Cliverd, 2001; Baba and Hayakawa, 1995; Otsuyama *et al*., 2003; Simpson and Taflove, 2004).

In this paper, some typical variations of amplitude of 40 kHz subionospheric Japanese signal due to solar flares and meteor showers will be presented. These are recorded at Agartala (Lat 23° N, Long 91° 24′ E) at different periods over the past twenty years.

The Features of the 40 kHz Sub-ionospheric Signal
Transmitter call sign JG2AS/JJF-2

Location	Japan
Latitude	36° 11′ N
Longitude	139° 51′ E

Transmitting antenna
Type	Omni-directional
Power at radiation	10 kW
Operation	Continuous

Receiver
The recording system consists of loop antenna feeding a number of OP-AMPs used in tuned radio frequency mode. The output of the AC amplifier is detected and the DC level is further amplified logarithmically. The DC gain has been used to adjust the receiver's sensitivity corresponding to the incoming signal which shows marked variation over the year. The DC output is used as the signature of the amplitude of 40 kHz signal. The overall gain of the amplifier is 120 dB with a band width of 200 Hz. The time constant of the recorder is 7.5 sec. A gyrator-II type VLF receiver has also been made useful for recording this signal (Simpson and Taflove, 2007). Using computer sound card, data were recorded at a sample rate of 10/s which have been analyzed through origin 5.0.

Observed Sub-ionospheric signals from Agartala
The diurnal behavior of the amplitude of 40 kHz signals under normal condition is depicted in figure 1. In the figure, the zones A, B, C and D represent sunrise minima,

_____

*Corresponding author email: de_syam_sundar@yahoo.co.in

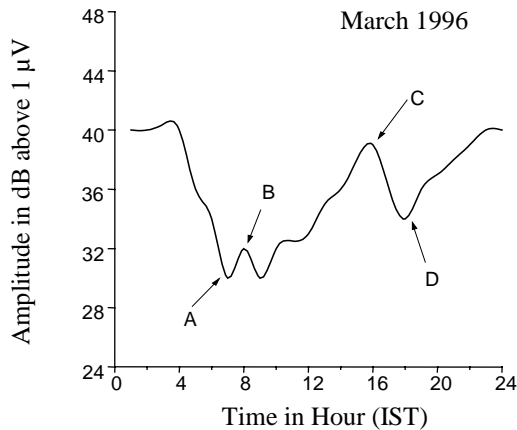recovery effect, afternoon maxima and sunset minima, respectively.

Fig. 1. Diurnal behavior of amplitude of 40 kHz radio signal.

Figure 2 shows a typical enhancement in signal strength due to solar flare in 40 kHz in relation to Sudden Enhancement in Signal Strength, SES, occurred during 0854 Hour to 0916 Hour on 24.01.2007. Here, C: commencement time and E is the end of the event.
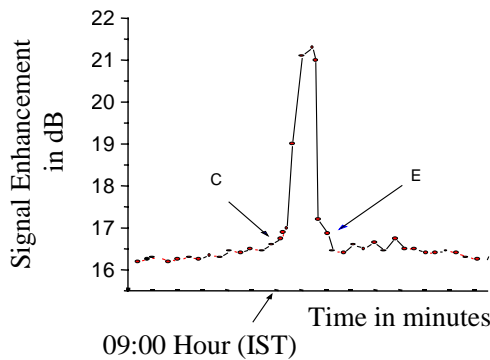

Fig. 2. Typical enhancement in signal strength due to solar flare.

During solar flare, the signal level rises and follows the sequences of enhanced solar radiation. This has been termed as SES.

Some of the observed SES
Occurrences of SES in different solar phases P1, P2, P3 and P4 and their relationship with different types of X-ray flares:

P1: The Sun moves from Tropic of Cancer to Equator (21 June-21 September)
P2: The Sun moves from Equator to Tropic of Capricorn (22 September-21 December)
P3: The Sun moves from Tropic of Capricorn to Equator (22 December-21 March)

P4: The Sun moves from Equator to Tropic of Cancer (22 March-21 June).

Solar cycle	Solar Phase	Percentage association of SES with X-ray flares of types		
		Impulsive	GRF	Spikes
22nd	P1	81	85	65
	P2	78	81	62
	P3	72	78	58
	P4	68	75	56
23rd	P1	79	79	61
	P2	74	76	57
	P3	68	72	54
	P4	65	68	51

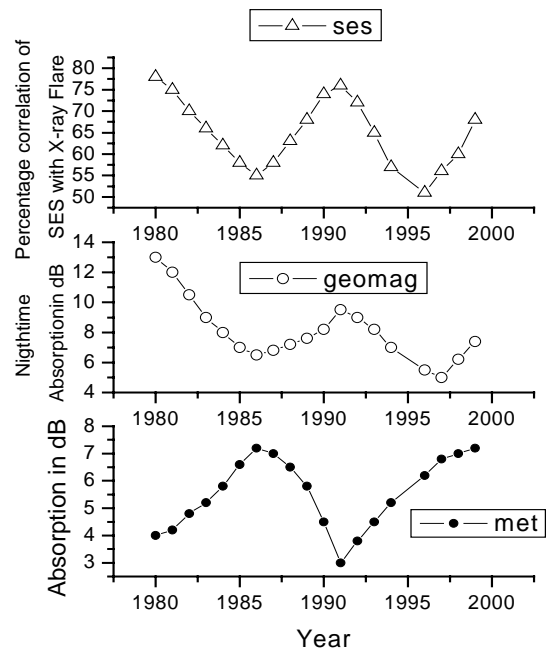Some correlation studies are presented in figure 3.

Fig. 3. Three graphs show the percentage correlation of SES, average nighttime absorption in geomagnetically active days and average absorption in sporadic meteorologically active days in various years of 21st- 22nd, 22nd-23rd solar cycles.

The results show good correlation with solar cycle variations. But the magnitudes are solar cycle dependent. It is seen that the effects are slightly higher in 21st – 22nd solar cycle than in 22nd – 23rd solar cycle.

Solar Cycles
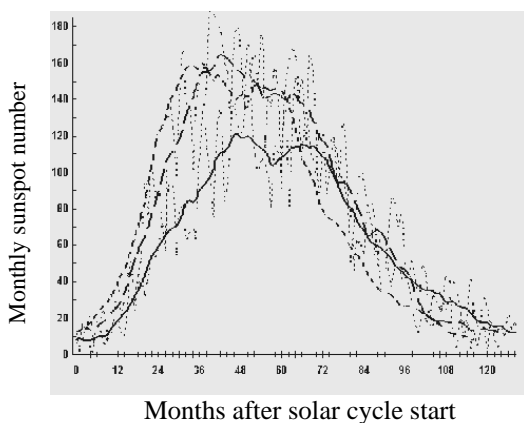Solar cycles are shown in figure 4.

Fig. 4. Different solar cycles.

Monthly smoothed sunspot number
21: Large dashed line curve
22: Small dashed line curve
23: Solid line curve

Actual monthly sunspot number
21: 22: 23: Shown by the corresponding dotted curve
- Cycle 21 started in June 1976 and lasted 10 years and 3 months.
- Cycle 22 started in September 1986 and lasted 9 years and 8 months.
- Cycle 23 started in May 1996.

The sunspot numbers during solar cycles are the representative points of the absorption of 40 kHz signal.

Leonid Meteor Showers
The Leonid meteor showers of 1998 have been presented in figure 5 by recording its effects on 40 kHz Japanese subionspheric signal over Agartala. The shower exhibited peak activities on Nov. 16, 1998. Detection of meteor showers by recording their effects on transmitted signals had been reported earlier from Kolkata (Lat 22° 34´ N, Long 88° 30´ E) at some other frequencies (De *et al.*, 2006; Chakrabarti *et al.*, 2002).
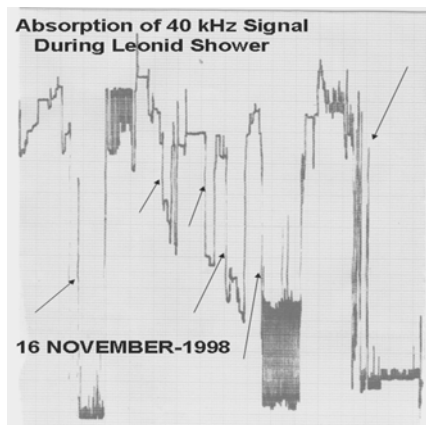

Fig. 5. Typical Leonid meteor shower of 16 November, 1998.

At 40 kHz signal frequency, the influences of atmospherics were relatively much lower compared to lower frequencies. The signal strength is sufficiently strong for detection over Agartala having great circle distance at 4884 km.

The day from 15 to 21 November, 1998 had very clear sky and no serious 'thunder-bolt' related events were reported at Agartala. So apart from the solar terrestrial influences on the ionosphere, the period was ideal for observing meteor showers. Moreover, no solar flare events were reported around the period of occurrence by GOES10 and GOES12 satellites which continuously monitor solar activity. At the predicted peak activity period, there were no local lightning or flare generated perturbations in the ionosphere that could alter the average signal received at Agartala.

The extra ionization produced by the supersonic meteoroids during their passage through lower ionosphere was the cause of high enhancement of signal level, which is about eight to nine times the normal value.

During the entry of the Leonid into the earth's atmosphere, there will be strong fluctuation of charge distribution in the medium which enhances the rate at which the energy gets randomized. As a result, instability is produced. For this, the relative electron-ion drift velocity may exceed the value for the onset of Kelvin-Helmholtz instability. The compressible ionospheric plasma driven by velocity shears and earth's magnetic field at the frontal path of the meteor increases the growth rate of Kelvin-Helmholtz instability thereby generating electromagnetic waves that produce the observed effects in the subionospheric signal.

ACKNOWLEDGEMENT

REFERENCES

Price, C. and Blum, M. 2000. ELF/VLF Radiation Produced by the 1999 Leonid Meteors. Earth, Moon and Planets. 82-83:545-554.

De, SS., De, BK., Guha, A. and Mandal, PK. 2006. Detection of 2004 Leonid meteor shower by observing its effects on VLF transmission. Indian J. Radio and Space Phys. 35**:**396-400.

Chakrabarti, SK., Pal, S., Acharya, K., Mandal, S., Chakrabarti, S., Khan, R. and Bose, B. 2002. VLF

observation during Leonid meteor shower-2002 from Kolkata. Indian J. Phys. 76B (6):693-697.

Keay, CSL. 1995. Continued Progress in Electrophonic Fireball Investigations. Earth, Moon and Planets. 68:361-368.

Beech, M., Brown, P. and Jones, J. 1995. VLF detection of fireballs. Earth, Moon and Planets. 68:181-188.

Volland, H. 1982. Handbook of Atmospherics. Eds. Volland, H. CRC Press, Boca Raton, Fla. 179-250.

Rodger, CJ. 2003. Subionospheric VLF perturbations associated with lightning discharges. J. Atmos. Sol. Terr. Phys. 65:591-606.

Dowden, RL. and Adams, CDD. 1990. Lightning - induced perturbations on VLF subionospheric transmissions. J. Atmos. Sol. Terr. Phys. 52:357-363.

Garaj, S., Vinkovic, D., Zgrablic, G., Kovacic, D., Gradecak, S., Biliskov, N., Grbac, N. and Andreic, Z. 2000. Observational detection of meteor-produced VLF electromagnetic radiations. FIZIKA A (Zagreb). 8:91-98.

Nickolaenko, AP., Hayakawa, M., Kudintseva, IG., Myand, SV. and Rabinowicz, LM. 1999. ELF subionospheric pulse in time domain. Geophys. Res. Lett. 26:999-1002.

Nickolaenko, AP., Hayakawa, M. 1998. Natural electromagnetic pulses in the ELF range. Geophys. Res. Lett. 25:3101-3106.

Thomson, NR. and Clilverd, MA. 2000. Solar cycle changes in daytime VLF subionospheric attenuation. J. Atmos. Sol. Terr. Phys. 62:601-608.

Thomson, NR. and Clilverd, MA. 2001. Solar flare induced ionospheric D-region enhancements from VLF amplitude observations. J. Atmos. Sol. Terr. Phys. 63: 1729-1737.

Baba, K. and Hayakawa, M. 1995. The effect of localized ionospheric perturbations on subionospheric VLF propagation on the basis of finite element method. Radio Sci. 30:1511-1518.

Otsuyama, T., Sakuma, D. and Hayakawa, M. 2003. FDTD analysis of ELF wave propagation and Schumann resonances for a subionospheric waveguide model. Radio Sci. 38: doi: 10.1029/2002RS002752.

Simpson, JJ. and Taflove, A. 2004. Three-dimensional FDTD modeling of impulsive ELF propagation about the Earth-sphere. IEEE Trans: Antennas and Propag. 52: 443-451.

Simpson, JJ. and Taflove, A. 2007. A Review of Progress in FDTD Maxwell's Equations Modeling of Impulsive Subionospheric Propagation Below 300 kHz. IEEE. Trans. Antennas and Propag. 55:1582-1590.

FUMED SILICA FIBER AS A NEW DRAG REDUCING AGENT FOR AQUEOUS MEDIAS FLOWING THROUGH PIPELINES

*Hayder A Abdul Bari[1], Emma Suali[2] and Zulkafli Hassan[3]
[1]Faculty of Chemical and Natural Resources Engineering, University Malaysia Pahang
[2]Faculty of Chemical and Natural Resources Engineering, University Malaysia Pahang
[3]Faculty of Chemical and Natural Resources Engineering, University Malaysia Pahang, Malaysia

ABSTRACT

In the present study, Fumed silica powders were presented as a new effective Drag Reducing Agent. The effects of using various concentrations of fiber and flow rate on increasing the flow in pipelines were investigated in a fully developed turbulent flow. The effects of pipe length to pipe diameter (L/D) on drag reduction were also investigated. A built experimental rig with different diameters of PVC pipes was used in order to investigate the performance of fumed silica fiber as drag reducing agent. The experimental results showed that the fume silica have a great ability to act as a good drag reducing agent in aqueous media. The addition of 600 ppm of the fumed silica to the main flow was enough to reach a maximum reading of the percentage drag reduction up to 40 % this maximum percentage was achieved in 59 L/D at Re equal to 22470. The drag reduction decreases as the Re exceeds 22470. These experimental results show that the fumed silica powder performed as a good DRA.

Keywords: DRA, drag reduction, fibers interaction, turbulent flows, fiber flexibility.

INTRODUCTION

The drag reduction in pipelines and in others devices such as heating and cooling systems during the transportation of fluids was identify through pressure drop. This pressure drop causes more pumping power requirements. When fluid transmission occurs in long distance and in high volume, energy saving become the most important issues. The concept of drag reduction allows pipelines to be operated at a lower pressure, reducing energy costs and more production with less energy consumption. Drag reduction is achieved by addition of drag reducing agent (DRA) which is polymers, surfactants and fibers. Many researchers through their experimental work have proved the capability of these DRA. Each of these DRA has their advantages and disadvantages. Drag reducing fibers are well known as safest and cheapest DRA compare to surfactants and polymer which some of the surfactants caused problems to environment in high consumptions. The drag reduction in a present of fibers occurs when the concentration was enough for fibers interaction to occur but below a critical concentration. Most of the researchers have a good agreement that the key to understand the mechanism behind the drag reduction of fibers additive is the interaction of fibers in core region of turbulent and the orientation distribution of fibers (Abdul Bari *et al*., 2008). The shear rate of fluid around fiber and the length scale of flow are the key factor for determining the orientation distribution of fibers, while the fiber velocity and the fiber Stokes number have marginal influence on the orientation distribution of fibers (Jianzhong *et al*., 2004). The flexibility of fibers also becomes one of the most

discussed topics to explain the drag reduction mechanism (Luettgen *et al*., 1991). Depending on the types and properties of fibers, the addition of fibers to a flow can have either a stabilizing or a destabilizing effect (Vaseleski *et al*., 1974). For a fiber suspension with hydrodynamic interactions, the shear stress disturbance induced by the misalignment of the fibers is the main driving term behind the decrease of the flow instability. Thus, the normal stress disturbance acts as a destabilizing factor (Azaiez, 2000). Flexibility of fibers and its interactions with the vortexes in flows has been reported as a reason of drag reduction in turbulent flow (Zhu and Peskin, 2007). Lin *et al*. (2006) conducted an experiment through iteration of fiber distributions and interaction in turbulent channel flow. They found that in a present of fibers, the relative turbulent intensity and the Reynolds stress is smaller than in Newtonian flow without fibers. These phenomena interpreted that the fiber suspensions capable on suppressing the turbulent flow. Barresi (1997) showed that the turbulence suppression can be attributed through the facts that in dense suspensions a significant fraction of fluid does not depend only on its concentration, but also its movements with the particles. These phenomena can be explained through action of surface friction and the work of viscous forces which arise as an effect of sudden changes in the fluid velocity that accompany any collision.

MATERIALS AND METHODS

Fumed Silica powder
Fumed silica which is product of Sigma-Aldrich Sdn.Bhd was used as an investigated material in this experiment. Table 1 shows the properties of fumed silica powders.

---

*Corresponding author email: hayder@ump.edu.my

Table 1. Properties of fumed silica.

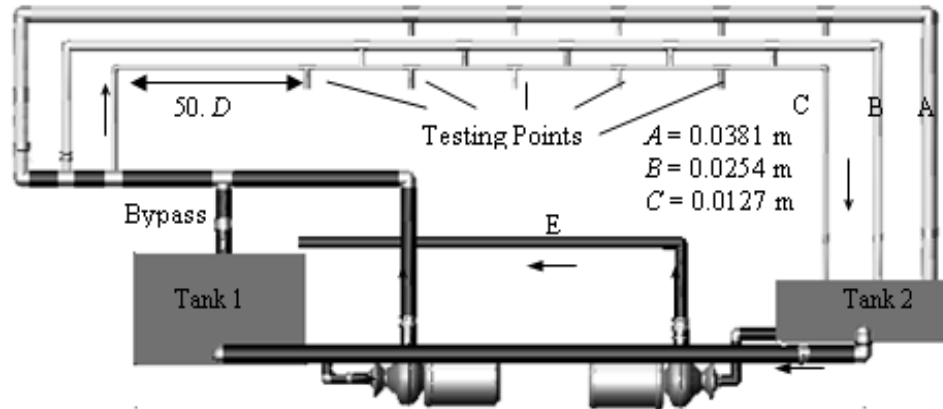| Particle size, (μm)	Length (μm)	Surface area (m²/g)	Density (g/cm³)	Molecular weight (g/mol)
0.011	0.1 - 0.2	255	2.2	60.09

Fig.1. The Experimental Rig.

Experimental systems
The experimental system consisted of build up rig, Baumer differential pressure gauge and Minisonic P flow meter. Baumer pressure gauge was used to detect the pressure drop and Minisonic P flow meter was used to measures the flow rate of fluid through pipes. The rig is consisted of three different internal diameters of pipes as shown in figure 1. Each pipe was completed with testing section in which these testing points are connected with the Baumer differential pressure gauge through portable rubber tube. The system consist pipes with 0.0127m, 0.0254m and 0.0381m inside diameter and the length of 2 m made from transparent PVC pipe to permit visual observation of flow pattern in the future was used as the test section. Each pipe divided into four pressure testing sections with a distance equal to 0.5 m. The first pressure testing point for each pipe was located about 50 times pipe diameter (50.D) of the testing pipe as shown in figure 1. This is to ensure the turbulent flows are fully developed before the testing point.

The flow rate of fluid in pipelines was measures by Ultraflux Portable Flow meter Minisonic P in which this ultrasonic flow measurement was sensitive with small changes in flow rate as low as 0.001m/s. The purpose of using this exterior portable ultrasonic measurement is to avoid any disturbance might happen in the flow pattern. Baumer Differential Pressure Gauges were used to detect the pressure drop in pipelines with maximum differential pressure readings up to 0.16bar.

Experimental procedures
The experimental work was carried out in 1.5m length and 00381m diameter pipe. The length to diameter (L/D) ratio was 59. The data of pressure drop for water alone are

initially used in the calculations of drag reduction in which the drag reduction in pipes is defined as:

$$\text{Reduction (\%)} = \left(1 - \frac{\Delta P_a}{\Delta P_b}\right)100 \tag{1}$$

Where; ΔP_b is pressure drop before and ΔP_a is after the addition of fibers solution. Fumed silica powders were tested and circulated in the experimental rig each time with different concentration. The addition concentrations were 200, 300, 400, 500 and 600 ppm. For each concentration, different flow rates are tested for the solution and pressure drop readings are taken and compared with the readings of the flow of the pure water flowing in the same pipelines.

RESULTS AND DISCUSSION

The initial data were presented in term of friction factors and compared with friction factor correlation of Blasius and Virk as shown in figure 2.

Friction factor is defined as below:

$$f = \frac{2\tau_w}{\rho V^2} \tag{2}$$

$$\tau_w = \frac{D\Delta P}{4L}$$

The Blasius equation is defined as (Yunus and Cimbala, 2006):

$$f = 0.0791 Re^{-0.25} \tag{3}$$

and Virk's asymptote is defined as (Virk et al. 1970):

$$f = 0.59Re^{-0.58} \qquad (4)$$

Whereas the Reynolds number in pipe is defined as:

$$Re = \frac{\rho VD}{\mu} \qquad (5)$$

Moreover, the friction factors in pipes based on laminar flow are defined as:
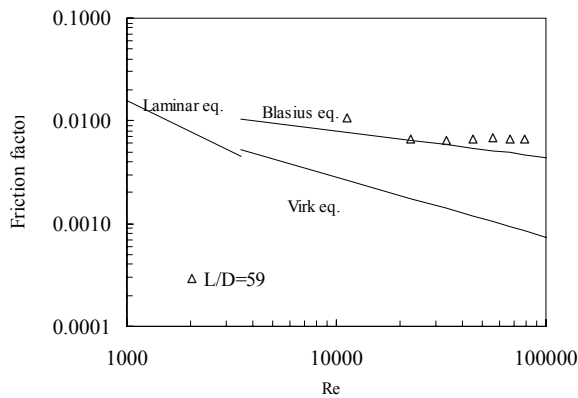
$$f = \frac{16}{Re} \qquad (6)$$

Fig. 2. Relationship between friction factor and Re of water in PVC pipe.

The experimental data of water flow are plotted in figure 2 and compared with Blasius asymptote for liquids additive free flow in pipelines. The figure included both the laminar flow and Virk maximum drag reduction flow asymptotes. It is clearly shown that the values of the additive-free water flow in pipes used in the present experiment lies near the Blasius asymptote which will give the experimental work a good starting point towards more accurate readings.
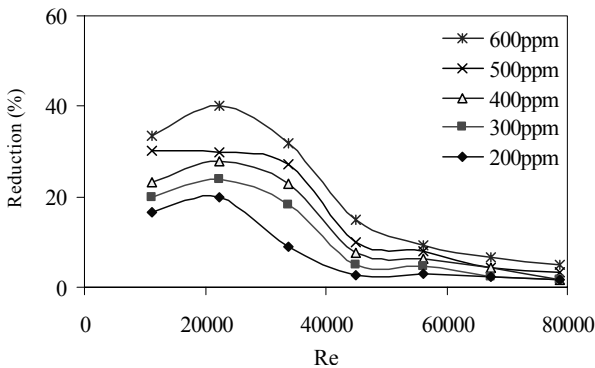

Fig. 3. The relation of drag reduction with Re for fumed silica in 59 L/D.

Figure 3 shows the relations of drag reduction with Reynolds number (Re) in different concentration of solution. The range for drag reduction likely to occurred is within the range of Re = 12000 and Re = 33000. At this range, the maximum drag reduction achieved is 40% at highest concentration which is 600 ppm and the minimum is 9 % observed at 200 ppm. It is clearly shown that the drag reduction is initially increases as the Re increases but begin to decrease after exceed 21000. At high Re, the drag reduction decreases and become almost constant which is in a range of 3% to 15%. This behavior may be due to the change in the degree of turbulence compatibility with the additive type and concentration which reaches certain optimum value where maximum percentage of drag reduction are achieved and in certain parts, increasing the degree of turbulence may be more than the optimum value which will lead to a less effective action.
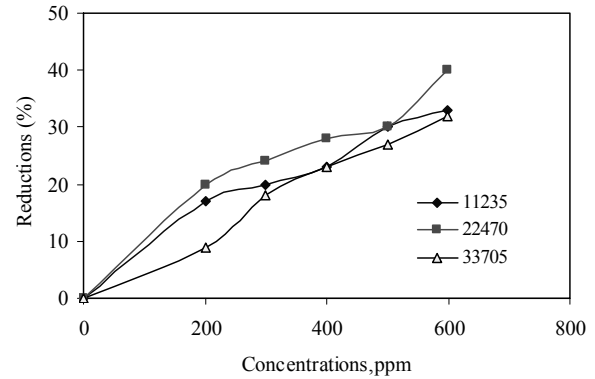
Fig. 4. Relations of drag reduction with concentration for Re at 11235 to 33705.
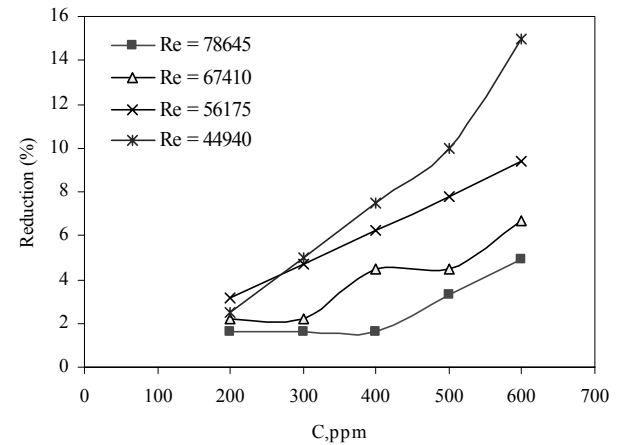
Fig. 5. Relation of drag reduction versus concentrations for Re at 44940 to 78645.

Figure 4 and 5 shows the comparison of three different Re of drag reduction versus concentration of solution. In figure 4; the first drag reduction was observed is at Re equal to 11235. From the figure, it can be noticed that the drag reduction continuously increases until Re reached 22470 and started to decreases but still in a good

performance until 33705 of Re. From figure it is clearly shown that each concentration of solution at 22470 Re obtained the highest drag reduction compare to others. At 600ppm concentrations, the average drag reduction was achieved for all Re is 35%, at 500ppm is 29%, at 400ppm is 25%, at 300ppm is 21% and at 200ppm is 15% (Fig. 5). Figure 5 shows the relations of drag reduction with different concentrations of solution at Re equal to 44940, 56175, 67410 and 78645. From figure, it shows that the drag reduction decreases as the Re increases. The highest drag reduction was achieved based on that figure is 15% and the lowest is 2%. This results show that, the DRA's concentration at 600 ppm was not appropriate when operated at Re higher than 78645. From the results shown by figures 4 and 5, it is easy to notice that by increasing the additive concentration the performance of the drag reducer will be better and that may be due to the increase of the turbulence spectrum that will be under the drag reducer effect which will balance the increasing degree of turbulence caused by increasing the flow rate (Re), another words, the drag reduction occurred probably caused by the rheology properties and interaction of fibers in flow. Flexibility of fibers important to form a network to surpassed the turbulent flow. The reductions of drag-reduction at high Re are probably caused by the concentration of fiber solution were not longer appropriate to surpass the high degree of turbulent flow. In order to maintain the drag reduction in flow, the concentration of fiber should be added.

CONCLUSION

It is proven that the solubility condition for any material to be classified as drag reducing agent is no longer dominating. Fumed silica powders showed high ability to increase the flow in pipelines carrying water by reducing the drag caused by turbulence. Maximum percentage of drag reduction achieved is 40% and the overall experiments which mean 40% power savings by the addition of only 600 ppm fume silica powder.

Notation

ρ solvent density	Re Reynolds number
μ absolute viscosity of solvent	L/D pipe ratio
D internal diameter of pipe	ΔP pressure drop in pipe
L pipe length	f friction factors
V means velocity of solvent	τ_w wall shear stress

REFERENCES

Abdul Bari, HA., Suali, E. and Hassan, Z. 2008. Glycolic Acid Ethoxylate Lauryl Ether Performance as Drag Reducing Agent in Aqueous Media Flow in Pipelines. Journal of Applied Sciences. 8(23):4410-4415.

Antonello, AB. 1997. Experimental investigation of interaction between turbulent liquid flow and solid particles and its effects on fast reactions. Chemical Engineering Science. 52(5):807-814.

Azaiez, J. 2000. Reduction of free shear flows instability: effects of polymer versus fiber additives. J. Non-Newtonian Fluid Mech. 91:233-254.

Lin, JZ., Gao, ZY., Zhou, K. and Chan, TL. 2006. Mathematical modeling of turbulent fiber suspension and successive iteration solution in the channel flow. Applied Mathematical Modelling. 30:1010-1020.

Jianzhong, JL., Zhang, WZ. and Zhaosheng, Y. 2004. Numerical research on the orientation distribution of fibers immersedin laminar and turbulent pipe flows. Aerosol Science 35:63-82.

Luettgen, CO., Lindsay, JD. and Stratton, RA. 1991. Turbulent Dispersion in Pulp Flow: Preliminary Results and Implications for the Mechanisms of Fiber-Turbulence Interactions: AIChE Forest Products Symposium Series. The Institute of Paper Science and Technology, Atlanta. No. 408.

Vaseleski, RC. and Metzner, AB. 1974. Drag reduction in the turbulent flow of fiber suspensions. AICHE J. 20:301-306.

Virk, PS., Mickley, HS. and Smith, KA. 1970. The Ultimate Asymptote and Mean Flow Structure in Toms' Phenomenon.Trans. Am. Soc. Eng., Ser. E. J. Appl. Mech. 37:488-493.

Yunus, AC. and Cimbala, JM. 2006. Fluid Mechanics: Fundamantals and applications. McGraw Hill. (ISBN-13: 978-007-125764-0).

Zhu, L. and Peskin, CS. 2007. Drag of a flexible fiber in a 2D moving viscous fluid. Computers & Fluids 36:398-406.

Canadian Journal of
pure&applied
sciences

MICROARRAY CLASSIFICATION WITH HYBRID APPROACHES

M Arif Wani
Computer Science Department, California State University Bakersfield, CA, USA

ABSTRACT

The work presented in this paper describes hybrid approaches that employ principal component analysis (PCA) and multiple discriminant analysis (MDA) methods for microarray classification. The paper first describes a hybrid approach that incorporates PCA and Fisher linear discriminant analysis (FDA) for microarray classification. This hybrid approach effectively solves the singular scatter matrix problem caused by small training samples. To increase the effective dimension of the projected subspace the use of MDA instead of FDA is explored. The performance of the system is evaluated by projecting data to several subspaces incrementally. The resulting incremental hybrid system improves the accuracy of classification. The paper discusses a comprehensive evaluation of the hybrid systems. The hybrid systems were tested on a dataset of 62 samples (40 colon tumor and 22 normal colon tissues). The results show that the use of incremental hybrid system increased the accuracy of classification of microarray data which will lead to better diagnosis of cancer and other diseases.

Keywords: Microarray classification, hybrid incremental algorithm, multiple discriminant analysis.

INTRODUCTION

One of the major applications of DNA microarray technology is to perform sample classification analyses between different disease phenotypes, for diagnostic and prognostic purposes. The classification analyses involve a wide range of algorithms such as differential gene expression analyses, clustering analyses and supervised machine learning. Machine learning algorithms are most frequently used to complete this task. Two of the most important and hard problems in microarray data analysis relate to the dimensionality of the data and to noise. Because many data analysis techniques involve exhaustive search over the object space, they are very sensitive to the size of the data in terms of time complexity. In case of microarrays, the solution is to reduce the search space vertically (in terms of genes) by using a feature selection method. The other problem is that errors occur during actual data collection and they are referred as noise in the data.

A comparative study of gene selection methods for multi-class classification of microarray data is presented by Chai and Domeniconi (2004). The authors compare several feature ranking techniques, including new variants of correlation coefficients, and Support Vector Machine (SVM) method based on Recursive Feature Elimination (RFE). A study by Hori *et al*. (2001) shows that an independent component analysis (ICA) based method can effectively and blindly classify a vast amount of gene expression data into biologically meaningful groups. Specifically, they show i) that genes, whose expression data are sampled at different times, can be classified into several groups, based on the correlation of each gene with

independent component curves over time, and ii) that these classified groups by ICA based method have a good match with the classified groups that are determined by use of domain knowledge and considered to be a benchmark. These results suggested that the ICA based method can be a powerful approach to discover unknown gene functions. The authors also examine classification by principal component analysis (PCA). Then they compared the classification using PCA and ICA methods. PCA only takes into account the second-order statistics and restricts itself to orthogonal transformation to obtain principal components. On the other hand, independent component analysis (ICA) can take into account higher order statistics and can utilize non orthogonal transformation for de-mixing. Zhnag and Deng (2007) discussed the gene selection for classification using DNA microarray data. They select a compact subset of discriminative genes from thousands of genes, which is a critical step for accurate classification of phenotypes. Several widely used gene selection methods often select top-ranked genes according to their individual discriminative power in classifying samples into distinct categories, without considering correlations among genes. A limitation of these gene selection methods is that they may result in gene sets with some redundancy and yield an unnecessary large number of candidate genes for classification analyses. Another study, Rapoport *et al*. (2007) proposed a general mathematical formalism to include a priori the knowledge of a gene network for the analysis of gene expression data. The method is independent of the nature of the network, although they focus on the gene metabolic network. It is based on the hypothesis that genes close on the network are likely to be co-expressed, and consequently a biologically relevant signal can be extracted from noisy gene expression measurement by removing the "high-frequency" components of the gene

*Corresponding author email: awani@csub.edu

expression vector over the gene network. The extraction of the low-frequency component of a vector is a classical operation in signal processing that can be adapted to their problem using discrete Fourier transforms and spectral graph analysis. Wall *et al*. (2001) describes the gene expression analysis by Singular Value Decomposition (SVD), emphasizing initial characterization of the data. They described SVD methods for visualization of gene expression data, representation of the data using a smaller number of variables, and detection of patterns in noisy gene expression data. In addition, they described the precise relation between SVD analysis and Principal Component Analysis (PCA) where PCA is calculated using the covariance matrix.

Pique-Regil *et al*. (2005) propose a novel sequential DLDA (sequential Diagonal Linear Discriminant Analysis) technique that combines gene selection and classification. At each iteration, one gene is sequentially added and the linear discriminate (LD) recomputed using the DLDA model (i.e., a diagonal covariance matrix). Classical DLDA will add the gene with highest t-test score without checking the resulting model. In contrast, SeqDLDA will find the one gene that better improves class separation after recomputing the model parameters using a robust t-test score. They evaluate the new method in several 2-class datasets (Neuroblastoma, Prostate, Leukemia, and Colon) using 10-fold cross-validation and report better results. A generalized output-coding scheme has been applied to multiclass microarray classification by Shen and Tan (2006). With this, different coding strategies and decoding functions can be put into one single framework. The validity of various combinations has been verified. Support Vector Machine (SVM) was chosen as the binary classifier. Kim and Cho (2006) proposed two different correlation methods for the generation of feature sets to learn ensemble classifiers. Each ensemble classifier combines several other classifiers that learn from different features to classify cancer precisely. They adopted several feature selection methods. These feature selection methods included the Pearson's and Spearman's correlation coefficients, the Euclidean distance, the cosine coefficient, information gain, mutual information and signal-to-noise ratio. Experimental results show that two ensemble classifiers whose components are learned from different feature sets that are negatively or complementarily correlated with each other produce the good recognition rates on the chosen datasets.

A data-dependent kernel for microarray data classification was presented by Xiong *et al*. (2007). This kernel function is engineered so that the class reparability of the training data is maximized. A bootstrapping-based resampling scheme is introduced to reduce the possible training bias. Wang *et al*. (2007) use a hybrid huberized support vector machine (HHSVM). The HHSVM uses the huberized hinge loss function to measure misclassification and the elastic-net penalty to control the complexity of the model. They develop an efficient algorithm that computes the entire regularized solution path for HHSVM. They have applied their method to real microarray data and achieved promising results on both classification and gene selection.

In this work a different approach is used to solve the microarray classification problem. The approach is based on a Hybrid PCA (principal component analysis) and FDA (Fisher linear discriminant analysis) classification. The details of this approach are discussed in the next section. To increase the effective dimension of the projected subspace, the use of MDA (multiple discriminant analysis) instead of FDA (Fisher linear discriminant analysis) is explored in this work. The use of several subspaces, where data is incrementally projected, is proposed in this work. The resulting incremental hybrid PCA (principal component analysis) and MDA (multiple discriminant analysis) approach helped in enhancing the classification accuracy of the microarrays.

Hybrid Approach for Microarray Classification
A hybrid feature dimension reduction scheme that merges PCA and FDA algorithms in a unified framework was used. This hybridization of approach exploits the favorable attributes of these two methods while simultaneously avoiding their unfavorable attributes.

Principal component analysis (PCA) is a widely-used statistical technique. It works by replacing the original (numerical) variables with new numerical variables called "Principal Components", PCA captures the most descriptive features with respect to packing most "energy".

Fisher linear discriminant analysis (FDA) is a simple algorithm that is used for both dimension reduction and classification. In either case, FDA attempts to minimize the Bayes error by selecting the most discriminant feature vectors. It plays a key role in many research areas in science and engineering such as face recognition, image retrieval, and bioinformatics.

PCA and FDA, each has its own pros and cons. FDA deals directly with discrimination between classes, whereas PCA does not pay particular attention to the underlying class structure. When the data of each class can be represented by a single Gaussian distribution and share a common covariance matrix, FDA will outperform PCA. By contrast, when the number of samples per class is small or when the training data non-uniformly sample the underlying distribution, PCA might outperform FDA. In addition, FDA cannot classify small sample data effectively because a singular scatter matrix problem occurs when the number of the feature dimensions is large

compared to the number of training examples. Unfortunately, the sample sizes of microarray data are often relatively small.

A well-known technique that extracts invariant but descriptive features is the maximization of the formula [12]:

$$J(w) = \frac{|W^t S_1 W|}{|W^t S_2 W|}$$

W is the weight vector of a linear feature extractor and S_1 and S_2 are symmetric matrices designed such that they measure the desired information and the undesired noise along the direction W.

We can choose S_B to measure the separability of class centers (between-class variance), i.e., S_1, and S_W to measure the within-class variance, i.e., S_2. In this case, we recover the well-known FDA, where S_B and S_W are given by:

$$S_B = \sum_{j=1}^{C} N_j \cdot (m_j - m)(m_j - m)^T$$

$$S_W = \sum_{j=1}^{C} \sum_{i=1}^{N_j} (x_i^{(j)} - m_j)(x_i^{(j)} - m_j)^T$$

Where $\{x_i^{(j)}, i=1,\dots,N_j\}, j=1,\dots C$ are feature vectors of training samples, C is the number of classes, N_j is the number of the samples of the jth class, $x_i^{(j)}$ is the ith sample from the jth class, m_j is mean vector of the jth class, and m is grand mean of all examples.

We use S_1 as the covariance matrix S_Σ of all the samples and S_2 as the identity matrix. In this case, we recover the well-known PCA, where:

$$S_\Sigma = \frac{1}{C} \sum_{j=1}^{C} \frac{1}{N} \sum_{i=1}^{N_j} (x_i^{(j)} - m)(x_i^{(j)} - m)^T$$

Our optimal function will be:

$$W_{opt} = \arg \max_W \frac{|W^T[(1-\lambda) \cdot S_B + \lambda \cdot S_\Sigma]W|}{|W^T[(1-\eta) \cdot S_W + \eta \cdot I]W|}$$

Where λ, η are two parameters, S_Σ is the covariance matrix of all the training samples, and I is the identity matrix. The range of the parametric pair (λ, η) is from (0,0) to (1, 1).

With different (λ, η) values, the last equation provides a rich set of alternatives to PCA and FDA: $(\lambda=0, \eta=0)$

reduces to the full FDA; $(\lambda=1, \eta=1)$ recovers the full PCA. Clearly, FDA and PCA are the special cases in the hybrid PCA and FDA analysis. $(\lambda=0, \eta=1)$ gives a subspace that is mainly defined by maximizing the scatters among all the classes with minimal effort on clustering each class; $(\lambda=1, \eta=0)$ gives a subspace that mainly preserves the most energy while minimizing the scatter matrices of within-classes; $(\lambda=1/2, \eta=1/2)$ gives a subspace that is discriminative while preserving as much energy as possible, a trade-off between FDA and PCA. Table 1 summarizes these five special hybrid cases.

One approach to improve the accuracy of classification of the PCA-FDA algorithm is to project the given data to a higher dimension space. The use of Multiple Discriminant Analysis (MDA) instead of FDA can help to project data to a higher dimensional space. We will use this modification to result in a hybrid scheme that employs PCA and MDA in a unified framework.

Multiple discriminant analysis is an extension of discriminant analysis and a cousin of multiple analysis of variance (MANOVA), sharing many of the same assumptions and tests. MDA is used to classify a categorical dependent which has more than two categories, using as predictors a number of interval or dummy independent variables. MDA is a generalization of linear discriminant analysis (LDA). MDA is sometimes also called discriminant factor analysis or canonical discriminant analysis (Table 1).

Table 1. Special cases of PCA-FDA.

(λ, η)	Hybrid PCA-LDA analysis	Note
(0, 0)	$W_{opt} = \arg \max_W \dfrac{|W^T S_B W|}{|W^T S_W W|}$	LDA
(0, 1)	$W_{opt} = \arg \max_W \dfrac{|W^T S_B W|}{|W^T \cdot I \cdot W|}$	Hybrid PCA-LDA
(1, 0)	$W_{opt} = \arg \max_W \dfrac{|W^T S_\Sigma W|}{|W^T S_W W|}$	Hybrid PCA-LDA
(1, 1)	$W_{opt} = \arg \max_W \dfrac{|W^T S_\Sigma W|}{|W^T \cdot I \cdot W|}$	PCA
$(\frac{1}{2}, \frac{1}{2})$	$W_{opt} = \arg \max_W \dfrac{|W^T (S_B + S_\Sigma) W|}{|W^T (S_W + I) W|}$	Trade-off

Multiple discriminant analysis adopts a perspective similar to Principal Components Analysis, but PCA and MDA are mathematically different in what they are maximizing. MDA maximizes the difference between

values of the dependent, whereas PCA maximizes the variance in all the variables accounted for by the factor.

In this modification, the same equations stated in the PCA-FDA algorithm were used. Instead of projecting the data into a 1D space, we projected the data into a 2D space. This was done by using the two eigenvectors that corresponds to the largest two eigenvaluse to classify the samples in the dataset. Note that only one eigenvector was used to classify data in the PCA-FDA method.

As shown in the results section, the accuracy of classification of the proposed PCA-MDA method was better than PCA-FDA approach but it was not satisfactory enough. This was mainly due to the reason that the projected data representing the various classes overlapped. This problem can be solved by projecting the data into several subspaces using an incremental approach that is described below.

The incremental PCA and MDA approach projects data into several subspaces using various values of eigen values. Each eigen value results into a space with a particular orientation. The steps to obtain various subspaces are summarized below:

Initialize λ to 0.2 and $\Delta\lambda$ to 0.2.
1. Project data into a subspace with the current value of λ. Identify ranges of values in the projected subspace that discriminate positive and negative examples correctly.
2. Update λ to $\lambda + \Delta\lambda$.
3. Terminate the procedure if $\lambda >= 1$. Otherwise go to step 1.

The several subspaces obtained incrementally are used to classify the given data. This procedure proved to be more efficient than the hybrid approaches described above.

RESULTS AND DISCUSSION

The dataset chosen in this work is the same that was used by Alon *et al*. (1999). The data set is composed of 40 colon tumor and 22 normal colon tissue samples which were analyzed with an Affymetrix oligonucleotide array complementary to more than 6,500 human genes. A two-way clustering algorithm was applied to both the genes and the tissues, revealing broad coherent patterns that suggest a high degree of organization underlying gene expression in these tissues. 2000 genes were chosen to be the features for each sample. The tissues were taken from 40 patients. The training data set consist of 40 samples (26 tumor and 14 normal) and the testing data set consists of 22 samples (14 tumor and 8 normal).

In the hybrid PCA-FDA method, different combinations of λ, η have been used to find out the best combination. With $\lambda=0$ and $\eta=1$, 35 out of 40 samples were correctly

classified in the training data set and 15 out of 22 samples were correctly classified in the testing data set. With $\lambda=1$ and $\eta=0$, 24 out of 40 samples were correctly classified in the training data set and 16 out of 22 samples were correctly classified in the testing data set. With $\lambda=1/2$, $\eta=1/2$, 40 out of 40 samples were correctly classified in the training data set and 15 out of 22 samples were correctly classified in the testing data set.

The accuracy of classification of the Hybrid PCA-FDA method is summarized below:

In the hybrid PCA-MDA method, we have also tried the same combinations of λ, η as we have done in the hybrid PCA-FDA method. With $\lambda=0$ and $\eta=1$, 36 out of 40 samples were correctly classified in the training data set and 16 out of 22 samples were correctly classified in the testing data set. With $\lambda=1$ and $\eta=0$, 25 out of 40 samples were correctly classified in the training data set and 16 out of 22 samples were correctly classified in the testing data set. With $\lambda=1/2$ and $\eta=1/2$, 40 out of 40 samples were correctly classified in the training data set, 15 out of 22 samples were correctly classified in the testing data set.

The accuracy of classification of the Hybrid PCA-MDA method is summarized in table 2 and 3.

Table 2. PCA-FDA accuracy.

	$\lambda = 0, \eta = 1$		$\lambda = 1, \eta = 0$		$\lambda = \frac{1}{2}, \eta = \frac{1}{2}$	
	Train	Test	Train	Test	Train	Test
Accuracy	87.5%	68.18%	60%	72.7%	100%	68.18%

Table 3. PCA-MDA accuracy.

	$\lambda = 0, \eta = 1$		$\lambda = 1, \eta = 0$		$\lambda = \frac{1}{2}, \eta = \frac{1}{2}$	
	Train	Test	Train	Test	Train	Test
Accuracy	90%	72.73%	62.5%	72.7%	100%	68.18%

The accuracy of the PCA-MDA method is better than the PCA-FDA method in some cases and is the same in other. This increase in accuracy in PCA-MDA is due to the projection of data into a 2D space which had helped in separating the data in a way that most of the samples of the same class are closer together.

The accuracy of classification was further improved by using the incremental hybrid approach. The results of classifying the training set with this approach were 100% while as that of test data set was 91%.

CONCLUSION

In this paper, incremental hybrid approaches for microarray data classification were employed. First the paper discussed PCA (principal component analysis) and FDA (Fisher linear discriminant analysis) hybrid approach for classification and evaluated the approach by noting its accuracy on different values of λ and η. The

results were improved by modifying the above approach that enabled projecting the data to a higher dimensional space. This modification was based on a hybrid PCA (principal component analysis) and MDA (Multiple discriminant analysis) method. The modified method is shown to improve classification performance. The results were further improved by employing incremental hybrid approach. These results guide the development of a software system that will fully automate cancer diagnostic model. In future this will be used in clinics and health care facilities to achieve better treatment for cancer patients.

REFERENCES

Alon, U., Barkai, N., Notterman, DA., Gish, K., Ybarra, S., Mack, D. and Levine, AJ. 1999. Broad patterns of gene expression revealed by clustering analysis of tumor and normal colon tissues probed by oligonucleotide arrays. Proceedings of the National Academy of Sciences. 96(12):6745-6750.

Chai, H. and Domeniconi, D. 2004. An Evaluation of Gene Selection Methods for Multi-class Microarray Data Classification. Proceedings of the Second European Workshop on Data Mining and Text Mining in Bioinformatics. 3-10.

Hori, G., Inoue, M., Nishimura, S. and Nakahara, H. 2001. Blind gene classification based on ICA of microarray data. Proceedings of 3rd International Conference on Independent Component Analysis and Blind Signal Separation. San Diego. 332-336.

Kim, K. and Cho, S. 2006. Ensemble classifiers based on correlation analysis for DNA microarray classification. Neurocomputing . 70:187-199.

Pique-Regi1, R., Ortega, A. and Asgharzadeh, S. 2005. Sequential Diagonal Linear Discriminant Analysis (SeqDLDA) for Microarray Classification and Gene Identification. Proceedings of the 2005 IEEE Computational Systems Bioinformatics Conference–Workshop. 112-116.

Rapaport, F., Zinovyev, A., Dutreix, M., Barillot, E. and Vert, J. 2007. Classification of microarray data using gene networks. BMC Bioinformatics. 8:35.

Shen, L. and Tan, E. 2006. A Generalized Output-Coding Scheme With SVM For Multiclass Microarray Classification. Proceedings of 4th Asia-Pacific Bioinformatics Conference.

Wall, ME., Dyck, PA. and Brettin, TS. 2001. SVDMAN: Singular Value Decomposition Analysis of Microarray Data. Bioinformatics. 17:566-68.

Wang, L., Zhu, J. and Zou, H. 2007. Hybrid Huberized Support Vector Machines for Microarray Classification.

Proceedings of the 24th International Conference on Machine Learning. Corvallis, Oregon. 983-990.

Xiong, H., Zhang, Y. and Chen, X. 2007. Data-dependent Kernel Machines for Microarray Data Classification. IEEE/ACM Trans. Comput. Biology Bioinform. 583-595.

Zhang, J. and Deng, H. 2007. Gene selection for classification of microarray data based on the Bayes error. BMC Bioinformatics. 8:370.